Modèles multi-échelles pour les problèmes électromagnétiques transitoires non linéaires avec courants induits confinés

Antoine Marteau

To cite this version:

Antoine Marteau. Modèles multi-échelles pour les problèmes électromagnétiques transitoires non linéaires avec courants induits confinés. Energie électrique. Université Grenoble Alpes [2020-..], 2024. Français. NNT : 2024GRALT019 . tel-04603453

HAL Id: tel-04603453
https://theses.hal.science/tel-04603453v1

Submitted on 6 Jun 2024

THÈSE

Pour obtenir le grade de

DOCTEUR DE L'UNIVERSITÉ GRENOBLE ALPES

École doctorale : EEATS - Electronique, Electrotechnique, Automatique, Traitement du Signal (EEATS)
Spécialité : Génie électrique
Unité de recherche : Laboratoire de Génie Electrique

Modèles multi-échelles pour les problèmes électromagnétiques transitoires non linéaires avec courants induits confinés

Multiscale models for nonlinear transient electromagnetic problems with confined eddy currents

Présentée par :

Antoine MARTEAU

Direction de thèse :

Olivier CHADEBEC DIRECTEUR DE RECHERCHE, CNRS	Directeur de thèse
Gerard MEUNIER DIRECTEUR DE RECHERCHE EMERITE, CNRS	Co-directeur de thèse
Innocent NIYONZIMA MAITRE DE CONFERENCES, Université Grenoble-Alpes	Co-encadrant de thèse
Nicolas GALOPIN MAITRE DE CONFERENCES, Université Grenoble-Alpes	Co-encadrant de thèse

Rapporteurs :

Laurent DANIEL
PROFESSEUR DES UNIVERSITES, CentraleSupélec
Johan GYSELINCK
PROFESSOR, Université libre de Bruxelles

Thèse soutenue publiquement le **3 avril 2024**, devant le jury composé de :

Christophe GEUZAINE FULL PROFESSOR, Université de Liège	Président
Christian GEINDREAU PROFESSEUR DES UNIVERSITES, Université Grenoble-Alpes	Examinateur
Laurent DANIEL PROFESSEUR DES UNIVERSITES, CentraleSupélec	Rapporteur
Johan GYSELINCK PROFESSOR, Université libre de Bruxelles	Rapporteur
Olivier CHADEBEC DIRECTEUR DE RECHERCHE, CNRS	Directeur de thèse
Gérard MEUNIER DIRECTEUR DE RECHERCHE EMERITE, CNRS	Co-directeur de thèse

Invités :

Innocent NIYONZIMA MAITRE DE CONFERENCES, Université Grenoble-Alpes	Co-encadrant de thèse
Nicolas GALOPIN MAITRE DE CONFERENCES, Université Grenoble-Alpes	Co-encadrant de thèse

If people do not believe that mathematics is simple, it is only because they do not realize how complicated life is.

— John von Neumann

Remerciements

Cette thèse est le résultat d'un long travail qui a été rendu possible par la présence de nombreuses personnes dans mon entourage. Je tiens tout d'abord à remercier mes encadrants qui m'ont donné l'opportunité de travailler avec eux sur ce sujet passionnant et m'ont accompagné :

- Innocent Niyonzima, pour ton enthousiasme et ta bonne humeur. Merci de m'avoir "tout appris" patiemment au début de la thèse et de ta disponibilité et de tes efforts quotidiens pour mener à bien ce long projet !
- Gérard Meunier, pour ton extrême gentillesse, humilité et écoute, ainsi que pour toutes les connaissances que tu as apportées.
- Olivier Chadebec, pour ta bienveillance, ton leadership et ton désir de partager ton expérience. Merci pour nos enrichissantes discussions et d'avoir fait l'effort de me transmettre un peu de ton pragmatisme et de ton efficacité.
- Nicolas Galopin, pour ta sympathie et tes précieux conseils et relectures.

Nous avons formé une super équipe et je vous suis très reconnaissant, j'espère que nous aurons l'occasion de travailler de nouveau ensemble et de se retrouver autour d'un verre de temps à autre.

I would also like to thank Janne Ruuskanen, Paavo Rasilo and Timo Tarhasaari for welcoming me in Tampere and for the fruitful collaboration, our exchanges had a significant impact on this thesis. Thanks Janne for introducing me to the Finnish way of sauna and crag climbing!

Je souhaite aussi adresser mes remerciements aux personnes qui ont accepté de constituer mon jury de thèse, les rapporteurs Johan Gyselinck et Laurant Daniel, ainsi que Christian Geindreau et Christophe Geuzaine le président du jury. J'ai été honoré de l'intérêt que vous avez porté pour mon travail et de vos retours positifs et j'ai apprécié nos échanges pendant la soutenance.

Merci aux collègues du G2Elab pour la super ambiance au labo, les pauses café et autres moments scientifiques et de convivialité. Merci entre autre à Laurent, Alberto, Léo, Gauthier, Robin, Quentin, Maxime, Diego, Denis, Mayra, Bertrand, Valérie, Léa, Leo, Aitor, Anthony, Manqi... Merci aussi à Loic Rondot et Charles Dapogny.

Big up à mes amis de tout lieux et de tout temps, en particulier Gaëtan et les autres gallinacés en furie, le S.T. treize, JPP, les Païens, l'UCloc et ses satellites, le Champignon, l'Adrien & Benzouille le Magnifique et leurs moitié-es + l'Abouillotte, Jo, les requins du CSU, messieurs Hugon, et les autres. Merci pour les bons délires passés ensemble, comme en témoigne la précédente phrase. Une pensée pour Simon que j'aurai aimé pouvoir inviter à partager mon pot de thèse.

Enfin, je remercie mes parents et leurs moitié-es, ma sœur, mes grands parents et le reste de la famille pour leur important soutient et les moments de repos et de ressourcement passés en leur compagnie.

Antoine

Contents

List of Symbols

Domains

Ω	Physical domain
$\boldsymbol{x}$	Position in Ω (m)
ε	Fine scale charactesistic size (m)
Ω_{C}	($_{\mathrm{C}}$ subscript) conducting domain
Ω_{N}	($_{\mathrm{N}}$ subscript) non conducting domain
Ω_s	($_s$ subscript) domain with current source
Ω_ε	Heterogeneous domain
Ω_{H}	Homogenized Ω_ε domain
Ω_{M}	Macroscopic non heterogeneous domain
$\Gamma_{\varepsilon\backslash\mathrm{M}}$	Interface between Ω_{M} and Ω_ε
$\Gamma_{\mathrm{H}\backslash\mathrm{M}}$	Interface between Ω_{M} and Ω_{H}
Y	Periodic rectangular exaedric cell
$\boldsymbol{k}$	Cell period vector (m)
$\boldsymbol{y}$	Position in Y, $\boldsymbol{y} = \boldsymbol{0}$ is at its center.
γ_Y	Cell edges
∂Y	Cell faces
$\boldsymbol{n}$	Normal vector (to a surface)
$\boldsymbol{t}$	Tangential vector (to a line)

Fields

$\boldsymbol{h}$	(bold) vector or tensor fields
$\boldsymbol{H}$	(capitals) macroscopic field
$\boldsymbol{h}_p$	($_p$ subscript) periodic cell field
$\boldsymbol{h}_a$	($_a$ subscript) anti-periodic cell correction field
$\boldsymbol{h}_c$	($_c$ subscript) periodic correction cell field

$\boldsymbol{\nu}_M$	($_M$ subscript) macroscopic material property
$\mathcal{P}_{\mathrm{JL}}$	Instantaneous Joule losses power in Ω_ε, see eq. (3.8)
$\mathcal{P}_{\mathrm{em}}$	Instantaneous total electromagnetic power in Ω_ε, see eq. (3.10)

Operators

$\vert\bullet\vert$	Volume, surface, length of a 3D, 2D, 1D region
$\Vert\bullet\Vert$	Norm of a vector or scalar (field)
$\#\bullet$	Cardinality (number of elements)
$\langle \bullet \rangle_l$	Spatial smoothing at scale l, see eq. (2.8)
$\langle \bullet \rangle_Y$	Volume average on Y, see eq. (2.2)
$\langle \bullet \rangle_{\partial Y_\perp}$	Normal average on the boundary of Y, see eq. (2.26)
$\langle \bullet \rangle_{\gamma_Y}$	Tangential average on the edges of Y, see eq. (2.25)
$\langle \bullet \rangle_{\partial Y_\parallel}$	Tangential average on the boundary of Y, see eq. (2.80)
$\langle \bullet \rangle_{\mathrm{P}_Y}$	Average on the corners of Y, see eq. (2.24)

Acronyms

PDE	Partial Differential Equations
MQS	MagnetoQuasiStatic
BC	Boundary Condition
RHS	Right-Hand Side
LHS	Left-Sand Side
FEM	Finite Element Method
DoF	Degree of Freedom
TS	Time Step
TSpp	Time Step per period (of the source of the problem)
NR	Newton-Raphson (method)
TSM	Two Scale Method
SMC	Soft Magnetic Composite
HMM	Heterogeneous Multiscale Method
STR	Scale Transition Relation
FM-STR	Free-space to matter scale transition relation
HHD	Helmholtz Hodge Decomposition
IPE	Integral percentage Error, the percentage of error of the integral over $[0, T]$, see eq. (3.1)
L2PE	Percentage of $L^2([0, T])$ error, see eq. (3.2)

Function spaces on a (sub)domain Ω

$L^2(\Omega)$	Real functions with integrable square on Ω, $\{\Omega \ni x \to f(x) \in \mathbb{R} \text{ s.t. } \int_\Omega f^2(x)dx < \infty\}$
$\boldsymbol{L}^2(\Omega)$	Real vector functions with integrable square on Ω, $\{\Omega \ni x \to \boldsymbol{f}(x) \in \mathbb{R}^3 \text{ s.t. } \int_\Omega \boldsymbol{f}(x) \cdot \boldsymbol{f}(x)dx < \infty\}$
Basic sobolev spaces	
$H(\mathbf{grad};\Omega)$=$H^1(\Omega)$	$\{\varphi \in L^2(\Omega) \mid \mathbf{grad}\,\varphi \in \boldsymbol{L}^2(\Omega)\}$
$\boldsymbol{H}(\mathbf{curl};\Omega)$	$\{\boldsymbol{h} \in \boldsymbol{L}^2(\Omega) \mid \mathbf{curl}\,\boldsymbol{h} \in \boldsymbol{L}^2(\Omega)\}$
$\boldsymbol{H}(\mathrm{div};\Omega)$	$\{\boldsymbol{b} \in \boldsymbol{L}^2(\Omega) \mid \mathrm{div}\,\boldsymbol{b} \in L^2(\Omega)\}$
Sobolev spaces with null trace, with $\Gamma = \partial\Omega$ if omitted	
$H_{0,\Gamma}(\mathbf{grad};\Omega)$=$H^1_{0,\Gamma}(\Omega)$	$\{\varphi \in H(\mathbf{grad};\Omega) \mid \varphi\|_\Gamma = 0\}$
$\boldsymbol{H}_{0,\Gamma}(\mathbf{curl};\Omega)$	$\{\boldsymbol{h} \in \boldsymbol{H}(\mathbf{curl};\Omega) \mid \boldsymbol{h} \times \boldsymbol{n}\|_\Gamma = \mathbf{0}\}$
$\boldsymbol{H}_{0,\Gamma}(\mathrm{div};\Omega)$	$\{\boldsymbol{b} \in \boldsymbol{H}(\mathrm{div};\Omega) \mid \boldsymbol{b} \cdot \boldsymbol{n}\|_\Gamma = 0\}$
Sobolev spaces with null derivative	
$H(\mathbf{grad}\,\mathbf{0};\Omega)$	$\{\varphi \in H(\mathbf{grad};\Omega) \mid \mathbf{grad}\,\varphi = \mathbf{0}\}$
$\boldsymbol{H}(\mathbf{curl}\ \mathbf{0};\Omega)$	$\{\boldsymbol{h} \in \boldsymbol{H}(\mathbf{curl};\Omega) \mid \mathbf{curl}\,\boldsymbol{h} = \mathbf{0}\}$
$\boldsymbol{H}(\mathrm{div}\,0;\Omega)$	$\{\boldsymbol{b} \in \boldsymbol{H}(\mathrm{div};\Omega) \mid \mathrm{div}\,\boldsymbol{b} = 0\}$
Sobolev spaces with null derivative and trace	
$H_{0,\Gamma}(\mathbf{grad}\,\mathbf{0};\Omega)$	$H_{0,\Gamma}(\mathbf{grad};\Omega) \cap H(\mathbf{grad}\,\mathbf{0};\Omega)$
$\boldsymbol{H}_{0,\Gamma}(\mathbf{curl}\,\mathbf{0};\Omega)$	$\boldsymbol{H}_{0,\Gamma}(\mathbf{curl};\Omega) \cap \boldsymbol{H}(\mathbf{curl}\ \mathbf{0};\Omega)$
$\boldsymbol{H}_{0,\Gamma}(\mathrm{div}\,0;\Omega)$	$\boldsymbol{H}_{0,\Gamma}(\mathrm{div};\Omega) \cap \boldsymbol{H}(\mathrm{div}\,0;\Omega)$
Cell function spaces	
$\boldsymbol{H}^{\#}$, $\boldsymbol{H}^{\times}$	Y-periodic ($^{\#}$) and anti-periodic ($^{\times}$) fields, see page 90
$\boldsymbol{H}^{\#}_{0\gamma_Y}(\mathbf{curl};Y)$	Space of cell periodic nodal elements with null value at the cell corners, see eq. (2.49)
$\boldsymbol{H}^{\#}_{0\gamma_Y}(\mathbf{curl};Y)$	Space of cell periodic edge elements with null circulation on the cell edges, see eq. (2.50)
$\boldsymbol{H}^{\#}_{0\partial Y_\perp}(\mathrm{div};Y)$	Space of cell periodic facet elements with null flux through the cell faces, see eq. (2.51)
Discrete function spaces	
$\boldsymbol{H}_{\dots,h}(\Omega)$	$\boldsymbol{H}_{\dots}$ discretized with Whitney elements on Ω_h, see Section 1.3.2
$H_h(\mathbf{grad};\Omega)\backslash\mathbb{R}$	Space of gauged scalar potentials, see page 27
$\boldsymbol{H}_{0\tau_h,h}(\mathbf{curl};\Omega)$	Space of tree gauged vector potentials, see eq. (1.79)

Introduction

Electricity is massively used as an energy vector thanks to the very high efficiency involved in its conversions as well as its easy transport and distribution. Using the electric energy involves energy conversion systems such as electrical generators, motors, transformers and actuators. In these devices, the losses of energy are mainly of electromagnetic origin. They occur in particular in heterogeneous materials and structures, such as the windings and magnetic cores.

Figure 0.1: Electric transformer with laminated magnetic core (left) and magnetic composites (right)

Indeed, laminated materials have been traditionally used to reduce eddy current losses in motors, generators and transformers (see e.g. the left image in Figure 0.1). Subsequently, magnetic composites (right of the figure) have emerged as an alternative to laminated cores. These materials are obtained by compacting iron powders with a non-conducting matrix, leading to a globally magnetic material with insulated grains, which limits the eddy current losses.

Although the margin for gains in efficiency of electric devices is limited, any improvement leads to important global energy savings due to the number of devices used worldwide. Such improvement is greatly facilitated by efficient numerical tools able to predict the performances of new designs, especially the energy efficiency. The faster the simulation, the easier it is for the engineers to explore the design space and find better solutions.

However, the numerical modeling of heterogeneous materials is a significant challenge that presents, depending on the setting, up to four difficulties:

1. nonlinear and hysteretic behavior of the magnetic components
2. complex dynamic effects due to electromagnetic couplings: the eddy currents are difficult to compute (meshing of the skin depth), and may affect the overall magnetic behavior of the medium (dynamic hysteresis)
3. the multiscale 3D structure of these materials
4. and their possible stochastic geometric distribution

The wide range of available numerical techniques provide different tradeoffs between accuracy and computational costs. The more accurate and general techniques, such as the Finite Element Method (FEM), involve computing the electromagnetic fields maps. But they cannot directly handle the third difficulty because they require a fine scale discretization of the heterogeneous geometry, which leads to unsatisfiable needs in memory and computational power.

Instead, the current common practice in the industry is to use material models which approximate the overall behavior of the materials using fairly light parametric models, and are fitted with measurements made on material samples. They treat all the aforementioned difficulties, but their accuracy and extrapolation ability are limited.

A promising direction to further improve the accuracy is to study the multiscale modeling of electromagnetic fields. Initially developed by the mechanical engineering community, the so-called homogenization and multiscale computational methods have also proved their worth in electromagnetism. But to the extent of our knowledge, at the beginning of this work, they had mainly been used in linear time harmonic regime [1, 2, 3, 4, 5], or on 2D geometries only for problems taking magnetically nonlinear material laws into account [6, 7, 8, 9, 10, 11]. There were applications on 3D nonlinear magnetoquasistatic problems, but only in the specific case of laminated cores [12, 13, 14, 15].

The work that will be presented in this thesis aims to prove the capabilities of multiscale methods to solve 3D magnetoquasistatic transient problems featuring nonlinear magnetic behavior and strong dynamic effects, on periodic medium. We thus address the first three difficulties previously described. The work was made in the Electrical Engineering laboratory of Grenoble, the G2Elab, with a funding provided by the Université Grenoble-Alpes (UGA). This work also benefited from fruitful collaborations with three researchers from the Tampere university (TAU) in Finland, Janne Ruuskanen, Paavo Rasilo and Timo Tarhasaari, who are co-authors of our scientific publications.

On the numerical viewpoint, the work focuses on the heterogeneous multiscale method (HMM) [16, 17, 10]. It features solving for a macroscopic problem where the heterogeneous material is homogenized. The physical behavior of this homogenized domain is given by equivalent homogenized material laws computed from fine scale problems. The latter are solved on one spatial period of the material called the cell, such that the solutions accurately correspond to the initial problem. The cell problems are independent of each other and are solved in parallel, one is associated to each point of the macroscopic mesh where the homogenized law is needed.

HMM has the advantages to be quite general as it makes no assumptions on the direction of the fields nor the choice of fine scale material laws. Yet, it allows a drastic reduction of the computational costs, because the latter do not depend on how small the fine scale features are anymore. However, this method requires the possibility to define a smooth macroscopic field at the scale of the device. This assumption will be called the scale separation hypothesis in this thesis.

Magnetoquasistatic problems are usually solved using magnetic flux (B-)conforming formulations for which the unknown is the magnetic induction and where the magnetic field strength is computed via the material law, or the dual H-conforming formulations for which the roles are reversed. In addition to meeting the technical challenge of implementing and validating the HMM on 3D time dependent nonlinear problems, the main contribution of this thesis is to make the B-conforming formulations robust to the second difficulty mentioned earlier. It is the emergence of complex dynamic effects in the homogenized magnetic law due to electromagnetic couplings at the fine scale, in particular the confined eddy currents, that may be responsible for macroscopic dynamic hysteresis.

Indeed, Meunier *et al.* warned from 2008 [7, 4] that computing the macroscopic magnetic field strength and electric field strength using the standard method could fail in presence of strong confined eddy currents. Computing the macroscopic magnetic strength is tantamount to computing the macroscopic reluctivity, the capacity to do it is mandatory to use the B-conforming formulation in multiscale modeling.

To circumvent this issue, we propose a new definition of the transition from the fine scale fields to the macroscopic ones. It is close to the definition used in multiscale methods for high-frequency electromagnetic problems [18, 19, 20, 21]. Also, four new numerical implementations of the magnetic field upscaling are proposed. It will be numerically shown that the new definition is required to use the B-conforming formulation for problems where the fine scale eddy currents create dynamic hysteresis in the macroscopic magnetic law.

The thesis has been divided in three chapters which are organized as follows. The first one is dedicated to the modeling of electromagnetic fields, and to their numerical computation using the finite element method. For that, local and global Maxwell's equations, the main properties of electromagnetic fields as well as the different formulations are introduced. We also review the elementary techniques required to solve magnetoquasistatic problems such as the spatial discretization, the temporal discretization and the linearization of nonlinear equations.

The second chapter focuses on multiscale modeling. We first describe different materials and situations for which multiscale modeling is required in electrical engineering, and we review the existing methods used for the numerical computation of multiscale electromagnetic fields. Then, a multiscale model is derived all the way from the choice of equations and macroscopic fields definition to the numerical implementation. The method is based on HMM, and is valid on periodic media with an electrically insulated periodic cell. The discrete problems at each scale are discretized using the techniques introduced in chapter one. The original contributions to the model are the new scale transition relation defining the macroscopic fields, and four numerical techniques implementing the computation of the macroscopic magnetic strength field.

In the third and last chapter, we provide and analyze the results of the numerical experiments conducted to validate the proposed model, using the GetDP [22] and Gmsh [23] softwares. The behavior of the cell problem alone is studied in the first section to validate that its H and B-conforming formulations are dual from each other, and to show that the proposed upscaling techniques behave as expected. In the second section, the accuracy of the proposed B-conforming multiscale formulation is validated on 3D transient magnetoquasistatic problems, featuring linear and nonlinear materials laws at the fine scale. We show the robustness of the method in the presence of strong skin effect and dynamic hysteresis in the homogenized magnetic law. We also validate the convergence properties of the multiscale method and apply it to a problem which cannot be solved using standard FEM.

Chapter 1

Electromagnetic fields modeling

In this work, we study electromagnetic problems at low and medium frequencies, which are used to model a wide range of the electromagnetic devices like electric machines, power transformers, etc.

This chapter aims at introducing the electromagnetic fields and their property, the fundamental equations that govern their behavior, the common formulations used to solve for these fields and how they are usually computed with the help of computers and the finite element method.

1.1 Nature and properties

Some remarks and notations

Before introducing the electromagnetic fields and the equations that govern them, we introduce some notations.

Our domain of study is an open set named Ω with a smooth boundary $\partial\Omega$.

The positions of the points of Ω are denoted $\boldsymbol{x}$. The coordinates of $\boldsymbol{x}$ are expressed in the usual Cartesian frame of reference with axes named x, y and z, with the Cartesian basis vectors denoted $\boldsymbol{e}_i$ for $i = \{x, y, z\}$.

We write vectors and tensors with bold font and scalars with regular font. For example, the writing of $\boldsymbol{x}$ in terms of its component on each axis is $\boldsymbol{x} = x\boldsymbol{e}_x + y\boldsymbol{e}_y + z\boldsymbol{e}_z$ where x, y, z are $\boldsymbol{x}$'s Cartesian coordinates.

In physics, *fields* are functions defined at each point $\boldsymbol{x}$ and at each time instant t of a defined space and time range. The explicit dependency of a field with space and time are often omitted for clarity, e.g. with $\boldsymbol{f}(x, t)$ can be written $\boldsymbol{f}(x)$ or $\boldsymbol{f}$.

A summary of the notations used in this document are available in the List of Symbols page 1.

1.1.1 Physics of the electromagnetic fields

Several models are available to describe the electromagnetic fields depending on the scale at which they are studied. In this thesis, we study the model of electromagnetism in continuous media which is valid from the microscale to wider scales, which enables to study the manufactured electromagnetic devices and their components up to the microscale. In particular, we will focus on the magnetoquasistatic problems, used for modeling in low frequency electromagnetic fields.

The Table A.1 in Appendix A.1 is a summary of the different electromagnetic quantities, including macroscopic quantities and fields, with their units in the international unit system.

Maxwell's equations

The heart of the electromagnetic model in continuous media are the four *Maxwell equations*. They are stated below in their *local* or *differential* version using the differential operators from vector field analysis. The operators definition and some explanation of their meaning will be given later in Section 1.1.3.

The four equations are:
the *Maxwell-Ampère* law

$$\mathbf{curl}\,\boldsymbol{h} = \partial_t \boldsymbol{d} + \boldsymbol{j}, \tag{1.1}$$

the *Maxwell-Faraday* law

$$\mathbf{curl}\,\boldsymbol{e} = -\partial_t \boldsymbol{b}, \tag{1.2}$$

the *Maxwell-Gauss* conservation law for *electricity*

$$\operatorname{div} \boldsymbol{d} = \rho, \tag{1.3}$$

and the *Maxwell-Gauss* conservation law for *magnetism*

$$\operatorname{div} \boldsymbol{b} = 0. \tag{1.4}$$

These equations can only be used if completed with additional relations between the fields.

Constitutive relations

The electromagnetic properties of continuous medium are most of the time determined by the relations between three couples of electromagnetic fields, $\boldsymbol{b}$ and $\boldsymbol{h}$, $\boldsymbol{j}$ and $\boldsymbol{e}$, and $\boldsymbol{d}$ and $\boldsymbol{e}$. Those *constitutive relations* or *constitutive laws* are commonly modeled using tensors, as follows.

The *permeability* tensor $\boldsymbol{\mu}$ links the magnetic flux density $\boldsymbol{b}$ with the magnetic field strength $\boldsymbol{h}$ with the relation

$$\boldsymbol{b} = \boldsymbol{\mu} \cdot \boldsymbol{h}. \tag{1.5}$$

It is also common to use the inverse law and consider the magnetic *reluctivity* tensor $\boldsymbol{\nu} = \boldsymbol{\mu}^{-1}$ with the relation

$$\boldsymbol{h} = \boldsymbol{\nu} \cdot \boldsymbol{b}. \tag{1.6}$$

When the relations are linear, the tensors are constant. But they can also be nonlinear, and should be written $\boldsymbol{b}(\boldsymbol{h}) = \boldsymbol{\mu}(\boldsymbol{h})\boldsymbol{h}$ or $\boldsymbol{h}(\boldsymbol{b}) = \boldsymbol{\nu}(\boldsymbol{b})\boldsymbol{b}$, but the dependency of the tensor with the variable is often omitted as in (1.5) and (1.6) to simplify the notations. To note, additional terms are necessary to account for hysteresis in the material law.

In conducting materials, the *conductivity* σ (assumed to be a scalar quantity in this thesis) links the electric current density $\boldsymbol{j}$ with the electric strength $\boldsymbol{e}$ with the relation

$$\boldsymbol{j} = \sigma \boldsymbol{e}, \tag{1.7}$$

or conversely, using the electric *resistivity* $\rho = \sigma^{-1}$, the relation is

$$\boldsymbol{e} = \rho \boldsymbol{j}. \tag{1.8}$$

Domains with conductivity equal to 0 are called nonconducting domains and denoted with a N subscript like Ω_{N}, conversely conducting domains are indicated with a C subscript like Ω_{C}.

Finally, the relation between the electric displacement $\boldsymbol{d}$ and the electric field strength $\boldsymbol{e}$ is described with the *permittivity* tensor $\boldsymbol{\varepsilon}$ by

$$\boldsymbol{d} = \boldsymbol{\varepsilon} \cdot \boldsymbol{e}. \tag{1.9}$$

There exist fundamental scalar permeability μ_0 called *vacuum* (or *free space*) permeability. It is a physical constant which has the approximated value

$$\mu_0 = 4\pi.10^{-7} \simeq 1.256\,637\,06 \times 10^{-6}\ \mathrm{H.m^{-1}}. \tag{1.10}$$

Likewise, the *vacuum permittivity* ε_0 is the fundamental dielectric permittivity and has the approximated value

$$\varepsilon_0 = \frac{1}{\mu_0 c^2} \simeq 8.854\,187\,81 \times 10^{-12}\ \mathrm{F.m^{-1}}, \tag{1.11}$$

with $c = 299\,792\,458\ \mathrm{m.s^{-1}}$ the speed of light.

As μ_0 is the "basic" underlying permeability, a medium permeability is often described in terms of its relative permeability $\boldsymbol{\mu}_r$ such that

$$\boldsymbol{\mu} = \mu_0 \boldsymbol{\mu}_r. \tag{1.12}$$

We also introduce the *vacuum reluctivity* $\nu_0 = \frac{1}{\mu_0}$ and relative reluctivity $\boldsymbol{\nu}_r$ such that

$$\boldsymbol{\nu} = \nu_0 \boldsymbol{\nu}_r, \tag{1.13}$$

and the relative permittivity $\boldsymbol{\varepsilon}_r$ such that

$$\boldsymbol{\varepsilon} = \varepsilon_0 \boldsymbol{\varepsilon}_r. \tag{1.14}$$

Interface conditions

An interface is the common boundary of two different media. As the material laws are often discontinuous at the interfaces, the Maxwell equations lead to discontinuity of the fields' *traces* at the interfaces and to so-called *interface conditions*.

The notion of trace of a field is necessary not only to define the interface conditions, but also to define the boundary conditions, introduced in Section 1.2.1, and the integral forms of Maxwell's equations, introduced in Section 1.1.3.

Let $\boldsymbol{n}$ be the unit normal vector to a surface S. The normal trace of a vector field $\boldsymbol{f}$ on S is defined by $\boldsymbol{f}(x) \cdot \boldsymbol{n}(x)\big|_{x \in S}$, abbreviated $\boldsymbol{f} \cdot \boldsymbol{n}\big|_S$ or $\boldsymbol{f} \cdot \boldsymbol{n}$ if there is no ambiguity on S. The tangential trace of $\boldsymbol{f}$ on S is $\boldsymbol{f}(x) \times \boldsymbol{n}(x)\big|_{x \in S}$ abbreviated $\boldsymbol{f} \times \boldsymbol{n}\big|_S$ or $\boldsymbol{f} \times \boldsymbol{n}$.

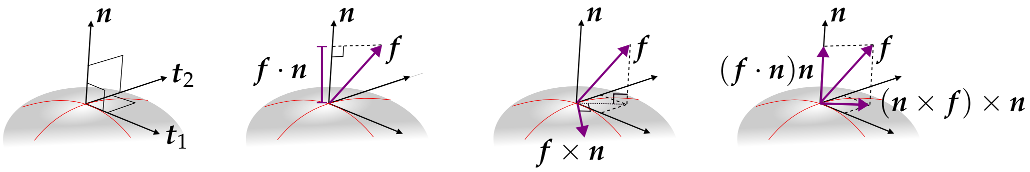

Figure 1.1: From left to right: a surface with a local frame with unit normal vector $\boldsymbol{n}$ and unit tangent vectors $\boldsymbol{t}_1$ and $\boldsymbol{t}_2$, the normal trace of a vector $\boldsymbol{f}$, the tangential trace of $\boldsymbol{f}$, the normal and tangential components of $\boldsymbol{f}$ such that $\boldsymbol{f} = (\boldsymbol{f} \cdot \boldsymbol{n})\boldsymbol{n} + (\boldsymbol{n} \times \boldsymbol{f}) \times \boldsymbol{n}$. The traces depend on the orientation of the surface, that is the choice of $\boldsymbol{n}$ or $-\boldsymbol{n}$ as outward direction, while the normal and tangential components do not.

Also, the trace of a scalar field φ on S is simply $\varphi(\boldsymbol{x})\big|_{\boldsymbol{x}\in S}$.

For an interface S between two media Ω_1 and Ω_2 with S oriented such that $\boldsymbol{n}\big|_S$ points towards Ω_1, the four interface conditions read

$$(\boldsymbol{h}_1 - \boldsymbol{h}_2) \times \boldsymbol{n}\big|_S = \boldsymbol{j}_S, \tag{1.15}$$

$$(\boldsymbol{e}_1 - \boldsymbol{e}_2) \times \boldsymbol{n}\big|_S = \boldsymbol{0}, \tag{1.16}$$

$$(\boldsymbol{d}_1 - \boldsymbol{d}_2) \cdot \boldsymbol{n}\big|_S = \rho_S, \tag{1.17}$$

$$(\boldsymbol{b}_1 - \boldsymbol{b}_2) \cdot \boldsymbol{n}\big|_S = 0, \tag{1.18}$$

where ρ_S is a surface charge density in C.m^{-2} and $\boldsymbol{j}_S$ is a surface current density in A.m^{-1} (it should not to be confused with source current $\boldsymbol{j}_s$), that is a current tangent to the surface ($\boldsymbol{j}_S \cdot \boldsymbol{n}\big|_S = 0$) and only defined on the interface using a Dirac distribution attached to the interface.

Magnetoquasistatic equations

This study is focused on the so-called low frequency inductive devices, i.e. they operate below few GHz of frequency and mainly driven by magnetism. Such devices can be electrical machines or low frequency power electronics and transformers. When modeling these devices, the displacement currents and medium dielectric permittivity can be neglected, leading to the following *magnetoquasistatic* (MQS) Maxwell equations

$$\begin{aligned} \mathbf{curl}\,\boldsymbol{h} &= \boldsymbol{j}, \\ \mathbf{curl}\,\boldsymbol{e} &= -\partial_t \boldsymbol{b}, \\ \operatorname{div} \boldsymbol{b} &= 0, \end{aligned} \tag{1.19}$$

that are completed with the constitutive laws (1.5) and (1.7).

Magnetostatic equations

At very low frequency or when the electric energy is negligible in comparison with the magnetic energy, the effect of Faraday law (1.2) in magnetoquasistatic equations is negligible and the equation can be removed. Then, plugging the ***b***-***h*** relation (e.g. (1.5)) into Maxwell Gauss's law for magnetism (1.4) leads to the system:

$$\begin{aligned} \mathbf{curl}\,\boldsymbol{h} &= \boldsymbol{j}_s, \\ \operatorname{div} \boldsymbol{b}(\boldsymbol{h}) &= 0, \end{aligned}$$

where the current should be known in advance and prescribed, it is thus named j_s for *source* current.

This couple of equations is called the *magnetostatic* equations. *Magneto* because it relates only to the magnetic fields and constitutive law, and *static* because the solutions are independent of the past as there is no time derivative anymore. The electric and magnetic behaviors are said to be decoupled.

1.1.2 Type of fields

In this section, the electromagnetic fields are classified in four categories that describe some of their essential properties, in particular the dimension of the geometric entities on which they can be integrated to yield their macroscopic physical meaning. These categories, further called *field types*, correspond to the *differential forms* of degree zero to three (also called 0-forms, 1-forms, 2-forms and 3-forms) defined by the de Rham - Hodge theory. The use of this framework in the computational electromagnetic community was pushed by Bossavit in [24], where he briefly introduces it and gives references for more detailed studies. Additionally, [25] explains how to translate between the differential form and the usual differential calculus language, and [26] reviews the theory and how it is used in engineering.

Beyond the power of the differential geometry framework to express the electromagnetism laws in a synthetic way compared to the usual differential calculus framework, adopting this point of view helps to understand what continuity naturally suits each type of electromagnetic field. But although we classify fields into these four types in order to be able to state only once the properties that are general to all fields of a given type, the equations in this thesis remain within the usual framework of differential calculus.

Potential fields

Scalar potential fields φ^0 (further called "scalar potentials" for shortness) are simply scalar function φ of space and time, this means that the value of φ^0 at a point $\boldsymbol{x}$, called $\varphi^0_{\boldsymbol{x}}$, is the scalar quantity defined by $\varphi^0_{\boldsymbol{x}} := \varphi(\boldsymbol{x})$, where ":=" denotes the definition of the left-hand side.

Usual potential fields in physics include altitude and temperature. In electromagnetism, we encounter the electric scalar potential v and magnetic scalar potential φ, that will be introduced in Section 1.2. These fields all share the following behavior.

Formally, a scalar potential φ^0 can be integrated on a set of oriented points P, e.g. $P = \{-\{\boldsymbol{a}\}, \{\boldsymbol{b}\}\}$, where the signs refer to the point's orientations. Those orientations are useful to consistently describe the boundaries of oriented paths, e.g. if γ is an oriented path joining point $\boldsymbol{b}$ from point $\boldsymbol{a}$, we can write $\partial\gamma = \{-\{\boldsymbol{a}\}, \{\boldsymbol{b}\}\}$. The integral of φ^0 on P is defined by

$$\int_P \varphi^0 := -\varphi(\boldsymbol{a}) + \varphi(\boldsymbol{b}). \tag{1.20}$$

A potential field φ^0 is continuous (in space) when the associated scalar function φ is continuous. The continuity of potential fields matters because it impacts the smoothness of their gradient, and the latter are commonly used in computational electromagnetics.

Strength fields

A strength fields $\boldsymbol{h}^1$ is defined based on a vector field $\boldsymbol{h}$. The strength fields in electromagnetism are the magnetic field strength $\boldsymbol{h}$, the electric field strength $\boldsymbol{e}$, the magnetic vector potential $\boldsymbol{a}$ and the electric vector potential.

The strength fields are locally evaluated on infinitesimal paths by averaging the associated vector field tangentially to the paths. For example, the value of a strength field $\boldsymbol{h}^1$ at $\boldsymbol{x}$ on an infinitesimal path $\boldsymbol{dl} = \boldsymbol{t}dl$, of direction $\boldsymbol{t}$ and length $dl = 2\varepsilon$, is the scalar quantity defined by

$$\boldsymbol{h}^1_{\boldsymbol{x}}(\boldsymbol{t}\,dl) := \int_{u\in[-\varepsilon,\varepsilon]} \boldsymbol{h}(\boldsymbol{x} + u\boldsymbol{t}) \cdot \boldsymbol{t}\,du \underset{\varepsilon\to 0}{\sim} \boldsymbol{h}(x) \cdot \boldsymbol{t}\,dl.$$

A strength field $\boldsymbol{h}^1$ is tangentially continuous across a path γ at $\boldsymbol{x}_0 \in \gamma$ when its value $\boldsymbol{h}^1_x(\boldsymbol{t}\,dl)$ varies continuously with $\boldsymbol{x}$ in the vicinity of $\boldsymbol{x}_0$ for a fixed $dl > 0$, where $\boldsymbol{t}$ is the unit tangent vector to γ at $\boldsymbol{x}_0$.

The tangential continuity is related to the smoothness of the curl of strength fields, and is often required across interfaces, so for any direction $\boldsymbol{t}$ tangent to the interface. For example, Figure 1.2 illustrates a tangentially continuous strength field, and a discontinuous one. Their underlying vector fields and their values on vertical and horizontal paths are plotted.

The physical meaning of a strength field is given by its *path integrals*. The integral of $\boldsymbol{h}^1$ on a path $\gamma = \{\gamma(u) \mid u \in [0,1]\}$ is defined by

$$\int_\gamma \boldsymbol{h}^1 := \int_\gamma \boldsymbol{h} \cdot \boldsymbol{t}\,dl = \int_{u\in[0,1]} \boldsymbol{h}(\gamma(u)) \cdot \gamma'(u)du, \tag{1.21}$$

where $\boldsymbol{t} = \frac{\gamma'}{\|\gamma'\|}$ is the unit tangent vector to γ at a given point $\gamma(u)$, and dl corresponds to $\|\gamma(u)\|du$. But from now on, we will omit dl and write

$$\int_\gamma \boldsymbol{h} \cdot \boldsymbol{t} \tag{1.22}$$

the path integral (1.21). When γ is a closed path, (1.22) is called *circulation* of $\boldsymbol{h}$ along γ.

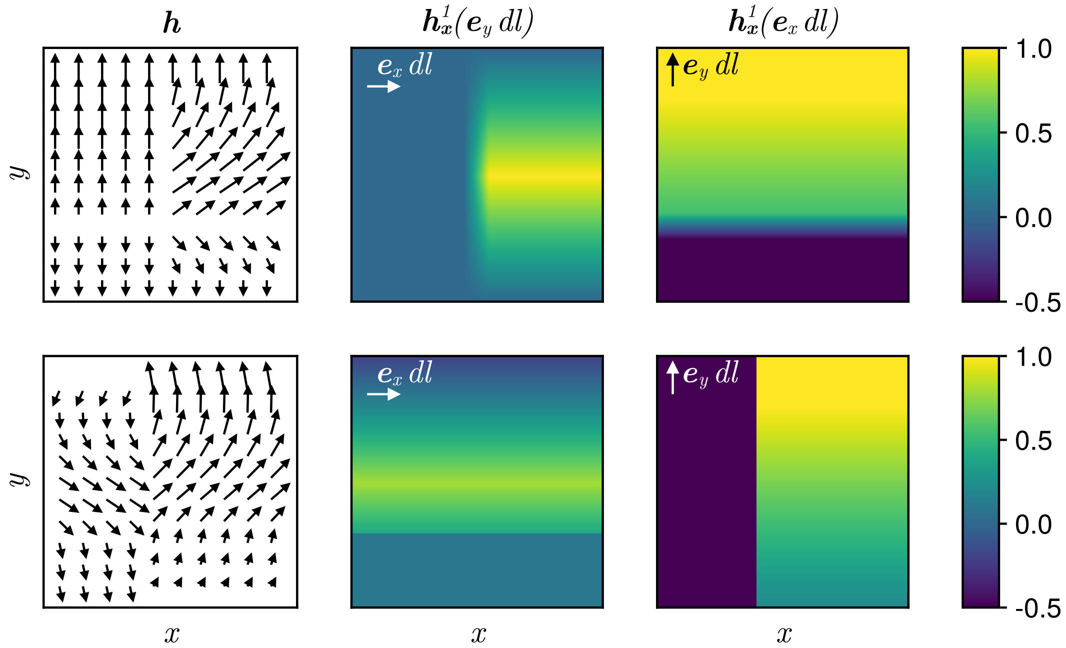

Figure 1.2: Example of tangentially continuous (top) and discontinuous (bottom) strength fields. The map of the values of the strength fields on horizontal infinitesimal paths with respect to the position is shown in the middle, and that on vertical infinitesimal paths on the left. We see that the bottom maps are discontinuous, showing that the bottom strength field is tangentially discontinuous.

Flux fields

Similarly to the strength fields, a *flux density field* $\boldsymbol{b}^2$ - that we abbreviate by *flux field* - is defined based on vector fields $\boldsymbol{b}$, but is not of the same nature. A flux field is locally evaluated on infinitesimal surfaces by averaging the underlying vector field normally to the surface. More precisely, the value of a flux field $\boldsymbol{b}^2$ at $\boldsymbol{x}$ on an infinitesimal surface $\boldsymbol{dS}$ of normal $\boldsymbol{n} = \boldsymbol{t}_1 \times \boldsymbol{t}_2$ and surface $dS = \varepsilon^2$ is the scalar defined by

$$\boldsymbol{b}^2_{\boldsymbol{x}}(\boldsymbol{n}\,dS) := \int_{u,v\in[-\varepsilon,\varepsilon]} \boldsymbol{b}(\boldsymbol{x}+u\boldsymbol{t}_1+v\boldsymbol{t}_2)\cdot\boldsymbol{n}\,du\,dv \underset{\varepsilon\to 0}{\sim} \boldsymbol{b}(\boldsymbol{x})\cdot\boldsymbol{n}\,dS.$$

The flux density fields in electromagnetism include the magnetic flux density $\boldsymbol{b}$, the free current density $\boldsymbol{j}$, the displacement current density $\partial_t \boldsymbol{d}$ and the Poynting vector $\boldsymbol{s} = \boldsymbol{e} \times \boldsymbol{h}$.

A flux field $\boldsymbol{b}^2$ is normally continuous across a surface S at $\boldsymbol{x}_0 \in S$ when its value $\boldsymbol{b}^2_{\boldsymbol{x}}(\boldsymbol{n}\,dS)$ varies continuously with $\boldsymbol{x}$ in the vicinity of $\boldsymbol{x}_0$ for a fixed $dS > 0$, where $\boldsymbol{n}$ is the unit normal vector to S at $\boldsymbol{x}_0$.

The normal continuity is related to the smoothness of the divergence of flux fields, it often required across interfaces. For example, Figure 1.3 illustrates the normal (dis)continuity of the flux fields associated with the same vector fields as those of Figure 1.2. It is important to note that the top vector field is a continuous strength field but a discontinuous flux field, and vice versa for the bottom one.

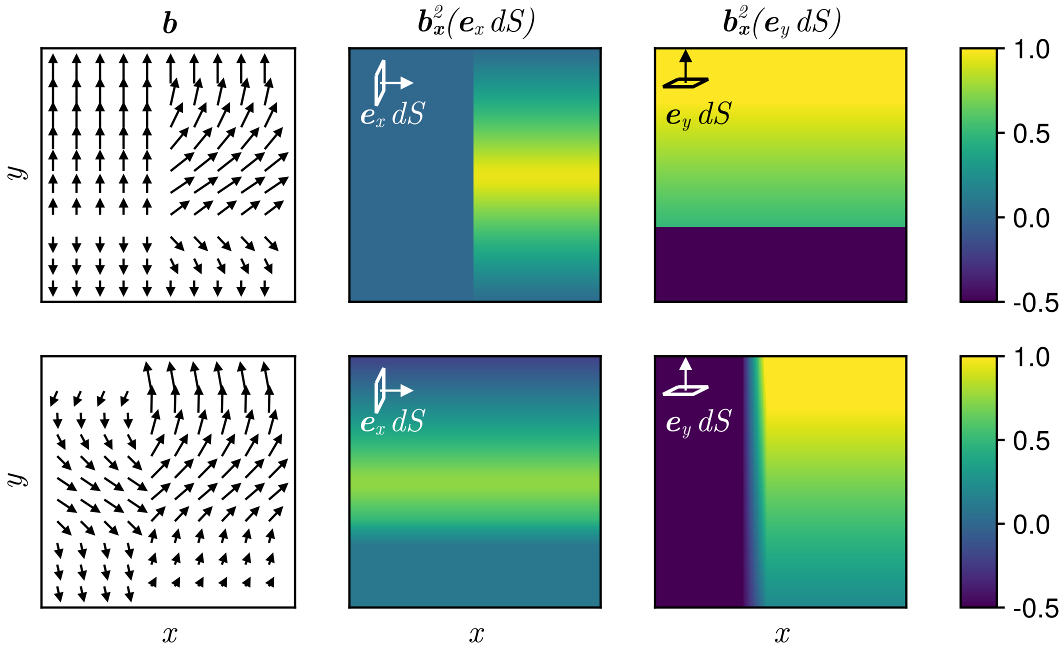

Figure 1.3: Example of normally discontinuous (top) and continuous (bottom) flux fields. The map of the values of the flux fields on infinitesimal surface normal to $\boldsymbol{e}_x$ with respect to the position is shown in the middle, and that on surfaces normal to $\boldsymbol{e}_y$ on the left. We see that the top maps are discontinuous, showing that the top flux field is normally discontinuous.

The physical meaning of a flux field is given by its *surface flux integrals*. The flux of $\boldsymbol{b}^2$ through a surface $S = \{\sigma(u,v) | u, v \in [0,1]\}$ is

$$\int_S \boldsymbol{b}^2 := \int_S \boldsymbol{b} \cdot \boldsymbol{n}\, dS = \int_{u,v \in [0,1]} \boldsymbol{b}(\sigma(u,v)) \cdot (\partial_u \sigma(u,v) \times \partial_v \sigma(u,v))\, du\, dv \tag{1.23}$$

where $\partial_u \sigma = \frac{\partial \sigma}{\partial u}$, $\partial_v \sigma = \frac{\partial \sigma}{\partial v}$ and $\boldsymbol{n} = \frac{\partial_u \sigma \times \partial_v \sigma}{\|\partial_u \sigma \times \partial_v \sigma\|}$ is the unit normal vector to S at a given point $\sigma(u,v)$, and dS corresponds to $\|\partial_u \sigma \times \partial_v \sigma\| du\, dv$.

In the rest of the manuscript, we will omit dS and write

$$\int_S \boldsymbol{b} \cdot \boldsymbol{n} \tag{1.24}$$

the flux (1.23).

Density fields

A *scalar density fields* ρ^3 - that we abbreviate by *density fields* - is represented by a scalar field ρ similarly to the potential fields, but they are not of the same nature. A density fields is locally evaluated of infinitesimal volume domains by averaging the associated scalar field in the volume. Indeed, the value of a density field ρ^3 at $\boldsymbol{x}$ on an infinitesimal cube of width ε is

$$\rho^3_{\boldsymbol{x}}(dV) := \int_{u,v,w\in[-\varepsilon,\varepsilon]} \rho(\boldsymbol{x} + u\boldsymbol{e}_x + v\boldsymbol{e}_y + w\boldsymbol{e}_z) du\, dv\, dw \underset{\varepsilon\to 0}{\sim} \rho(\boldsymbol{x})dV, \tag{1.25}$$

where dV represents the infinitesimal domain volume $8\varepsilon^3$.

There is no requirement on the continuity of ρ to ensure the continuity of ρ^3, the volume average already makes it smooth.

The physical meaning of the density field is given by its *volume integrals*. The integral of ρ^3 on a domain V reads

$$\int_V \rho^3 := \int_V \rho\, dV = \int_{(u,v,w)\in V} \rho(\,(u,v,w)\,)\, du\, dv\, dw, \tag{1.26}$$

where dV corresponds to $du\, dv\, dw$. From now on, we will omit dV and write

$$\int_V \rho \tag{1.27}$$

the integral (1.26).

There are many examples of density fields in physics, from the mass density field in mechanics to species volume concentrations in chemistry. In electromagnetism, the first that comes in mind is the electric charge density ρ. But there are many others, namely the energy and power densities:

- the magnetic energy density $\frac{1}{2}\boldsymbol{h}\cdot\boldsymbol{b}$, or $\frac{1}{2}\mu\, \boldsymbol{b}\cdot\boldsymbol{b}$ if μ is scalar,
- the magnetic power density $\boldsymbol{h}\cdot\partial_t\boldsymbol{b}$,
- the electric energy density $\frac{1}{2}\boldsymbol{e}\cdot\boldsymbol{d}$, or $\frac{1}{2}\varepsilon\, \boldsymbol{e}\cdot\boldsymbol{e}$ if ε is scalar,
- the electric power density $\boldsymbol{e}\cdot\partial_t\boldsymbol{d}$,
- the total electromagnetic energy density $\boldsymbol{u} = \frac{1}{2}(\boldsymbol{h}\cdot\boldsymbol{b} + \boldsymbol{e}\cdot\boldsymbol{d})$,
- the Joule losses power density $\boldsymbol{j}\cdot\boldsymbol{e}$, or $\sigma\boldsymbol{e}\cdot\boldsymbol{e}$ or $\rho\boldsymbol{j}\cdot\boldsymbol{j}$ if σ is scalar.

Hodge operator

To keep the consistency of the previously introduced model of the fields with Maxwell's equations, it should be noticed that the product of a field by a material law exchanges the type of the field. For example, the product by the conductivity σ and permeability $\boldsymbol{\mu}$ respectively change the strength fields $\boldsymbol{e}$ and $\boldsymbol{h}$ into the flux fields $\boldsymbol{j}$ and $\boldsymbol{b}$.

Conversely, the product by the resistivity ρ and reluctivity $\boldsymbol{\nu}$ change flux fields into strength fields. In theory of the differential forms, the material laws are called Hodge operators [24, 26].

1.1.3 Fields derivatives, Stokes theorem and global properties

Maxwell's equations and many electromagnetism relations are described using the differential operators gradient (**grad**), curl (**curl**) and divergence (div).

In this section, some properties of these differential operators related with the field types and field integrals are presented. In particular, we introduce the *generalized Stokes theorem* used to derive the global Maxwell equations, which are themselves useful to define the macroscopic electric and magnetic quantities like the current, the voltage, the flux, etc.

Formally, the generalized Stokes theorem [26] states that the integral of the exterior derivative $d\omega$ of a differential form ω over a domain $\mathcal{M}$ equals the integral of ω itself on the boundary of the domain $\partial\mathcal{M}$, that is

$$\int_{\mathcal{M}} d\omega = \int_{\partial\mathcal{M}} \omega. \tag{1.28}$$

To use the theorem on the electromagnetic fields, we need to replace the exterior derivative d with the appropriate differential operator **grad** , **curl** or div and to integrate on the appropriate type of domain (point, path, surface or volume) according to the type of field involved.

Gradient, path integral and voltage

A scalar potential is sometimes called a "grad conform" field because its natural derivative is the gradient operator. Scalar potentials are thus often taken in the function space $H^1(\Omega) = H(\mathbf{grad};\Omega)$.

The gradient of a scalar potential v is a strength field. Let γ be an oriented path from a point $\boldsymbol{a}$ to a point $\boldsymbol{b}$, which means that $\partial\gamma = \{\{\boldsymbol{b}\}, -\{\boldsymbol{a}\}\}$. We can integrate $\mathbf{grad}\, v$ along γ and apply the Stokes theorem to get

$$\int_{\gamma} \mathbf{grad}\, v \cdot \boldsymbol{t} = \int_{\partial\gamma} v = v(\boldsymbol{b}) - v(\boldsymbol{a}), \tag{1.29}$$

which is the so-called *gradient theorem for path integrals*.

In electrostatics, the electric field $\boldsymbol{e}$ is written as the gradient of an *electric scalar potential* v. The expressions of (1.29) then give the *voltage* between $\boldsymbol{a}$ and $\boldsymbol{b}$. This voltage can be computed with a path integral of $\boldsymbol{e}$ on any path linking $\boldsymbol{a}$ to $\boldsymbol{b}$ as the right-hand side (RHS) is clearly independent of γ, $\boldsymbol{e}$ is said to be *conservative*.

Curl, Stokes theorem and Ampère's circuital law

A strength field is sometimes called a "curl conform" field because its natural exterior derivative is the curl operator. Thus, strength fields are often taken in the function space $\boldsymbol{H}(\mathbf{curl};\Omega)$.

The curl of a strength field $\boldsymbol{h}$ is a flux field, and the generalized Stokes theorem (1.28) applies to its integral over a surface S and yields

$$\int_S \mathbf{curl}\,\boldsymbol{h}\cdot\boldsymbol{n} = \int_{\partial S} \boldsymbol{h}\cdot\boldsymbol{t} \tag{1.30}$$

which is the classic form of the *Stokes theorem*.

In magnetoquasistatic, one gets the *Ampère's circuital law* (also called *Ampère's theorem*) by applying theorem (1.30) to the magnetic field strength and combining it with Maxwell-Ampère law (1.19), it yields

$$I = \int_S \boldsymbol{j}\cdot\boldsymbol{n} = \int_{\partial S} \boldsymbol{h}\cdot\boldsymbol{t}. \tag{1.31}$$

Indeed, Ampère's theorem states that the current I going through a surface S equals the path integral of the magnetic field strength on the boundary of S. It is also called the *integral* or *global Maxwell-Ampère law*.

Divergence and Gauss's laws

A flux field is sometimes called a "div conform" field because its natural exterior derivative is the divergence. Thus, flux fields are often modelled as belonging to the function space $\boldsymbol{H}(\mathrm{div};\Omega)$.

The divergence of a strength field $\boldsymbol{d}$ is a density field, and the Stokes theorem applied to its integral over a domain V reads

$$\int_V \mathrm{div}\,\boldsymbol{d} = \int_{\partial V} \boldsymbol{d}\cdot\boldsymbol{n}, \tag{1.32}$$

this is called the *divergence theorem*.

Combining the divergence theorem where $\boldsymbol{d}$ is the electric displacement with the Maxell-

Gauss law for electricity (1.3) yields the Gauss law for electric charges

$$Q = \int_V \rho = \int_{\partial V} \boldsymbol{d} \cdot \boldsymbol{n}, \tag{1.33}$$

which states that the total charges Q contained in a given volume V equals the flux of the electric displacement threw its boundary. This is also called the *global Maxwell-Gauss* law for *electricity*.

The *global Gauss* law for *magnetism* is derived in the same way from (1.4) and reads

$$\int_{\partial V} \boldsymbol{b} \cdot \boldsymbol{n} = 0, \tag{1.34}$$

one says that the magnetic flux density $\boldsymbol{b}$ is *solenoidal* or *incompressible*. The physical interpretation of this law is that there exist no magnetic charges.

The divergence theorem also applies on the local Poynting theorem to give the global Poynting theorem, where the involved flux field is the Poynting vector $\boldsymbol{s} = \boldsymbol{e} \times \boldsymbol{h}$, an energy flux density.

Other properties and summary diagrams

To finish with this section on the nature and properties of the electromagnetic fields, two diagrams provide a summary of the main information. Figure 1.4 represents the properties of the four types of fields related to their exterior derivatives and integrals, and holds the necessary information to apply the Stokes theorem (1.28).

$$\begin{tikzcd}
\text{degree / dimension} & 0 & 1 & 2 & 3 & \\
& \varphi \arrow[r, "d", "\textbf{grad}"'] \arrow[dd] & \boldsymbol{h} \arrow[r, "d", "\textbf{curl}"'] \arrow[dd] & \boldsymbol{j}, \boldsymbol{d} \arrow[r, "d", "\mathrm{div}"'] \arrow[dd] & \rho \arrow[dd] & dd\bullet = 0 \\
\text{integrated on} & & & & & \\
& P & \gamma \arrow[l, "\partial"'] & S \arrow[l, "\partial"'] & V \arrow[l, "\partial"'] & \partial\partial\bullet = \emptyset \\
\text{fields values} & \varphi & \boldsymbol{h}\cdot\boldsymbol{t}\,dl & \boldsymbol{j}\cdot\boldsymbol{n}\,dS & \rho\,dV &
\end{tikzcd}$$

Figure 1.4: Summary of field types and geometric entities properties related to their exterior derivatives and integration introduced in subsections 1.1.2 and 1.1.3.

The two equations on the right of Figure 1.4 have not been introduced yet. The second one

$$\partial\partial\bullet = \emptyset \tag{1.35}$$

relates to geometric entities (paths, surfaces…) and means that all boundaries are closed.

For example, the boundary of a ball V is a sphere $S = \partial V$, and S has no boundaries, that is $\partial S = \emptyset$. S is called a *closed* surface.

Similarly, the first equation

$$dd\bullet = 0 \tag{1.36}$$

which is commonly known as

$$\mathbf{curl}\,\mathbf{grad}\bullet = \mathbf{0} \tag{1.37}$$

$$\mathrm{div}\,\mathbf{curl}\bullet = 0 \tag{1.38}$$

and is stated *"all exact forms are closed"* in the language of differential geometry. Equations (1.35) and (1.36) are the base of the so-called Homology and Cohomology theories that are useful to work with potentials, which are essential in computational electromagnetism [24]. They also help to define the different *Helmholtz-Hodge decompositions* (HHD), which will be used to analyze the properties of the fine scale fields in Section 2.3.2. The HHD detailed in [25, 27], and its numerical implementation is deeply studied in [28].

The (co)homology theories mainly introduce three concepts of interest for us, we cannot explicitly define theme here and refer again to [24, 25, 26]. But an overview of the useful notations can be given. The homology groups $\mathcal{H}_n(\Omega)$ contain sets of geometric entities of Ω of dimension $n = 0, 1, 2, 3$, which respectively are (particular) points, closed paths, closed surface and volumes. The de Rham cohomology groups $\mathcal{H}^n(\Omega)$ contain sets of harmonic fields of degree n. Harmonic fields of degree 1 and 2 are fields with vanishing curl and divergence, and the $\mathcal{H}^n(\Omega)$spaces for a 3D domain Ω can usually be defined by

$$\begin{aligned}
&\mathcal{H}^0(\Omega) = \{\text{constant scalar on connected components of } \Omega\},\\
&\mathcal{H}^1(\Omega) = \{\ \boldsymbol{h_n} \text{ s.t. } \mathrm{div}\,\boldsymbol{h_n} = 0,\ \mathbf{curl}\,\boldsymbol{h_n} = \mathbf{0},\ \boldsymbol{n}\cdot\boldsymbol{h_n} = 0\},\\
&\mathcal{H}^2(\Omega) = \{\ \boldsymbol{h_t} \text{ s.t. } \mathrm{div}\,\boldsymbol{h_t} = 0,\ \mathbf{curl}\,\boldsymbol{h_t} = \mathbf{0},\ \boldsymbol{n}\times\boldsymbol{h_t} = \mathbf{0}\},\\
&\mathcal{H}^3(\Omega) = \emptyset.
\end{aligned} \tag{1.39}$$

The dimension of the (co)homology spaces are the so-called *Betti numbers* β_n. They verify $\beta_n = \dim(\mathcal{H}_n(\Omega)) = \dim(\mathcal{H}^n(\Omega))$, and usually have the following intuitive meaning: β_0 is the number of connected components of Ω, β_1 is the number of tunnels or handles that Ω forms, β_2 is the number of cavities enclosed by Ω.

The second diagram, in Figure 1.5, is a *Tonti diagram* [24, 29]. It specifically represents the relations between the electromagnetic fields in terms of spatial/exterior derivatives (up/down movement in the graph), time derivatives (behind/front) and duality by Hodge operator (left/right, including the constitutive relations).

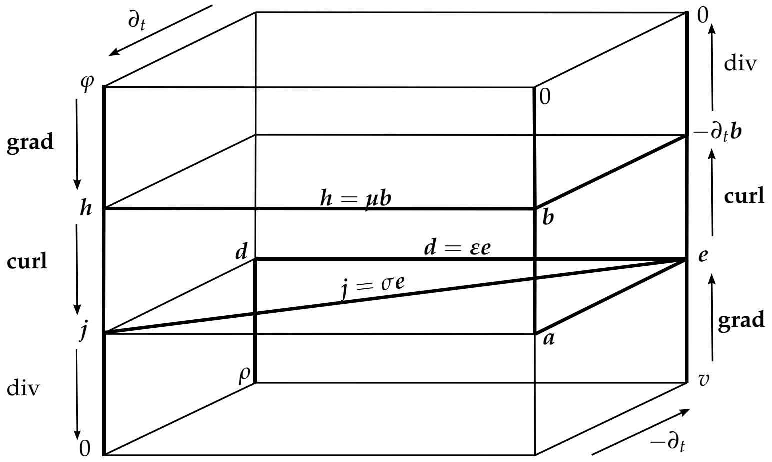

Figure 1.5: Tonti diagram for the electromagnetic fields (inspired from [10, Figure 2.8]). The thick lines represent actual equality relations in MQS or statics.

1.2 Usual formulations

Section 1.1 introduced some general properties of the electromagnetic fields. The current section will focus on describing how these notions are assembled in sets of equations - called *formulations* used to model the behavior of actual devices in electrical engineering.

1.2.1 Usual boundary conditions

In any partial differential equation (PDE) model, it is necessary to specify the so-called *boundary conditions* (BC). They are relations that relate to the field traces at the domain boundaries to ensure that the problem is well-defined, namely that the solution is unique and has the expected physical properties. Different boundary conditions commonly used in magnetoquasistatic (MQS) and their physical meaning are presented next.

Null normal magnetic flux density

This condition is used on boundary far from the device where the fields vanish to ensure that there are no magnetic flux leakages. When the problem is symmetric with an anti-symmetry of the current sources, the induction is tangential to the symmetry plane and the null normal magnetic flux condition also applies, as illustrated in Figure 1.6.

The condition reads

$$\boldsymbol{b} \cdot \boldsymbol{n}\big|_{\Gamma_b} = 0 \tag{1.40}$$

where $\Gamma_b \subset \partial\Omega$ is the aforementioned boundary.

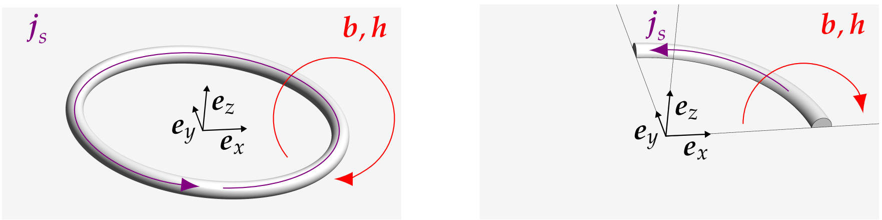

Figure 1.6: Geometry of a coil with current source j_s surrounded by air with exterior boundary. This geometry admits three symmetry planes: $P_x = \{x = 0\}$, $P_y = \{y = 0\}$ and $P_z = \{z = 0\}$. b and h (which are collinear in air) are normal to P_z (the plane of current symmetry), and tangent to the others. Only 1/8th of the geometry is necessary for the computation, if the boundaries $\Gamma_b = P_x \cup P_y$ and $\Gamma_h = P_z$ are added.

Null tangential magnetic field strength

When the geometry is cut on a symmetry plane $\Gamma_h \subset \partial\Omega$ which is a symmetry plane for the current (e.g. P_z in Figure 1.6), the normal current to the plane is 0 because otherwise it would be discontinuous. Similarly, the tangential component of the magnetic field is also 0, that is

$$h \times n\big|_{\Gamma_h} = \mathbf{0}, \tag{1.41}$$

$$j \cdot n\big|_{\Gamma_h} = 0. \tag{1.42}$$

Periodic boundary condition

When the geometry repeats itself or is invariant in one or several directions, it may not be necessary to consider the complete geometry. Instead, it is possible to cut it and apply *periodic boundary condition* to simulate the complete domain.

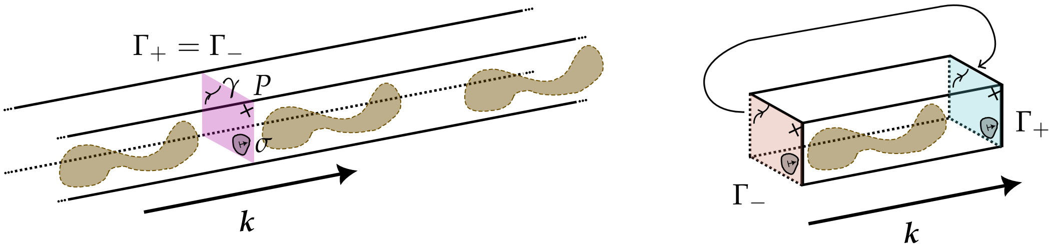

Figure 1.7: A periodic domain Ω of period k (left) and one periodic unit cell that generates it (right). Γ_+ and Γ_- correspond to one surface of Ω, so assuming that the fields had a unique value on any point P, path γ and surface σ, the values of the fields should be constant by translation from Γ_- to Γ_+ in the cut domain.

The periodic boundary Γ_p is then composed of two parts, Γ_+ and Γ_-, such that Γ_+ is the translation by a *period vector* k of Γ_-:

$$\Gamma_+ = \{x + k \mid x \in \Gamma_-\}.$$

The constraint to apply depends on the field type. The value of the field should be the same on translationally symmetric points, lines and surfaces of Γ_p. In other word, the field values should be unique on Γ_p if two copies of the periodic domain would be put side-by-side such that Γ_+ and Γ_- are stacked, as shown in Figure 1.7.

The *periodicity* of a scalar field φ, a strength field $\boldsymbol{h}$ and flux field $\boldsymbol{b}$ on Γ_p is respectively defined by

$$\begin{aligned} \varphi(\boldsymbol{x}+\boldsymbol{k})\big|_{\Gamma_+} &= \varphi(\boldsymbol{x})\big|_{\Gamma_-}, \\ \boldsymbol{h}(\boldsymbol{x}+\boldsymbol{k}) \times \boldsymbol{n}\big|_{\Gamma_+} &= \boldsymbol{h}(\boldsymbol{x}) \times \boldsymbol{n}\big|_{\Gamma_-}, \\ \boldsymbol{b}(\boldsymbol{x}+\boldsymbol{k}) \cdot \boldsymbol{n}\big|_{\Gamma_+} &= \boldsymbol{b}(\boldsymbol{x}) \cdot \boldsymbol{n}\big|_{\Gamma_-}. \end{aligned} \tag{1.43}$$

There is no constraint for scalar densities, as they cannot be evaluated on a boundary (a surface doesn't contain any volume).

Anti-periodic boundary condition

The *anti-periodic boundary conditions* on a periodic boundary $\Gamma_a = \Gamma_+ \cup \Gamma_-$ ($_a$ subscript means anti-periodic) are

$$\begin{aligned} \varphi(\boldsymbol{x}+\boldsymbol{k})\big|_{\Gamma_+} &= -\varphi(\boldsymbol{x})\big|_{\Gamma_-}, \\ \boldsymbol{h}(\boldsymbol{x}+\boldsymbol{k}) \times \boldsymbol{n}\big|_{\Gamma_+} &= -\boldsymbol{h}(\boldsymbol{x}) \times \boldsymbol{n}\big|_{\Gamma_-}, \\ \boldsymbol{b}(\boldsymbol{x}+\boldsymbol{k}) \cdot \boldsymbol{n}\big|_{\Gamma_+} &= -\boldsymbol{b}(\boldsymbol{x}) \cdot \boldsymbol{n}\big|_{\Gamma_-}. \end{aligned} \tag{1.44}$$

They may happen when the sources in the domain have alternating signs in two consecutive repetition of the periodic domain.

1.2.2 H-conforming formulations

There are numerous equations featuring different unknown fields in the electromagnetic problems description. But in order to solve for them, it is more convenient to eliminate several fields and equations by combining them while keeping one or two unknown fields. This leads to the definition of different *formulations* of the equations. The eliminated equations will be said to be strongly satisfied, while the equations that appear in the formulation that need to be solved for will be weakly satisfied.

The two main families of formulation choose to satisfy strongly either the left or right side of the Tonti diagram (Figure 1.5). We introduce first the H-conforming formulations, where the unknown will be the magnetic field strength $\boldsymbol{h}$ or the *magnetic scalar potential*

φ. The physical continuity properties of $\boldsymbol{h}$, the left side equations of the Tonti diagram and the material laws will be strongly respected.

This leads to approximate the right side quantities in the wrong space (e.g. $\boldsymbol{b}$ as a strength field), and to weakly satisfy the Faraday's law and Gauss's law for magnetism. The weakly satisfied laws are the ones it is necessary to solve for, as shown next in the derivation of the formulation.

Magnetoquasistatic formulation

The general magnetoquasistatic H-conforming formulation is derived by injecting $\boldsymbol{b} = \boldsymbol{\mu}\cdot\boldsymbol{h}$ (1.5), and $\boldsymbol{e} = \rho\boldsymbol{j} = \rho\,\mathbf{curl}\,\boldsymbol{h}$ (1.8)-(1.19) in Faraday and Gauss laws (1.2)-(1.4), which yields

$$\mathbf{curl}\,(\rho\,\mathbf{curl}\,\boldsymbol{h}) + \partial_t(\boldsymbol{\mu}\boldsymbol{h}) = \mathbf{0}, \tag{1.45}$$

$$\operatorname{div}\,(\boldsymbol{\mu}\cdot\boldsymbol{h}) = 0. \tag{1.46}$$

The formulation (1.45)-(1.46) is to be completed with appropriate boundary conditions, interface conditions and sources.

Magnetic scalar potential and gauge

In magnetostatics or in non-conducting regions, solving (1.46) is enough respectively because $\partial_t(\boldsymbol{\mu}\boldsymbol{h}) = \mathbf{0}$ or $\mathbf{curl}\,(\rho\,\mathbf{curl}\,\boldsymbol{h}) = \mathbf{0}$. In both cases, the unknown part of $\boldsymbol{h}$ is curl free and can be decomposed in the gradient of a magnetic scalar potential φ plus possibly a finite number of other terms $\boldsymbol{h}_{t,i}$, leading to the equation

$$\operatorname{div}(\,\boldsymbol{\mu}\cdot(-\mathbf{grad}\,\varphi + \boldsymbol{h}_{t,i})) = 0. \tag{1.47}$$

Indeed, $\mathbf{curl}\,\boldsymbol{h} = \mathbf{0}$ in a domain $\Omega_x \subset \Omega$ implies that

$$\boldsymbol{h} = -\mathbf{grad}\,\varphi + \boldsymbol{h}_{t,i} \tag{1.48}$$

where $\boldsymbol{h}_{t,i}$ for $i = 1, \ldots \beta_1$[1] lies in $\mathcal{H}^1(\Omega_x)$, the first cohomology group of Ω_x [24, 30]. Ways of dealing with the cohomology terms in practice are detailed in Section 1.3.5.

There is also a gauge issue for the potential φ. As the gradient of a constant is $\mathbf{0}$, $\mathbf{grad}\,(\varphi + C) = \mathbf{grad}\,\varphi$ for any field C constant on each connected components of Ω[2].

To uniquely define the scalar potentials φ, it is necessary to fix the degree of freedom (DoF) of the choice of C. It is for example possible to fix the potentials at one point of

---

[1] Ω_x forms β_1 tunnels, the first Betti number of the domain.

[2] The number of connected components of Ω_x is β_0, the zeroth Betti number of the domain.

each connected component of Ω, or to fix their average value over each. In any case, the corresponding function space for φ is called $H(\mathbf{grad};\Omega_x)\backslash\mathbb{R}^{\beta_0}$, where the ${}^{\beta_0}$ superscript is omitted when the domain is connected ($\beta_0 = 1$).

The space $H(\mathbf{grad};\Omega_x)\backslash\mathbb{R}^{\beta_0}$ is the smallest space that contain a potential for any gradient field in $\boldsymbol{H}(\mathbf{curl};\Omega_x)$ [31].

In practice, it often happens that there is a boundary of Ω_x where the potential is fixed with a Dirichlet BC. In this case, the scalar potential is already gauged.

Sources for H-conforming formulation

In general, a *source term* with an appropriate boundary condition (Dirichlet, Neumann, etc.) or by adding a term in the volume. In H-conforming formulation, in volumes where the current is known, the magnetic field can be split in a prescribed source $\boldsymbol{h}_s$ and an unknown *reaction field* $\boldsymbol{h}_r$ with

$$\boldsymbol{h} = \boldsymbol{h}_s + \boldsymbol{h}_r,$$

where $\boldsymbol{h}_r$ might be computed with a scalar potential φ.

Usually, $\boldsymbol{h}_s$ is deduced from a known current source distribution $\boldsymbol{j}_s$ to fullfill $\mathbf{curl}\,\boldsymbol{h}_s = \boldsymbol{j}_s$, e.g. by applying *Biot-Savart* formula

$$\boldsymbol{h}_s(\boldsymbol{x}) = \frac{1}{4\pi}\int_\Omega \frac{\boldsymbol{j}_s(\boldsymbol{y}) \times (\boldsymbol{x}-\boldsymbol{y})}{\|\boldsymbol{x}-\boldsymbol{y}\|^3} d\boldsymbol{y} \quad \forall \boldsymbol{x} \in \Omega. \tag{1.49}$$

Things are more complicated in case of coupled formulations with different set of equations on subset of Ω. The volume sources are not necessarily defined in each subdomain, and are then transmitted via tangential continuity of $\boldsymbol{h}$ through the subdomain boundaries.

In a nonconducting subdomain surrounding a coil fed with current $\boldsymbol{j}_s$, it is common to set the source by fixing $\boldsymbol{h}_{t,i}$ in (1.48) consistently with $\boldsymbol{j}_s$ to respect Ampère's law, possibly with a circuital equation [32, 33, 34].

1.2.3 B-conforming formulations

The B-conforming formulations respect strongly the right side of the Tonti diagram. The unknowns are the fields $\boldsymbol{b}$ and $\boldsymbol{e}$ (or more precisely $\boldsymbol{a}$ and v that are defined below). They are approximated in spaces strongly ensuring their continuity. The material laws and the right side equations (1.2)-(1.4) are strongly satisfied.

The weakly satisfied equations, the one the formulation is based on, is the Ampère law (1.19).

Magnetic vector potential

In order to strongly respect div $\boldsymbol{b} = 0$ (1.4) and eliminate it from the system, we introduce the *magnetic vector potential* (MVP) $\boldsymbol{a}$ such that

$$\boldsymbol{b} = \textbf{curl}\,\boldsymbol{a}. \tag{1.50}$$

$\boldsymbol{a}$ is a strength field and (1.50) always works because (1.4) is true everywhere in Ω (there can be no cohomology issue). Eq. (1.50) implies (1.4) as div $\textbf{curl}\,\boldsymbol{a} = 0$ (1.38).

Electric scalar potential

Faraday's law can also be eliminated from B-conforming formulations by introducing the *electric scalar potential* v.

In electrostatics, the time derivatives vanish and Faraday's law (1.2) becomes $\textbf{curl}\,\boldsymbol{e} = 0$. Similarly to the magnetic potential φ, the electric potential v is defined such that

$$\boldsymbol{e} = -\textbf{grad}\,v. \tag{1.51}$$

In MQS, v is defined in relation with $\boldsymbol{a}$. There is $-\partial_t \boldsymbol{b} = -\partial_t \textbf{curl}\,\boldsymbol{a} = \textbf{curl}\,(-\partial_t \boldsymbol{a})$, that lead to $\textbf{curl}\,(\boldsymbol{e}) = \textbf{curl}\,(-\partial_t \boldsymbol{a})$ due to (1.2). This means that $\boldsymbol{e}$ and $\partial_t \boldsymbol{a}$ can differ from a gradient, because $\textbf{curl}\,\textbf{grad}\,\bullet = 0$ (1.37). So v is then defined by

$$\boldsymbol{e} = -\partial_t \boldsymbol{a} - \textbf{grad}\,v. \tag{1.52}$$

Sometimes, like when modeling coils, the current is split in a known "source" part $\boldsymbol{j}_s$ and an unknown part $\sigma\boldsymbol{e}$, and the full expression of the current is

$$\boldsymbol{j} = \boldsymbol{j}_s - \sigma(\partial_t \boldsymbol{a} + \textbf{grad}\,v). \tag{1.53}$$

Both terms generally belong to different domains of the device.

Magnetoquasistatic formulation

Plugging $\boldsymbol{h} = \boldsymbol{\nu} \cdot \boldsymbol{b} = \boldsymbol{\nu} \cdot \textbf{curl}\,\boldsymbol{a}$ (1.6)-(1.50) and $\boldsymbol{j} = \boldsymbol{j}_s - \sigma(\partial_t \boldsymbol{a} + \textbf{grad}\,v)$ (1.53) into Ampère's law (1.19) yields the MQS B-conforming formulation

$$\begin{aligned} \textbf{curl}\,(\boldsymbol{\nu}\cdot\textbf{curl}\,\boldsymbol{a}) + \sigma(\partial_t \boldsymbol{a} + \textbf{grad}\,v) &= \boldsymbol{j}_s, \\ \text{div}(\boldsymbol{j}_s - \sigma(\partial_t \boldsymbol{a} + \textbf{grad}\,v)) &= 0, \end{aligned} \tag{1.54}$$

where the second equation is obtained by taking the divergence of the first one. This second equation is sometimes needed because there are two unknown fields in the formulation, it accounts for the conservation of the current.

As for H-conforming formulation, the boundary conditions, interface condition and optional volume sources are required.

As the choice of v is free, it is sometimes taken to be 0. The MVP is then noted $\boldsymbol{a}^*$, defined by $\boldsymbol{e} = -\partial_t \boldsymbol{a}^*$ and called modified MVP or "A star". The $\boldsymbol{a}^*$ formulation writes

$$\mathbf{curl}\,(\boldsymbol{\nu}\cdot\mathbf{curl}\,\boldsymbol{a}^*) + \sigma\partial_t\boldsymbol{a}^* = \boldsymbol{j}_s, \tag{1.55}$$

as the second equation is no more needed.

Magnetostatic formulation

In magnetostatics and in nonconducting domains, (1.54) is reduced to

$$\mathbf{curl}\,(\boldsymbol{\nu}\cdot\mathbf{curl}\,\boldsymbol{a}) = \boldsymbol{j}_s. \tag{1.56}$$

The equations (1.54) and (1.56) might coexist in different subdomains of Ω, in which case they are coupled by the (tangential) continuity of $\boldsymbol{a}$ at the domains interfaces.

Sources for B-conforming formulation

As stated above, the most frequent source in B-conforming formulation is to split $\boldsymbol{j} = \boldsymbol{j}_s - \sigma\partial_t(\boldsymbol{a} + \mathbf{grad}\,v)$ and to put the source $\boldsymbol{j}_s$ in the RHS.

In nonmagnetic regions (where $\boldsymbol{\nu} = \nu_0$), the source/reaction splitting $\boldsymbol{a} = \boldsymbol{a}_s + \boldsymbol{a}_r$ can be done [35, 36] where $\boldsymbol{a}_r$ is the reaction field and $\boldsymbol{a}_s$ is computed with Biot-Savart law, which then writes

$$\boldsymbol{a}_s(\boldsymbol{x}) = \frac{1}{4\pi\nu_0}\int_\Omega \frac{\boldsymbol{j}_s(\boldsymbol{y})}{\|\boldsymbol{x}-\boldsymbol{y}\|}dy \quad \forall \boldsymbol{x} \in \Omega. \tag{1.57}$$

It is also possible to use a $\boldsymbol{h}_s$ source by splitting $\boldsymbol{h} = \boldsymbol{h}_s + \boldsymbol{\nu}\mathbf{curl}\,\boldsymbol{a}_r$, where $\boldsymbol{h}_s$ is computed with (1.49), such that the first equation of (1.54) writes

$$\mathbf{curl}\,(\boldsymbol{\nu}\cdot\mathbf{curl}\,\boldsymbol{a}_r) + \sigma(\partial_t\boldsymbol{a}_r + \mathbf{grad}\,v) = -\mathbf{curl}\,\boldsymbol{h}_s.$$

Gauging the potentials

None of previously introduced φ and $\boldsymbol{a}$ have been properly defined, it is necessary to add appropriate *gauge conditions* to make them unique.

The electric scalar potential should be taken in $H(\mathbf{grad};\Omega)\backslash\mathbb{R}$ for the same reason given in Section 1.2.2 for the magnetic scalar potential φ.

Similarly, $\boldsymbol{a}$ is not uniquely defined until the gauge freedom of adding curl free fields is fixed. One possible gauge is the *Coulomb gauge*, defined by

$$\operatorname{div} \boldsymbol{a} = 0. \tag{1.58}$$

Another possibility is the Lorenz gauge, but it is not often used in MQS fields computation. But the more common gauges are set numerically after the discretization of the equations, they are detailed in Section 1.3.6.

The modified MVP $\boldsymbol{a}^*$ doesn't need a gauge in the conducting domain, only in the air or other nonconducting domains.

1.2.4 Other formulations

To finish with the formulation, we mention two other kind of formulations which are less commonly used. They both weakly satisfy Faraday and Ampère laws.

E-H conforming formulation

The $\boldsymbol{e} - \boldsymbol{h}$ formulation is often used in *high-frequency* problems [37], especially for homogenization [1, 2, 38], could also be used in magnetoquasistatic, under the form

$$\begin{aligned} \mathbf{curl}\, \boldsymbol{h} &= \sigma \boldsymbol{e}, \\ \mathbf{curl}\, \boldsymbol{e} &= -\partial_t \boldsymbol{\mu} \cdot \boldsymbol{h}, \end{aligned}$$

in conducting region, and $\operatorname{div}(\boldsymbol{\mu}\boldsymbol{h}) = 0$ (1.46) in nonconducting regions. This formulation doesn't feature differential operator composition in the conducting domain, so the order of spatial derivatives is 1 instead of 2, but it requires a couple of vector unknowns instead of one.

A-T conforming formulation

The $\boldsymbol{a} - \boldsymbol{t}$ formulations is rarely used but has been recently studied for multiscale formulations [39], so we quickly introduce it here. It reads

$$\begin{aligned} \mathbf{curl}\,(\boldsymbol{\nu} \cdot \mathbf{curl}\, \boldsymbol{a}) &= \mathbf{curl}\, \boldsymbol{t}, \\ \mathbf{curl}\,(\rho\, \mathbf{curl}\, \boldsymbol{t}) &= -\partial_t \mathbf{curl}\, a, \end{aligned}$$

in conducting region, and $\mathbf{curl}\,(\boldsymbol{\nu} \cdot \mathbf{curl}\, \boldsymbol{a}) = \mathbf{0}$ (1.56) in nonconducting regions. This formulation uses two vector potentials, which enables to strongly satisfy both Gauss's laws, but costs the approximation of the double spatial derivatives compared with the E-H formulation. But its main advantage is to use $\boldsymbol{e}(\boldsymbol{j})$ and $\boldsymbol{h}(\boldsymbol{b})$ material laws, which are hopefully easier to work with than the inverse laws $\boldsymbol{j}(\boldsymbol{e})$ and $\boldsymbol{b}(\boldsymbol{h})$ in highly nonlinear settings (superconductivity and or ferromagnetism).

1.3 Weak formulations and numerical modeling

This last section is devoted to the numerical modeling of electromagnetic fields, which is the approximation of the fields and their numerical computation on a computer. The main steps leading to the numerical resolution of the formulations introduced in the previous section are reviewed. Those steps are the derivation of the weak formulation, the space and time discretization of the equations using the finite element method and finite difference method, and finally the linearization of the nonlinear problem. These steps are then applied to both H and B-conforming formulations.

The chapter ends with an example showing the limits of the single scale FEM on a periodic geometry.

1.3.1 Weak formulations

The Galerkin method, a core principle of FEM [40], uses a weak formulation of the PDE as an intermediate step towards its discretization.

In general, the weak form of an equation is a version of the equation which is less restrictive than the original/strong form, so the solution of the strong form is a solution of the weak one, but the reverse is not necessary true. They are usually defined with a scalar product of the unknown field with so-called *test functions* that we will write with a $\bullet'$ symbol.

For PDE discretization, the standard framework is to model the fields in the Sobolev spaces $H(\mathbf{grad};,)$ $\boldsymbol{H}(\mathbf{curl};,)$ etc [40]. The scalar products of these spaces are based on that of L^2, the integral of the product of the fields : $< u,v >_{L^2} = \int uv$. Weak forms with integrals are convenient because they minimize the error in average in Ω rather than the error on the fields pointwise values. So they reduce the error on integral quantities that we are interested in.

They also lead to reduce the order of space derivatives with the following integration by part formulas:

$$\int_\Omega \operatorname{div} \boldsymbol{b}\ \varphi' = -\int_\Omega \boldsymbol{b} \cdot \mathbf{grad}\, \varphi' + \int_{\partial\Omega} \boldsymbol{b} \cdot \boldsymbol{n}\, \varphi' \tag{1.59}$$

for any $\boldsymbol{b}$ in $\boldsymbol{H}(\mathrm{div};\Omega)$ and φ' in $H^1(\Omega)$, and

$$\int_\Omega \mathbf{curl}\, \boldsymbol{h} \cdot \boldsymbol{a}' = \int_\Omega \boldsymbol{h} \cdot \mathbf{curl}\, \boldsymbol{a}' - \int_{\partial\Omega} \boldsymbol{h} \times \boldsymbol{n} \cdot \boldsymbol{a}' \tag{1.60}$$

for any $\boldsymbol{h}$ and $\boldsymbol{a}'$ in $\boldsymbol{H}(\mathbf{curl};\Omega)$.

With the standard Ritz-Galerkin method used in FEM, the test fields are taken in same space as the unknown field. There are many resources explaining the method and studying mathematically the equivalence of the weak and strong formulations [40, 34, 41, 30, 42].

$\boldsymbol{a}$-v weak formulation example

As a first example, the weak formulation of the $\boldsymbol{a}$-v (1.54) in the following setting described in Figure 1.8 is derived. The domain Ω includes a coil Ω_s fed with an imposed current $\boldsymbol{j}_s$, and a conducting domain Ω_C assumed disjoint from Ω_s (the conductivity of Ω_s is ignored as the current is known there). We assume the continuity of all fields at the subdomain interfaces, and that the exterior boundary has null magnetic flux and null tangential magnetic strength boundary conditions (1.40)-(1.41), namely $\partial\Omega = \Gamma_b \cup \Gamma_h$. The conducting domain's boundary is disjoint from Γ_b, but may have a comon part with Γ_h. We split it into $\partial\Omega_\mathrm{C} = \Gamma_{\mathrm{C}\backslash\mathrm{N}} \cup (\Gamma_h \cap \partial\Omega_\mathrm{C})$, where $\Gamma_{\mathrm{C}\backslash\mathrm{N}} = \partial\Omega_\mathrm{C} \cap \partial\Omega_\mathrm{N}$ is the interface between the conducting and the nonconducting domains.

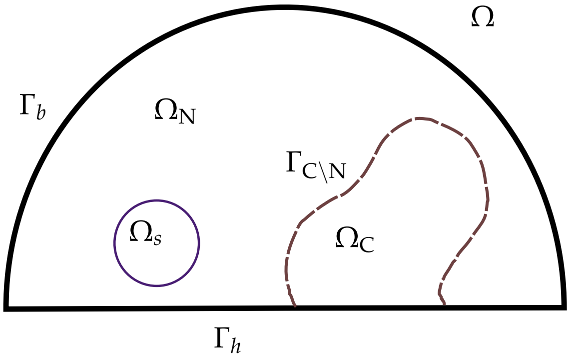

Figure 1.8: Sketch of the physical domain.

Each equation of (1.54) is integrated over Ω and multiplied by the appropriate test functions, respectively $\boldsymbol{a}'$ and v':

$$\int_\Omega \mathbf{curl}\,(\nu \cdot \mathbf{curl}\, \boldsymbol{a}) \cdot \boldsymbol{a}' + \int_{\Omega_\mathrm{C}} \sigma(\partial_t \boldsymbol{a} + \mathbf{grad}\, v) \cdot \boldsymbol{a}' = \int_{\Omega_s} \boldsymbol{j}_s \cdot \boldsymbol{a}',$$

$$\int_{\Omega_\mathrm{C}} \mathrm{div}(\sigma(\partial_t \boldsymbol{a} + \mathbf{grad}\, v))\, v' = 0,$$

where the integrals have been restricted to the domains where the terms are not necessarily zero.

Those two equations both contain a differential operator composition, respectively **curl**-**curl** and div-**grad**, that have to be split with respectively (1.60) and (1.59).

Using (1.60) with $\boldsymbol{\nu}\cdot\mathbf{curl}\,\boldsymbol{a}$ in place of $\boldsymbol{h}$ yields

$$\int_{\Omega} \mathbf{curl}\,(\boldsymbol{\nu}\cdot\mathbf{curl}\,\boldsymbol{a})\cdot\boldsymbol{a}' = \int_{\Omega} \boldsymbol{\nu}\cdot\mathbf{curl}\,\boldsymbol{a}\cdot\mathbf{curl}\,\boldsymbol{a}' - \int_{\partial\Omega} (\boldsymbol{\nu}\cdot\mathbf{curl}\,\boldsymbol{a})\times\boldsymbol{n}\cdot\boldsymbol{a}'.$$

The integral over $\partial\Omega$, called *boundary term* can be split on Γ_b and Γ_h, and we show that it is null. On Γ_h, the integrand vanishes as by definition $\mathbf{0} = \boldsymbol{h}\times\boldsymbol{n} = \boldsymbol{\nu}\cdot\mathbf{curl}\,\boldsymbol{a}\times\boldsymbol{n}$.

On Γ_b, one remarks that $\boldsymbol{a}\times\boldsymbol{n} = \mathbf{0}$ is sufficient to have $0 = \mathbf{curl}(\boldsymbol{a})\cdot\boldsymbol{n} = \boldsymbol{b}\cdot\boldsymbol{n}$. In fact, $\boldsymbol{a}\times\boldsymbol{n}$ could be the gradient of any surface potential, but only the curl of $\boldsymbol{b}$ matters, so one can choose to impose $\boldsymbol{a}\times\boldsymbol{n} = \boldsymbol{a}'\times\boldsymbol{n} = \mathbf{0}$ on Γ_b. By doing it, the triple product $(\boldsymbol{\nu}\cdot\mathbf{curl}\,\boldsymbol{a})\times\boldsymbol{n}\cdot\boldsymbol{a}' = -(\boldsymbol{a}'\times\boldsymbol{n})\cdot(\boldsymbol{\nu}\cdot\mathbf{curl}\,\boldsymbol{a})$ cancels, and the whole boundary term is removed.

To split the div-**grad** term, (1.59) is used in the conducting domain with $\sigma(\partial_t\boldsymbol{a} - \mathbf{grad}\,v)$ and v' in place of $\boldsymbol{b}$ and φ', we get

$$\begin{aligned}\int_{\Omega_{\mathrm{C}}} \operatorname{div}\sigma(\partial_t\boldsymbol{a} + \mathbf{grad}\,v)\; v' = &- \int_{\Omega_{\mathrm{C}}} \sigma(\partial_t\boldsymbol{a} + \mathbf{grad}\,v)\cdot\mathbf{grad}\,v' \\ &+ \int_{\partial\Omega_{\mathrm{C}}} \sigma(\partial_t\boldsymbol{a} + \mathbf{grad}\,v)\cdot\boldsymbol{n}\; v'.\end{aligned}$$

Again, the boundary term disappears. Indeed, the continuity of the current through the interface $\Gamma_{\mathrm{C}\backslash\mathrm{N}}$ with the null current in the nonconducting domain yields $0 = \boldsymbol{j}\cdot\boldsymbol{n}\big|_{\Gamma_{\mathrm{C}\backslash\mathrm{N}}}$. As there is also $\boldsymbol{j}\cdot\boldsymbol{n}\big|_{\Gamma_h} = 0$ by definition of Γ_h, we have $\sigma(\partial_t\boldsymbol{a} - \mathbf{grad}\,v)\cdot\boldsymbol{n}\big|_{\partial\Omega_{\mathrm{C}}} = 0$.

We finally get the following weak formulation of (1.54):
find $\boldsymbol{a}$ and v s.t.

$$\begin{aligned}\int_{\Omega} \boldsymbol{\nu}\cdot\mathbf{curl}\,\boldsymbol{a}\cdot\mathbf{curl}\,\boldsymbol{a}' + \int_{\Omega_{\mathrm{C}}} \sigma(\partial_t\boldsymbol{a} + \mathbf{grad}\,v)\cdot\boldsymbol{a}' &= \int_{\Omega_s} \boldsymbol{j}_s\cdot\boldsymbol{a}', \\ \int_{\Omega_{\mathrm{C}}} \sigma(\partial_t\boldsymbol{a} + \mathbf{grad}\,v)\cdot\mathbf{grad}\,v' &= 0, \quad \forall\boldsymbol{a}', v'\end{aligned} \tag{1.61}$$

where $\boldsymbol{a}$, $\boldsymbol{a}'$ are in $\boldsymbol{H}_{0,\Gamma_b}(\mathbf{curl};(\Omega))$ and v, v' are in $H(\mathbf{grad};\Omega_{\mathrm{C}})\backslash\mathbb{R}$. The formulation (1.61) would be the same if there were periodic or anti-periodic boundary conditions, only the function spaces in which the fields are defined change.

Although any solution of (1.61) yields correct $\boldsymbol{b}$ and $\boldsymbol{e}$, the solution is not unique due to the Gauge freedom. This $\boldsymbol{a}$-v formulation is commonly gauged after discretization as described in Section 1.3.6.

It is possible to mathematically study the equivalence of the strong and weak forms of the formulations [41, Section 3.3], or directly the existence and uniqueness of the solution of the weak forms, see [40].

1.3.2 Spatial discretization with Whitney finite elements

FEM consists in approximating the unknown field as the sum of polynomial basis functions with small support, leading to a sparse linear system when the weak formulation is discretized.

A finite element basis is defined on a mesh, which is a discretization of the domain. We note Ω_h a mesh approximating Ω. It is made of different entities, namely:

- 3D polyhedra called *elements* $\mathcal{K}(\Omega_h) = \{k_i \mid 1 \leq i \leq N_k\}$,
- 2D polyhedra *faces* $\mathcal{F}(\Omega_h) = \{f_i \mid 1 \leq i \leq N_f\}$,
- 1D *edges* $\mathcal{E}(\Omega_h) = \{e_i \mid 1 \leq i \leq N_e\}$,
- and 0D *nodes* (or *vertices*) $\mathcal{N}(\Omega_h) = \{n_i \mid 1 \leq i \leq N_n\}$,

where N_n, N_e, N_f and N_k are respectively the number of nodes, edges, faces and elements of the mesh.

The length h is the maximum radius of an element of Ω_h. In this work, we assume that all meshes are conforming, meaning all intersection of elements of the mesh is either empty or an entity of the mesh. Any boundary of a set of elements of same dimension of Ω_h is a set of lower dimension elements of Ω_h.

There are numerous possible finite element bases, they differ in the type of field they represent (scalar, vectors of forms), the geometric element on which they are defined, their regularity, their continuity at element boundaries, the degree of their polynomials and associated number of degrees of freedom (DoFs), etc.

Among all FEM spaces, the *Whitney elements* are frequently used in MQS. It is a family of finite elements using polynomial basis functions that respect the physical properties of each field type [43]. They were initially developed on so-called *simplicial* or *tetrahedral* meshes which contain only tetrahedra elements and triangular faces, but where generalized to other element types, including quadrangles, hexahedra and pyramids. The following paragraphs describe the four elements corresponding to the four types of field and their properties.

Nodal or Lagrangian elements

The Lagrangian finite element space $\mathcal{W}^0(\Omega_h)$ is a space of scalar function on Ω_h. It is also called *nodal elements* space because its *basis* functions (or *shape* functions) φ_i are defined for every node $n_i \in \mathcal{N}(\Omega_h)$ and are supported by the elements containing n_i (see Figure 1.9). The shape functions are defined such that their values at the mesh nodes are

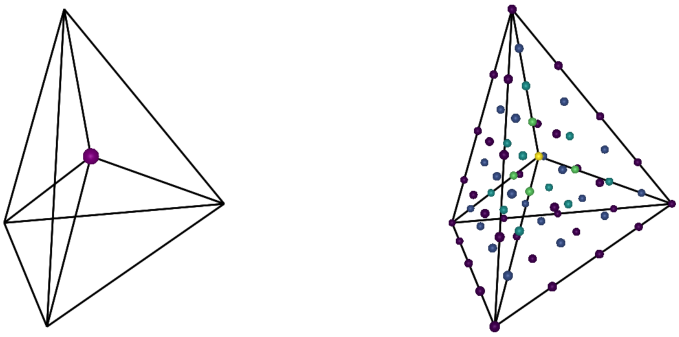

Figure 1.9: Nodal element basis function associated with the central node. The color of the dots indicate the scalar value at the point, the darker is 0 and the lighter color is 1 (at the central node).

$\varphi_i(n_j) = \delta_{ij}$. A field v in $\mathcal{W}^0(\Omega_h)$ can be decomposed in

$$v(\boldsymbol{x}) = \sum_i v_i \varphi_i(\boldsymbol{x}),$$

where v_i are the DoFs, the unknown of the FEM problem. Fields in $\mathcal{W}^0(\Omega_h)$ verify the node interpolation property

$$v(n_i) = v_i. \tag{1.62}$$

It can also be proven that each shape function is continuous on Ω_h independently of the others, and so is any v in $\mathcal{W}^0(\Omega_h)$. It is due to the fact that each nodal basis function is continuous on its support, and vanishes at its support boundary [24].

Finally, $\mathcal{W}^0(\Omega_h)$ is a space of continuous scalar function controlled by their values at points, like the electric scalar potentials v and magnetic scalar potential φ, having well-defined gradients. $\mathcal{W}^0(\Omega_h)$ is thus a finite dimensional subspace of $H^1(\Omega)$, which explains why it is the appropriate space to discretize the potential fields. Nodal elements are also called Whitney 0-forms.

Edge or Nedelec elements

The Nedelec finite element space $\boldsymbol{\mathcal{W}}^1(\Omega_h)$ [44] is the space for discretized strength fields on Ω_h. It is also called *edge elements* space as its shape functions $\boldsymbol{\varphi}_i$ are defined for every edge $e_i \in \mathcal{E}(\Omega_h)$ and supported by the elements containing e_i (see Figure 1.10). The shape functions are defined such that the values of the associated strength field on the

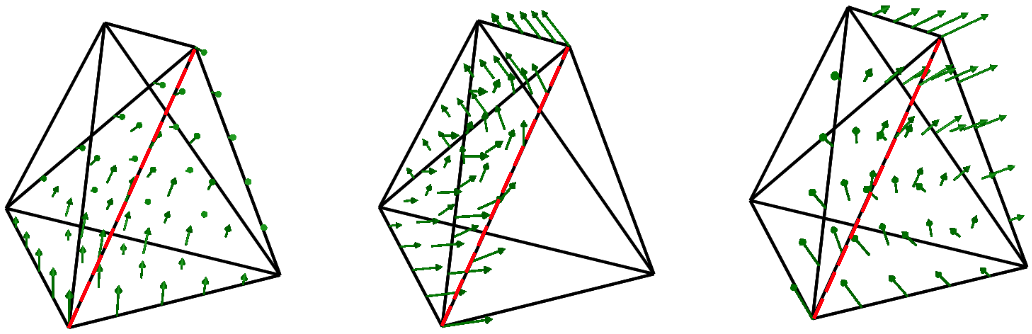

Figure 1.10: The edge element basis function associated to the central edge (in red), plotted separately in the three elements of its support.

mesh edges are $\int_{e_j} \boldsymbol{\varphi}_i(\boldsymbol{x}) \cdot \boldsymbol{t} = \delta_{ij}$. A field $\boldsymbol{h}$ in $\mathcal{W}^1(\Omega_h)$ is decomposed in

$$\boldsymbol{h}(\boldsymbol{x}) = \sum_i c_i \boldsymbol{\varphi}_i(\boldsymbol{x}),$$

where c_i are the DoFs, which are the path integral of $\boldsymbol{h}$ over edges e_i:

$$\int_{e_i} \boldsymbol{h}(\boldsymbol{x}) \cdot \boldsymbol{t} = c_i. \tag{1.63}$$

The edge shape functions are tangentially continuous across any path (and surface) in the volume of Ω_h, because they are continuous in the interior of the elements, tangentially continuous across the interior facets of their support, and their tangential traces vanish at their support boundary [24, 45]. However, they are not normally continuous.

We have seen that $\mathcal{W}^1(\Omega_h)$ (also called Whitney 1-forms) is a space of discrete continuous strength fields controlled by its path integral over the mesh edges, such as $\boldsymbol{h}$, $\boldsymbol{e}$, $\boldsymbol{a}$ and $\boldsymbol{t}$ (see page 15). Their curl is well-defined and $\mathcal{W}^1(\Omega_h)$ is a finite dimensional subspace of $\boldsymbol{H}(\mathbf{curl};\Omega)$.

Facet or Raviart-Thomas elements

The Raviart-Thomas finite elements space $\mathcal{W}^2(\Omega_h)$ [46] is the space for discretized flux fields on Ω_h. It is also called *facet elements* space as its shape functions $\boldsymbol{\varphi}_i$ are defined for every facet $f_i \in \mathcal{F}(\Omega_h)$ and supported by the elements containing f_i (Figure 1.11). The shape functions are defined such that the values of the associated flux fields through the mesh facets are $\int_{f_j} \boldsymbol{\varphi}_i(\boldsymbol{x}) \cdot \boldsymbol{n} = \delta_{ij}$. A field $\boldsymbol{b}$ in $\mathcal{W}^2(\Omega_h)$ is decomposed in

$$\boldsymbol{b}(\boldsymbol{x}) = \sum_i \phi_i \boldsymbol{\varphi}_i(\boldsymbol{x}),$$

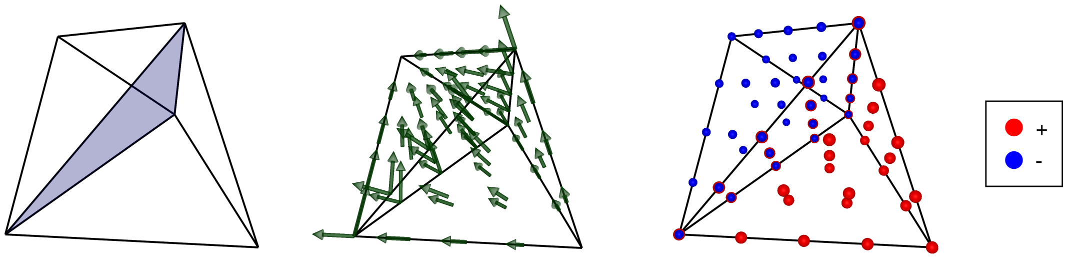

Figure 1.11: Facet element basis function (middle) associated to the interior facet (left), and its divergence (right).

where ϕ_i are the DoFs, which are the flux of $\boldsymbol{b}$ through facets f_i,

$$\int_{f_i} \boldsymbol{b}(\boldsymbol{x}) \cdot \boldsymbol{n} = \phi_i. \tag{1.64}$$

The facet shape functions are normally continuous across any surface in Ω_h, because they are continuous inside the elements, normally continuous across the facet in their support and are their normal trace vanish at their support boundary [24]. However, they are not tangentially continuous.

Finally, the Whitney 2-forms $\boldsymbol{\mathcal{W}}^2(\Omega_h)$, used to interpolate $\boldsymbol{b}$ and $\boldsymbol{j}$, are discrete continuous flux fields controlled by their flux through the mesh facets. Their divergence is well-defined, $\boldsymbol{\mathcal{W}}^2(\Omega_h)$ is a finite dimensional subspace of $\boldsymbol{H}(\mathrm{div};\Omega)$.

Volume elements

The lower possible degree for a polynomial representing continuous density field in Ω_h is simply a constant by element polynomial, as a density field is always continuous. The shape functions φ_i of the *volume elements* $\mathcal{W}^3(\Omega_h)$ are defined such that $\int_{k_j} \varphi_i(x) = \delta_{ij}$ for $k_j \in \mathcal{K}(\Omega_h)$, that is

$$\varphi_i(\boldsymbol{x}) = \frac{\mathbb{1}_{k_i}(\boldsymbol{x})}{\mathrm{vol}(k_i)}$$

where $\mathrm{vol}(k_i)$ is the volume of k_i and $\mathbb{1}_{k_i}$ is the indicator function of k_i.

A density field ρ in $\mathcal{W}^3(\Omega_h)$ is written

$$\rho(x) = \sum_i q_i \, \varphi_i(x), \tag{1.65}$$

where q_i are DoFs, which are the integrals of ρ over elements k_i,

$$\int_{k_i} \rho(x) = q_i. \tag{1.66}$$

But these shape functions have the particularity to have disjoint support, they are all orthogonal one from each other for the L^2 norm ($\int_{\Omega_h} \varphi_i \varphi_j = 0$ when $i \neq j$). So they cannot be used with usual Galerkin method and FEM. Instead, they are used with discontinuous Galerkin method or with the *finite volume method* (FVM) [47].

The Whitney element spaces are subspace of the Sobolev spaces, which are generally used to derive the weak formulations. Although many other FEM spaces could be used to discretize them, we will restrict ourselves to Whitney elements. In the rest of the document, we will write with a $_h$ subscript the Sobolev spaces discretized in the appropriate Whitney FEM space, e.g. $H^1_h(\Omega)$ is $\mathcal{W}^0(\Omega_h)$.

It is straightforward to discretize the Sobolev spaces with prescribed traces with the Whitney elements, one just has to fix the DoFs associated with the shape function supported by the boundary mesh entities.

1.3.3 Time discretization

There exist several types of methods to deal with the time variation and time derivatives of PDEs. Harmonic and multi-harmonic methods provide the best compromises to solve respectively linear and non-linear steady-state problems, because they use global basis functions [48]. More involved extensions exist to treat transient problems, but the study of the time discretization or of irregular or stiff time variations is not the aim of this work. We use the basic but general finite difference time discretization method, and we implicitly assume that the functions and fields vary smoothly in time, allowing us to exchange spatial and time derivatives.

We will use the θ-scheme method with θ a parameter in $[0, 1]$. It is a *finite difference* or *time stepping* scheme, which generalizes the explicit Euler ($\theta = 0$), implicit Euler ($\theta = 1$) and Crank-Nicolson ($\theta = 0.5$) methods. The solution will be computed at a set of time steps t_n, separated by a step size of $\Delta t = t_n - t_{n-1}$, with n the time instant number, also called time steps (TS) number.

The discretization of a time dependent ODE system $M\frac{d\boldsymbol{y}(t)}{dt} = \boldsymbol{f}(t, \boldsymbol{y}(t))$ with the θ-scheme reads

$$M\left(\boldsymbol{y}(t_n) - \boldsymbol{y}(t_{n-1})\right) = \Delta t\left[(1-\theta)\boldsymbol{f}(t_{n-1}, \boldsymbol{y}(t_{n-1})) + \theta \boldsymbol{f}(t_n, \boldsymbol{y}(t_n))\right] \tag{1.67}$$

where f is a vector functions and M a matrix.

By default, we use the method with $\theta = 1$ and omit the time dependency and the index of the current time step to write time discretized equation, e.g. (1.67) becomes

$$M\left(\boldsymbol{y} - \boldsymbol{y}^{n-1}\right) = \Delta t\, \boldsymbol{f}(y). \tag{1.68}$$

To note, only $\theta > 0.5$ may be used in the formulation studied in this work. Indeed, $\theta > 0.5$ is necessary when solving PDE systems where some derivative isn't defined in the full domain Ω, in other word, when M is not of maximum rank. This is the case for B-conforming MQS equations as the time derivative $\partial_t \boldsymbol{a}$ is not defined in the nonconducting domain Ω_{N}. Such equations are called Algebraic PDEs [49, 50].

Sometimes, when the convergence of a resolution is difficult, some adaptive time stepping can be used. The step size is shortened if the resolution converges badly, and sometimes extended is the convergence is very good. The step size $\Delta t_n = t_n - t_{n-1}$ thus depends on n.

For comparison with (multi-)harmonic methods, one should be careful that time stepping can introduce a time offset on the phase of the solution, as it is initialized to 0. Setting a very short first time step (or computing initial solutions to have consistent solution time derivative) can improve accuracy.

1.3.4 Resolution of nonlinear problem

Although it is convenient and often enough to approximate the material law tensors as constants, some problems require considering the nonlinearity of the material law. Common examples are the nonlinear magnetic response of ferromagnetic materials, or the variable electric conductivity with temperature.

But the nonlinear matrix system of equations that one gets after spatial and temporal discretization of a PDE is impossible to solve directly with a computer. So-called iterative linearization methods are required. We will use the classic *Newton-Raphson* (NR) method [51] in this work.

Let

$$\boldsymbol{F}(\boldsymbol{X}) = \boldsymbol{0} \tag{1.69}$$

be a nonlinear equation derived from a FEM formulation, where $\boldsymbol{X}$ is the unknown vector, and $\boldsymbol{F}$ is a vector function nonlinearly dependent on $\boldsymbol{X}$. The Newton-Raphson method at iteration $k+1$ consists in solving the linear system

$$\boldsymbol{J_F}^k \cdot (\boldsymbol{X} - \boldsymbol{X}^k) + \boldsymbol{F}^k = \boldsymbol{0}, \tag{1.70}$$

where $\boldsymbol{X}^k$ is the solution of the previous nonlinear iteration, $\boldsymbol{F}^k$ is $\boldsymbol{F}(\boldsymbol{X}^k)$ and ${\boldsymbol{J}_{\boldsymbol{F}}}^k = \frac{\partial \boldsymbol{F}}{\partial \boldsymbol{X}}(\boldsymbol{X}^k)$ is the Jacobian of $\boldsymbol{F}$ at $\boldsymbol{X}^k$. It is common to relax a Newton-Raphson iteration if the convergence is difficult, or to over relax in it is too fast. It means that the next iterate $\boldsymbol{X}^{k+1}$ is defined by

$$\boldsymbol{X}^{k+1} = \omega \boldsymbol{X} + (1-\omega)\boldsymbol{X}^k \tag{1.71}$$

where $\omega \in (0, 2)$ is the relaxation factor and $\boldsymbol{X}$ is solution of (1.70). A relaxation factor of $\omega = 1$ corresponds to unrelaxed NR, $\omega < 1$ to relaxed NR for difficult convergence and using $\omega > 1$ is called over relaxation to speed up an easy convergence. Several methods are available for choosing the relaxation factor, like linear or binary search or adaptive relaxation [52, 53].

If the series $\left(\boldsymbol{X}^k\right)_k$ converges, the limit is solution of the aforementioned problem (1.69). In practice, one or several *stopping criteria* are necessary to decide whether the method converged or not, e.g. the following:

$$\begin{array}{llcll}
\text{Residual norm} & \mathrm{R}(\boldsymbol{X}) & = & \|\boldsymbol{F}(\boldsymbol{X}^{k+1})\| & < \mathrm{R}_{\mathrm{tol}} \\
\text{Relative residual norm} & \mathrm{RR}(\boldsymbol{X}) & = & \frac{\|\boldsymbol{F}(\boldsymbol{X}^{k+1})\|}{\|\boldsymbol{F}(\boldsymbol{X}^{0})\|} & < \mathrm{RR}_{\mathrm{tol}} \\
\text{Increment} & \mathrm{I}(\boldsymbol{X}) & = & \|\boldsymbol{X}^{k+1} - \boldsymbol{X}^k\| & < \mathrm{I}_{\mathrm{tol}} \\
\text{Relative increment} & \mathrm{RI}(\boldsymbol{X}) & = & \frac{\|\boldsymbol{X}^{k+1} - \boldsymbol{X}^k\|}{\|\boldsymbol{X}^{k+1}\|} & < \mathrm{RI}_{\mathrm{tol}}.
\end{array}$$

To avoid multiplying the indices and equations, we may omit the NR index k and associated terms in the nonlinear problem formulations. Also, it often happens that some term $\boldsymbol{T}$ of the weak formulation do not contain any nonlinear step. In this case, the term is a linear function (at least integration and multiplication by the test function happen), so the differential ($\boldsymbol{X} \to \boldsymbol{J}_{\boldsymbol{T}} \cdot \boldsymbol{X}$) is the function $\boldsymbol{T}$ itself and (1.70) becomes $\boldsymbol{T}(\boldsymbol{X} - \boldsymbol{X}^k) + \boldsymbol{T}^k = \boldsymbol{T}(\boldsymbol{X}) - \boldsymbol{T}^k + \boldsymbol{T}^k = \boldsymbol{T}(\boldsymbol{X}) = \boldsymbol{0}$. So linear terms are left unmodified in the NR scheme for FEM.

We now have all the tools required to write the discrete form of the MQS formulations.

1.3.5 Discrete h-φ formulation

The weak form of the MQS problem (1.45)-(1.46) fully discretized with $\boldsymbol{h}$-φ formulation in the specific case of a massive inductor (where the current density distribution is unknown in the inductor) is given below for reference without deep explanation. We refer to [41, 30] for the details of the formulation derivation.

Find $\boldsymbol{h} \in \boldsymbol{H}_{0,\Gamma_h,h}(\mathbf{curl};\Omega_{\mathrm{C}})$ and $\varphi \in H_{0,\Gamma_h,h}(\mathbf{grad};\Omega_{\mathrm{N}})$ such that

$$\int_{\Omega_{\mathrm{C}}} \rho\, \mathbf{curl}\,(\boldsymbol{h}) \cdot \mathbf{curl}\, \boldsymbol{h}' + \int_{\Omega_{\mathrm{C}}} \frac{1}{\Delta t} \left(\boldsymbol{b}(\boldsymbol{h}) - \boldsymbol{b}^{n-1}\right) \cdot \boldsymbol{h}' = 0, \tag{1.72}$$

$$\int_{\Gamma_{\mathrm{C}\setminus\mathrm{N}}} \boldsymbol{h} \times \boldsymbol{n} \cdot \boldsymbol{h}' = \int_{\Gamma_{\mathrm{C}\setminus\mathrm{N}}} (\mathbf{grad}\, \varphi + \boldsymbol{h}_t) \times \boldsymbol{n} \cdot \boldsymbol{h}', \tag{1.73}$$

$$\int_{\Omega_{\mathrm{N}}} \boldsymbol{b}(\mathbf{grad}\, \varphi + \boldsymbol{h}_t) \cdot \mathbf{grad}\, \varphi' = 0, \tag{1.74}$$

for all $\boldsymbol{h}' \in \boldsymbol{H}_{0,\Gamma_h,h}(\mathbf{curl};\Omega_{\mathrm{C}})$ and all $\varphi' \in H_{0,\Gamma_h,h}(\mathbf{grad};\Omega_{\mathrm{N}})$, where:

- $\boldsymbol{h} = \mathbf{grad}\, \varphi + \boldsymbol{h}_t$ in Ω_{N}
- $\Gamma_{\mathrm{C}\setminus\mathrm{N}} = \partial\Omega_{\mathrm{C}} \cap \partial\Omega_{\mathrm{N}}$ is the interface between the conducting and nonconducting domains,
- $\boldsymbol{h}_t \in \mathcal{H}_h^1(\Omega_{\mathrm{N}})$ is a discretized cohomology term which can be used to impose the current in the inductor,
- $\boldsymbol{b}(\boldsymbol{h})$ is $\boldsymbol{\mu}\cdot\boldsymbol{h}$ in the linear case,
- $\boldsymbol{b}(\boldsymbol{h})$ is $\frac{\partial \boldsymbol{b}}{\partial \boldsymbol{h}}^k(\boldsymbol{h} - \boldsymbol{h}^k) + \boldsymbol{\mu}(\boldsymbol{h}^k)\cdot\boldsymbol{h}^k$ in the nonlinear case, where k indicates a quantity from the previous NR iteration,
- $\boldsymbol{b}^{n-1}$ is $\boldsymbol{\nu}^{n-1} \cdot \boldsymbol{h}^{n-1}$, the solution at the previous time step.

It is possible to eliminate equation (1.73) by ensuring it strongly via some constraints in the function spaces. As the gradients of node elements form a subspace of edge elements, it is possible to impose the traces equalities with linear constraints between the boundary DoFs. Those linear constraints eliminate some DoFs and equation (1.73). We refer to the documentation of GetDP [22, section 7.5.6] for an example of implementation.

There are three ways to implement the discrete cohomology term $\boldsymbol{h}_t$, they are described next.

Cohomology term in Ω_{N}

In electrical engineering, the usual reason for the existence of the $\boldsymbol{h}_t$ cohomology terms in the nonconducting domain Ω_{N} is the presence of N_{C} closed thick inductors and coils called $(\Omega_{\mathrm{C},i})_{1\leq i \leq N_{\mathrm{C}}}$ and forming loops - they have $\beta_1(\Omega_{\mathrm{C},i}) = 1$. In this case, if we assume that Ω is simply connected (which is a weak assumption as it contains an air box around the device), then $\beta_1(\Omega_{\mathrm{N}}) = N_{\mathrm{C}}$ and there are N_{C} independent $\boldsymbol{h}_{t,i}$ terms.

The cohomology terms are responsible for the correctness of the Ampère's theorem in Ω_{N}. Indeed, if a total current of I_i feeds $\Omega_{\mathrm{C}i}$, and if $\mathcal{C}_i$ is a cycle of edges of Ω_{N} looping around Ω_{Ci} (meaning $\mathcal{C}_i \in \mathcal{H}_1(\Omega_N)$), then Ampère's theorem requires

$$\int_{\mathcal{C}_i} \boldsymbol{h}_{t,i} \cdot \boldsymbol{t} = I_i.$$

It is often possible to find a surface $\Sigma_{c,i}$ in Ω_N cutting any closed loop turning around $\Omega_{C,i}$. Removing those surfaces from Ω_N "cuts" the loops and removes the associated (co)homology dimensions :

$$\beta_1(\Omega_N \setminus \underset{i}{\cup}\Sigma_{c,i}) = 0,$$

the Σ_i surfaces are therefore called *cut surfaces* or simply *cuts* [30, Section 2.3.3].

For FEM computation, it is not practical to modify the domain topology with the cuts to suppress the (co)homology space $\mathcal{H}_1(\Omega_N)$ and $\mathcal{H}^1(\Omega_N)$, but the cuts can be used to discretize the cohomology fields $\boldsymbol{h}_{t,i} \in \mathcal{H}^1(\Omega_N)$ instead.

A first possibility is to create potential jumps at the cuts. Let $(n_{ij})_j \in \mathcal{N}(\Sigma_i)$ be the nodes of Σ_i and $\mathbb{1}_{i+}$ a function that is 1 on the elements in Ω_N placed on the positive side of Σ_i (the side to which the normal points out), and 0 on the other side. We can define the potential cut basis function

$$\varphi^i_+(\boldsymbol{x}) = \sum_j \varphi_j(\boldsymbol{x})\mathbb{1}_{i+}(\boldsymbol{x}) \tag{1.75}$$

with φ_j the Lagrange basis function associated to the node n_{ij}.

Unlike the gradient of continuous potentials of $H(\mathbf{grad};\Omega_N)$, this function has the property that, for any cycle $\mathcal{C}_i$ defined above, the circulation of $\mathbf{grad}\,\varphi^i_+$ along $\mathcal{C}_i$ is 1. Moreover, there is

$$\int_{\mathcal{C}_i} \mathbf{grad}\,\varphi^j_+ \cdot \boldsymbol{t} = \delta_{ij} \tag{1.76}$$

and it can be proven [30, 40] that the functions $(\mathbf{grad}\,\varphi^i_+)_i$ together with the usual gradients of Lagrange basis functions can represent any curl free magnetic field of $\boldsymbol{H}_h(\mathbf{curl};\Omega_N)$. This technique is well illustrated in [30, Section 4.1.2, Fig. 2].

There is a second way of defining the $\mathbf{grad}\,\varphi^i_+$ functions, they are actually equal to the sum of all the Nedelec basis functions associated with the edges having a node in Σ_s and lying on the positive side of Σ_i, that is

$$\boldsymbol{\varphi}^i_+(\boldsymbol{x}) = \mathbf{grad}\,\varphi^i_+(\boldsymbol{x}) = \sum_j \boldsymbol{\varphi}_j(\boldsymbol{x})\mathbb{1}_{i+}(\boldsymbol{x}) \tag{1.77}$$

where $\boldsymbol{\varphi}_j$ are the aforementioned edge basis functions.

It is also possible to discretize $\boldsymbol{h}_{t,i}$ without cuts by computing a field verifying Ampère's law in the volume. When the current distribution in the inductor is known, Biot-Savart law (1.49) applies.

When the current distributions are unknown, it is possible to compute $\boldsymbol{h}_{t,i}$ by solving a vector Laplace equation with suitable boundary conditions on the conductors boundaries, such procedure is described in [25, Section 3.8].

Those volume methods are expected to yield better conditioned discrete systems, but require a pre computation of the basis for $\boldsymbol{h}_t$ and adds more terms to assemble in the system compared with using cuts [54].

1.3.6 Discrete B-conforming formulation

In this section, we describe the main ways to implement a discrete B-conforming formulation. We review the four possibilities to leverage the gauge, and also the four ways to implement the discrete current source $\boldsymbol{j}_{s,h}$.

Current source discretization

Any MVP formulation based on a current source $\boldsymbol{j}_s$ requires that the discretized current source $\boldsymbol{j}_{s,h}$ is in the range of the discrete **curl** operator to yield a compatible set of linear equations [55]. In other words, we need

$$\operatorname{div} \boldsymbol{j}_{s,h} = 0. \tag{1.78}$$

It is also a requirement for the validity of the mathematical proofs of convergence [42, 56, 57].

The naive discretization of $\boldsymbol{j}_s$ is to interpolate it at nodes or integration Gauss points using the Lagrange operator I_h, but $I_h \boldsymbol{j}_s$ can be not divergence free even if $\boldsymbol{j}_s$ is.

This issue often requires to be treated. When $\boldsymbol{j}_s$ is an analytic continuous formula which is divergence free in Ω_s, it might be enough to interpolate it with the Raviart-Thomas projection (with the flux integrals of $\boldsymbol{j}_s$ through the facets), or to precompute a projection of $\boldsymbol{j}_{s,h}$ in $\boldsymbol{H}_{0,h}(\mathrm{div};\Omega_s)$ [54] with

$$\int_{\Omega_s} (I_h \boldsymbol{j}_s - \boldsymbol{j}_{s,h}) \cdot \boldsymbol{j}'_{s,h} = 0, \quad \forall \boldsymbol{j}'_{s,h} \in \boldsymbol{H}_{0,h}(\mathrm{div};\Omega_s),$$

but there is no numerical guarantee of (1.78), even in the weak sense.

With an analytic $\boldsymbol{j}_s$, it is also possible to strongly enforce (1.78) by precomputing an approximation of $\boldsymbol{j}_s$ as the curl of an electric vector potential with Biot-Savart law (1.49), or as the curl of a magnetic source field $\boldsymbol{h}_{s,h}$ in $\boldsymbol{H}_{0,h}(\mathbf{curl};\Omega_s)$, e.g. with

$$\int_{\Omega_s} (I_h \boldsymbol{j}_s - \mathbf{curl}\,\boldsymbol{h}_{s,h}) \cdot \mathbf{curl}\,\boldsymbol{h}_{s,h}{}' = 0, \quad \forall \boldsymbol{h}'_{s,h} \in \boldsymbol{H}_h(\mathbf{curl};\Omega_s).$$

But suitable BC and gauge conditions on $\boldsymbol{h}_{s,h}$ have to be set [54], and this method might not yield great approximation of $\boldsymbol{j}_s$ if the discretization of Ω_s is not adapted [57].

Another possibility is to weakly ensure (1.78) by using the source $\boldsymbol{j}_{s,h} = I_h \boldsymbol{j}_s + \mathbf{grad}\,\xi_h$ where ξ_h is precomputed with

$$\int_{\Omega_s} (I_h \boldsymbol{j}_s + \mathbf{grad}\,\xi_h) \cdot \mathbf{grad}\,\xi_h{}' = 0, \quad \forall \xi'_h \in H_{0,\Gamma_b,h}(\mathbf{grad};\Omega_s).$$

This method can increase the number of DoFs, but it is implicitly applied when the MVP $\boldsymbol{a}$ is weakly gauged with the Coulomb gauge implemented with a scalar potential Lagrange multiplier [57, eq (42)], which will be presented later (1.81).

Other techniques exist for more specific applications, such as those in [36, 58]. Also, the methods from [59][28, chap. II, sec. 2] use a projection with a penalization method to ensure (1.78).

Gauging during the linear system resolution

The discrete linear system resulting from the FEM discretization can either be solved with a direct solver that inverses the system with some kind of Gauss elimination, or with an iterative solver (using e.g. gradient descent methods or Krylov methods [60, 61]) which are less accurate but whose algorithmic complexity is lower for a same number of unknowns.

If a MVP formulation is discretized without gauging, that is with $\boldsymbol{a}, \boldsymbol{a}'$ in $\boldsymbol{H}_{0,\Gamma_b,h}(\mathbf{curl};(\Omega))$, the linear system is not invertible and the solution $\boldsymbol{a}$ is not unique. It is also said that the system has a *rank deficiency*. But any solution will yield correct fields $\boldsymbol{b}$ and $\boldsymbol{e}$. If the linear solver could deal with the rank deficiency to find a solution, everything would be fine.

In [62], the authors propose to leverage the modern direct solvers capabilities to deal with the rank deficiency in order to find a solution. Indeed, the solvers MUMPS and PARDISO can avoid using pivots too close to zero during the Gauss elimination, by replacing them with a chosen less small value on the diagonal. This chosen diagonal value becomes the smallest eigenvalue, which is now positive instead of zero. According to the authors, this method works well but will require a fine-tuning of the solvers pivoting parameters for difficult problems.

It is also possible to solve the ungauged problem with an iterative solver [55]. With such solver, the divergence of each MVP increment of the iterative resolution $(\boldsymbol{a}^k - \boldsymbol{a}^{k-1})$ is weakly set to 0. Consequently, the divergence of $\boldsymbol{a}^k$ is that of $\boldsymbol{a}^0$ (which is zero when starting from null initialization $\boldsymbol{a}(t=0)=\mathbf{0}$), the solution is implicitly gauged by the solver.

While the solver gauging strategies can be convenient, they have their drawbacks. It is also possible to build a full rank system that is directly solvable by applying a gauge before the resolution. Two such gauges are presented next.

Tree gauge

Tree-cotree gauging enables a strong gauging of the MVP by setting to 0 its DoFs associated with the edges of a spanning tree $\tau_h \subset \mathcal{E}(\Omega_h)$. Such a tree is a set of edges that spans all the nodes of Ω_h without forming any cycle, meaning there is no set of edges $\mathcal{C} \subset \tau_h$ such that $\partial\mathcal{C} = \emptyset$. The function space of edge elements in Ω_h gauged on a tree τ_h is called $\boldsymbol{H}_{0\tau_h,h}(\mathbf{curl};\Omega)$ and defined by:

$$\boldsymbol{H}_{0\tau_h,h}(\mathbf{curl};\Omega) := \left\{ \boldsymbol{a} \in \boldsymbol{H}_h(\mathbf{curl};\Omega) \;\middle|\; \int_{e_i} \boldsymbol{a}\cdot\boldsymbol{t} = 0 \quad \forall e_i \in \tau_h \right\} \tag{1.79}$$

The idea is that the dimension of the null space of the system is that of the freedom of choice of a field in the kernel of the discrete curl operator. In a simply connected domain, such a field is a gradient field and is determined by $N_n - 1$ DoFs, the dimension of $H_h(\mathbf{grad};\Omega)\backslash\mathbb{R}$ [55]. $N_n - 1$ is exactly the number of edges of τ_h, hence the choice of DoFs to remove.

In non simply connected domains, $\mathcal{H}_h^1(\Omega)$ is not empty and its fields are also in the kernel of **curl** (1.48), this adds β_1 DoFs to fix. Indeed, β_1 edges should be added to τ_h to form one cycle through each tunnel of Ω_h, the tree can then be called a *belted* tree [63, 31]. Also, if the domain is not connected - that is $\beta_0 > 1$ - the tree has β_0 connected components and its number of edges, which is still the correct number of DoFs to remove, is $N_n - \beta_0 + \beta_1$.

Coulomb gauge

Using the Coulomb gauge consists in adding to the system the equation $\operatorname{div}\boldsymbol{a} = 0$ (1.58) in the domain where the gauge is needed. We will apply it to the $\boldsymbol{a}^*$ formulation (1.55) where the gauge is only needed in Ω_N. It is natural to derive the weak formulation of (1.58) with a scalar potential test function ξ' in order to use (1.59), leading to

$$\int_{\Omega_\mathrm{N}} \boldsymbol{a}^*\cdot\mathbf{grad}\,\xi' + \int_{\partial\Omega_\mathrm{N}} \boldsymbol{a}^*\cdot\boldsymbol{n}\,\xi' = 0.$$

The boundary term can be split on the three sub-boundary of Ω_{N}, namely Γ_b, Γ_h and $\Gamma_{\mathrm{C}\setminus\mathrm{N}}$, and we show that it vanishes completely. Indeed, there are boundary conditions for $\boldsymbol{a}$ on boundaries Γ_b and $\Gamma_{\mathrm{C}\setminus\mathrm{N}}$, which are respectively $\boldsymbol{a} \times \boldsymbol{n} = 0$ and $(\sigma \partial_t \boldsymbol{a}^*) \cdot \boldsymbol{n} = 0$, so $\boldsymbol{a}$ is uniquely defined there. Therefore, the gauge is not needed on $\Gamma_{\xi 0} = \Gamma_b \cup \Gamma_{\mathrm{C}\setminus\mathrm{N}}$ and ξ' is set to 0 there.

On the other hand, it is possible to weakly impose the boundary condition $\boldsymbol{a}^* \cdot \boldsymbol{n} = 0$ on Γ_h. It was proven that the solution still exists, and the condition actually makes it unique, under different conditions on the material laws [42, 56]. The discrete Coulomb gauge condition can thus be written

$$\int_{\Omega_{\mathrm{N}}} \boldsymbol{a}^* \cdot \mathbf{grad}\, \xi' = 0, \quad \forall \xi' \in H_{0,\Gamma_{\xi 0},h}(\mathbf{grad}; \Omega_{\mathrm{N}}). \tag{1.80}$$

Finally, (1.80) should be coupled with the discretized weak form of (1.55), if possible while maintaining the symmetry of the matrix of the system. The usual way to do this is to introduce a Lagrange multiplier ξ, leading to the following discrete weak form.
Find $\boldsymbol{a}^*$ in $\boldsymbol{H}_{0,\Gamma_b,h}(\mathbf{curl}; \Omega)$ and ξ in $H_{0,\Gamma_{\xi 0},h}(\mathbf{grad}; \Omega_{\mathrm{N}})$ such that

$$\begin{aligned} \int_{\Omega} \boldsymbol{\nu} \cdot \mathbf{curl}\, \boldsymbol{a}^* \cdot \mathbf{curl}\, \boldsymbol{a}^{*\prime} + \int_{\Omega_{\mathrm{N}}} \lambda_1 \mathbf{grad}\, \xi \cdot \boldsymbol{a}^{*\prime} + \int_{\Omega_{\mathrm{C}}} \sigma \partial_t \boldsymbol{a}^* \cdot \boldsymbol{a}^{*\prime} &= \int_{\Omega_s} \boldsymbol{j}_s \cdot \boldsymbol{a}^{*\prime}, \\ \int_{\Omega_{\mathrm{N}}} \lambda_1 \boldsymbol{a}^* \cdot \mathbf{grad}\, \xi' + \lambda_2 \xi \xi' &= 0, \end{aligned} \tag{1.81}$$

for all $\boldsymbol{a}^{*\prime}$ in $\boldsymbol{H}_{0,\Gamma_b,h}(\mathbf{curl}; \Omega)$ and all ξ' in $H_{0,\Gamma_{\xi 0},h}(\mathbf{grad}; \Omega_{\mathrm{N}})$, with $\lambda_1 > 0$ and $\lambda_2 \geq 0$ two parameters that can be tuned to improve the conditioning of the system. Their naive values would be $\lambda_1 = 1$ and $\lambda_2 = 0$. If the resolution converges well, the solution for ξ should be 0 [57].

When Ω_{N} has a nonzero β_1 number, the naive Coulomb gauge is not enough because fields $\boldsymbol{a}_t \in \mathcal{H}^1_h(\Omega_{\mathrm{N}})$ respect both $\operatorname{div} \boldsymbol{a}_t = 0$ and $\mathbf{curl}\, \boldsymbol{a}_t = \mathbf{0}$, they are free to change in (1.81). In this case, the $\mathbf{grad}\, \xi$ field in (1.81) should be replaced with a field living in $H_{0,\Gamma_{\xi 0},h}(\mathbf{grad}; \Omega_{\mathrm{N}}) \bigoplus \mathcal{H}^1_h(\Omega_{\mathrm{N}})$[3] with techniques similar to Section 1.3.5, see [64].

1.4 Example and motivation for multiscale methods

To finish with this chapter on the electromagnetic fields computation, an example of eddy current problem resolution with a B-conforming formulation featuring materials with nonlinear magnetic laws is presented. We compute the eddy currents in a small cube of periodic magnetic material made of conducting inclusions electrically insulated from each other.

---

[3] $\bigoplus$ stands for the direct sum of the two spaces.

This example shows the state of the art of eddy currents computation in nonlinear materials, as well as the limitations faced in the simulation of materials with such heterogeneous geometry.

The periodic material is a cubic magnetic core made of $8 \times 8 \times 8 = 512$ spheres, surrounded by an insulator that we assume has the same physical properties as the air, that is $\sigma = 0$ and $\boldsymbol{\mu} = \mu_0$. The cube is centered around the origin. Only one eighth of the geometry is represented and meshed for the computation (see Figure 1.12), because it has three planes of symmetry similarly to Figure 1.6.

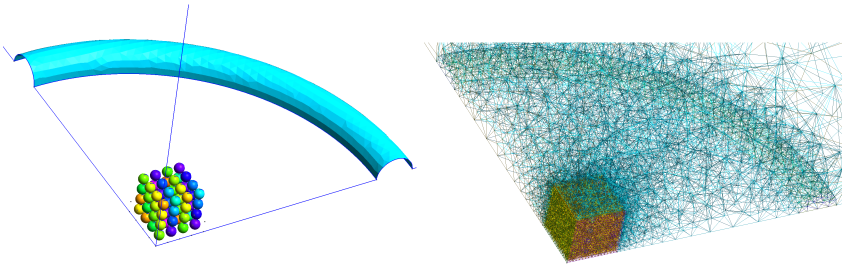

Figure 1.12: Geometry and mesh of an heterogeneous periodic magnetic material surrounded by a coil.

The spheres have a diameter of 80 μm and are placed such that their centers are separated by a distance of 100 μm. They have a conductivity of 5×10^7S.m^{-1} and the permeability follows the Fröhlich-Kennelly nonlinear law (1.82) with parameters $\mu_{r,\max} = 100$ and $B_s = 1.5$ T.

The Fröhlich-Kennelly magnetic law [65] is an analytical law defined by

$$\mu(\boldsymbol{h}) = \mu_0 + \frac{(\mu_{r,\max} - 1)B_s}{(\mu_{r,\max} - 1)\|\boldsymbol{h}\| + B_s/\mu_0} \tag{1.82}$$

with parameters B_s the saturation induction and $\mu_{r,\max}$ the maximum relative permeability. The law is equivalent to $\boldsymbol{b}(\boldsymbol{h}) = \mu_0\mu_{r,\max}\boldsymbol{h}$ near $\|\boldsymbol{h}\| = 0$, and to $\boldsymbol{b}(\boldsymbol{h}) = \mu_0\boldsymbol{h}$ when $\mu_0\|\boldsymbol{h}\| \gg B_s$. The Jacobian matrix of the law is given by

$$\frac{\partial \boldsymbol{b}}{\partial \boldsymbol{h}}(\boldsymbol{h}) = \mu(\boldsymbol{h})\boldsymbol{I}_3 + \frac{1}{\|\boldsymbol{h}\|}\frac{\partial \mu(\boldsymbol{h})}{\partial \|\boldsymbol{h}\|}\boldsymbol{h} \otimes \boldsymbol{h} \tag{1.83}$$

where

$$\frac{\partial \mu(\boldsymbol{h})}{\partial \|\boldsymbol{h}\|} = \frac{(\mu_{r,\max} - 1)^2 B_s}{((\mu_{r,\max} - 1)\|\boldsymbol{h}\| + B_s/\mu_0)^2} \tag{1.84}$$

with $\boldsymbol{I}_3$ the identity second order tensor of size 3, and $\boldsymbol{h} \otimes \boldsymbol{h} = \boldsymbol{h}\boldsymbol{h}^T$ the dyadic product of $\boldsymbol{h}$ and $\boldsymbol{h}$, also a second order tensor of size 3. The $\boldsymbol{h}(\boldsymbol{b})$ analytic inverse law is given in Appendix A.2.

The magnetic core is excited by a coil with circular section of diameter 200 μm, the coil respects a revolution symmetry around the origin, and has an outer radius (maximum distance of a point of the torus from the origin) of 3 mm. The device is surrounded by a wide spherical air box of diameter 6 cm.

The simulated domain Ω is thus constituted of the inductor Ω_s, the air Ω_A, the insulator in between the balls Ω_I and the conducting magnetic balls Ω_{C}. The nonconducting domain (more precisely the domain where no eddy currents is computed) is $\Omega_{\mathrm{N}} = \Omega_A \cup \Omega_s \cup \Omega_I$. The heterogeneous core domain is thus defined by $\Omega_M = \Omega_{\mathrm{C}} \cup \Omega_I$. As we consider one eighth of the geometry, all the domains have $\beta_1 = 0$. But Ω_{C} has $\beta_0 = 256/8 = 64$ connected components.

The problem is solved with the $\boldsymbol{a}$-v formulation (1.61) where $\boldsymbol{a}$ is discretized with edge elements and gauged with the tree gauge in Ω, and v discretized with nodal elements in Ω_{C} and gauged in each sphere by fixing the potential to 0 at one node.

It is assumed that the coil has enough turns to consider the current source density constant on the coil section. The coil is fed with the current

$$\boldsymbol{j}_s(\boldsymbol{x}, t) = \frac{I(t)}{A_{\mathrm{C}}} \begin{pmatrix} -\sin(\theta(\boldsymbol{x})) \\ \cos(\theta(\boldsymbol{x})) \\ 0 \end{pmatrix} \tag{1.85}$$

with

- $A_{\mathrm{C}} = \pi 10^{-8}$ m^2 the coil section area,
- $I(t) = 1000 \sin(2\pi f t)$ A the total imposed AC current (this value accumulates the current of all the turns of the coil),
- $f = 300$ kHz the frequency,
- $\theta(\boldsymbol{x}) = \mathrm{atan2}(y, x)$.

The initial conditions are $\boldsymbol{a}(t = 0) = \boldsymbol{0}$ and $v(t = 0) = 0$ everywhere. It is not necessary to correct the discretization of the current source here, because the analytic source formula has null divergence, and the inductor has a smooth and well meshed shape.

The problem is solved during $4.1\overline{6}$ μs with a step size of $20.8\overline{3}$ ns, that is during 1.25 periods at 160 TS per period. Theta scheme with $\theta = 1$ is used. At this frequency, the skin depth is $\delta \simeq 29$ μm. This number $\delta = \left(\sqrt{\pi\mu\sigma f}\right)^{-1}$ is an approximation of the distance from the boundary of the conductor on which the current flows. In general, it is necessary to adapt the mesh to refine the conductor near its boundary on a depth of few times δ, which may be very expensive. But here, δ is just slightly shorter than the balls radii 40 μm, so the meshes of the balls don't need to be extremely fine near their boundaries.

The number of elements in the mesh and associated degrees of freedom in the system are shown in Table 1.1, the system is small enough ($\approx$ 600k DoFs) to use a direct solver. The MUMPS linear solver [66] will be used for all linear system resolutions in this work. Both absolute residual and relative residual stopping criteria are used for the Newton-Raphson algorithm, with a tolerance of 10^{-8}.

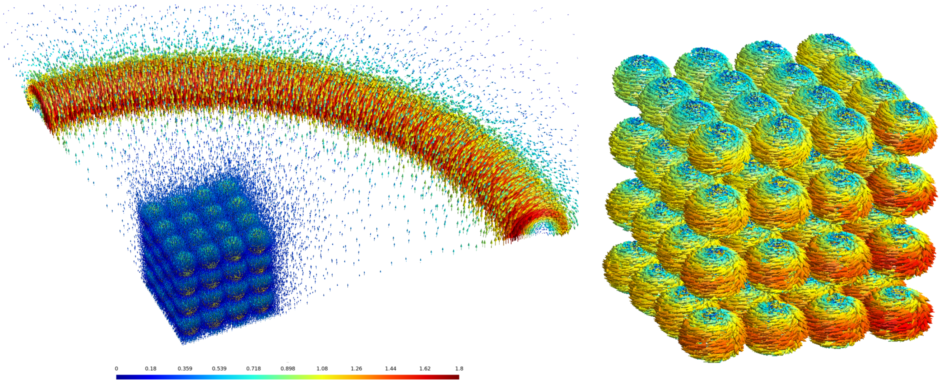

Figure 1.13: Example magnetic induction (left) and current (right) field maps. The eddy currents in the balls turn in opposite direction compared with the source current in the inductor.

Some field maps are displayed Figure 1.13 and the Joule losses and magnetic energy stored in the core are plotted over time on Figure 1.14, they are respectively computed with

$$\begin{aligned}\mathcal{P}_{\mathrm{JL}} &= \int_{\Omega_C} \sigma(-\partial_t \boldsymbol{a} - \mathbf{grad}\, v) \cdot (-\partial_t \boldsymbol{a} - \mathbf{grad}\, v),\\ \mathcal{E}_{\mathrm{m}} &= \int_{\Omega_M} \boldsymbol{\nu} \cdot \mathbf{curl}\, \boldsymbol{a} \cdot \mathbf{curl}\, \boldsymbol{a},\end{aligned}$$

where Ω_M is the magnetic core. For this problem, the nonlinear loops always converged in 2 or 3 iterations, and 55 hours were necessary to complete the 200 time steps. Each iteration, that is one assembly and resolution of the linear system, took nearly 5 min in average.

We can also pay attention to the cost of the different $\boldsymbol{a}$ formulations on this problem. The degrees of freedom involved in the $\boldsymbol{a} - v$ and $\boldsymbol{a}^*$ formulations using either the tree gauge, the Coulomb gauge with Lagrange multiplier and a solver gauge are shown on Table 1.1.

Those possibilities are not equivalent. We could not make well work the $\boldsymbol{a}^*$ formulation with the tree gauge here, possibly because the tree is harder to generate due to the spheres which it has to avoid. Our few attempts lead to an ill-conditioned system. The $\boldsymbol{a}$-v formulation with solver or Coulomb gauge requires much more DoFs. In our

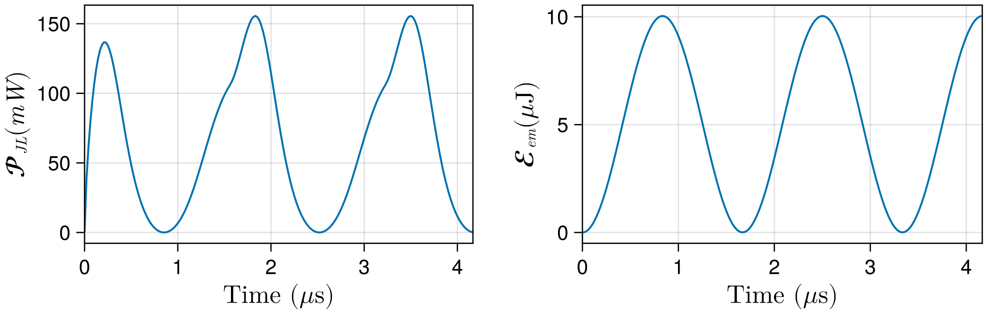

Figure 1.14: Joule losses (left) and magnetic energy stored in the core (right) during 2.25 periods. The nonlinear magnetic law in the balls results in non-sinusoidal signals.

experiments, the formulations with the best tradeoffs between efficiency and convenience to implement were the $\boldsymbol{a}$-v formulation with the tree gauge and the $\boldsymbol{a}^*$ formulation with Coulomb gauge, the former has the minimum possible number of DoFs and the tree used for gauging is straightforward to generate.

	Ω	Ω_C	Ω_N
nodes/N_n	88.5k	64.7k	72.4k
tets./N_k	509k	231k	278k

Number of elements

Gauge	Tree	Solver	Coulomb
$\boldsymbol{a} - v$	574k	660k	749k
$\boldsymbol{a}^*$	574k	596k	619k

Degrees of freedom

Table 1.1: Number of elements in the mesh Figure 1.12 (left) and degrees of freedom with the two $\boldsymbol{a}$ formulations (right). The numbers of DoFs are given for three gauges, the **tree** gauge, the ungauged system (meant to be gauged via the **solver**) and the **Coulomb** gauge.

There are 48.6k nodes on the boundary of Ω_C only, and out of the 278k tetrahedra in Ω_N, 239k (86%) are in the insulator Ω_I. In total, more than 90% of the total DoFs are associated with the simulation of the periodic magnetic core.

We did not use all the state-of-the-art techniques to solve this problem. For example, using performant iterative solver and domain decomposition methods could enable solving bigger linear system with drastically parallelized computations. Nonetheless, those techniques do not help a lot with the eddy currents computation in the nonlinear conducting domain, or cannot scale with the increase of DoFs with respect to the number of periods of the material. In 3D, it grows as n^3 if n is the number of material period in one direction. For illustration, the number of tetrahedra meshing the spheres in the previous example, with respect to the number of sphere in one direction, is given in the following table, along with the associated computation time to solve one linear system of this size (with the MUMPS solver). The value are extrapolated using a fitting with a $O(n^3)$ polynomial.

n	1	3	6	10	100	1000
Ω_C tets.	3.6k	98k	778k	3.6M	3.6G	3.6T
One system solve	4 s	96 s	10 m	35 m	>7 d	$\gg$ 13 y

This large increase in computational burden with the number of material fine-scale components makes it impossible to apply the usual methods to highly heterogeneous materials.

Summary

This first chapter was dedicated to the review of the workflow commonly used to achieve the computational modeling of the electromagnetic fields in the magnetoquasistatic regime, which is used to model many devices in electrical engineering. The different modeling steps were described, from the definition of Maxwell's equations to their numerical resolution using spatial and temporal discretization and the linearization of nonlinear equations.

At the end, it was shown that the usual single scale methods are limited, the computational costs in time and memory are not affordable to study actual heterogeneous material with thousands of fine scale features. Multiscale modeling techniques are studied in the next chapter to circumvent this problem.

As mentioned in the introduction, a particular care will be given to the computation of the macroscopic field strength from the fine scale solutions. Indeed, this research was originally motivated by the lack of understanding of the scale transition of the electric and magnetic fields strength pointed out by Meunier *et al.* in [4], hindering the use of the B-conforming formulation for multiscale modeling. But this formulation converges far better than the dual H-conforming one on the strongly nonlinear ferromagnetic cores, hence the will to understand and fix potential issues.

Chapter 2

Multiscale modeling

This chapter is dedicated to the multiscale modeling of electromagnetic fields. The first section gives a short overview of the homogenization and multiscale methods used in electrical engineering. In the next sections, an improved multiscale model using a scale separation hypothesis is introduced and analyzed. In particular, the last section details different methods that can be used to compute the homogenized electromagnetic fields from the fine-scale fields and describes their advantages and disadvantages.

2.1 Usual heterogeneous media and multiscale methods

This section lists some examples of heterogeneous media commonly encountered in electrical engineering for which multiscale modeling techniques can be useful. Then, several relevant state-of-the-art multiscale methods that are applicable to most of the heterogeneous media are summarized. Finally, the multiscale methods requiring a scale separation hypothesis are introduced, including the heterogeneous multiscale method which is used in this research work.

2.1.1 Heterogeneous materials

Periodic and stochastic heterogeneous materials

A heterogeneous material is a material having a complex structure featuring elements significantly smaller than the overall material size. In general, those structures have complex and random shapes, like a pile of sand made of many grains of variable size and shapes. But these random shapes are not arbitrary, it is possible to model them with probability distributions. Such material are thus called stochastic heterogeneous materials.

Some manufactured material admit a regular periodic structure, they are called periodic media. Although we will only work on the homogenization of periodic media in this work, the periodic homogenization methods can be extended to stochastic materials by building a *periodic cell* - called the *representative volume elements* (RVE) - holding a representative portion of the material.

Let us introduce some notations used in the periodic setting as illustrated in Figure 2.1. The modeling domain is Ω, it contains a periodic domain Ω_ε. The exterior of the periodic domain is called Ω_{M}, such that $\Omega = \Omega_{\mathrm{M}} \cup \Omega_\varepsilon$, and the interface between Ω_ε and Ω_{M} is called $\Gamma_{\varepsilon\backslash\mathrm{M}}$. The periodicity of Ω_ε translates the invariance by a translation by a period vector $\boldsymbol{k}$, that we further call $\boldsymbol{k}$*-periodicity* for shorteness, with $\varepsilon = \|\boldsymbol{k}\|$ the characteristic size of the fine-scale features. The interior of the periodic domain can be generated by the translation of the periodic cell by vectors $\boldsymbol{z_k} = (z_x k_x, z_y k_y, z_z k_z)$ where $(z_x, z_y, z_z) \in \mathbb{Z}^3$. If desired, it is always possible to choose Y as a rectangular hexahedron[1] of diagonal $\boldsymbol{k}$.

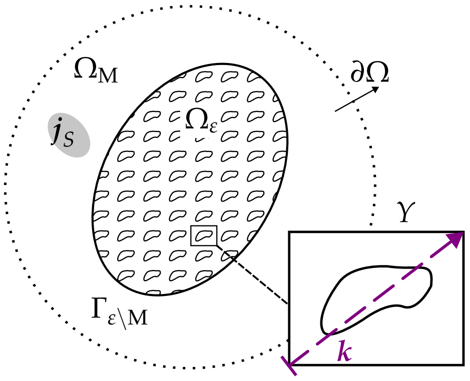

$$
\begin{array}{lll}
 & \boldsymbol{b}^\varepsilon \cdot \boldsymbol{n} = 0 & \text{on } \partial\Omega \\
(\mathrm{E}_{\mathrm{M}}) & \mathbf{curl}\, \nu_0 \boldsymbol{b}^\varepsilon = \boldsymbol{j}_s & \text{in } \Omega_{\mathrm{M}} \\
 & \operatorname{div} \boldsymbol{b}^\varepsilon = 0 & \text{in } \Omega_{\mathrm{M}} \\
 & & \\
(\mathrm{E}_\varepsilon) & \mathbf{curl}\, \boldsymbol{\nu}^\varepsilon \cdot \boldsymbol{b}^\varepsilon = \boldsymbol{0} & \text{in } \Omega_\varepsilon \\
 & \operatorname{div} \boldsymbol{b}^\varepsilon = 0 & \text{in } \Omega_\varepsilon \\
 & & \\
(\mathrm{C}_{\varepsilon\backslash\mathrm{M}}) & \boldsymbol{b}^\varepsilon \cdot \boldsymbol{n} \quad \text{continuous} & \text{on } \Gamma_{\varepsilon\backslash\mathrm{M}} \\
 & \boldsymbol{\nu}^\varepsilon \cdot \boldsymbol{b}^\varepsilon \times \boldsymbol{n} \ \text{continuous} & \text{on } \Gamma_{\varepsilon\backslash\mathrm{M}}
\end{array}
$$

Figure 2.1: Left: sketch of an heterogeneous periodic material Ω_ε of period $\boldsymbol{k}$ with a zoom on the periodic cell Y. Right: an example of problem with heterogeneous solutions in Ω_ε. It is a magnetostatic problem written in the B-conforming formulation of unknown $\boldsymbol{b}^\varepsilon$.

We are interested in solving a PDE in $\Omega_\varepsilon \cup \Omega_{\mathrm{M}}$ that we call the fine-scale problem. The set of equations defined in Ω_{M} is called $(\mathrm{E}_{\mathrm{M}})$, and that defined in Ω_ε is called (E_ε), with its fields noted with a $\bullet^\varepsilon$ superscript - e.g. $\boldsymbol{b}^\varepsilon$ - to highlight that they have fine-scale features. Finally, the interface conditions defined on $\Gamma_{\varepsilon\backslash\mathrm{M}}$ are denoted $(\mathrm{C}_{\varepsilon\backslash\mathrm{M}})$. The fine-scale problem $\mathcal{P}_{\varepsilon\backslash\mathrm{M}}$ is thus summed up by the following system of equations:

$$
\mathcal{P}_{\varepsilon\backslash\mathrm{M}}: \quad \{(\mathrm{E}_{\mathrm{M}}),\ (\mathrm{E}_\varepsilon),\ (\mathrm{C}_{\varepsilon\backslash\mathrm{M}})\} \qquad \text{on } \Omega = \Omega_{\mathrm{M}} \cup \Omega_\varepsilon. \tag{2.1}
$$

It is also called the *reference problem*. An example of fine-scale magnetostatic problem with a B-conforming formulation is given in Figure 2.1.

To make things more concrete, several examples of actual heterogeneous media for which multiscale methods are used are presented next.

---

[1] A rectangular hexahedron has 6 rectangle faces with all having right angles

Coils

Wire coils are made of a long wire wrapped several times around an axis. The wires are insulated from each other to force the current to make the expected number of turns around the axis. Coils are widely used for the conversion between electric energy and magnetic energy. Indeed, they multiply the current imposed in the wire by the number of turns of the coil, leading to the creation of a large magnetic flux thanks to Ampère's law [67].

A coil is a site of Joule losses. These losses might be difficult to predict in dynamic settings, because of the skin effect inside the turns, and the proximity magnetic effects between the turns. Depending on the manufacturing process, the wire turns might be regularly aligned in space, or not, so both periodic and stochastic homogenization techniques can be relevant.

Source: [68]

Laminated magnetic cores

Many electrical engineering devices such as actuators, electrical machines and electrical transformers contain so-called magnetic cores. Those are made of ferromagnetic materials that have high magnetic permeability, which allows them to canalize and better conduct the magnetic flux [69].

Source: [70]

The best ferromagnetic materials are based on specific metals, mainly iron, which are also conducting materials. As a result of the presence of these conducting materials, eddy currents appear and create unwanted losses of energy in the material due to Joule effect. To reduce these losses, magnetic cores are often made of ferromagnetic sheets separated by thin insulating layers. Such cores are thus periodic, the thickness of the sheets is generally between 10^{-4} m and 10^{-3} m, and that of the core between 10^{-3} m and 2×10^{-1} m. When the flux traverses the core in the sheet plane, the eddy currents cannot loop around the whole core, but only in the sheet thickness. In the end, the total losses in a laminated core are divided by the number of sheet, compared with a massive one.

Other soft magnetic materials

The laminated cores have disadvantages. They are anisotropic and limited in the frequency at which they operate because there can still be significant eddy currents inside them. Also, they cannot admit a wide range of shapes. Many other magnetic materials exist, including soft ferrites, sintered material and soft magnetic composites (SMC) [71]. They are designed to have a high density in magnetic material (s.t. iron, nickel and cobalt) along with a minimal conductivity to reduce the Joule losses. This is achieved by splitting the metal in small grains and reducing the conductivity at their interfaces. The grain size can range from about 10^{-6} m to 10^{-4} m. The SMCs have the best electric resistivity because the grains are insulated with a coating made of some resins. Examples of possible resins are listed in [71].

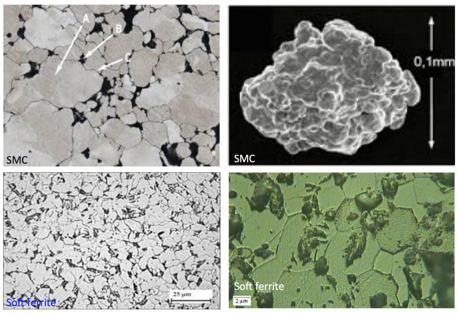

Source: [10, Figure 1.2]

Those materials are a motivation to develop multiscale modeling because a piece of SMC contains a very large amount of grains, it is impossible to compute the electromagnetic fields with a fine-scale model of the whole material. The main objective is to accurately estimate quantities such as the Joule losses and magnetic flux through the core. As mentioned in the general introduction, the four sources of difficulties are the handling of complex material laws, the dynamic effects (skin effect, Joule losses, possible dynamic hysteresis), and the multiscale and stochastic nature of the geometry. The first three difficulties are addressed in this thesis with experiments on a basic periodic geometry. As for the fourth issue, it is at least possible to find some RVE of stochastic geometry [72], and multiscale methods should be adapted to it. But determining the fine scale material laws to feed the model might be an issue in practice.

Large heterogeneous systems

The previously given examples of heterogeneous material feature scales of electrical engineering devices and the smaller scales of their components, but the multiscale modeling of Maxwell's equations can be useful at many other scales.

In geophysics, multiscale methods are studied to help detect bodies of mineral deposits and water or hydrocarbon reserves in the ground by measuring the conductivity of the ground. This is done by solving inverse problems on domains of sizes ranging from 1 to 10^2 km. The ground is modeled considering its very heterogeneous nature, with features decscribed at many different scales e.g. from 10^{-3} m to kilometers [73].

Similarly, the electric networks used to transport electric energy across countries are multiscale in essence, they have the size of continents while being made of components of many sizes.

These two examples close our listing of heterogeneous media of various scales which are commonly encountered in electromagnetic. Next, a review of some of the general purpose homogenization and multiscale methods is presented.

2.1.2 Homogenization and multiscale methods

Homogenization and multiscale modeling are used to model complex heterogeneous materials or structures as homogeneous medium, by defining equivalent homogenized material properties in it. Homogenization can be viewed as a step of multiscale modeling, consisting in defining or computing the homogeneous fields or equivalent properties of the medium from a fine scale model. The multiscale modeling is the whole process of determining the fine scale model, the homogenization technique and the way to use the homogenized quantities into the macroscopic homogenized model.

There exist a wide range of homogenization and multiscale methods. We will divide them into two categories:

- the framework of *effective medium theory*, including the *mean field methods*, in which approximations are made on the fine scale geometry, the distribution of the fields and the fine scale material laws in order to derive analytic or semi-analytic models,
- the *computational multiscale methods*, or *full-field methods*, that rely on solving PDEs to compute the fine scale field maps and deduce the homogenized material properties from them.

This thesis will study a method of the computational category. We could include the computational multiscale methods into the framework of effective medium theory as they share the same core principle and objective. The difference is that computational methods aims at providing solutions as accurate as a complete fine scale resolution of Maxwell's equations.

Computational methods are still the most expensive methods, most of the time, some accuracy can be sacrificed to benefit from large reduction of cost. The method of the effective medium theory provide a wide range of tradeoffs between accuracy and cost of computation. The literature is well summarized in [74] and [10, Section 3.3], but we shall give some example here.

The book [75] discusses how to perform homogenization using so called mixing rules. The base building bloc of the macroscopic properties are the volume ratio of the different phases of the fine scale description of the material.

The mean field homogenization methods enable to take hysteretic behaviors into account [76], to model the material at a scale where it cannot be described as phases of different matter [77], or to consider multi-physic couplings, such as magneto-elastic coupling [78].

These analytic and semi-analytic methods are generally designed for specific applications. On the other hand, computational method are generally meant to be applicable on any problem. But they have also been derived and specialized to the cases of coils and laminated magnetic cores, which were described before. The multiscale modeling of laminated cores have been continuously developed in the last decades, recent advancements include [79, 15, 80, 81, 82]. About coils, some methods enable to compute equivalent permeability and conductivity tensors that take into account both skin and proximity dynamic effects, in harmonic [83, 4] and time stepping [84] regime.

We now focus on the general purpose computational multiscale methods that we present next, starting from the more widely applicable ones to the more restricted ones. The latter require more simplifying hypothesis on the solutions or equations, but are therefore more efficient. We do not review the theories used to analyze mathematically the multiscale methods accuracies, but refer to [10] for a review of them.

Multiscale finite element method

The Multiscale Finite Element Method (MsFEM) [85] employs coarse and fine-scale basis functions in a single FEM resolution. The material to homogenize is coarsely meshed, but a set of a few fine-scale basis functions is added in each coarse element. These basis functions are pre-computed with solution of the fine-scale model and should permit an accurate representation of the fine-scale features using only few DoFs per coarse element. The basis functions might be computed individually on each coarse element when the shape of the fine-scale features vary in the material. More details are given in [10, Sec. 4.2.1][86], usage of the method for electrical engineering was made in [5, 8].

This method is very general but has drawbacks. The fine-scale basis function must be computed again for each new fine scale geometry. Also, storing them in memory is not cheaper than storing the complete fine-scale mesh and solutions, the method is thus limited when there is a large difference between the coarse and fine scale characteristic lengths.

Variational multiscale method and localized orthogonal decomposition

The Variational Multiscale Method (VMS) [87, 86] and the associated similar Localized Orthogonal Decomposition (LOD) method use a splitting of the unknown field into a coarse and a fine component. The space of the solution is decomposed into spaces of fine and coarse components and the governing formulations are derived for both components. In the context of the FEM, the coarse and fine linear systems can be transformed into a single linear system by using some kind of Schur complement.

Similarly to MsFEM, one of the advantage of VMS and LOD is that they don't rely on any scale separation assumption. However, this comes at the expense of taking into account as much fine scale variation of the field as in the original fine-scale problem, in particular, the cost of storing the solution in memory is not much reduced.

The scale separation hypothesis in multiscale modeling

Before introducing the *Heterogeneous Multiscale Method* (HMM), which is the **numerical** multiscale method used in this work, we introduce the *scale separation hypothesis* that it requires. Indeed, the **continuous** set of equations that HMM discretizes and solves for is based on it. In particular, the need for an averaging strategy used to define the scale separation hypothesis and the continuous multiscale equations is discussed.

Our introduction of these notions follows an **intuitive** approach inspired by the community of computational electromagnetics [1, 2, 4]. This approach is different from the standard derivations made in asymptotic homogenization theories [10, Chap. 3][88]. The reason is mainly the difficulty to understand and study these mathematical frameworks. The approach we adopt enables to be more general while being compatible with the them, as both models lead to the very same discrete problems on the simpler setting (magnetostatic).

There are several possible definitions for the scale separation assumption. In asymptotic homogenization, it is possible to define it using comparison between the size of the device L and some geometrical or physical characteristic sizes like the cell size ε, the skin depth δ or the electromagnetic wavelength λ. This is studied in detail in [89] for problems based on time-harmonic Maxwell's equation including permittivity.

In this thesis, we adopt a definition that directly relates to the fields, that is on the solutions of the equations on the given geometry, not the physical parameters or geometry themselves. The general idea is the following. First, we define a *macroscopic field* by applying a homogenization formula to the fine scale fields $\boldsymbol{b}^\varepsilon$. Then, the scale separation hypothesis is defined as assuming that all macroscopic fields are smooth at the fine scale and slowly vary on distances larger than the geometric period ε.

The macroscopic field are denoted by capital letters like $\boldsymbol{B}(\boldsymbol{x})$. We call *scale transition relation* (STR) the homogenization formula that defines the macroscopic fields from the fine-scale fields. In periodic homogenization, any macroscopic field $\boldsymbol{B}$ is classically defined using the cell *volume average* of the fine-scale field $\boldsymbol{b}^\varepsilon$, that is

$$\boldsymbol{B}(\boldsymbol{x}) = \langle\, \boldsymbol{b}^\varepsilon \,\rangle_{Y_{(\boldsymbol{x})}} := \frac{1}{|Y_{(\boldsymbol{x})}|} \int_{Y_{(\boldsymbol{x})}} \boldsymbol{b}^\varepsilon(\boldsymbol{y}) d\boldsymbol{y}, \tag{2.2}$$

where $|Y_{(\boldsymbol{x})}| = k_x k_y k_z$ is the volume of $Y_{(\boldsymbol{x})}$, the cell centered at $\boldsymbol{x}$. But it will be shown in

Section 2.2 that this definition does not always work for electromagnetic fields, so we temporarily let the scale transition relation undefined and call it $\langle\ \rangle_{\mathrm{STR}}$.

To define the set of continuous multiscale equations, the dependency in space of the fine-scale field $\boldsymbol{b}^{\varepsilon}(\boldsymbol{x})$ has to be split into the slow macroscopic variation at scale L and in a *fast* or *fine-scale* variation at the scale ε. The slow variation of the field is modeled by the macroscopic field $\boldsymbol{B}(\boldsymbol{x})$. The fine scale variation is the rest, $\boldsymbol{b}^{\varepsilon}_{\text{fine}}(\boldsymbol{x}) = \boldsymbol{b}^{\varepsilon}(\boldsymbol{x}) - \boldsymbol{B}(\boldsymbol{x})$.

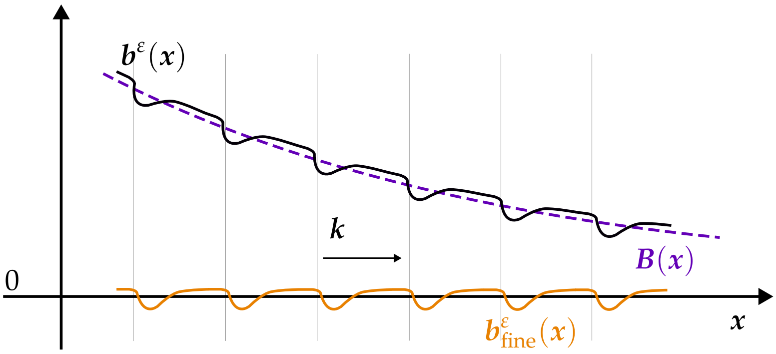

Figure 2.2: 1D sketch of the scale separation of a fine scale field $\boldsymbol{b}^{\varepsilon}$ into its macroscopic smooth variation $\boldsymbol{B}$ and its nearly $\boldsymbol{k}$-periodic variation $\boldsymbol{b}^{\varepsilon}_{\text{fine}}$.

In a neighborood around $\boldsymbol{x}$ of few ε of radius, the small variation of $\boldsymbol{b}^{\varepsilon}_{\text{fine}}$ is due to the $\boldsymbol{k}$-periodic[2] heterogeneities of the material and not to interaction with surrounding fields (the macroscopic fields are smooth). So we can make the approximation that its fine scale variation is $\boldsymbol{k}$-periodic, that is:

$$\boldsymbol{b}^{\varepsilon}_{\text{fine}}(\boldsymbol{x}+\boldsymbol{k}) \approx \boldsymbol{b}^{\varepsilon}_{\text{fine}}(\boldsymbol{x}). \tag{2.3}$$

In other word, the (assumed small) variation of the field $\boldsymbol{b}^{\varepsilon}$ between points that are $\boldsymbol{k}$-periodic is only attributed to the variation of the macroscopic field:

$$\boldsymbol{b}^{\varepsilon}(\boldsymbol{x}+\boldsymbol{k}) \approx \boldsymbol{b}^{\varepsilon}(\boldsymbol{x}) + \boldsymbol{B}(\boldsymbol{x}+\boldsymbol{k}) - \boldsymbol{B}(\boldsymbol{x}). \tag{2.4}$$

We can thus transform $\boldsymbol{b}^{\varepsilon}(\boldsymbol{x})$ into a *two-scale field* $\boldsymbol{b}(\boldsymbol{x},\boldsymbol{y})$ in all neighborhood of $\boldsymbol{x}$, for $\boldsymbol{x} \in \Omega_{\mathrm{H}}$ and for $\boldsymbol{y} \in Y$, where $\boldsymbol{y} \to \boldsymbol{b}^{\varepsilon}(\boldsymbol{x},\boldsymbol{y})$ is $\boldsymbol{k}$-periodic. So $\boldsymbol{x}$ is now the position in the macroscopically homogenous domain Ω_{H} which replaces Ω_{ε}.

The advantage is that the fine-scale distribution $\boldsymbol{y} \to \boldsymbol{b}(\boldsymbol{x},\boldsymbol{y})$ can be computed in the domain Y independently of what happens further away at the macroscopic scale, i.e. at distances large compared to ε. It only depends on the macroscopic fields at $\boldsymbol{x}$. The macroscopic and fine scales are **separated**. Now, the macroscopic field map is computed

---

[2] Periodic by translation by vectors $\boldsymbol{z_k} = (z_x k_x, z_y k_y, z_z k_z)$ where $(z_x, z_y, z_z) \in \mathbb{Z}^3$.

using the scale transition relation on the two scale field as follows:

$$\boldsymbol{B}(\boldsymbol{x}) = \langle\, \boldsymbol{b}(\boldsymbol{x},\boldsymbol{y})\, \rangle_{\mathrm{STR}} \qquad \forall \boldsymbol{x} \in \Omega_{\mathrm{H}},$$

where the integration variable of the STR is $\boldsymbol{y}$.

Unlike other approaches, the definition of the scale separation hypothesis adopted here doesn't provide an *a priori* criterion (depending only on the geometrical and physical parameters of the problem) indicating whether the assumption is valid or not. On the other hand, our definition is more general because it relates to the essential property required to use HMM, that is the possibility to define two scale fields. We believe that this definition is valid whatever the skin depth and wavelength inside conducting inclusions in the heterogeneous material. In general, a geometric scale difference between the heterogeneous material components and the size of the material itself is required for the scale separation hypothesis to hold, but it is not sufficient[3]. For periodic materials, it means $\varepsilon \ll L$ if L is the characteristic size of the material.

Derivation of the multiscale model

To build the multiscale model, all the physical fields (not necessarily the potentials) are splitted in two scale fields. From there, the original heterogeneous equations (E_ε) are split in equations for the macroscopic fields $(\mathrm{E}_{\mathrm{H}})$ and set of cell equations $(\mathrm{E}_{Y(\boldsymbol{x})})$ defined for $\boldsymbol{x}$ in Ω_{H}. The fields and unknowns of the $(\mathrm{E}_{\mathrm{H}})$ PDE are macroscopic fields, and the fields and unknowns of the $(\mathrm{E}_{Y(\boldsymbol{x})})$ PDEs are fine-scale *cell fields*. An example two-scale problem is given in Figure 2.3. Thanks to the scale separation hypothesis, the cell problems $(\mathrm{E}_{Y(\boldsymbol{x})})$ are implicitly coupled with each other by the macroscopic equations via the STR, they are not explicitly coupled with each other like in the original fine scale model.

In the macroscopic homogenized domain, equivalent material laws replace the original ones. Material laws usually link dual fields, such as $\boldsymbol{H}$ and $\boldsymbol{B}$ in the case of the magnetic law. In the proposed model, the macroscopic laws are implicitly defined by the scale transient relation and the cell problem. For example, in B-conforming formulation, the $\boldsymbol{H}(\boldsymbol{B})$ function can be computed by applying the STR to the fine scale $\boldsymbol{h}(\boldsymbol{x},\boldsymbol{y},\boldsymbol{B}(\boldsymbol{x}))$, which is the solution of the cell problem with imposed $\boldsymbol{B}(\boldsymbol{x})$. In summary:

$$\boldsymbol{H}(\boldsymbol{B}(\boldsymbol{x})) = \langle\, \boldsymbol{h}(\boldsymbol{x},\boldsymbol{y},\boldsymbol{B}(\boldsymbol{x}))\, \rangle_{\mathrm{STR}}.$$

---

[3] If there are electromagnetic wave propagation in the material with a wavelength of the same size of the cell, the scale separation hypothesis cannot be made because it is not possible to define a smooth macroscopic field. There are no wave propagation in MQS, but for a material with macroscopic conductivity, the macroscopic skin depth should be greater than the cell size, otherwise the macroscopic current will vary too fast compare to the cell size. We won't study this case in this thesis, however.

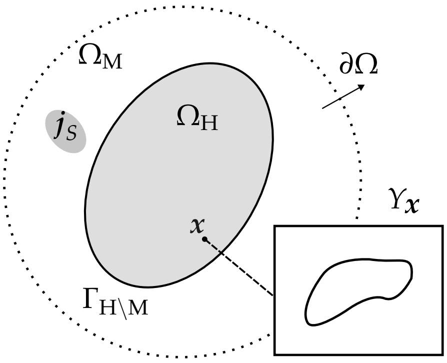

$$\begin{array}{lll}
(\mathrm{E_M}) & \boldsymbol{B}\cdot\boldsymbol{n} = 0 & \text{on } \partial\Omega \\
 & \textbf{curl}\, \nu_0 \boldsymbol{B} \; = \boldsymbol{j}_s & \text{in } \Omega_{\mathrm{M}} \\
 & & \\
(\mathrm{E_H}) & \textbf{curl}\, \boldsymbol{H}(\boldsymbol{B}) = \boldsymbol{0} & \text{in } \Omega_{\mathrm{H}} \\
 & & \\
(\mathrm{C_{H\backslash M}}) & \boldsymbol{H}(\boldsymbol{B}) \times \boldsymbol{n} \text{ continuous} & \text{on } \Gamma_{\mathrm{H}\backslash\mathrm{M}} \\
 & & \\
 & \textbf{curl}_{\boldsymbol{y}}\, \boldsymbol{\nu}(\boldsymbol{y})\cdot\boldsymbol{b}(\boldsymbol{x},\boldsymbol{y}) = \boldsymbol{0} & \text{in } \Omega_{\mathrm{M}} \times Y \\
(\mathrm{E}_{Y}(\boldsymbol{x})) & \boldsymbol{B}(\boldsymbol{x}) = \langle\, \boldsymbol{b}(\boldsymbol{x},\boldsymbol{y}) \,\rangle_{\mathrm{STR}} & \text{in } \Omega_{\mathrm{M}} \times Y \\
 & \boldsymbol{H}(\boldsymbol{x}) = \langle\, \boldsymbol{\nu}(\boldsymbol{y})\cdot\boldsymbol{b}(\boldsymbol{x},\boldsymbol{y}) \,\rangle_{\mathrm{STR}} & \text{in } \Omega_{\mathrm{M}} \times Y
\end{array}$$

Figure 2.3: Diagram of the continuous two scale model of the fine scale magnetostatic problem introduced in Figure 2.1. The cell problems $(\mathrm{E}_Y(\boldsymbol{x}))$ are strongly coupled with the macroscopic equation $(\mathrm{E_H})$ via the scale transition relation $\langle\ \rangle_{\mathrm{STR}}$. In the example, the coupling is written in the form of a $\boldsymbol{H}(\boldsymbol{B})$ relation defined by applying $\langle\ \rangle_{\mathrm{STR}}$ to $\boldsymbol{h}$ and $\boldsymbol{b}$. The equations $\operatorname{div}\boldsymbol{B} = 0$, $\operatorname{div}\boldsymbol{b} = 0$ and conservation of $\boldsymbol{B}\cdot\boldsymbol{n}$ on $\Gamma_{\mathrm{H}\backslash\mathrm{M}}$ are omitted, it is assumed that they will be enforced in the function space using the magnetic vector potential.

It should be highlighted that an interface condition $(\mathrm{C_{H\backslash M}})$ should be defined at the homogenized domain boundary in place of $(\mathrm{C}_{\varepsilon\backslash\mathrm{M}})$. Both interface conditions will generally be a continuity condition like in the example Figure 2.3. But the consistency of the homogenized interface condition $(\mathrm{C_{H\backslash M}})$ with the original interface condition $(\mathrm{C}_{\varepsilon\backslash\mathrm{M}})$ depends on the choice of scale transition relation $\langle\ \rangle_{\mathrm{STR}}$ and macroscopic equations $(\mathrm{E_H})$, because $(\mathrm{C_{H\backslash M}})$ relates to the macroscopic fields and not to the fine scale ones.

The continuous two scale problem $\mathcal{P}_{\mathrm{H\backslash M}}$ is summarized in the following system of coupled problems:

$$\mathcal{P}_{\mathrm{H\backslash M}} : \begin{cases} (\mathrm{E_M}),\ (\mathrm{E_H}),\ (\mathrm{C_{H\backslash M}}) & \text{on } \Omega_{\mathrm{M}} \cup \Omega_{\mathrm{H}}, \\ (\mathrm{E}_Y(\boldsymbol{x})) & \text{on } Y, \qquad\qquad \text{for } \boldsymbol{x} \in \Omega_{\mathrm{H}}. \end{cases} \tag{2.5}$$

In general, this system contains an infinite number of cell problems $(\mathrm{E}_Y(\boldsymbol{x}))$. As will be explained later, when the cell problems are linear[4], they are independent of $\boldsymbol{x}$ and decoupled from $(\mathrm{E_M}) - (\mathrm{E_H}) - (\mathrm{C_{H\backslash M}})$. So only solving one cell problem (E_Y) is necessary. In this case, its solutions can be pre-computed once for all, and they are summarized in a homogenized material law tensor to use in $(\mathrm{E_H})$, e.g. $\boldsymbol{\nu}_M$ to replace $\boldsymbol{H}(\boldsymbol{B})$ by $\boldsymbol{\nu}_M\cdot\boldsymbol{B}$, as will be detailed later.

But if the cell problems feature a nonlinear material law[5], then their solutions depend on the macroscopic fields and thus depend on $\boldsymbol{x}$. It means that the macroscopic problem is

---

[4] If using time stepping method, this is only true if the macroscopic fields are numerically independent of previous time step solutions.

[5] Or if the cell problem time derivative terms affects the homogenized material law when using time stepping (Footnote 4).

nonlinear, and that an approximation of the cell problems solutions using a finite number of resolutions is necessary. This is the issue that the heterogeneous multiscale method solves.

Heterogeneous Multiscale Method

The *heterogeneous multiscale method* (HMM) [17, 16, 10] consists in doing two things. The first is reducing the number of cell problems to solve from an infinite number to a finite and reasonably small one, which allows to drastically reduce the amount of fine scale meshing and resolution compared with the original problem. The second is solving the two-scale problem iteratively using a weak coupling between the macroscopic problem and the cell problems. This allows to parallelize the cell problem resolutions.

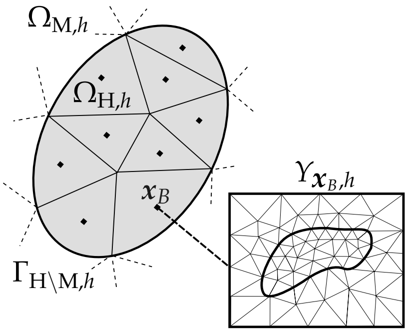

$(\mathrm{E}_Y(\boldsymbol{x}_B))$ for $\boldsymbol{x}_B \in \mathcal{B}(\Omega_{\mathrm{H},h})$:

$$\begin{aligned} &\mathbf{curl}_{\boldsymbol{y}}\, \nu(\boldsymbol{y}) \cdot \mathbf{curl}_{\boldsymbol{y}}\, \boldsymbol{a}(\boldsymbol{x}_B, \boldsymbol{y}) = \mathbf{0} \quad \text{in } Y_{\boldsymbol{x}_B,h} \\ &\mathbf{curl}\, \boldsymbol{A}(\boldsymbol{x}_B) = \left\langle \mathbf{curl}_{\boldsymbol{y}}\, \boldsymbol{a}(\boldsymbol{x}_B, \boldsymbol{y}) \right\rangle_{\mathrm{STR}} \end{aligned}$$

Figure 2.4: Diagram of the discretized two scale domain (left) used to define the discrete problem of the continuous model from Figure 2.3. The equations for the discrete cell problem are shown on the right.
A cell problem is associated to each macroscopic element, at their barycenters x_B. The macroscopic and cell problems are discretized using classic FEM. In general, the source of the problem is the downscaled field and its macroscopic derivative, like $\boldsymbol{B}$ and $\operatorname{div}\boldsymbol{B}$. But in this example, only the former is used because the latter is 0. The upscaling scale transition is a source of the macroscopic equations $(\mathrm{E_H})$. Here, both the macroscopic and cell magnetic induction fields are discretized using the magnetic vector potential (cf. Section 1.2.3), s.t. $\boldsymbol{B} = \mathbf{curl}\,\boldsymbol{A}$ and $\boldsymbol{b} = \mathbf{curl}_{\boldsymbol{y}}\,(\boldsymbol{a})$.

When the FEM is used to spatially discretize $(\mathrm{E_H})$ and (E_Y), it is natural to associate one cell problem to each Gauss point of the macroscopic mesh, because the macroscopic material laws are needed at these points. However, only one cell problem per macro element will be used in this work, associated with the barycenters of the element. We call $\mathcal{B}(\Omega_{\mathrm{H},h})$ the set of the barycenters $\boldsymbol{x}_B$ of the elements in the macroscopic mesh $\Omega_{\mathrm{H},h}$. The spatially discretized two-scale problem $\mathcal{P}_{\mathrm{H}\backslash\mathrm{M},h}$ thus becomes:

$$\mathcal{P}_{\mathrm{H}\backslash\mathrm{M},h} : \begin{cases} (\mathrm{E_M}) - (\mathrm{E_H}) - (\mathrm{C}_{\mathrm{H}\backslash\mathrm{M}}) & \text{on } \Omega_{\mathrm{M},h} \cup \Omega_{\mathrm{H},h}, \\ (\mathrm{E}_Y(\boldsymbol{x}_B)) & \text{on } Y_h, \qquad \text{for } \boldsymbol{x}_B \in \mathcal{B}(\Omega_{\mathrm{H},h}). \end{cases} \tag{2.6}$$

But the system (2.6) has still a strong coupling between all the equations of the system. To be able to parallelize the cell problem resolutions, their strong coupling with the macroscopic problem is transformed into a weak coupling. That is, the macro and cell problems are solved asynchronously by freezing (assuming constant) the quantities explicitly depending on the other scale during the resolution. The resolutions at each scale alternate until the macroscopic problem converges.

The frozen fields should be updated between each resolution. The transmission of the macroscopic field to the cell problems is denoted *downscaling*, while the computation and transmission of the homogenized material law to the macroscale is called *upscaling*. The pseudo algorithm for a HMM resolution of a nonlinear B-conforming magnetostatic problem is summarized in Algorithm 1.

Algorithm 1 HMM algorithm for a B-conforming static problem

```
Initialization
do                                                  ▷ Macro NL Loop
    for $x_B$ in $\mathcal{B}(\Omega_\mathrm{H})$ do       ▷ Cell resolutions, can be fully parallelized
        Downscale $\boldsymbol{B}(\boldsymbol{x}_B)$
        Solve Meso problem $(\mathrm{E}_{Y(\boldsymbol{x}_B)})$          ▷ Involves cell NL loop
        Upscale $\boldsymbol{H}(\boldsymbol{x}_B)$, $\frac{\partial \boldsymbol{H}}{\partial \boldsymbol{B}}(\boldsymbol{x}_B)$    ▷ Might involve FEM computations
    Solve Macro problem $(\mathrm{E}_\mathrm{M}) - (\mathrm{E}_\mathrm{H}) - (\mathrm{C}_{\mathrm{H}\backslash\mathrm{M}})$
while  Macro problem converged (or diverged)
```

Unlike the reference problem, the computational cost of the HMM resolution no longer depend on the number of geometric periods of the heterogeneous material. Indeed, the mesh size and computational cost of the FE-HMM is constant as ε decreases. Furthermore, the smaller ε is, the smaller the approximation error due to the multiscale approximation should be.

Time stepping Heterogeneous Multiscale Method

In this thesis, we will treat the time variation of the fields using the time stepping method. It enables a relatively easy validation of nonlinear multiscale formulation in both steady state and transient regime, in comparison with the methods presented later. Indeed, once the time derivatives are discretized with a θ-scheme (1.67), a finite number of PDEs that are solvable in a time loop is obtained.

HMM can be extended to time dependent problems by simply adding the time dependency to the equations and including Algorithm 1 in a time loop, this is the *time stepping* heterogeneous multiscale method (TS-HMM). Although TS-HMM can handle any time regime, more efficient methods exist when the problem is linear and/or steady state.

Asymptotic Homogenization Method

For problems featuring linear fine-scale material laws, the discrete equations yielded by using HMM on the previously introduced multiscale framework can be simplified. Indeed, the homogenized material law can be put in the form of a product by a second order tensor, e.g. $\boldsymbol{H}(\boldsymbol{B})$ can be written $\boldsymbol{H}(\boldsymbol{B}) = \boldsymbol{\nu}_M \cdot \boldsymbol{B}$. The material law tensor is constant and can be computed using three cell problem resolutions, where the cell is excited with three unitary sources in each spatial direction. It can be pre-computed and used in the macroscopic problem (see Section 2.3.1).

The obtained multiscale discrete system is the same as that obtained using the *asymptotic homogenization method* (AHM) [90]. But AHM is derived in a mathematically rigorous way, using an asymptotic analysis of the multiscale problems where the size of the cell tends to zero, see [10, Section 3.4][88].

For linear time dependent problems with harmonic sources, the solutions are also harmonic and the time variation of fields can be represented using phasors. Asymptotic homogenization also works in this case, one just has to consider a complex material law tensor. We call it the *harmonic asymptotic homogenization method* (H-AHM). This method is very efficient and widely used on electrical engineering problems [1, 2, 4, 5, 3, 89], but is limited to steady-state harmonic problems.

Multi-harmonic Heterogeneous Multiscale Method

General time periodic solutions, also called *multi-harmonic* solutions, are encountered in two situations. When the source of the linear problem is an arbitrary periodic signal, or as a steady state solution of a nonlinear problem excited with a periodic source.

In this case, the asymptotic homogenization method is extended by using time Fourier series basis function in place of phasors, leading to the *multi-harmonic* heterogeneous multiscale method (MH-HMM). To the extent of our knowledge, the first 3D nonlinear results in MQS with MH-HMM were obtained in parallel of this thesis work by [91].

In the steady state regime, multi-harmonic HMM is more efficient than time stepping HMM because there are fewer harmonics than the number of time steps to compute. Furthermore, the computational cost of MH-HMM does not depend on the time duration of the simulation, it only depends on the frequency content of the fields.

To note, it could be possible to use other type of time basis function to find alternatives to the time stepping method even on non steady-state problems, like polynomial functions with finite support.

Type of problem	Method	Macro. nonlinearity	Cell resolutions
Static regime			
Linear	AHM	No	1
Nonlinear	HMM	Yes	$N_B\, N_{mes}\, N_{Mac}$
Steady state regime			
Linear, harmonic	H - AHM	No	1
Linear, MH	MH - AHM	No	N_{harm}
Linear	TS - HMM	No	$N_B\, N_{TS}$
Linear	TS - HMM	Yes	$N_B\, N_{Mac}\, N_{TS}$
Nonlinear	MH - HMM	Yes	$N_B\, N_{mes}\, N_{Mac}\, N_{\text{harm}}$
Nonlinear	TS - HMM	Yes	$N_B\, N_{mes}\, N_{Mac}\, N_{TS}$
Transient regime			
Linear	TS - HMM	No	$N_B\, N_{TS}$
Linear	TS - HMM	Yes	$N_B\, N_{Mac}\, N_{TS}$
Nonlinear	TS - HMM	Yes	$N_B\, N_{mes}\, N_{Mac}\, N_{TS}$

Table 2.1: Summary of available general purpose multiscale methods with scale separation hypothesis. The "Type of problem" column relates to the time regime and the (non)-linearity of the **fine-scale** material laws. The last column gives the complexity of the cell problems resolutions in function of the type of problem and possible nonlinearity of the macroscopic problem. The **macroscopic** nonlinearity (third column) happen if the fine scale laws are nonlinear, or if there is macroscopic dynamic hysteresis in time-stepping time dependent problems (this depends on the problem), which is why two TS-HMM lines are duplicated. For non time-stepping methods, there cannot be macroscopic hysteresis in linear thanks to the time periodicity of the fields, this is a noteworthy advantage in practice.

Summary of the multiscale methods using the scale separation hypothesis

Several multiscale methods using the scale separation hypothesis have been presented, each is valid in specific cases and has different numerical cost. The Table 2.1 gives a summary of the methods and their main characteristics.

The computational cost can be well described in terms of the number of cell problem resolutions, which is representative of the difficulty to estimate the equivalent macroscopic material law. This number of resolutions is counted in terms of:

- N_B the number of macroscopic points to which a cell problem is associated (e.g. the number of macro elements Gauss points or barycenters)
- N_{mes} the number of nonlinear iterations needed for the convergence of a cell problem
- N_{Mac} the number of nonlinear iterations needed for the convergence of the macroscopic problem
- N_{TS} the number of time steps (in TS-HMM)
- N_{harm} the number of harmonics used to represent the time variation of the macroscopic unknown field (in MH-HMM)

The cost associated to each method is shown in Table 2.1.

Also, there are additional cell problem resolutions due to the computation of the Jacobian of the macroscopic law, e.g. $\frac{\partial \boldsymbol{H}}{\partial \boldsymbol{B}}$. It can be done using finite differences on the cell problem resolution. This multiplies the number of cell resolutions by a factor up to $1 + D$ where D is the spatial dimension (2 or 3), but only when the macroscopic problem is nonlinear. This cost is omitted in Table 2.1.

Steps for the derivation of a better two scale model

This section reviewed the main general purpose multiscale methods used in electrical engineering and other domains. The next sections consist in a step by step derivation of a two scale model for the magnetoquasistatic problems that belongs to the previously introduced setting: it assumes the scale separation hypothesis and uses the HMM for the numerical resolution.

A reference MQS fine-scale problem defined on $\Omega_{\mathrm{M}} \cup \Omega_{\varepsilon}$ is split into a macroscopic problem on $\Omega_{\mathrm{M}} \cup \Omega_{\mathrm{H}}$ and several fine scale problems in Y. The equations governing each scale are Maxwell's equations in the matter in the MQS approximation (1.19). The material laws and formulations in the cell problems are that of the reference problem. The macroscopic formulation is deduced from the nature of the equivalent material laws, which are determined from the cell topology. Concretely, we will make the assumption that there are no macroscopic current by restricting ourselves to electrically insulated cells, so the macroscopic conductivity will be zero and the magnetostatic equations will be used in the homogenized material.

The two-scale model derivation is split in three steps, each of them featuring original contributions. In a first step, in Section 2.2, a new scale transition relation that is more general than the volume average is defined. It is contextualized and based on classical and recent works. A particular focus is made on the notion of bound and free fields and there impact on the macroscopic magnetization.

In a second time, a cell field splitting enabling the implementation of the cell problem equations is given in Section 2.3. Although the derived formulas are already known, their consistency with the new scale transition relation will be shown. The derivation of the macroscopic problem is also conducted.

Finally, several methods that help to correctly upscale the macroscopic fields, in particular the magnetic field strength $\boldsymbol{H}$, are derived in Section 2.4.

2.2 Study of the scale transition relation

The objective of this section is to define the scale transition relation suitable for the multiscale modeling of electromagnetic fields under the scale separation hypothesis.

We start with the review of electromagnetic fields scale transition relations in the literature, especially the classical one from Maxwell's equations in the free space to Maxwell's equations in the matter (further called FM-STR for *Free-space to Matter STR*). A particular focus is made on the notion of bound and free fields, magnetization and polarization. It will be highlighted that several homogenized fields are defined differently from each others, supporting the idea of not using the volume average for every scale transitions in our multiscale framework.

In fact, we want to highlight the links between the classical FM-STR and the scale transition used in multiscale modeling. Indeed, they aim at modeling the same macroscopic behaviors. Also, state-of-the-art works on the scale transition of electromagnetic fields are studied in order to consolidate our understanding of the requirement for the sought scale transition relation.

This lead us to propose a new scale transition relation that depends on the field-type and is consistent with both the state-of-the-art in computational multiscale modeling and the classical FM-STR, especially with the usual definition of the magnetic field strength and electric displacement using magnetization and polarization.

2.2.1 Scale transition from free space to matter

The fundamental model for the electromagnetic fields are Maxwell's equations in free space (or in vacuum). They can be written at the scale of molecule when the elementary charged particles can be approximated by pointwise charges, that is at a scale larger than that of possible quantum effects to be considered [92]. Maxwell's equations in the free space read:

$$\begin{aligned} \mathbf{curl}\, \boldsymbol{e}_v &= \partial_t \boldsymbol{b}_v, & \operatorname{div} \boldsymbol{b}_v &= 0, \\ \mathbf{curl}\, \mu_0^{-1} \boldsymbol{b}_v &= \boldsymbol{j}_v + \partial_t \varepsilon_0 \boldsymbol{e}_v, & \operatorname{div} \varepsilon_0 \boldsymbol{e}_v &= \rho_v, \end{aligned} \tag{2.7}$$

where free space fields are identified with the $\bullet_v$ subscript. The source of these equations are the charges ρ_v and currents $\boldsymbol{j}_v$, and their solution are the free space electric field $\boldsymbol{e}_v$ and magnetic induction $\boldsymbol{b}_v$[6].

But the resolution of these equations at the scale of molecule over a complete macroscopic device is impossible and irrelevant, the fields in such problems can only be described at larger scale than that of molecules. The standard way of modeling electromagnetic fields at larger scales is to use Maxwell's equations in matter. They are related to those in free space according to several authors that have developed theories on how to transition from Maxwell's equations in free space to larger scales. We refer to [92] and to [94], where comparison with other theories can be found. In the meantime, a summary of the classical FM-STR is proposed hereafter.

---

[6] In matter, some magnetization is explained by quantum effect [93] at scales smaller than molecules, so it might be required to add as a source of the equations (2.7). But this does not change the equations nor their homogenization.

Smoothing of the free space fields

Let L be the characteristic length of the targeted larger scale to which one wants to write Maxwell's equations in matter. One can think of L as the spatial resolution at the larger scale, that is the minimal distance between two points for which it is possible to distinguish between them. L should be large compared to the scale of molecule, which is the nanometer.

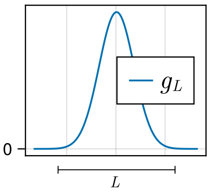

The fields at scale L, further called *macroscopic fields* (macro fields), are defined using averages of free space fields. More precisely, the idea is to define them as convolutions of free space fields with a smoothing kernel g_L. The smoothing kernel g_L should be a function symmetric around 0 with a support of diameter $\approx L$. It should slowly decay to 0 near the support boundary to maximize the smoothing of higher spatial frequencies [92], like a Gaussian curve for example. So a smooth macro field $\boldsymbol{F}$ can be obtained from the fine scale field $\boldsymbol{f}$ with

$$\boldsymbol{F}(\boldsymbol{x}) = \langle \boldsymbol{f} \rangle_L(\boldsymbol{x}) := \int_{\|\boldsymbol{x}-\boldsymbol{y}\|<L} g_L(\boldsymbol{y})\, \boldsymbol{f}(\boldsymbol{x}-\boldsymbol{y}) d\boldsymbol{y} \tag{2.8}$$

where $\langle \bullet \rangle_L$ denotes the spatial smoothing. The integration is restricted to the neighborhood of diameter L of the point $\boldsymbol{x}$ because it is the support of the smoothing kernel g_L.

The smoothing is applied to Maxwell's equations themselves, and as the spatial and time derivative operators commute with the convolution (because it is a linear operation), it yields the following equation set:

$$\begin{aligned} \mathbf{curl}\,\langle \boldsymbol{e}_v \rangle_L &= \partial_t \langle \boldsymbol{b}_v \rangle_L, & \operatorname{div} \langle \boldsymbol{b}_v \rangle_L &= 0, \\ \mathbf{curl}\left\langle \mu_0^{-1} \boldsymbol{b}_v \right\rangle_L &= \langle \boldsymbol{j}_v \rangle_L + \partial_t \langle \varepsilon_0 \boldsymbol{e}_v \rangle_L, & \operatorname{div} \langle \varepsilon_0 \boldsymbol{e}_v \rangle_L &= \langle \rho_v \rangle_L. \end{aligned} \tag{2.9}$$

These equations could be used as macroscopic Maxwell's equations. However, the fields contain inconvenient features that depend on the fine-scale matter physics, including discontinuities at the macroscopic interface between matter and free space. In particular, the current $\langle \boldsymbol{j}_v \rangle_L$ contains so-called bound currents. Consequently, the fields $\langle \mu_0^{-1} \boldsymbol{b}_v \rangle_L$ and $\langle \varepsilon_0 \boldsymbol{e}_v \rangle_L$ contain discontinuities and bulk contributions associated with the bound fields that are called magnetization and polarization, respectively. Let's focus on these bound fields.

Bound charges and currents, polarization and magnetization

The literature considers the existence of bound charges ρ_b and bound currents $\boldsymbol{j}_b$. The rest of the smoothed fields are called *free charges* ρ and *free currents* $\boldsymbol{J}$, leading to the macroscopic splitting

$$\begin{aligned}\langle\, \rho_v \,\rangle_L &= \rho + \rho_b, \\ \langle\, \boldsymbol{j}_v \,\rangle_L &= \boldsymbol{J} + \boldsymbol{J}_b.\end{aligned} \tag{2.10}$$

At the fine scale, bound charges and currents are classically defined using specific physics models. For example, nanometer scale bound charges are often defined as the charges that cannot move outside their molecule. And molecular bound current are sometimes defined as current loops created by the movement of electrons confined in a molecule. On the other hand, the free charges and currents correspond to charges really flowing from molecules to molecules, such that their movements can be followed at a larger matter scale. Although the average of the bound charges and currents over a molecule cancel out, they do not completely disappear from macroscopic equations after spatial smoothing.

Furthermore, Maxwell-Faraday equation imposes that bound charges are associated with microscopic electric field, and Maxwell-Ampere equation imposes that bound currents are associated with a microscopic magnetic field and/or bound charges movement in time. The smoothing of these two microscopic fields yield macroscopic fields respectively called polarization $\mathscr{P}$ and magnetization $\mathscr{M}$, which verify the following equations:

$$\begin{aligned}\rho_b &= -\operatorname{div} \mathscr{P}, \\ \boldsymbol{J}_b &= \mathbf{curl}\, \mathscr{M} + \partial_t \mathscr{P}.\end{aligned} \tag{2.11}$$

In (2.11), ρ_b and $\boldsymbol{J}_b$ are implicitly considered as generalized functions, respectively admitting possible bound surface charges and bound surface currents, that are usually called σ_b and $\boldsymbol{K}_b$, respectively.

A more illustrated and detailed explaination of bound charges, bound currents, polarization and magnetization is given in [95] and [96].

Passing the smoothed bound fields in the material laws

As mentioned before, those fields are inconvenient to work with at macro scale. Indeed, the bound fields nearly always contain a surface field at the interface between free space and matter, which are cumbersome to add in the discrete function space. Furthermore, all these fields cannot be computed at macroscopic scale only, either $\boldsymbol{j}_b$ and ρ_b or $\mathscr{M}$ and $\mathscr{P}$ need to be determined by a microscopic model.

As bound fields are classically not considered in Maxwell-Faraday's equation, the macroscopic fields $\boldsymbol{B}$ and $\boldsymbol{E}$ are defined by:

$$\boldsymbol{E} = \langle\, \boldsymbol{e} \,\rangle_L, \quad \boldsymbol{B} = \langle\, \boldsymbol{b} \,\rangle_L. \tag{2.12}$$

From there, combining (2.9)-(2.10)-(2.11)-(2.12) leads to Maxwell's equations in the matter, which were already introduced in the first chapter 1:

$$\begin{aligned} \mathbf{curl}\, \boldsymbol{E} &= \partial_t \boldsymbol{B}, & \operatorname{div} \boldsymbol{B} &= 0, \\ \mathbf{curl}\, \boldsymbol{H} &= \boldsymbol{J} + \partial_t \boldsymbol{D}, & \operatorname{div} \boldsymbol{D} &= \rho, \end{aligned} \tag{2.13}$$

where the magnetic field strength $\boldsymbol{H}$ and electric displacement $\boldsymbol{D}$ were introduced, such that:

$$\boldsymbol{H} = \frac{1}{\mu_0}\boldsymbol{B} - \mathscr{M}, \quad \boldsymbol{D} = \varepsilon_0 \boldsymbol{E} + \mathscr{P}. \tag{2.14}$$

This way, the bound currents and charges are removed from the macroscopic fields and equations.

But written like this, the equations cannot be solved at the macroscopic scale because of the implicit dependency on the polarization and magnetization, which are defined using the free-space fields. To avoid relying on the knowledge of the free-space fields, the macroscopic relation between the macroscopic fields is approximated via *constitutive relations*, also called the material laws. In absolute generality, the constitutive relation link all the fields together, because the microscopic equations link them all. So for example, in a B-conforming formulation of (2.13), the constitutive relation should define $\boldsymbol{H}$, $\boldsymbol{J}$ and $\boldsymbol{D}$ as function of the unknowns $\boldsymbol{B}$ and $\boldsymbol{E}$ at each instant in time [4], that is $\boldsymbol{H}(\boldsymbol{B}, \boldsymbol{E})$, $\boldsymbol{J}(\boldsymbol{B}, \boldsymbol{E})$ and $\boldsymbol{D}(\boldsymbol{B}, \boldsymbol{E})$, where these functions **implicitly depend** on the **time** t and the **fine scale field** distributions.

But most of the time, it is enough to consider the $\boldsymbol{B} - \boldsymbol{H}$, $\boldsymbol{D} - \boldsymbol{E}$ and $\boldsymbol{J} - \boldsymbol{E}$ relations. In this case, the macroscopic effects of the bound fields may be hidden in macroscopic material laws such as

$$\begin{aligned} \boldsymbol{\varepsilon} &= \varepsilon_0(1 + \mathrm{X}_e) & \text{s.t. } \boldsymbol{D} &= \boldsymbol{\varepsilon}\boldsymbol{E}, \\ \boldsymbol{\mu} &= \mu_0(1 + \mathrm{X}_m) & \text{s.t. } \boldsymbol{B} &= \boldsymbol{\mu}\boldsymbol{H}, \end{aligned} \tag{2.15}$$

where X_e and X_m are the electric and magnetic susceptibility, respectively. Also, the following conductivity relation is added:

$$\sigma \qquad \text{s.t. } \boldsymbol{J} = \sigma \boldsymbol{E}. \tag{2.16}$$

The conductivity expresses the ability of a material to conduct electric current, i.e. a flow of free electric charges, which is driven in the medium by the electromagnetic force resulting from the application of an electric field.

But it is only possible to define the constitutive laws using only tensors if they are not hysteretic. In any case, they are usually defined by models adapted to specific problems and calibrated using experimental data.

To sum up the classical FM-STR, the scale transition of the fields $\boldsymbol{e}$ and $\boldsymbol{b}$ are defined using a simple smoothing. On the other hand, the scale transition of $\frac{1}{\mu_0}\boldsymbol{b}$, $\varepsilon_0\boldsymbol{e}$, $\boldsymbol{\mu}$ and $\boldsymbol{\varepsilon}$ is made using a smoothing of the free space fields followed by a filtering of the bound fields. The magnetization and polarization are transferred to the material laws in order to eliminate bound currents and charges.

2.2.2 On the scale transition between different matter scales

The goal of this subsection is to show that the classical FM-STR can be linked to the scale transition needed for multiscale modeling, and to explain what is required to make both transitions compatible and consistent.

It will be defended that the definition of what is a bound field should depend on the considered scale, as contributions to the magnetization and polarization can arise from scales larger than that of molecules. In particular, this might happen at the finer scale of multiscale computational model. Consequently, these additional polarization and magnetization should be identified and taken into account in the STR used in multiscale modeling.

Some notations will be introduced to differentiate the different components of the macroscopic magnetization depending on the scale of the current loop that creates it, and an example of periodic material with bound currents will be used to illustrate how macroscopic magnetization can be created at an intermediate matter scale.

Finally, the state of the art of the scale transition used in computational multiscale modeling of electromagnetic fields will be reviewed.

Scale dependency of Maxwell's equations in the matter

Maxwell's equations in the matter are commonly used at many different scales, from the micrometer scale for modeling SMC materials to scales of hundreds of kilometers for geosciences applications or continental electrical networks, with numerous examples at intermediate scales. Indeed, the radius of the smoothing kernel used to homogenize the electromagnetic fields in the FM-STR is the spatial resolution at the scale for which they are written.

In the multiscale modeling of electromagnetic fields, we are interested in computing the fields at a given large scale L from their distribution at a finer scale l. We can apply the definition of the fields in matter from free-space fields at both scales, for example that of the magnetic field strength in Figure 2.5, where $\bullet_l$ or $\bullet_L$ scale indices are added to $\mathscr{M}$ to differentiate the scale at which it is defined. But the following question occurs: is the magnetization at scale L the same as the smoothing of that of scale l, that is $\langle \mathscr{M}_l \rangle_L$? In other word, is it possible to assume that the magnetic strength field can be upscaled using a simple smoothing, that is $\boldsymbol{H} = \langle \boldsymbol{h} \rangle_L$?

To note, when the spatial smoothing of two separated scales l and L are chained, it is possible to approximate that the result is the same as just only applying the larger smoothing, because chaining averages is just doing a larger average[7]. That is

$$\langle \langle \boldsymbol{f} \rangle_l \rangle_L = \langle \boldsymbol{f} \rangle_L \tag{2.17}$$

whenever $l \ll L$.

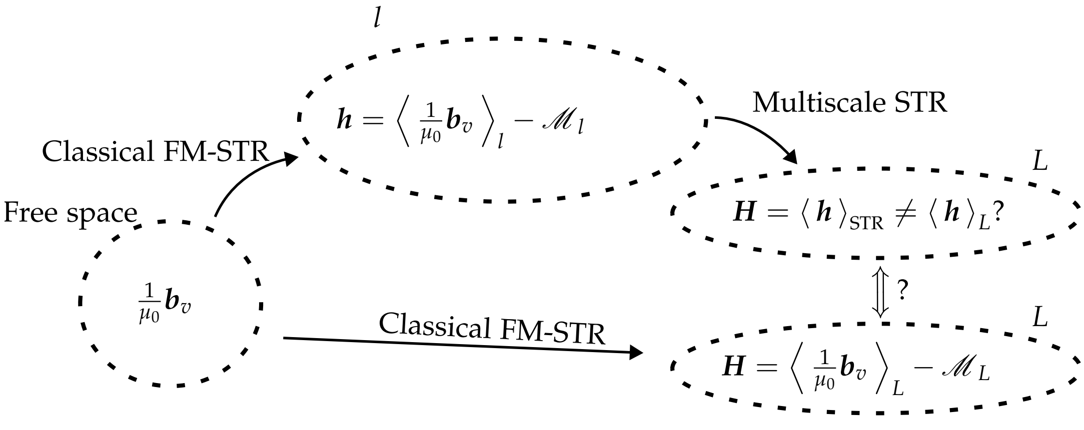

Figure 2.5: Sketch of scale transition of the magnetic field strength between two different scales l and L. It will be shown that to have $\langle \boldsymbol{h} \rangle_{\mathrm{STR}}$ equal to the L-scale $\boldsymbol{H}$, the STR $\langle\ \rangle_{\mathrm{STR}}$ needs to be different than the simple smoothing $\langle\ \rangle_L$, similarly to the fact that $\boldsymbol{H}$ is not only $\langle \frac{1}{\mu_0}\boldsymbol{b}_v \rangle_L$. This is because the L-scale magnetization $\mathscr{M}_L$ is not the smoothing of the l-scale one ($\mathscr{M}_L \neq \langle \mathscr{M}_l \rangle_L$). Indeed, the l-scale current loops may create additional L-scale magnetization.

When there is a scale separation between l and L, it is reasonable to think that some currents may loop in a conducting inclusion at scale l, and thus that they are bound at scale l. But as such current flows freely through the conductive inclusion, it cannot be considered a bound field on the free-space scale. The magnetic field it creates is therefore ignored in the magnetization at the scale l. However, if magnetic field of this current loop is not negligible in comparison to $\boldsymbol{h}$, all the ingredients for additional macroscopic

---

[7] For example, the composition of two convolutions with Gaussian kernels of radii (standard deviation) l and L is equal to a convolution with a Gaussian kernel of radius $L + l$. But as $l \ll L$, the kernels of radii L and $L + l$ are approximately the same.

magnetization are met.

This possibility of having magnetization sources at several scales was anticipated by authors who worked on the definition of Maxwell's equations in matter. For example, Russakoff stated the following remark at the end of [94]: " The motion of the conduction electron may give rise to a magnetization (electron diamagnetism in metals, for example). However, the orbit of such electrons will be quite large compared to atomic dimensions and must therefore be analyzed in a manner different that than used here. [...] The magnetization of the conduction electrons should be grouped together with the molecular contribution to form the total magnetization ".

However, no notations were introduced to describe this multiscale definition of the magnetization. But having some will be useful to quantitatively define the $l \to L$ scale transition of the magnetic field strength in multiscale modeling, so we introduce them for the purpose of this thesis.

Let us call l_s the scales at which we wish to write Maxwell's equations in the matter, including that at which some magnetization is created. l_s is defined for $0 \leq s \leq N$ with $N \in \mathbb{N}$, the first scale l_0 is the atomic/molecular scale noted v and the last one l_N is the macroscopic scale L. Additionally, it is assumed that there is large difference between all intermediate scales, that is:

$$v = l_0 \ll \cdots \ll l_s \ll \cdots \ll l_N = L.$$

At a scale of index s, we denote $\mathscr{M}_{l_s}$ the total magnetization field at the scale l_s. It is the one from the classical definition of the magnetic fields strength that satisfies:

$$\boldsymbol{h}_{l_s} = \left\langle \frac{1}{\mu_0} \boldsymbol{b}_v \right\rangle_{l_s} - \mathscr{M}_{l_s}, \tag{2.18}$$

where $\boldsymbol{h}_{l_s}$ is the magnetic field at scale l_s. Additionally, a notation for the fine scale distribution of the magnetization field would be useful. Let us call $\boldsymbol{m}_{l_i}$ the distribution of the magnetization created at scale l_i by the currents $\boldsymbol{j}_{b,l_i}$ which are bound at the scale l_i, but that are free currents for all smaller scales. That is, it holds

$$\mathbf{curl}\, \boldsymbol{m}_{l_i} = \boldsymbol{j}_{b,l_i}.$$

These two fields are a portion of the l_i-scale magnetic field $\boldsymbol{h}_{l_i}$ and currents $\boldsymbol{j}_{l_i}$. For now, their definition is only qualitative, but quantitative definitions will be detailed at the end of this section.

The magnetization $\mathscr{M}_{l_s}$ at scale l_s can be computed by summing and smoothing the fine-scale magnetization distributions at all smaller scales l_i where $i < s$, that is

$$\mathscr{M}_{l_s} = \sum_{i<s} \langle\, \boldsymbol{m}_{l_i} \,\rangle_{l_s}. \tag{2.19}$$

If l_s is not the largest scale, there can be bound currents $\boldsymbol{j}_{b,l_s}$ at this scale and thus a local magnetization distribution $\boldsymbol{m}_{l_s}$. So $\mathscr{M}_{l_s}$ and $\boldsymbol{m}_{l_s}$ coexist at scale l_s, but they are completely different things. $\mathscr{M}_{l_s}$ is the magnetization created at smaller scales, it is included in the magnetic material law governing at scale l_s, and cannot be determined at the scale l_s. On the other hand, $\boldsymbol{m}_{l_s}$ is created by the bound currents $\boldsymbol{j}_{b,l_s}$ that cancel in average at scales larger than l_s. The field $\boldsymbol{m}_{l_s}$ is actually a part of the magnetic field $\boldsymbol{h}_{l_s}$. It is not taken into account in $\mathscr{M}_{l_s}$, because from the point of view of the scales smaller than l_s, the currents $\boldsymbol{j}_{b,l_s}$ are macroscopic currents.

It is a standard field distribution that can be visualized and computed at scale l_s, but its smoothing has to be removed from the magnetic field strength of higher scales because it contributes to higher scales magnetization $\mathscr{M}_{>l_s}$. Thus, we have

$$\langle\, \mathscr{M}_{l_s} + \boldsymbol{m}_{l_s} \,\rangle_{l_{s+1}} = \mathscr{M}_{l_{s+1}}. \tag{2.20}$$

To make it easier to describe the scale transition of the magnetic field strength in multiscale modeling, we introduce a notation for the macroscopic magnetization at scale l_s that is created by bound currents from a finer scale l_i, $\mathscr{M}_{l_i \to l_s}$. It is defined by:

$$\mathscr{M}_{l_i \to l_s} = \langle\, \boldsymbol{m}_{l_i} \,\rangle_{l_s}. \tag{2.21}$$

This notation helps to express what is the macroscopic magnetization to add to the smoothing of a lower scale magnetic field to obtain the macroscopic magnetic field. For example, it allows to transform (2.20) into:

$$\mathscr{M}_{l_{s+1}} = \langle\, \mathscr{M}_{l_s} \,\rangle_{l_{s+1}} + \mathscr{M}_{l_s \to l_{s+1}}. \tag{2.22}$$

In the end, in the example from Figure 2.5 with scales v, l and L, the scale transition $l \to L$ of the magnetic field strength is defined by:

$$\boldsymbol{H} = \langle\, \boldsymbol{h} \,\rangle_{\mathrm{STR}} = \langle\, \boldsymbol{h} - \boldsymbol{m}_l \,\rangle_L = \langle\, \boldsymbol{h} \,\rangle_L - \mathscr{M}_{l \to L}. \tag{2.23}$$

This scale transition is consistent with the classical FM-STR, as shown in Figure 2.6.

A similar multiscale definition of the polarization could be used for the homogenization problem that take the electric permitivity and electric displacement into account. $\mathscr{P}_l$,

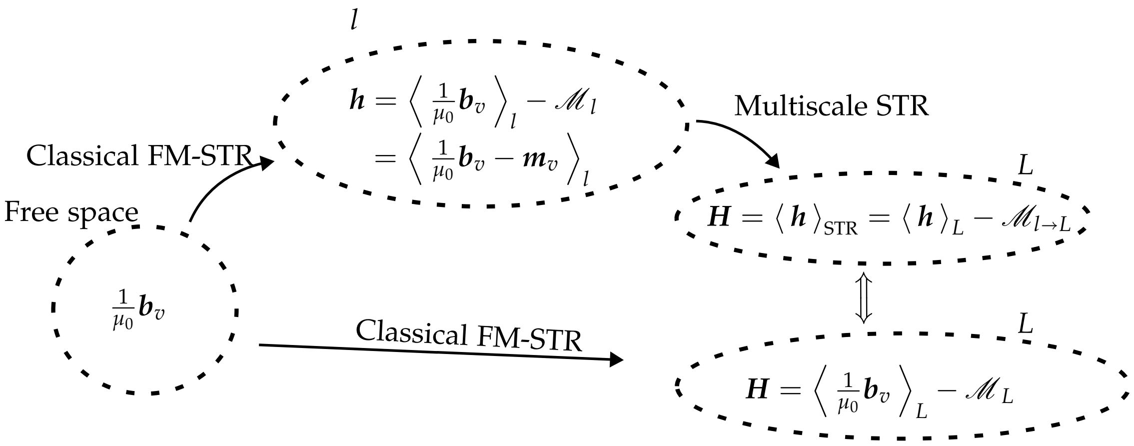

Figure 2.6: Illustration of the multiscale definition of the magnetization with three scales v, l and L. We suppose that magnetization is only created at the free-space scale and from current loops from the l-scale, that is $\mathscr{M}_L = \langle \mathscr{M}_{v\to l} \rangle_L + \mathscr{M}_{l\to L}$. By plugging this expression for the magnetization in the classical definition of $\boldsymbol{H}$ (below right bubble), one gets: $\boldsymbol{H} = \langle \frac{1}{\mu_0} \boldsymbol{b}_v - \mathscr{M}_{v\to l} \rangle_L - \mathscr{M}_{l\to L}$. Finally, the smoothing kernel composition property (2.17) allows to write $\langle \frac{1}{\mu_0} \boldsymbol{b}_v \rangle_L = \langle \langle \frac{1}{\mu_0} \boldsymbol{b}_v \rangle_l \rangle_L$, the classical FM-STR (bottom right) is thus consistent with the scale transition of multiscale modeling (middle right).

$\boldsymbol{p}_l$ and $\mathscr{P}_{l\to L}$ would be defined similarly to $\mathscr{M}_l$, $\boldsymbol{m}_l$ and $\mathscr{M}_{l\to L}$ but with $\operatorname{div} \boldsymbol{p}_l = -\rho_{b,l}$ at scale l and $\boldsymbol{D} = \langle \boldsymbol{d} \rangle_l + \mathscr{P}_{l\to L}$.

In multiscale modeling of periodic media, the intermediate l scale is the size of the periodic cell ε and the macroscopic one is denoted H. A quantitative definition of $\boldsymbol{m}_\varepsilon$ (or at least $\boldsymbol{H}$ or $\mathscr{M}_{\varepsilon\to \mathrm{H}}$) based on the cell fields distribution is required.

Example of scale transition with bound currents and magnetization

In the previous section, notations for a multiscale definition of the magnetization have been introduced. In order to better visuallize how magnetization emerges during the smoothing procedures, let us take an example of a smoothing of 1D magnetic field strength $\boldsymbol{h}$ and electric current density $\boldsymbol{j}$ at a scale l. This example is inspired from the explanations of bound currents an magnetization found in the books [95, 65], but adapted in the context of periodic homogenization.

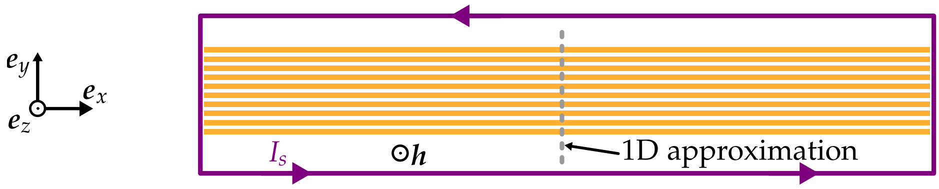

Figure 2.7: Example setup to illustrate bound currents and magnetization. It is a stack of 10 copper sheets inside a long solenoid.

Let us consider a stack of thin laminated copper sheets separated from another by thin layers of insulator as shown in Figure 2.7. This stack is placed inside a very long solenoid with a square section, aligned parallel to the $\boldsymbol{e}_z$ axis. It has a rectangular section such that the thickness of the solenoid and stack in the direction $\boldsymbol{e}_y$ is negligible compared to its width in direction $\boldsymbol{e}_x$. We assume that the insulator has the same property as the free space, and that the copper has a permeability of μ_0 and a nonzero constant conductivity.

If a constant current I_s flows in the solenoid wire, $\boldsymbol{h}$ and $\boldsymbol{b}$ are constant and homogeneous inside it because $\boldsymbol{\mu}$ is equal to μ_0 everywhere and there are no eddy currents, as if the solenoid were enclosing only air. In case of time varying I_s, $\boldsymbol{h}$ will vary inside the copper sheets because eddy currents $\boldsymbol{j}$ appear in the $\boldsymbol{x}/\boldsymbol{y}$ plane. Far from the ends of the solenoid and the sides of the stack, we assume that the fields are constant in the $\boldsymbol{e}_z$ and $\boldsymbol{e}_x$ directions, and that $\boldsymbol{h}$ and $\boldsymbol{j}$ are respectively aligned with $\boldsymbol{e}_z$ and $\boldsymbol{e}_x$, as shown in Figure 2.7. Then, typical profile of $j_x = \|\boldsymbol{j}\|$ and $h_z = \|\boldsymbol{h}\|$ can be plotted, taken on a line in the $\boldsymbol{e}_y$ direction (the gray dotted line in Figure 2.7) to analyze how a smoothing affects them. They verify $j_x = \frac{\partial h_z}{\partial_y}$, the 1D Ampère's law.

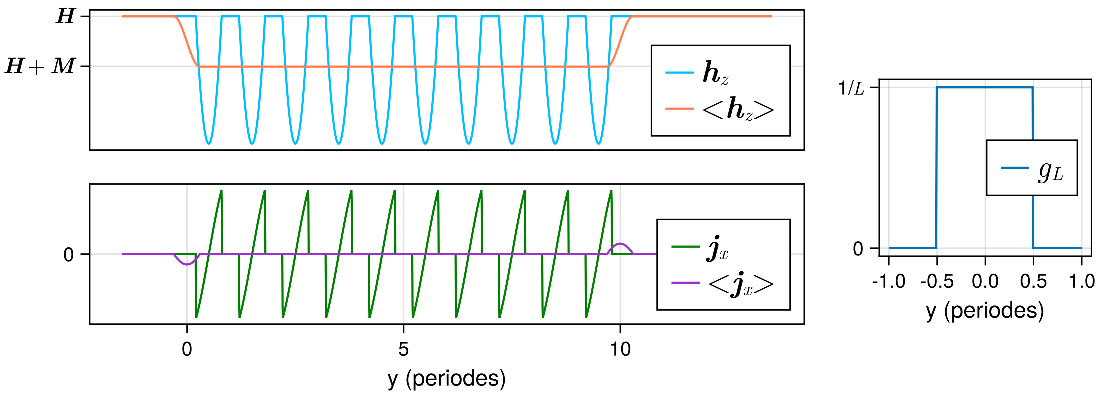

Figure 2.8: Periodic magnetic field h_z and current distribution $j_x = \frac{\partial h_z}{\partial_y}$ in copper sheets (h_z is not an actual solution but a fictive example), and their smoothing with the cell average kernel (shown on the right) which is classically employed in computational multiscale modeling. The x-axis is the number geometric spatial periods. A macroscopic bound current $\langle j_x \rangle$ appears around the boundaries of the sheets stack. If we zoom out and look at it a coarser resolution, this smoothed bound current is a surface field. The bound current is associated with magnetization that affects the smoothed magnetic field level in the material. $\boldsymbol{H}$ and $\mathscr{M}$ correspond to the standard definition of the macroscopic magnetic field strength, where $\boldsymbol{H} = \langle \mu^{-1}\boldsymbol{b} \rangle - \mathscr{M} = \langle h_z \rangle - \mathscr{M}$.

The smoothing using the kernel corresponding to the volume average (2.2), which is commonly used in computational multiscale modeling, is applied to the field maps. This kernel is constant equal to $1/\varepsilon$ on a support of width ε, where ε is the width of one sheet plus one insulation layer. The smoothed fields and the kernel are shown in Figure 2.8. The rest of the discussion applies independently of the choice of smoothing kernel, because the obtained smoothed field are macroscopically equivalent[8].

The smoothed current $\langle j_x \rangle$ (violet curve in Figure 2.8) is null inside the material as confined current loops cancel on average. But at the material boundaries, the kernel spans vacuum and a half of a current loops, so a net current is measured . If we zoom out at a resolution larger than the kernel support, this current must be modelled as a surface bound current $\boldsymbol{J}_b$. On the other hand, the smoothed magnetic field $\langle h_z \rangle$ (in orange) is discontinuous at the material boundary. Indeed, its value inside the material drops compared to its value in vacuum.

These observations help to explain the two possible strategies used to define the macroscopic fields. The first is the use of the full smoothed fields $\boldsymbol{H} = \langle \boldsymbol{h} \rangle$ and $\boldsymbol{J} = \langle \boldsymbol{j} \rangle$, in orange and violet on the plots. In this case, $\boldsymbol{H}$ is discontinuous at the material boundary and the bound surface current $\boldsymbol{J}_b$ is into $\boldsymbol{J}$. This choice respects the classic macroscopic interface condition (1.15) relating to tangential discontinuities of $\boldsymbol{H}$ associated with the surface current in $\boldsymbol{J}_b$.

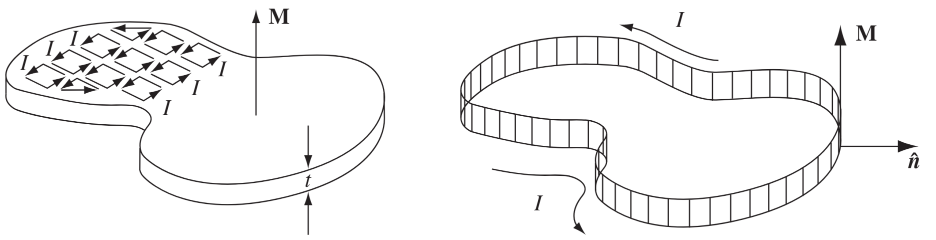

FIGURE 6.15 **FIGURE 6.16**

Figure 2.9: Figures taken from [95] that illustrate the emergence of macroscopic bound surface currents from microscopic current loops of same intensity. The current I from the left figure is what is denoted the surface $\boldsymbol{J}_b$ in our dissertation. The author also explains that volume bound currents emerge inside the material when neighboring fine-scale current loops are of different intensities.

But this strategy has three flaws that are the reason for the introduction of the magnetization in the free-space to matter scale transition. Firstly, the surface current and $\boldsymbol{h}$ discontinuity can only be determined via the microscopic model. Secondly, the discontinuous / generalized fields (containing Diracs) are not convenient to work with both on paper and numerically. And last but not least, the macroscopic current is not zero everywhere, although the plates are insulated from each other. In particular, macroscopic bound currents flow in the direction $\boldsymbol{e}_y$ on the right and left sides of the sheet stack, although the material is macroscopically nonconducting in direction $\boldsymbol{e}_y$ due to the insulation between the sheets. This phenomenon is well described by Griffiths in [95,

---

[8] The Gaussian kernel is very robust, but has a quite wide support. On the other hand, the kernel constant on the cell enables using a smaller support, but it can only smooth periodic fields with a period equal to an exact fraction of the kernel support. Although the kernels have different characteristics, they lead to equivalent macroscopic fields when they work. See the discussion in Appendix A.3.

Figures 6.15 & 6.16], they are given in Figure 2.9. In conclusion, this first strategy leads to consider bound current as part of the macroscopic current $\boldsymbol{J}$, and it is inconsistent with the usual Maxwell equations in matter.

The second possible macroscopic field definition is to remove the bound currents $\boldsymbol{J}_b$ and the associated magnetization $\mathscr{M}_{\varepsilon\to\mathrm{H}}$ respectively from $\langle\, \boldsymbol{j}\,\rangle$ and $\langle\, \boldsymbol{h}\,\rangle$, which leads to $\boldsymbol{J} = \langle\, \boldsymbol{j}\,\rangle - \boldsymbol{J}_b$ and $\boldsymbol{H} = \langle\, \boldsymbol{h}\,\rangle - \mathscr{M}_{\varepsilon\to\mathrm{H}}$ (2.23), that are similar to (2.10)-(2.14). In our example, it means defining $\boldsymbol{J} = \boldsymbol{0}$, and consequently $\boldsymbol{H}$ is constant equal to its value outside the sheets (the y-axis value labelled $\boldsymbol{H}$ in Figure 2.8).

But in general, it is hard to define and compute $\boldsymbol{J}_b$ and $\mathscr{M}$ with only a sample of the fine-scale field maps. Indeed, the macroscopic bound current $\boldsymbol{J}_b$ appears when the smoothing average kernel contains an incomplete portion of a loop of confined current. Also, the part of fine scale magnetic field $\boldsymbol{h}$ that becomes the macroscopic magnetization after averaging is hard to define, especially in dimension two or three. In our understanding, it requires the precise identification of the fine scale current. Defining quantitatively the scale transition relation, which is necessary in multiscale modeling, is thus particularly challenging.

Our proposition for STR will be defined in the next subsection, after reviewing the literature in computational multiscale modeling related to the STR definition.

Scale transition relation in the electromagnetic multiscale modeling literature

Several authors from the community of the electromagnetic fields multiscale modeling use the volume average of the cell fields to define the macroscopic fields [1, 2, 3, 6, 5, 10, 97], other authors from different areas of electrical engineering (mainly from the high-frequency wave scattering community) worked on the necessity for other definitions, mainly for the magnetic field strength.

There are four main points of interest:

1. The macroscopic fields should be computed outside the material constituents of the cell
2. The cell fields should be averaged on domains of the correct dimension corresponding to their field *type*, for example on paths for the magnetic field strength and surfaces for the magnetic flux density
3. The macroscopic magnetic field strength is the so-called *geometric average* of the cell magnetic field, that is, its value in one direction is the average of the path integral of the magnetic field along a periodic path in the air.
4. The macroscopic electric field strength is not always the average of the local one either

In their article [18], Pendry *et al.* (1999) define the macroscopic magnetic field strength in direction $\boldsymbol{e}_i$ as the path integral average of the cell magnetic field along one of the edges of the cell that is aligned with $\boldsymbol{e}_i$, and the macroscopic magnetic flux density as the flux average of the cell induction through one of the faces of the cell. The authors precise that the chosen edges and faces should not cross the material inclusion in the cell, and that this choice of averaging domain is made for consistency with the theorems defining the global Maxwell equations from the microscopic ones (the Stokes and divergence theorems (1.29)-(1.30)-(1.32)).

Similarly, Kohn and Shipman (2007) explained in [20, Section 4.4] that the macroscopic fields should be measured consistently with their differential form nature (called *field types* in this thesis), which corresponds to the second item above. They also embraced the idea that additional magnetization and polarization appear in cells with strong conductivity contrast or with material inclusion with large capacitance, and that the macroscopic magnetic field strength should be measured outside the conducting or capacitive inclusion.

The series of articles [19, 98, 99, 100, 101, 21, 102, 38] is due to collaborations between other authors from the applied mathematics community studying high-frequency electromagnetic problems, mainly Bouchitté, Felbacq, Schweizer, and others. In [103, 104], Felbacq and Bouchitté remarked that the cell current loops create a macroscopic bound current that introduces a magnetic field discontinuity, but they kept them in the macroscopic equations.

The *geometric average* was introduced later in [19] to define the macroscopic magnetic field strength. This average is equal to the path integral averages of the cell magnetic field over any periodic path in the nonconducting cell domain, which removes the macroscopic boundary discontinuity. An alternative equivalent definition that uses test fields is defined in [98]. The definition is extended to insulated nonconducting inclusions in [21], this article also contains very interesting discussion about the link between the topology of the conducting domain of the cell and the homogenization of the electromagnetic fields.

In particular, the articles from Bouchitté and Schweizer *et al.* explain that their method is consistent with a correct upscaling of the Poynting vector[9], and show that it guarantees the magnetic field tangential continuity at the homogenized domain boundary.

Among the low-frequency community, it seems that only Meunier *et al.* discussed the strength fields upscaling issue. In [105, 7, 4], the authors defended that the macroscopic value of the magnetic field strength and electric field strength are not equal to their

---

[9] When using the volume average to upscale the electric field strength, this is likely conditioned to the fact that the electric field is curl free in the cell, which they have in their setting.

volume average. In particular, the authors explain that in windings, the skin effect results in magnetic induction loops associated with the decrease of the electric field in the center of the wires (due to Maxwell-Faraday's law). Consequently, using the volume average would result in a macroscopic tangential discontinuity of the electric field and bound surface magnetic induction.

Next, a scale transition relation that applies to all electromagnetic fields is derived consistently with the findings previously mentioned in the bibliography above.

2.2.3 The scale transition relation selected for this work

In this subsection, we will define precisely what is the scope of application of the multiscale formulations derived in the thesis. It appeared that it is too difficult to define in general what is the local distribution of bound fields and of their macroscopic smoothing, so some restrictive assumptions on the geometry and topology of the conducting domain of the cell are made. Then, the scale transition relation used in this work is introduced.

Handling the additional magnetization in the scale transition relation

Let us describe the strategy we use to quantitatively define a STR consistent with the usual Maxwell equations in matter. For that, the ability to quantitatively define and compute the macroscopic magnetization is necessary[10]. We restrict our definition to periodic media, for which the usual smoothing is the cell volume average $\langle\ \rangle_Y$.

Our idea is to define the macroscopic fields using averages that avoid measuring $\boldsymbol{m}_\varepsilon$, the fine-scale distribution of the magnetization. Indeed, we want $\boldsymbol{H}$ to be the volume average $\langle\, \boldsymbol{h} - \boldsymbol{m}_\varepsilon \,\rangle_Y$, but if it is possible to use another averaging $\langle\ \rangle_{\mathrm{STR}}$ such that $\langle\, \boldsymbol{m}_\varepsilon \,\rangle_{\mathrm{STR}}$ is zero, the new definition verifies $\boldsymbol{H} = \langle\, \boldsymbol{h} \,\rangle_{\mathrm{STR}}$. For consistency, the new average has to give the same result as the direct smoothing when there are no fine-scale current loops, that is $\langle\, \boldsymbol{h} \,\rangle_{\mathrm{STR}} = \langle\, \boldsymbol{h} \,\rangle_Y$ when $\boldsymbol{j}_b = \boldsymbol{m}_\varepsilon = \boldsymbol{0}$.

---

[10] The handling of additional polarization is not discussed here, but it is likely done correctly in the proposed STR.

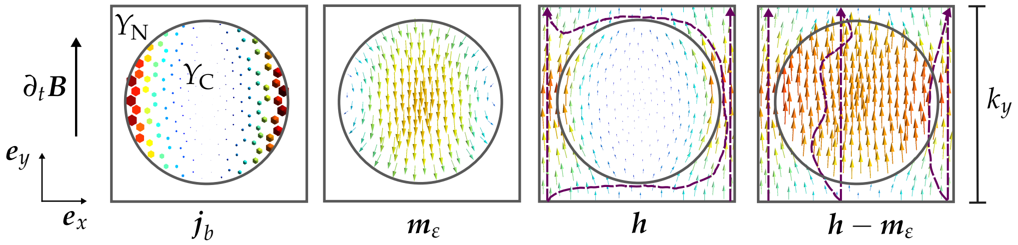

Figure 2.10: Solutions of a 2D periodic cell problem exited by variable upward magnetic field, creating confined currents in a round conducting inclusion Y_C surrounded by air Y_N. Due to the electric insulation of the cell, $\boldsymbol{h}$ (and therefore $\boldsymbol{h} - \boldsymbol{m}_\varepsilon$) are periodic in Y. As a consequence, the path integrals of $\boldsymbol{h}$ (and $\boldsymbol{h} - \boldsymbol{m}_\varepsilon$) along the violet paths drawn in the cell are all equal, and are k_y times the macroscopic $\boldsymbol{H} \cdot \boldsymbol{e}_y$. This is essentialy the definition of the geometric average introduced in [19].

In the literature of periodic homogenization with electrically insulated cell (originally [18, 19]), the periodicity of $\boldsymbol{h}$ and existence of periodic paths traversing the cell without going through any current loop make it easy to define $\boldsymbol{H}$. Indeed, the path integral of $\boldsymbol{h}$ along the aforementioned paths is **equal** and defines each component of $\boldsymbol{H}$, as illustrated in Figure 2.10.

But this definition has a flaw, it does not apply if the field has a nonzero macroscopic exterior derivative, e.g. when $\boldsymbol{J} = \langle\, \textbf{curl}\, \boldsymbol{h} \,\rangle_\text{STR} \neq \boldsymbol{0}$, or $\boldsymbol{B} = \langle\, \textbf{curl}\, \boldsymbol{a} \,\rangle_\text{STR} \neq \boldsymbol{0}$, because $\boldsymbol{h}$ and $\boldsymbol{a}$ cannot be periodic (this will be detailed in the next section). To handle this case and define a STR general to all fields, we will define it using a periodic integration domain, in order to remove the non-periodic contribution of the cell field from the average.

Strong restrictions on the geometry of the cell are necessary to guaranty that it is possible to find periodic paths that do not measure $\boldsymbol{m}_\varepsilon$. In particular, these restrictions will allow us to quantitatively define $\boldsymbol{m}_\varepsilon$ as a strength field verifying $\textbf{curl}\, \boldsymbol{m}_\varepsilon = \boldsymbol{j}_b$ in the conducting domain and $\boldsymbol{m}_\varepsilon = \boldsymbol{0}$ "outside" the confined currents. The condition $\boldsymbol{m}_\varepsilon = \boldsymbol{0}$ outside the current is motivated by the observation that the magnetization only exist in the material, at all scales. It does not extend beyond the bound current that create it. At the macroscopic scale, this bound current exist on the boundary of the material, but at the scale where it is created, the bound currents only exist in the conducting domain. This idea was studied and used in [106].

Applying this definition for $\boldsymbol{m}_\varepsilon$ requires precisely identifying currents loops $\boldsymbol{j}_b$, and their inside and outside. To make this easier, we make the assumption that all the **currents** in the cell are **confined** in it, hence, the homogenized domain is macroscopically nonconducting. This way, there is $\boldsymbol{j} = \boldsymbol{j}_b$ at the fine scale, so all the magnetic field "created" by the cell currents contribute to $\boldsymbol{m}_\varepsilon$, and no current can get confined at a scale larger than the cell scale. Having $\boldsymbol{j}_b$ entirely contained in the cell also guarantees that $\langle\, \boldsymbol{j}_b \,\rangle_\text{STR} = \boldsymbol{0} = \boldsymbol{J}$, there are no free currents at the macroscopic scale. The STR must also filter the bound currents.

These assumptions on the cell geometry are mathematically formulated next.

Assumption on the cell geometry

The aforementioned assumptions should be translated in mathematic constraints on the geometry of the periodic cell. The two goals are to avoid macroscopic currents and make STR definition easier to understand.

To achieve this, a definition for a macroscopically conducting cell is needed. In addition, we assume that the cell is chosen as a rectangular hexahedron with edges aligned with the $i = \{x, y, z\}$ axes (which is always possible with translational periodic domain). Having right angles between the cell edges and faces will enable an easy definition of the averaging procedures, because each component of the vectors are treated separately.

Also, we impose that the conducting domain does not intersect the sides of the cell, that is $Y_\mathrm{C} \cap \partial Y = \emptyset$. We call such cell an *insulated cell*. This guarantees that the boundary of the cell is also out/exterior of to any cell bound field distribution. However, this hypothesis is more restrictive than just supposing that the material is macroscopically nonconducting.

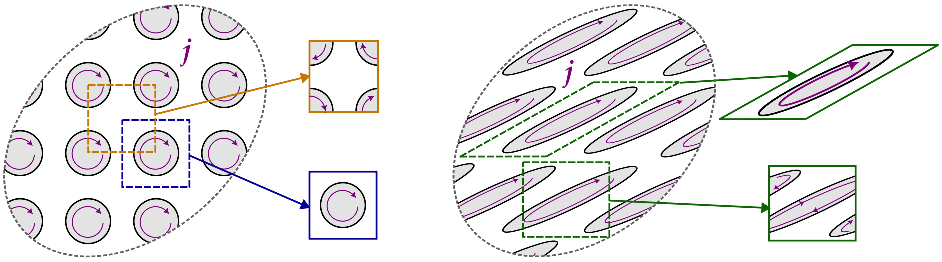

Figure 2.11: Examples of two macroscopically nonconducting periodic material with conducting inclusions, having eddy current loops represented inside. It is possible to find an insulated rectangular hexahedral cell for the left one, but not for the right one. However, the latter admits an insulated non-rectangular cell. It is always possible to find an insulated periodic cell for macroscopically nonconducting materials (but its faces might not be polygons, but curvy surfaces).

Indeed, there are macroscopically nonconducting heterogeneous materials for which the conducting domain intersects the boundary of any rectangular cell, see Figure 2.11 on the right. It is always possible to know if a periodic heterogeneous material is macroscopically conducting by studying one of its periodic cell. The criteria to identify a *macroscopically conducting cell* is the following:
A cell is macroscopically conducting in a direction i (for $i = \{x, y, z\}$) if there is a closed periodic path $\mathcal{C}_i$ in Y_C such that $\int_{\mathcal{C}_i} \boldsymbol{e}_i \cdot \boldsymbol{t} \neq \boldsymbol{0}$, where the path is still considered closed if it has endpoints which are Y-periodic.

There are interesting discussions relating to the topology of cell conducting inclusions and the closed path in the periodic cell in [21, Section 1.2][11].

Two options to generalize the work presented in this thesis to any marcroscopically nonconducting domain are available. The first and probably easier one would be to generalize the scale transition relation definition and field boundary conditions to periodic cells with arbitrary shapes, that is non-hexahedral ones, in order to choose one such that $\partial Y \cap Y_{\mathrm{C}} = \emptyset$. It is always possible when the cell is not macroscopically conducting.

A second possibility could be to adapt the non-periodic terms of the formulation to give total freedom to the non-periodic traces components on $\partial Y \cap Y_{\mathrm{C}}$.

Definition of the selected scale transition relation

The scale transition used in this work will be very similar to that defined in [18] and [21][12]. We define, in 3D, the macroscopic value of any cell field distribution as its averaged value over the outermost closed geometric part of the cell on which the field can be evaluated. These are:

- the cell corners for scalar potentials,
- the cell edges for strength fields,
- the cell faces for flux densities,
- and the whole volume of the cell for the scalar densities.

Let us introduce notations and mathematical definitions for these averages.

The macroscopic value V of a cell scalar potential field v is its *corner average* $\langle\, v \,\rangle_{\mathrm{P}_Y}$ defined by:

$$V = \langle\, v \,\rangle_{\mathrm{P}_Y} := \frac{1}{8} \sum_{p \in \mathrm{P}_Y} v(p), \tag{2.24}$$

where $\mathrm{P}_Y = \{\ (\pm\frac{1}{2}k_x, \pm\frac{1}{2}k_y, \pm\frac{1}{2}k_z)\ \}$ are the eight corners of Y, with k_i for $i = \{x, y, z\}$ the components of the geometric period vector $\boldsymbol{k}$.

The macroscopic value $\boldsymbol{H}$ of a cell strength field $\boldsymbol{h}$ is its *edge tangential average* $\langle\, \boldsymbol{h} \,\rangle_{\gamma_Y}$ (or

---

[11] With their notations, Y_{C} becomes U and the closed path $\mathcal{C}_i$ is called a i-loop in U.

[12] They are actually equivalent in the insulated cell setting. But the definition from [18] and [21] surely fails when the cell fields are not periodic, so they are less likely to be easily generalized to macroscopically conducting domains. Curiously, in [21], the definition for macroscopic $\boldsymbol{H}$ is extended to insulated nonconducting domains in a conducting heterogeneous grid, e.g. a metal with holes containing air regularly dug in it, but they later conclude that the upscaled $\boldsymbol{H}$ is always zero for this material. The reason to consider this definition and result might be specific to the scattering setting.

simply *edge average*) defined by:

$$\boldsymbol{H} = \langle\, \boldsymbol{h} \,\rangle_{\gamma_Y} := \begin{bmatrix} \frac{1}{4k_x} & 0 & 0 \\ 0 & \frac{1}{4k_y} & 0 \\ 0 & 0 & \frac{1}{4k_z} \end{bmatrix} \cdot \int_{\gamma_Y} (\boldsymbol{h} \cdot \boldsymbol{t})\boldsymbol{t}, \tag{2.25}$$

where γ_Y is the set of the twelves edges of Y. With this definition, the i^{th} component of $\langle\, \boldsymbol{h} \,\rangle_{\gamma_Y}$, that is $\boldsymbol{e}_i \cdot \langle\, \boldsymbol{h} \,\rangle_{\gamma_Y}$, is the average of the path integral of $\boldsymbol{h}$ over the four edges that are parallel to $\boldsymbol{e}_i$, which are of length k_i. This explains the normalization by 1 over $4k_i$ made via the matrix product in (2.25).

The macroscopic value $\boldsymbol{B}$ of a cell flux density field $\boldsymbol{b}$ is its *face normal average* $\langle\, \boldsymbol{b} \,\rangle_{\partial Y_\perp}$ (or simply *face average*) defined by:

$$\boldsymbol{B} = \langle\, \boldsymbol{b} \,\rangle_{\partial Y_\perp} := \begin{bmatrix} \frac{1}{2k_y k_z} & 0 & 0 \\ 0 & \frac{1}{2k_z k_x} & 0 \\ 0 & 0 & \frac{1}{2k_x k_y} \end{bmatrix} \cdot \int_{\partial Y} (\boldsymbol{b} \cdot \boldsymbol{n})\boldsymbol{n}, \tag{2.26}$$

where ∂Y is the set of the eight faces of Y. Similarly to the edge average, the i^{th} component of a face normal average is the average flux of $\boldsymbol{b}$ through the two faces normal to $\boldsymbol{e}_i$. Hence, the integral in (2.26) is normalized componentwise by 1 over the two time the correct surface area.

Finally, the macroscopic density ρ_M of a cell scalar density ρ is its volume average $\langle\, \rho \,\rangle_Y$:

$$\rho_M = \langle\, \rho \,\rangle_Y, \tag{2.27}$$

which was defined by (2.2).

A general name for these definitions could be *outer average*, because they measure the value of the fields outside the material constituent. We insist that this definition only makes sense if it is certain that the loops of bound currents are contained in the interior of the cell. This hypothesis is guaranteed when the cell is insulated.

The reason for averaging over all the cell edges or faces and not only along one of the edge or face like in the definitions from [18] and [21] is that our average is not impacted if a center anti-periodic[13] field is added to the periodic cell field. This property will be used to define the discretization of the cell fields in the next section. Also, this definition might still be correct in a general setting featuring macroscopic conductivity of the heterogeneous material.

---

[13] The center (anti-)periodicity relates to points symmetric with respect to the center of the cell, the symmetric of the point $\boldsymbol{y} \in Y$ is $-\boldsymbol{y}$. This notion is well-defined for rectangular hexahedric cells.

Summary of the material presented in this section

Maxwell's equations in matter and associated material laws depend on the scale at which they are written. They are classically obtained by smoothing the fields and equations from the free space scale. In this process, part of the fields create bound charges, bound currents, magnetization and polarization, that are inconvenient to work with at the macroscopic scale because they can only be determined with a fine-scale model and have surface components at the material boundary. The classical solution to this issue is to remove the bound fields, polarization and magnetization from the macroscopic fields.

Due to the multiscale nature of the matter, magnetization and polarization may have sources at different scales. Consequently, it might be required to consider the emergence of additional magnetization and polarization when performing homogenization from an intermediate matter scale. Some notation have been proposed to qualitatively and quantitatively describe the multiscale nature of these fields. But the identification of the magnetization and polarization from a sample of fine-scale fields remains difficult, including from the periodic cell fields used in computational multiscale modeling. It is thus hard to quantitatively define a general scale transition relation.

For this reason, the work of this thesis is restricted to macroscopically nonconducting periodic matter admitting an insulated rectangular periodic cell. In this context, the local distribution of bound fields are contained in the interior of the cell, and macroscopic fields can be defined as the outer average of the cell fields. This way, the effect of bound cell fields and associated magnetization and polarization are automatically removed from the macroscopic field. This principle is consistent with the macroscopic fields definition adopted in works from Pendry, Bouchitté, Felbacq, Kohn, Meunier, Schweizer *et al.*

2.3 Derivation of the two scale magnetoquasistatic equations

In this section, we present a general methodology used to derive two-scale formulations for magnetoquasistatic problems, in the particular setting of macroscopically nonconducting heterogeneous materials. At first, different methods to implement the homogenized law in the macroscopic problem are reviewed. In a second time, the focus is put on the modeling of the cell fields with a precise analysis on how the downscaled fields can be prescribed. Finally, the complete two-scale B and H-conforming MQS formulation are derived and discretized with time stepping HMM.

2.3.1 Macroscopic homogenized law

At the macroscopic scale, there are two components to specify to define the two-scale model, the interface condition $(\mathrm{C}_{\mathrm{H}\backslash\mathrm{M}})$ and the homogenized domain equations $(\mathrm{E}_{\mathrm{H}})$.

The interface conditions are the usual ones (1.15)-(1.18). As the setting is restricted to macroscopically nonconducting homogenized domains, there are no macroscopic surface currents on $\Gamma_{\mathrm{H}\setminus\mathrm{M}}$, so all fields are continuous on $\Gamma_{\mathrm{H}\setminus\mathrm{M}}$.

The macroscopic equation (E_H) in Ω_H does not take electric permittivity nor conductivity into account because it is a magnetoquasistatic problems solved on a nonconducting domain. As a consequence, the magnetostatic formulations (1.47) and (1.56) are used inside Ω_H. So only the implementation of the magnetic law is detailed, but the method presented below could be applied to the other laws.

The cell problem naturally output the material law under the form of $\boldsymbol{B} \to \boldsymbol{H}(\boldsymbol{B})$ or $\boldsymbol{H} \to \boldsymbol{B}(\boldsymbol{H})$ functions, which implicitly depend on time t and the fine scale state of the fields $\boldsymbol{b}$ and $\boldsymbol{h}$ respectively, for B-conforming and H-conforming formulations respectively, where the function consist in **solving the cell problem** with the downscaled field as source **and** computing the **upscaled field from the cell solutions**. Using the standard magnetic vector potential and magnetic scalar potential formulations, the macroscopic B-conforming equation (cf. Eq. (1.56)) is:

$$\mathbf{curl}\,\boldsymbol{H}(\mathbf{curl}\,\boldsymbol{A}) = \mathbf{0} \quad \text{in } \Omega_\mathrm{H},$$

and the H-conforming (cf. Eq. (1.47)) one is:

$$\operatorname{div} \boldsymbol{B}(\boldsymbol{H}_s - \mathbf{grad}\,\varphi_\mathrm{H}) = 0 \quad \text{in } \Omega_\mathrm{H}.$$

Several aspects of the magnetic material law implementation are given next for the case of the B-conforming formulation. The first is the computation of the Jacobian of the macroscopic law necessary for the Newton-Raphson method, as the law is in general nonlinear. A second point of interest is the computation of a $\boldsymbol{\nu}_M$ or $\boldsymbol{\mu}_M$ macroscopic law tensor.

Macroscopic law Jacobian

The Newton-Raphson scheme (1.82) applied to the macroscopic B-conforming formulation writes:

$$\begin{aligned} \mathbf{curl}\,\boldsymbol{H}^k + \mathbf{curl}\left(\frac{\partial \boldsymbol{H}}{\partial \boldsymbol{B}}^k \cdot \left(\mathbf{curl}\,\boldsymbol{A} - \mathbf{curl}\,\boldsymbol{A}^k\right)\right) &= \mathbf{0}, \\ \boldsymbol{A}^{k+1} &= \omega \boldsymbol{A} + (1-\omega)\boldsymbol{A}^k, \end{aligned} \tag{2.28}$$

where $\boldsymbol{H}^k = \boldsymbol{H}(\boldsymbol{B}^k) = \boldsymbol{H}(\mathbf{curl}\,\boldsymbol{A}^k)$ and $\frac{\partial \boldsymbol{H}}{\partial \boldsymbol{B}}^k = \frac{\partial \boldsymbol{H}}{\partial \boldsymbol{B}}(\boldsymbol{B}^k)$ is the Jacobian of the $\boldsymbol{B} \to \boldsymbol{H}(\boldsymbol{B})$ macroscopic material law. The simplest way to compute this Jacobian is to use the finite difference method on the $\boldsymbol{B} \to \boldsymbol{H}(\boldsymbol{B})$ function (which, again, involves solving the cell problem and upscaling $\boldsymbol{H}$ from the cell solutions). Indeed, the first order Taylor expansion in the direction $\boldsymbol{e}_i$ of this function is:

$$\boldsymbol{H}(\boldsymbol{B} + \eta \boldsymbol{e}_i) = \boldsymbol{H}(\boldsymbol{B}) + \frac{\partial \boldsymbol{H}}{\partial \boldsymbol{B}}(\boldsymbol{B}) \cdot \eta \boldsymbol{e}_i + O(\eta), \quad i = \{x, y, z\}$$

with $\eta \geq 0$. But the term $\frac{\partial \boldsymbol{H}}{\partial \boldsymbol{B}}(\boldsymbol{B}) \cdot \eta \boldsymbol{e}_i$ is η times the i^{th} column of $\frac{\partial \boldsymbol{H}}{\partial \boldsymbol{B}}$. By neglecting the $O(\eta)$ term and passing the term $\boldsymbol{H}(\boldsymbol{B})$ to the LHS, we obtain the following formula for $\frac{\partial \boldsymbol{H}}{\partial \boldsymbol{B}}$:

$$\frac{\partial \boldsymbol{H}}{\partial \boldsymbol{B}}(\boldsymbol{B}) = \eta^{-1} \Big[\boldsymbol{H}(\boldsymbol{B}_{px}) - \boldsymbol{H}(\boldsymbol{B}) \quad \boldsymbol{H}(\boldsymbol{B}_{py}) - \boldsymbol{H}(\boldsymbol{B}) \quad \boldsymbol{H}(\boldsymbol{B}_{pz}) - \boldsymbol{H}(\boldsymbol{B}) \Big], \tag{2.29}$$

where $[\bullet \bullet \bullet]$ is a column by column tensor definition, and $\boldsymbol{B}_{pi}$ is a shortcut for $\boldsymbol{B} + \eta \boldsymbol{e}_i$. This requires four evaluations of the cell problem ($D + 1$ in dimension D), which is quite expensive, but the resolutions are independent and can be solved in parallel. It is also possible to use variants of the classic Newton-Raphson method, such as the quasi Newton method, to reduce the computational costs. Possible algorithm and there rate of convergence are detailed in [107, Section 7.1].

The η parameter should be chosen relatively to the order of magnitude of $\boldsymbol{B}$. It should not be too big in order to reduce the error related to neglecting $O(\eta)$, and not too small to keep accuracy of $\boldsymbol{H}(\boldsymbol{B})$ computation. It should ideally depend on $\|\boldsymbol{B}\|$[107].

Macroscopic tensor for linear cell problems

Having the macroscopic material tensor is handy for several reasons. In general, the tensor contains more information than the upscaled field because it describes the material law for any direction of the unknown/downscaled field, not only for its particular direction during the cell problem resolution.

When the macroscopic law $\boldsymbol{H}(\boldsymbol{B})$ is linear[14], it can be summarized in a constant second order tensor $\boldsymbol{\nu}_M$ such that $\boldsymbol{H} = \boldsymbol{\nu}_M \cdot \boldsymbol{B}$, that can be computed once for all. Indeed, the linearity of $\boldsymbol{B} \to \boldsymbol{H}(\boldsymbol{B})$ implies that

$$\begin{aligned} \boldsymbol{H}(\boldsymbol{B}) = \boldsymbol{H}(B_x \boldsymbol{e}_x + B_y \boldsymbol{e}_y + B_z \boldsymbol{e}_z) &= B_x \boldsymbol{H}(\boldsymbol{e}_x) + B_y \boldsymbol{H}(\boldsymbol{e}_y) + B_z \boldsymbol{H}(\boldsymbol{e}_z) \\ &= \Big[\boldsymbol{H}(\boldsymbol{e}_x) \quad \boldsymbol{H}(\boldsymbol{e}_y) \quad \boldsymbol{H}(\boldsymbol{e}_z) \Big] \cdot \boldsymbol{B}, \end{aligned}$$

---

[14] As explained in Table 2.1, in time stepping HMM, this the case when the cell magnetic law is linear and when the eddy currents do not affect the upscaled $\boldsymbol{H}$. Mathematically, this assumption is that the sensitivity of $\boldsymbol{H}$ to the downscaled $\partial_t \boldsymbol{B}$ and the previous time step solution $\boldsymbol{a}^n$ is negligible.

for any $\boldsymbol{B}$[15]. So the definition

$$\boldsymbol{\nu}_M = \begin{bmatrix} \boldsymbol{H}(\boldsymbol{e}_x) & \boldsymbol{H}(\boldsymbol{e}_y) & \boldsymbol{H}(\boldsymbol{e}_z) \end{bmatrix} \tag{2.30}$$

is such that $\boldsymbol{H}(\boldsymbol{B}) = \boldsymbol{\nu}_M \cdot \boldsymbol{B}$. And the macroscopic equation (2.28) becomes

$$\mathbf{curl}\, \boldsymbol{\nu}_M \cdot \mathbf{curl}\, \boldsymbol{A} = \mathbf{0}, \tag{2.31}$$

there is no macroscopic iterations.

2.3.2 Modeling of the cell fields

The definition of the cell fields has to be compatible with the scale transition relation in the sense that it should allow prescribing all downscaled macro fields values to the cell fields. Let us take the example of a B-conforming multiscale formulation. The fields $\boldsymbol{b}$ and $\boldsymbol{e}$ (and by extension $\boldsymbol{a}$ and v) are the unknowns of the formulation, and the fields $\boldsymbol{h}$ and $\boldsymbol{j}$ are their dual fields, linked to the former via the material laws. The fields $\boldsymbol{B}$ and $\boldsymbol{E}$ are downscaled (although $\boldsymbol{E}$ will be arbitrarily set to $\mathbf{0}$ because it is undefined in $(\mathrm{E_H})$). If the cell unknown is a modified magnetic vector potential $\boldsymbol{a}$, the following constraints should be imposed on it:

- $\boldsymbol{B} = \langle\, \boldsymbol{b} \,\rangle_{\partial Y_\perp} = \langle\, \mathbf{curl}\, \boldsymbol{a} \,\rangle_{\partial Y_\perp}$ (face normal average),
- $\boldsymbol{E} = \langle\, \boldsymbol{e} \,\rangle_{\gamma_Y} = \langle\, -\partial_t \boldsymbol{a} \,\rangle_{\gamma_Y}$ (edge tangential average).

So the downscaling is not obvious to implement, it involves putting constraints on the average of the spatial/exterior and time derivatives of the cell fields. This is usually done via a splitting of these fields, using periodic and Dirichlet boundary conditions and the properties of periodic, anti-periodic and center anti-periodic fields.

To derive the splitting of the cell fields, it is useful to first state some of these properties. In particular, the need for non-periodic components in the cell fields will be shown, which is a difference with multiscale modeling in other fields like mechanics where fully periodic cell fields are often used.

Periodic and anti-periodic cell fields properties

The periodic and anti-periodic boundary conditions were defined by (1.43) and (1.44), they can be used in the three axes of the cell between the opposite faces of the cell boundaries. They enable to avoid using other boundary conditions that would assume a certain behavior outside the cell, the cell is its own neighbor. Indeed, we want the cell solutions to be similar to the original ones and independent of the other cells. Cell

---

[15] The sources of the problems $\boldsymbol{e}_i$ for $i = \{x, y, z\}$ are dimensionless, so $\boldsymbol{H}(\boldsymbol{e}_i)$ are in m.H^{-1}.

periodic and anti-periodic fields are respectively written with $_p$ and $_a$ subscripts, and the function spaces containing them are respectively written with $\boldsymbol{H}^{\#}$ and $\boldsymbol{H}^{\times}$ superscripts, like $v_p \in H^{\#}(\mathbf{grad}; Y)$ and $\boldsymbol{b}_a \in \boldsymbol{H}^{\times}(\mathrm{div}; Y)$. To avoid duplicating the following equations for all types of fields, spaces for scalar and vector Y-periodic fields can respectively be written $H^{\#}(Y)$ and $\boldsymbol{H}^{\#}(Y)$, and that for anti-periodic fields can respectively be written $H^{\times}(Y)$ and $\boldsymbol{H}^{\times}(Y)$[16].

Constant cell fields $F \in \mathbb{R}$ and $\boldsymbol{F} \in \mathbb{R}^3$ are periodic:

$$\begin{aligned} f(\boldsymbol{y}) &= F \in H^{\#}(Y), \\ \boldsymbol{f}(\boldsymbol{y}) &= \boldsymbol{F} \in \boldsymbol{H}^{\#}(Y). \end{aligned} \tag{2.32}$$

The sum of two periodic fields is periodic: let $f_p, g_p \in H^{\#}(Y)$ and $\boldsymbol{f}_p, \boldsymbol{g}_p \in \boldsymbol{H}^{\#}(Y)$, then

$$\begin{aligned} f_p + g_p &\in H^{\#}(Y), \\ \boldsymbol{f}_p + \boldsymbol{g}_p &\in \boldsymbol{H}^{\#}(Y). \end{aligned} \tag{2.33}$$

And the product of two periodic fields is also periodic:

$$\begin{aligned} f_p g_p,\ \boldsymbol{f}_p \cdot \boldsymbol{g}_p &\in H^{\#}(Y), \\ f_p \boldsymbol{g}_p,\ \boldsymbol{f}_p \times \boldsymbol{g}_p &\in \boldsymbol{H}^{\#}(Y). \end{aligned} \tag{2.34}$$

The sum of two anti-periodic fields is anti-periodic: if $f_a, g_a \in H^{\times}(Y)$ and $\boldsymbol{f}_a, \boldsymbol{g}_a \in \boldsymbol{H}^{\times}(Y)$ then

$$\begin{aligned} f_a + g_a &\in H^{\times}(Y), \\ \boldsymbol{f}_a + \boldsymbol{g}_a &\in \boldsymbol{H}^{\times}(Y). \end{aligned} \tag{2.35}$$

But the product of two anti-periodic fields is periodic:

$$\begin{aligned} f_a g_a,\ \boldsymbol{f}_a \cdot \boldsymbol{g}_a &\in H^{\#}(Y), \\ f_a \boldsymbol{g}_a,\ \boldsymbol{f}_a \times \boldsymbol{g}_a &\in \boldsymbol{H}^{\#}(Y). \end{aligned} \tag{2.36}$$

And the product of a periodic and an anti-periodic field is anti-periodic:

$$\begin{aligned} f_p g_a,\ \boldsymbol{f}_p \cdot \boldsymbol{g}_a &\in H^{\times}(Y), \\ f_p \boldsymbol{g}_a,\ f_a \boldsymbol{g}_p,\ \boldsymbol{f}_p \times \boldsymbol{g}_a &\in \boldsymbol{H}^{\times}(Y). \end{aligned} \tag{2.37}$$

It is now possible to study some properties of the cell fields traces. To start with, the unit

---

[16] For vector fields, the periodicity relates to the tangential component on ∂Y for (anti-)periodic $\boldsymbol{H}(\mathbf{curl}; Y)$ and to the normal component for (anti-)periodic $\boldsymbol{H}(\mathrm{div}; Y)$. Therefore, in the equations (2.32)-(2.39), $\boldsymbol{H}^{\#}(Y)$ and $\boldsymbol{H}^{\times}(Y)$ can be replaced by either curl or div-conforming fields, but not a mix of them.

normal vector $\boldsymbol{n}\big|_{\partial Y}$ is an anti-periodic field on ∂Y:

$$\boldsymbol{n}\big|_{\partial Y} \in \boldsymbol{H}^{\times}(\partial Y). \tag{2.38}$$

As consequence of (2.37) and (2.38), the traces of periodic cell fields are anti-periodic on ∂Y, that is if $v_p \in H^{\#}(\mathbf{grad};Y)$, $\boldsymbol{h}_p \in \boldsymbol{H}^{\#}(\mathbf{curl};Y)$ and $\boldsymbol{b}_p \in \boldsymbol{H}^{\#}(\mathrm{div};Y)$ then

$$\begin{aligned} v_p\boldsymbol{n} &\in \boldsymbol{H}^{\times}(\partial Y), \\ \boldsymbol{h}_p \times \boldsymbol{n} &\in \boldsymbol{H}^{\times}(\partial Y), \\ \boldsymbol{b}_p \cdot \boldsymbol{n} &\in H^{\times}(\partial Y). \end{aligned} \tag{2.39}$$

This is interesting because the integrals on ∂Y of anti-periodic surface fields vanish. As a consequence, the integral of traces of periodic cell fields on ∂Y are zero, that is:

$$\begin{aligned} \int_{\partial Y} v_p\boldsymbol{n} &= \mathbf{0} \quad \text{for } v_p \in H^{\#}(\mathbf{grad};Y), \\ \int_{\partial Y} \boldsymbol{h}_p \times \boldsymbol{n} &= \mathbf{0} \quad \text{for } \boldsymbol{h}_p \in \boldsymbol{H}^{\#}(\mathbf{curl};Y), \\ \int_{\partial Y} \boldsymbol{b}_p \cdot \boldsymbol{n} &= 0 \quad \text{for } \boldsymbol{b}_p \in \boldsymbol{H}^{\#}(\mathrm{div};Y). \end{aligned} \tag{2.40}$$

To prove it, the integrals should be split onto two halves of ∂Y, each half containing one of each opposite face of all three face couples. Due to the anti-periodicity, the two integrals are opposite and therefore the sum is zero.

This last equation is a key point to understand the following important property. The macroscopic value (outer average) of the exterior derivative of a periodic cell field is zero, that is:

$$\begin{aligned} \left\langle\, \mathbf{grad}\, v_p \,\right\rangle_{\gamma_Y} = \left\langle\, \mathbf{grad}\, v_p \,\right\rangle_Y &= \mathbf{0} \quad \text{for } v_p \in H^{\#}(\mathbf{grad};Y), \\ \left\langle\, \mathbf{curl}\, \boldsymbol{h}_p \,\right\rangle_{\partial Y_\perp} = \left\langle\, \mathbf{curl}\, \boldsymbol{h}_p \,\right\rangle_Y &= \mathbf{0} \quad \text{for } \boldsymbol{h}_p \in \boldsymbol{H}^{\#}(\mathbf{curl};Y), \\ \left\langle\, \mathrm{div}\, \boldsymbol{b}_p \,\right\rangle_Y &= 0 \quad \text{for } \boldsymbol{b}_p \in \boldsymbol{H}^{\#}(\mathrm{div};Y). \end{aligned} \tag{2.41}$$

This is also true for the **volume averages** of periodic fields, it is not specific to the average used in our definition of the macroscopic fields. It means that periodic fields alone are not sufficient to model the electromagnetic cell problems, non-periodic ones will be used in addition. However, the edge average of a periodic curl field has no reason to be zero, as well as the normal average of a periodic gradient field[17].

For the volume average, (2.41) can be proven using the Stokes theorem on the volume

---

[17] The actual reason why edge and face averages differ from the volume average, and why they respectively enable to take into account how the macroscopic magnetization and polarization depend on the curl and divergence of the magnetic field and electric displacement. This can be understood by studying the Helmoltz-Hodge Decomposition (2.86).

integral involved in the average. It results in boundary integrals on ∂Y of traces of periodic fields, which are zero (2.40). For the average of the divergence of a periodic flux fields $\boldsymbol{b}_p$, the proof is

$$\left\langle \operatorname{div} \boldsymbol{b}_p \right\rangle_Y \overset{\text{def.}}{=} \frac{1}{|Y|} \int_Y \operatorname{div} \boldsymbol{b}_p \overset{\text{Stokes}}{=} \frac{1}{|Y|} \int_{\partial Y} \boldsymbol{b}_p \cdot \boldsymbol{n} \overset{(2.40)}{=} 0.$$

The other proofs of (2.41) are similar but necessitate to decompose the integrals over the cell edges and faces specifically for each case. They are given in Appendix A.4.2.

Definition of the splitting of the cell field

We can now derive the definition of the downscaled cell fields. Any cell vector field $\boldsymbol{f}$ that is downscaled should verify the following equations:

$$\begin{aligned} \boldsymbol{F}(\boldsymbol{x}) &= \langle \boldsymbol{f}(\boldsymbol{y},\boldsymbol{x}) \rangle_{\text{STR}}, \\ d_{\boldsymbol{x}}\boldsymbol{F}(\boldsymbol{x}) &= \left\langle d_{\boldsymbol{y}}\boldsymbol{f}(\boldsymbol{x},\boldsymbol{y}) \right\rangle_{\text{STR}}, \end{aligned}$$

where $d_{\boldsymbol{x}}\boldsymbol{F}$ is the macroscopic exterior derivative of $\boldsymbol{F}$ ($\mathbf{grad}$, $\mathbf{curl}$ or div), which also happens to be the macroscopic value of $\boldsymbol{f}$'s cell derivative $d_{\boldsymbol{y}}\boldsymbol{f}$ (where d is the gradient, curl or divergence), and $\langle\ \rangle_{\text{STR}}$ is the appropriate scale transition formula depending on the field type.

In order to define $\boldsymbol{f}$ using (non-)periodic boundary conditions, it is possible to use a splitting of $\boldsymbol{f}$ into three terms as follows:

$$\boldsymbol{f}(\boldsymbol{x},\boldsymbol{y}) = \boldsymbol{F}(\boldsymbol{x}) + \boldsymbol{f}_c(\boldsymbol{x},\boldsymbol{y}) + \boldsymbol{f}_a(\boldsymbol{x},\boldsymbol{y}), \tag{2.42}$$

where $\boldsymbol{F}(\boldsymbol{x}) \in \mathbb{R}^3$ is the macroscopic value of $\boldsymbol{f}$, $\boldsymbol{f}_c \in \boldsymbol{H}^{\#}(Y)$ is a periodic correction field that can contain the fine scale variations of $\boldsymbol{f}$, and $\boldsymbol{f}_a$ is a prescribed non-periodic field that fixes the macroscopic value of $d_{\boldsymbol{y}}\boldsymbol{f}$. With this splitting, the cell unknown is $\boldsymbol{f}_c$ because $\boldsymbol{f}_a$ is prescribed. Otherwise, the bulk unknown would be duplicated and the splitting of $\boldsymbol{f}$ would surely not be unique.

The same splitting is done for the scalar fields, but considering scalars in place of vectors, and with the exception that the non-periodic term in the splitting of density fields is removed.

The consistency of the splitting (2.42) requires the following properties on the different terms of the decomposition:

$$\langle \boldsymbol{F} \rangle_{\mathrm{STR}} = \boldsymbol{F}, \quad (2.43) \qquad \langle \boldsymbol{f}_c \rangle_{\mathrm{STR}} = \boldsymbol{0}, \quad (2.44) \qquad \langle \boldsymbol{f}_a \rangle_{\mathrm{STR}} = \boldsymbol{0}, \quad (2.45)$$

$$\left\langle d_{\boldsymbol{y}}\boldsymbol{F} \right\rangle_{\mathrm{STR}} = \boldsymbol{0}, \quad (2.46) \qquad \left\langle d_{\boldsymbol{y}}\boldsymbol{f}_c \right\rangle_{\mathrm{STR}} = \boldsymbol{0}, \quad (2.47) \qquad \left\langle d_{\boldsymbol{y}}\boldsymbol{f}_a \right\rangle_{\mathrm{STR}} = d_{\boldsymbol{x}}\boldsymbol{F}. \quad (2.48)$$

Equation (2.43) is a fundamental property of averages, and (2.46) is true because $\boldsymbol{F}(\boldsymbol{x})$ is constant in Y. Equation (2.47), the nullity outer average of the exterior derivative of the periodic part $\langle d_{\boldsymbol{x}}\boldsymbol{f}_c \rangle_{\mathrm{STR}}$, was explained before in (2.41).

But (2.44), the nullity of $\langle \boldsymbol{f}_c \rangle_{\mathrm{STR}}$ is not naturally guaranteed. It can be added to the cell problem equations and later be numerically implemented using integral constraints. Alternatively, a stronger sufficient condition can be used, like prescribing the Dirichlet boundary conditions

$$v_c\big|_{\mathrm{P}_Y} = 0, \qquad \boldsymbol{h}_c \cdot \boldsymbol{t}\big|_{\gamma_Y} = 0 \quad \text{and} \quad \boldsymbol{b}_c \cdot \boldsymbol{n}\big|_{\partial Y} = 0$$

respectively on periodic scalar potentials fields, strength fields and flux fields. We define three new function spaces for these fields:

$$\begin{aligned}
H^{\#}_{0\mathrm{P}_Y}(\mathbf{grad};Y) \quad &:= \quad \left\{ \quad v_c \in H^{\#}(\mathbf{grad};Y) \quad \middle| \quad v_c\big|_{\mathrm{P}_Y} = 0 \quad \right\}, && (2.49)\\
\boldsymbol{H}^{\#}_{0\gamma_Y}(\mathbf{curl};Y) \quad &:= \quad \left\{ \quad \boldsymbol{h}_c \in \boldsymbol{H}^{\#}(\mathbf{curl};Y) \quad \middle| \quad \boldsymbol{h}_c \cdot \boldsymbol{t}\big|_{\gamma_Y} = 0 \quad \right\}, && (2.50)\\
\boldsymbol{H}^{\#}_{0\partial Y_\perp}(\mathrm{div};Y) \quad &:= \quad \left\{ \quad \boldsymbol{b}_c \in \boldsymbol{H}^{\#}(\mathrm{div};Y) \quad \middle| \quad \boldsymbol{b}_c \cdot \boldsymbol{n}\big|_{\partial Y} = 0 \quad \right\}. && (2.51)
\end{aligned}$$

These function spaces are easy to implement with Whitney elements, they consist in explicit periodic and Dirichlet boundary conditions applied on the appropriate DoFs of ∂Y_h.

Finally, the splitting definition should be completed with the choice of a non-periodic field $\boldsymbol{f}_a$ such that (2.45) and (2.48) are respected. It is possible to define one using only the macroscopic derivative and the cell vector coordinate $\boldsymbol{y}$[18]. The non-periodic scalar potential v_a, strength field $\boldsymbol{h}_a$ and flux field $\boldsymbol{d}_a$ of respective macroscopic derivatives

---

[18] It is assumed that the origin of $\boldsymbol{y}$ coordinates is at the center of Y, which always exists for rectangular periodic cells.

$\mathbf{grad}_{\boldsymbol{x}}\, V = \boldsymbol{E}$, $\mathbf{curl}_{\boldsymbol{x}}\, \boldsymbol{H} = \boldsymbol{J}$ and $\operatorname{div}_{\boldsymbol{x}} \boldsymbol{D} = \rho$ are:

$$v_a := \boldsymbol{E} \cdot \boldsymbol{y} \qquad \in H^{\times}(\mathbf{grad}; Y), \tag{2.52}$$

$$\boldsymbol{h}_a := \frac{\boldsymbol{J} \times \boldsymbol{y}}{D-1} \qquad \in \boldsymbol{H}(\mathbf{curl}; Y), \tag{2.53}$$

$$\boldsymbol{d}_a := \frac{\rho \boldsymbol{y}}{D} \qquad \in \boldsymbol{H}^{\times}(\operatorname{div}; Y), \tag{2.54}$$

where D is the dimension (2 or 3). These fields are actually center anti-periodic, but not anti-periodic in Y. It can be easily verified that

$$\begin{aligned} \mathbf{grad}\,(\boldsymbol{E} \cdot \boldsymbol{y}) &= \boldsymbol{E}, \\ \mathbf{curl}\left(\frac{\boldsymbol{J} \times \boldsymbol{y}}{D-1}\right) &= \boldsymbol{J}, \\ \operatorname{div}\left(\frac{\rho \boldsymbol{y}}{D}\right) &= \rho, \end{aligned}$$

anywhere in Y, which explains why the property of macroscopic derivative downscaling (2.48) is fulfilled. It can rapidly be understood that (2.52)-(2.53)-(2.54) have null macroscopic value (property (2.45)) by noticing that the integration domains of the scale transition formulas are center symmetric, so the contributions of center symmetric subdomains of integration cancel.

To note, the definitions (2.52)-(2.53)-(2.54) are not perfect because they are stronger than (2.48). Indeed, they prescribe the anti-periodic part of the traces of the split cell fields[19], which is not necessary and may cause issues. In addition, it seems that having Y-constant non-periodic field derivative prevents the formulation from working in macroscopically conducting cells[20].

To finish with the derivation of the cell fields model, a summary of the four splittings for each field type is given. A cell scalar potential field is split into

$$v(\boldsymbol{x}, \boldsymbol{y}) = V(\boldsymbol{x}) + v_c(\boldsymbol{y}) + \mathbf{grad}_{\boldsymbol{x}}(V(\boldsymbol{x})) \cdot \boldsymbol{y} \quad \text{for } \boldsymbol{y} \in Y, \tag{2.55}$$

---

[19] The bulk variation of a cell field f split using (2.42) is not really prescribed by f_a because the f_p term is completely free in the bulk, because the periodicity constraint only applies at the boundary.

[20] If a non-periodic field derivative is constant in the cell, it is periodic. For this reason, the dual of the derivative field is periodic (because the material laws are all periodic), and the derivative of the latter is zero. For example, if $\boldsymbol{a} = \boldsymbol{A} + \boldsymbol{a}_c + \boldsymbol{B} \times \boldsymbol{y}$, then $\boldsymbol{h} = \boldsymbol{\nu} \cdot \mathbf{curl}\, \boldsymbol{a} = \boldsymbol{\nu} \cdot (\boldsymbol{B} + \mathbf{curl}\, \boldsymbol{a}_c)$ is periodic, so $\boldsymbol{J} = \langle\, \mathbf{curl}\, \boldsymbol{h} \,\rangle_{\partial Y_{\perp}} = \mathbf{0}$, the magnetic field cannot create macroscopic currents, the discretization of $\boldsymbol{a}$ prevents it. In H-conforming formulation were all the cell is conducting, if $\boldsymbol{h}$ is discretized as $\boldsymbol{H} + \boldsymbol{h}_c + \boldsymbol{J} \times \boldsymbol{y}$, then $\boldsymbol{e} = \rho \mathbf{curl}\, \boldsymbol{h} = \rho(\boldsymbol{J} + \mathbf{curl}\, \boldsymbol{h}_c)$ is periodic, so $\partial_t \boldsymbol{B} = \langle\, \mathbf{curl}\, \boldsymbol{e} \,\rangle_{\partial Y_{\perp}} = \mathbf{0}$. However, when the cell is insulated, $Y_C \cap \partial Y = \emptyset$ so $\boldsymbol{h}_c$ is replaced with $\boldsymbol{h}_C$ defined in Y_C, its curl is not periodic and the previous problem disappears.

with $v_c \in H^{\#}_{0\mathrm{P}_Y}(\mathbf{grad}; Y)$. Its gradient in the cell is

$$\mathbf{grad}_{\boldsymbol{y}}\, v = \mathbf{grad}_{\boldsymbol{y}}\, v_c + \mathbf{grad}_{\boldsymbol{x}}(V(\boldsymbol{x})). \tag{2.56}$$

A cell strength field is split into

$$\boldsymbol{h}(\boldsymbol{x},\boldsymbol{y}) = \boldsymbol{H}(\boldsymbol{x}) + \boldsymbol{h}_c(\boldsymbol{y}) + \frac{1}{D-1}\mathbf{curl}_{\boldsymbol{x}}(\boldsymbol{H}(\boldsymbol{x})) \times \boldsymbol{y} \quad \text{for } \boldsymbol{y} \in Y, \tag{2.57}$$

with $\boldsymbol{h}_c \in \boldsymbol{H}^{\#}_{0\gamma_Y}(\mathbf{curl}; Y)$. Its curl is

$$\mathbf{curl}_{\boldsymbol{y}}\, \boldsymbol{h} = \mathbf{curl}_{\boldsymbol{y}}\, \boldsymbol{h}_c + \mathbf{curl}_{\boldsymbol{x}}(\boldsymbol{H}(\boldsymbol{x})). \tag{2.58}$$

A cell flux field is split into

$$\boldsymbol{b}(\boldsymbol{x},\boldsymbol{y}) = \boldsymbol{B}(\boldsymbol{x}) + \boldsymbol{b}_c(\boldsymbol{y}) + \frac{1}{D}\mathrm{div}_{\boldsymbol{x}}(\boldsymbol{B}(\boldsymbol{x}))\, \boldsymbol{y} \quad \text{for } \boldsymbol{y} \in Y, \tag{2.59}$$

with $\boldsymbol{b}_c \in \boldsymbol{H}^{\#}_{0\partial Y_\perp}(\mathrm{div}; Y)$. Its divergence is

$$\mathrm{div}_{\boldsymbol{y}}\, \boldsymbol{b} = \mathrm{div}_{\boldsymbol{y}}\, \boldsymbol{b}_c + \mathrm{div}_{\boldsymbol{x}}(\boldsymbol{B}(\boldsymbol{x})). \tag{2.60}$$

And finally, a cell scalar density field is split into

$$\rho(\boldsymbol{x},\boldsymbol{y}) = \mathrm{P}(\boldsymbol{x}) + \rho_c(\boldsymbol{y}) \quad \text{for } \boldsymbol{y} \in Y, \tag{2.61}$$

with $\langle \rho_c \rangle_Y = 0$. Adding an integral condition in the system is necessary to guarantee the null average condition on ρ_c.

It is then possible to obtain the cell problem equations by using the split cell field for the unknown of the desired formulation. In particular, the fields that are not downscaled are defined by the usual material law relation. For example, in a H-conforming formulation, the cell magnetic induction is defined by $\boldsymbol{b} = \boldsymbol{\mu}\boldsymbol{h}$ where $\boldsymbol{h}$ is decomposed using the splitting (2.57). As a consequence, the model for the cell field may not be exactly the same depending on the considered formulation[21].

---

[21] For example, in an H-conforming formulation with macroscopic currents $\boldsymbol{J} = \mathbf{curl}_{\boldsymbol{x}}\, \boldsymbol{H}$, the field $\boldsymbol{h}$ is $\boldsymbol{H} + \boldsymbol{h}_c + \frac{1}{D-1}\boldsymbol{J} \times \boldsymbol{y}$, but in a B-conforming formulation it would be $\boldsymbol{\nu}\,(\boldsymbol{B} + \boldsymbol{b}_c)$. In the former, the anti-periodic part of $\boldsymbol{h} \times \boldsymbol{n}\big|_{\partial Y}$ is prescribed by the cross product term, while in the latter it is not constrained at all. Also, if $\boldsymbol{b}_c \in \boldsymbol{H}^{\#}_{0\partial Y_\perp}(\mathrm{div}; Y)$ then $\boldsymbol{b} \cdot \boldsymbol{n} = \boldsymbol{B} \cdot \boldsymbol{n}\big|_{\partial Y}$ is constant on the faces of the cell, while $\boldsymbol{\mu}\left(\boldsymbol{H} + \boldsymbol{h}_c + \frac{1}{D-1}\boldsymbol{J} \times \boldsymbol{y}\right) \cdot \boldsymbol{n}\Big|_{\partial Y}$ is not.

Downscaling and upscaling of the time derivatives of the fields

The homogenization described in this work only relates to space, not to time. As a consequence, in time dependent problems, the upscaling and downscaling of a field's time derivatives is equivalent to that of the field itself. It is easy to understand in the (multi-)harmonic settings: the time variations are prescribed by a time basis with known time derivatives. For example, the knowledge of $\boldsymbol{f}$ or $\boldsymbol{F}$ directly implies that of their harmonic time derivatives $j\omega\boldsymbol{f}$ and $j\omega\boldsymbol{F}$. When using the time stepping method, a time derivative is discretized using samplings at different time instants, for example as $\partial_t\boldsymbol{f} = \frac{1}{\Delta t}(\boldsymbol{f} - \boldsymbol{f}^n)$, but as the solution at the previous time steps $\boldsymbol{f}^n$ is known and fixed, the knowledge of $\boldsymbol{f}$ and $\partial_t\boldsymbol{f}$ is numerically equivalent.

This has implications on the downscaling of the magnetoquasistatic fields: downscaling one field forces to downscale its time derivative, and possibly other fields due to Maxwell's equations. In B-conforming formulations, the downscaling of $\boldsymbol{B}$ implies that of $\partial_t\boldsymbol{B}$, which also implies the downscaling of $\mathbf{curl}_{\boldsymbol{x}}\,\boldsymbol{E}$ due to Maxwell-Faraday's law. Similarly, downscaling $\boldsymbol{A}$ is equivalent to downscaling $\partial_t\boldsymbol{A}$ and $\boldsymbol{E}$. Downscaling $\boldsymbol{D}$ in electrodynamics would imply downscaling $\partial_t\boldsymbol{D}$, and thus also $\operatorname{div}_{\boldsymbol{x}}\rho$ to respect the charge conservation law.

2.3.3 Derivation of the B-conforming discretized formulation

All the components of our multiscale model have been described for the electromagnetic fields in general. The goal of the next paragraphs is to derive the B-conforming formulation of the two-scale model of a heterogeneous medium. The formulation is derived using the modified vector potential. The strong and discrete weak forms of the cell problem equations are given first, and then that of the macroscopic problem.

Cell equations of unknown A with downscaled magnetic field B

The standard way to derive the two-scale MVP formulation is to downscale $\boldsymbol{B}$ and upscale $\boldsymbol{H}(\boldsymbol{B})$ and $\frac{\partial \boldsymbol{H}}{\partial \boldsymbol{B}}$ [6, 108, 9, 11], which in practice means downscaling $\mathbf{curl}\,\boldsymbol{A}$ because the unknown of the formulation is $\boldsymbol{A}$, not $\boldsymbol{B}$. Alternatively, the model proposed in the last section should be able to deal with the downscaling of $\boldsymbol{A}$ and the upscaling of $\boldsymbol{H}(\boldsymbol{A})$ and $\frac{\partial \boldsymbol{H}}{\partial \boldsymbol{A}}$ instead. But it was chosen to stick with the usual method in this thesis' experiments, mostly because of habits, but also because it enables to choose different MVP gauges at each scale.

Let's derive the cell formulation with downscaled $\boldsymbol{B}$. We use the cell splitting (2.59) of $\boldsymbol{b}$, but without the Dirichlet condition $\boldsymbol{b}_c \cdot \boldsymbol{n}\big|_{\partial Y} = 0$ because it will not be needed to guarantee $\langle\, \boldsymbol{b}_c \,\rangle_{\partial Y_\perp} = \boldsymbol{0}$, so there is:

$$\boldsymbol{b}(\boldsymbol{y}) = \boldsymbol{B} + \boldsymbol{b}_c(\boldsymbol{y}),$$

where the anti-periodic term disappear because $\operatorname{div} \boldsymbol{B} = 0$. Also, the cell splitting (2.57) applied to $\boldsymbol{e}$ yields:

$$\boldsymbol{e}(\boldsymbol{y}) = \boldsymbol{E} + \boldsymbol{e}_c(\boldsymbol{y}) - \frac{1}{D-1}\partial_t \boldsymbol{B} \times \boldsymbol{y},$$

where $-\partial_t \boldsymbol{B}$ replaced $\operatorname{\mathbf{curl}} \boldsymbol{E}$, and that of $\boldsymbol{a}$ is

$$\boldsymbol{a}(\boldsymbol{y}) = \boldsymbol{A} + \boldsymbol{a}_c(\boldsymbol{y}) + \frac{1}{D-1}\boldsymbol{B} \times \boldsymbol{y}, \tag{2.62}$$

where $\operatorname{\mathbf{curl}} \boldsymbol{A}$ is replaced with $\boldsymbol{B}$.

From there, the standard equations $\boldsymbol{b}(\boldsymbol{y}) = \operatorname{\mathbf{curl}} \boldsymbol{a}(\boldsymbol{y})$ and $\boldsymbol{e}(\boldsymbol{y}) = -\partial_t \boldsymbol{a}(\boldsymbol{y})$ imply

$$\boldsymbol{b}_c(\boldsymbol{y}) = \operatorname{\mathbf{curl}} \boldsymbol{a}_c(\boldsymbol{y}), \tag{2.63}$$

$$\boldsymbol{E} = -\partial_t \boldsymbol{A}, \quad \boldsymbol{e}_c(\boldsymbol{y}) = -\partial_t \boldsymbol{a}_c(\boldsymbol{y}). \tag{2.64}$$

In other word, the cell splittings are perfectly compatible with the usual potential equations[22].

The field $\boldsymbol{A}$ is not downscaled, but it is determined from the downscaling of $\boldsymbol{E} = \boldsymbol{0} = \partial_t \boldsymbol{A}$ (the cell is insulated) and the initial condition $\boldsymbol{A}(t = 0)$. $\boldsymbol{E} = \boldsymbol{0}$ is arbitrarily chosen because the cell is insulated[23]. As a result, there is $\boldsymbol{A} = \boldsymbol{0}$. At this point, the fields $\boldsymbol{b}(\boldsymbol{y})$ and $\boldsymbol{e}(\boldsymbol{y})$ are completely determined once $\boldsymbol{a}_c(\boldsymbol{y})$ is known. The usual B-conforming cell formulation is derived by plugging the splitting (2.62) of $\boldsymbol{a}(\boldsymbol{y})$ in the standard modified MVP formulation (1.55) (with $\boldsymbol{j}_s = \boldsymbol{0}$). The formulation is:
find $\boldsymbol{a}_c \in \boldsymbol{H}^{\#}_{0\gamma_Y}(\mathbf{curl}; Y)$ such that

$$\operatorname{\mathbf{curl}} \big(\nu \cdot (\boldsymbol{B} + \operatorname{\mathbf{curl}} \boldsymbol{a}_c(\boldsymbol{y}))\big) + \sigma\Big(\partial_t \boldsymbol{a}_c(\boldsymbol{y}) + \frac{1}{D-1}\partial_t \boldsymbol{B} \times \boldsymbol{y}\Big) = \boldsymbol{0} \quad \forall \boldsymbol{y} \in Y, \tag{2.65}$$

where the dependency of ν in $\boldsymbol{B} + \operatorname{\mathbf{curl}} \boldsymbol{a}_c$ has been omitted for conciseness, and the tangential continuity of $\boldsymbol{a}_c$ at the ∂Y_{C} interface is implicitly specified by the choice of function space.

But a gauge must be added in Y_{N}. The simpler one here would be the tree-cotree gauge introduced in Section 1.3.6. But in order to be consistent with the periodic boundary

---

[22] This is true when dealing with fields on one side of the Tonti diagram Figure 1.5, that is without considering dual fields linked via a material laws. Some counter examples were given in Footnote [21].

[23] In reality, the macroscopic electric field is unknown (not computed) rather than zero, but its curl is known via Maxwell-Faraday's law. It is possible to assume $\boldsymbol{E} = \boldsymbol{0}$ in the cell while imposing a nonzero $\partial_t \boldsymbol{B} = \operatorname{\mathbf{curl}}_{\boldsymbol{x}} \boldsymbol{E}$.

condition, it is necessary that the tree be periodic. It would require the mesh to be periodic, and that any edge of $\partial Y_h \subset \mathrm{Y_N}$ is in the tree if and only if the corresponding periodic edge is also in the tree. Alternatively, if the algorithm to find the periodic tree is not implemented, the Coulomb gauge with Lagrange multiplier can be used (similarly to (1.81)). It is done by using a periodic scalar potential $\xi_p \in \boldsymbol{H}^{\#}_{0\partial \mathrm{Y_C}}(\mathbf{grad}; \mathrm{Y_N})$. ξ_p is zero at the conductor boundary because the gauge is not needed there[24].

So finally, the discrete weak form of equation (2.65) using the Coulomb gauge yields the following cell problem (E_Y):
find $\boldsymbol{a}_c \in \boldsymbol{H}^{\#}_{0\gamma_Y,h}(\mathbf{curl}; Y)$, $\xi_p \in \boldsymbol{H}^{\#}_{0\partial \mathrm{Y_C},h}(\mathbf{grad}; \mathrm{Y_N})$ s.t.

$$\begin{aligned}\int_{\mathrm{Y}_h} \boldsymbol{\nu} \cdot (\boldsymbol{B} + \mathbf{curl}\, \boldsymbol{a}_c) \cdot \mathbf{curl}\, \boldsymbol{a}_c{}' + \int_{\mathrm{Y_{C,\mathit{h}}}} \sigma\Big(\frac{1}{\Delta t}(\boldsymbol{a}_c - \boldsymbol{a}_c{}^n) + \frac{1}{D-1}\partial_t \boldsymbol{B} \times \boldsymbol{y}\Big) \cdot \boldsymbol{a}_c{}' \\ + \int_{\mathrm{Y_{N,\mathit{h}}}} \lambda_1 \mathbf{grad}\, \xi_p \cdot \boldsymbol{a}_c{}' = 0, \\ \int_{\mathrm{Y_{N,\mathit{h}}}} \lambda_1 \boldsymbol{a}_c \cdot \mathbf{grad}\, \xi_p{}' + \lambda_2 \xi_p \xi_p{}' = 0\end{aligned} \tag{2.66}$$

for all $\boldsymbol{a}_c{}' \in \boldsymbol{H}^{\#}_{0\gamma_Y,h}(\mathbf{curl}; Y)$, $\xi_p{}' \in \boldsymbol{H}^{\#}_{0\partial \mathrm{Y_C},h}(\mathbf{grad}; \mathrm{Y_N})$, where $\boldsymbol{a}_c{}^n$ is the solution at the previous time step, $\partial_t \boldsymbol{B} = \frac{1}{\Delta t}(\boldsymbol{B} - \boldsymbol{B}^n)$ and $\lambda_1 > 0$ and $\lambda_2 \geq 0$ are the Lagrange multiplier parameters. The Jacobian term for the nonlinear resolution is omitted.

Also, it should be highlighted that the boundary term $\int_{\partial Y_h} \boldsymbol{\nu} \cdot (\boldsymbol{B} + \mathbf{curl}\, \boldsymbol{a}_c) \cdot (\boldsymbol{n} \times \mathbf{curl}\, \boldsymbol{a}_c{}')$ is absent from (2.66) because it is zero by definition of the periodic boundary conditions.

Indeed, two boundary periodic faces act like the common interfaces of their two adjacent elements (on the opposite sides of the cell), it is not a domain boundary. It means that the dual field $\boldsymbol{h} = \boldsymbol{\nu}\, (\boldsymbol{B} + \mathbf{curl}\, \boldsymbol{a}_c)$ is weakly tangentially periodic, like it is at the interfaces between the elements in the bulk of the domain.

Macroscopic B-conforming equations with upscaled H

The strong form of the macroscopic formulation has already been given in (2.28). The discrete weak forms of $(\mathrm{E_H})$ and $(\mathrm{C_{H\backslash M}})$ are given below. They are meant to be completed with the equations in the non homogenized domain $(\mathrm{E_M})$, determined via usual FEM modeling of the device.

The discrete weak form of $(\mathrm{E_H})$ using the tree gauge is as follows:
find $\boldsymbol{A} \in \boldsymbol{H}_{0\tau_h,h}(\mathbf{curl}; \Omega_\mathrm{H})$ s.t.

$$\int_{\Omega_{\mathrm{H},h}} \boldsymbol{H}^k \cdot \mathbf{curl}\, \boldsymbol{A}' + \frac{\partial \boldsymbol{H}^k}{\partial \boldsymbol{B}} \cdot \mathbf{curl}\Big(\boldsymbol{A} - \boldsymbol{A}^k\Big) \cdot \mathbf{curl}\, \boldsymbol{A}' = 0, \tag{2.67}$$

---

[24] It would probably be necessary to set ξ_p to 0 at P_Y if $\partial \mathrm{Y_C}$ is empty and if $\lambda_2 = 0$, in order to gauge it.

for all $A' \in H_{0\mathcal{T}_h,h}(\mathbf{curl};\Omega_\mathrm{H})$. In our implementation, H^k and $\frac{\partial H}{\partial B}^k$ are constant by element of $\Omega_{\mathrm{H},h}$ and approximated at the barycenter of the elements using the cell problems. The solution at the next iteration is given by $A^{k+1} = \omega A + (1-\omega)A^k$ where ω is the relaxation factor.

The continuity condition at the homogenized domain interface is the classic tangential continuity of the magnetic vector potential, the weak form of ($\mathrm{C}_{\mathrm{H}\backslash\mathrm{M}}$) writes:

$$\int_{\Gamma_{\mathrm{H}\backslash\mathrm{M},h}} (A|_{\Omega_{\mathrm{M},h}} - A|_{\Omega_{\mathrm{H},h}}) \cdot A' = 0, \tag{2.68}$$

for all $A' \in H_h(\mathbf{curl};\Gamma_{\mathrm{H}\backslash\mathrm{M}})$. But this equation is usually removed by enforcing it strongly in the function space.

2.3.4 Derivation of the H-conforming discretized formulation

In this section, a H-conforming two-scale formulation is stated. Its derivation is similar to that of the B-conforming ones, so we do not give as much detail, finer explanations can be found in [10].

Cell equations of unknowns h and φ with downscaled H

The h-φ formulation uses an unknown magnetic scalar potential φ in Y_N and the unknown magnetic field strength h in Y_C. The formulation is derived by taking the general cell splitting of φ and h, and then applying $h = \mathbf{grad}\,\varphi$ in Y_N[25] and $\varphi = 0$ in the interior of Y_C. The macroscopic value of φ is arbitrarily fixed to 0, and its downscaled macroscopic derivative is $\mathbf{grad}_x\,\varphi = H$, so its cell splitting is

$$\varphi(y) = \varphi_c(y) + H \cdot y, \tag{2.69}$$

with $\varphi_c \in H^{\#}_{0\mathrm{P}_Y}(\mathbf{grad};Y)$. The magnetic field is split in

$$h(y) = H + h_c(y), \tag{2.70}$$

with $h_c \in H^{\#}(\mathbf{curl};)$ and $\mathbf{curl}_x\,H = J = \mathbf{0}$. Then, the equation $h(y) = \mathbf{grad}\,\varphi(y)$ yields:

$$h_p(y) = \mathbf{grad}\,\varphi_c(y) \quad \text{in } Y_\mathrm{N}. \tag{2.71}$$

So the unknowns of the problem are $\varphi_c \in H^{\#}_{0\mathrm{P}_Y}(\mathbf{grad};Y_\mathrm{N})$ only defined in Y_N, and the magnetic field conductor correction $h_\mathrm{C} := h_c|_{Y_\mathrm{C}} \in H(\mathbf{curl};Y_\mathrm{C})$ only defined in Y_C. The latter has no periodicity constraint because the cell is insulated.

---

[25] If Y_C is not simply connected, an additional term is needed because h is not only $\mathbf{grad}\,\varphi$ in Y_N, as usual when using the h-φ formulation.

The $\boldsymbol{h}$-φ strong form of the cell problem equations (E_Y) is:
find $\varphi_c \in H^{\#}_{0\mathrm{P}_{\mathrm{Y}}}(\mathbf{grad}; \mathrm{Y}_\mathrm{N})$ and $\boldsymbol{h}_\mathrm{C} \in \boldsymbol{H}(\mathbf{curl}; \mathrm{Y}_\mathrm{C})$ s.t.

$$\begin{aligned} \operatorname{div}\left(\partial_t\, \boldsymbol{\mu} \cdot (\boldsymbol{H} + \mathbf{grad}\, \varphi_c)\right) &= 0 \text{ in } \mathrm{Y}_\mathrm{N}, \\ \mathbf{curl}\left(\rho\, \mathbf{curl}\, \boldsymbol{h}_\mathrm{C}\right) + \partial_t\, \boldsymbol{\mu} \cdot (\boldsymbol{H} + \boldsymbol{h}_\mathrm{C}) &= \mathbf{0} \text{ in } \mathrm{Y}_\mathrm{C}, \\ (\mathbf{grad}\, \varphi_c - \boldsymbol{h}_\mathrm{C}) \times \boldsymbol{n} &= \mathbf{0} \text{ on } \partial\mathrm{Y}_\mathrm{C}, \end{aligned} \tag{2.72}$$

where the boundary term comes from the tangential continuity of $\boldsymbol{h}$ at the conducting domain interface.
Finally, the $\boldsymbol{h}$-φ discrete weak equations for (E_Y) becomes:
find $\varphi_c \in H^{\#}_{0\mathrm{P}_{Y},h}(\mathbf{grad}; \mathrm{Y}_\mathrm{N})$, $\boldsymbol{h}_\mathrm{C} \in \boldsymbol{H}_h(\mathbf{curl}; \mathrm{Y}_\mathrm{C})$ s.t.

$$\begin{aligned} \int_{\mathrm{Y}_{\mathrm{N},h}} \frac{1}{\Delta t}\left(\boldsymbol{\mu} \cdot (\boldsymbol{H} + \mathbf{grad}\, \varphi_c) - \boldsymbol{b}^n\right) \cdot \mathbf{grad}\, \varphi'_c &= 0, \\ \int_{\mathrm{Y}_{\mathrm{C},h}} \rho\, \mathbf{curl}\, \boldsymbol{h}_\mathrm{C} \cdot \mathbf{curl}\, \boldsymbol{h}' + \frac{1}{\Delta t}\left(\boldsymbol{\mu} \cdot (\boldsymbol{H} + \boldsymbol{h}_\mathrm{C}) - \boldsymbol{b}^n\right) \cdot \boldsymbol{h}' &= 0, \\ \int_{\partial\mathrm{Y}_{\mathrm{C},h}} (\mathbf{grad}\, \varphi_c - \boldsymbol{h}_\mathrm{C}) \times \boldsymbol{n}\ \cdot\ \boldsymbol{h}' &= 0, \end{aligned} \tag{2.73}$$

for all $\varphi'_c \in H^{\#}_{0\mathrm{P}_{Y},h}(\mathbf{grad}; \mathrm{Y}_\mathrm{N})$, $\boldsymbol{h}' \in \boldsymbol{H}_h(\mathbf{curl}; \mathrm{Y}_\mathrm{C})$, with $\boldsymbol{b}^n = \boldsymbol{\mu}^n \cdot (\boldsymbol{H}^n + \mathbf{grad}\, \varphi^n_c)$ the previous time step solution. The dependency of $\boldsymbol{\mu}$ in $\boldsymbol{h}$ and the Jacobian for the nonlinear iterations are omitted.

Similarly to the B-conforming cell formulation (2.66), there is no boundary term on ∂Y_h and the normal periodicity of the dual field $\partial_t \boldsymbol{b} = \partial_t \boldsymbol{\mu} \boldsymbol{h}$ is weakly enforced by the bulk term adjacent to the periodic interface.

Macroscopic H-conforming equations with upscaled $\boldsymbol{B}$

The H-conforming macroscopic homogenized equation (E_H) is the magnetostatic[26] H-conforming formulation with upscaled $\boldsymbol{B}(\boldsymbol{H})$ law. Its weak discrete form reads:
find $\varphi_\mathrm{H} \in H_h(\mathbf{grad}; \Omega_\mathrm{H})$ s.t.

$$\int_{\Omega_{\mathrm{H},h}} \boldsymbol{B}^k \cdot \mathbf{grad}\, \varphi'_\mathrm{H} - \frac{\partial \boldsymbol{B}}{\partial \boldsymbol{H}}^k \cdot \mathbf{grad}\left(\varphi_\mathrm{H} - \varphi^k_\mathrm{H}\right) \cdot \mathbf{grad}\, \varphi'_\mathrm{H} = 0, \tag{2.74}$$

for all $\varphi'_\mathrm{H} \in H_h(\mathbf{grad}; \Omega_\mathrm{H})$, with $\boldsymbol{B}^k = \boldsymbol{B}(\boldsymbol{H}^k)$, $\frac{\partial \boldsymbol{B}}{\partial \boldsymbol{H}}^k = \frac{\partial \boldsymbol{B}}{\partial \boldsymbol{H}}(\boldsymbol{H}^k)$ and $\boldsymbol{H}^k = \boldsymbol{H}_s - \mathbf{grad}\, \varphi^k_\mathrm{H}$. Assuming that the material is surrounded by a nonconducting domain where a scalar magnetic potential $\varphi_\mathrm{H}\big|_{\Omega_{\mathrm{M},h}}$ is used, the discrete continuity condition $(\mathrm{C}_{\mathrm{H}\backslash\mathrm{M}})$ simply

---

[26] Technically, the weak equation of $\partial_t \boldsymbol{B} = \mathbf{0}$ should be used in time dependent setting, that is $\int \partial_t \boldsymbol{B} \cdot \mathbf{grad}\, \varphi'_\mathrm{H} = 0$. But it breaks down to $\int \frac{1}{\Delta t}(\boldsymbol{B} - \boldsymbol{B}^n) \cdot \mathbf{grad}\, \varphi'_\mathrm{H}$, and as we can strongly impose $\operatorname{div} \boldsymbol{B}^n = \mathbf{0}$ in this equation, the magnetostatic weak equation $\int \boldsymbol{B} \cdot \mathbf{grad}\, \varphi'_\mathrm{H} = 0$ appears.

writes:

$$\int_{\Gamma_{\mathrm{H}\backslash\mathrm{M},h}} \left(\varphi_{\mathrm{H}}\big|_{\Omega_{\mathrm{M},h}} - \varphi_{\mathrm{H}}\big|_{\Omega_{\mathrm{H},h}} \right) \varphi'_{\mathrm{H}} = 0, \tag{2.75}$$

for all $\varphi'_{\mathrm{H}} \in H_h(\mathbf{grad}; \Gamma_{\mathrm{H}\backslash\mathrm{M}})$. But (2.75) is usually removed from the macroscopic system by enforcing it strongly in the function space.

2.4 Upscaling the electromagnetic fields

A two-scale implementation of the usual B and H-conforming formulation was introduced in the previous section. A particular care was taken to guaranty the correct downscaling of the macroscopic fields in the cell. In this section, we focus on the implementation of the upscaling of the macroscopic fields from the solutions of the cell problems, consistently with the outer averages (2.24)-(2.27) defining the scale transition relation.

The upscaling of scalar density fields must be made with the volume average over all the cell. But for the upscaling of flux densities and strength fields, it is possible to perform the average over larger part of the cell than its edges and faces, in order to increase the accuracy of the numerical integration. This section reviews several techniques usable to upscale those two types of fields.

In particular, a formulation that enables computing the local distribution of the magnetization due to the cell eddy currents will be introduced in order to upscale the magnetic field strength. It will be used to validate the model describing the multiscale definition of the magnetization proposed in Section 2.2.2, for the specific case of insulated cells.

2.4.1 Strength fields upscaling

This section will be focused on the upscaling of the magnetic field strength $\boldsymbol{h}$ because there is no reason to upscale the other strength fields in our setting. Indeed, $\boldsymbol{E}$ is not computed in a macroscopically nonconducting domain in MQS, and $\boldsymbol{A}$ could possibly be downscaled but not upscaled because it is always unknown in the formulation in which it appears.

Volume average

The volume average has been widely used in the literature to upscale every field, including the magnetic field strength. On the solutions of the B-conforming formulation, it is:

$$\boldsymbol{H} = \langle\, \boldsymbol{\nu} \cdot (\boldsymbol{B} + \mathbf{curl}\, \boldsymbol{a}_c)\, \rangle_Y. \tag{2.76}$$

When solving for a magnetostatic problem with no current, the volume average always works to upscale the magnetic field strength. Indeed, one can prove that if a strength field is periodic with vanishing curl in the whole cell, that is if $\boldsymbol{h}_p \in \boldsymbol{H}^{\#}(\mathbf{curl}; Y)$ and $\mathbf{curl}\, \boldsymbol{h}_p = 0$ in Y, then

$$\langle\, \boldsymbol{h}_p \,\rangle_Y = \langle\, \boldsymbol{h}_p \,\rangle_{\gamma_Y}. \tag{2.77}$$

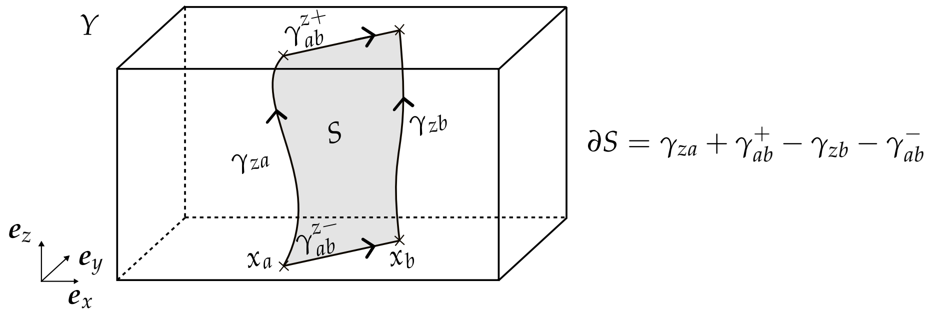

Figure 2.12: Sketch of the proof that the magnetic field strength $\boldsymbol{h}$ has identical path integrals on parallel paths crossing the cell, given that $\mathbf{curl}\, \boldsymbol{h} \cdot \boldsymbol{n} = 0$ in the cell. Indeed, Ampère's law applies to the surface S enclosed by the paths (here γ_{za} and γ_{zb}) and their junction on the oposite faces of the cell (here γ_{ab}^{z+} and γ_{ab}^{z-}), but the paths integrals on the latter cancel due to tangential periodicity of $\boldsymbol{h}$. Hence, $0 = \int_{\partial S} \boldsymbol{h} \cdot \boldsymbol{t} = \int_{\gamma_{za}} \boldsymbol{h} \cdot \boldsymbol{t} - \int_{\gamma_{zb}} \boldsymbol{h} \cdot \boldsymbol{t}$, the latter path integrals are equal.

The main property necessary to understand (2.77) should be detailed. It holds that the path integrals of a periodic strength field $\boldsymbol{h}$ over any periodic path γ_i (path having its ends ∂Y_C-periodic) are all equal. This is due to the periodicity and Ampère's law, as illustrated in Figure 2.12. In particular, the path integrals along the four edges are equal, so averaging over these edges *or* over all the parallels in the boundary is mathematically equivalent for periodic $\boldsymbol{h}$.

But the volume average does not always work in dynamic setting at high-frequencies, as will be shown in the numerical examples in Section 3.1.4. This happens when the magnetic field created by the confined current loops become a significant part of $\boldsymbol{h}$ (in average). Indeed, the path integrals of $\boldsymbol{h}$ on paths crossing Y inside the eddy current loops become too different compared to that on paths outside them.

When the cell permeability is linear, we observed (see Section 3.1.4) that the following criterion comparing the power of the eddy currents (the Joule losses) and the magnetic power seems to predict if the volume average works:
we observed that $\boldsymbol{H} = \langle\, \boldsymbol{h} \,\rangle_Y$ whenever

$$\left| \int_Y \boldsymbol{j} \cdot \boldsymbol{e} \right| \ll \left| \int_Y \boldsymbol{h} \cdot \partial_t \boldsymbol{b} \right|. \tag{2.78}$$

However, this indicator is less accurate in the nonlinear case.

Edges average

To circumvent the limitations of the volume average, we introduce four others computation methods, including two original ones which will allow using volume averages.

The first method is applying the definition proposed in this work, the edge average, theoretically equivalent to the method from [18] (in each direction, the integration is done on four edges instead of one). In practice, applying it to the $\boldsymbol{h}$ field obtained by solving for the B-conforming cell problem (2.66) leads to

$$\boldsymbol{H} = \langle\, \boldsymbol{\nu} \cdot (\boldsymbol{B} + \mathbf{curl}\, \boldsymbol{a}_c)\, \rangle_{\gamma_Y}. \tag{2.79}$$

To implement this formula, it is necessary to compute $\mathbf{curl}\, \boldsymbol{a}_c$ using the information in the volume of the elements adjacent to the edges of the cell, before taking its tangential trace on the edges. Indeed, the tangential trace of $\mathbf{curl}\, \boldsymbol{a}_c$ on a path depends on the variation of $\boldsymbol{a}_c$ orthogonally to the path. If the FEM software used doesn't automatically support such computation, it is possible to use a FEM projection to compute (2.79) which consists in projecting the solution on edge elements associated to the mesh edges of the cell edges γ_Y, that is $\mathcal{E}(\gamma_{Yh})$, as follows:
find $\boldsymbol{h}_\gamma \in \boldsymbol{H}_h(\mathbf{curl}; \gamma_Y)$ s.t.

$$\int_{\mathcal{K}(\gamma_{Yh})} (\boldsymbol{h}_\gamma - \boldsymbol{\nu} \cdot (\boldsymbol{B} + \mathbf{curl}\, \boldsymbol{a}_c)) \cdot \boldsymbol{h}' = 0,$$

for all $\boldsymbol{h}' \in \boldsymbol{H}_h(\mathbf{curl}; \gamma_Y)$, where $\mathcal{K}(\gamma_{Yh})$ is the set of all the elements of Y_h that are adjacent to edges of $\mathcal{E}(\gamma_Y)$. $\boldsymbol{H}$ can then easily be computed by averaging correctly (direction by direction) the DoFs of $\boldsymbol{h}_\gamma$, which are the path integrals of $\boldsymbol{h}_\gamma$ on edges of $\mathcal{E}(\gamma_{Yh})$, by definition of Nedelec elements.

In 2D, the edge average of a "perpendicular to the plane" $\boldsymbol{h}$ becomes an average of the normal value at the four corners of Y. The edge average of the in-plane $\boldsymbol{h}$ is that on the four edges of the rectangular Y.

Boundary tangential average

In practice, the edge average formula might not be optimally precise and numerically stable because it uses only a fraction of the solutions (the fields near the edges). Alternatively, it is possible to compute $\boldsymbol{H}$ with the *boundary tangential average* $\langle\ \rangle_{\partial Y_\parallel}$, this method was used in high-frequency problems in [109] to increase the accuracy compared to the edge average. The boundary tangential average is defined by:

$$\langle\, \boldsymbol{h} \,\rangle_{\partial Y_\parallel} := \begin{bmatrix} \frac{1}{2(k_x k_y + k_x k_z)} & 0 & 0 \\ 0 & \frac{1}{2(k_y k_x + k_y k_z)} & 0 \\ 0 & 0 & \frac{1}{2(k_z k_x + k_z k_y)} \end{bmatrix} \cdot \int_{\partial Y} \boldsymbol{h_t}, \tag{2.80}$$

where $\boldsymbol{h_t} = (\boldsymbol{n} \times \boldsymbol{h}) \times \boldsymbol{n}$ is the tangential component of $\boldsymbol{h}$ (see Figure 1.1) and each component of the result $H_i = \boldsymbol{e}_i \cdot \langle\, \boldsymbol{h} \,\rangle_{\partial Y_\parallel}$ is an average over the four faces of ∂Y which are not normal to $\boldsymbol{e}_i$, hence the normalization factor.

The boundary tangential average respects the following property:
if $\boldsymbol{h}_p$ is a periodic strength field with null curl trace on ∂Y, that is $\boldsymbol{h}_p \in \boldsymbol{H}^{\#}(\mathbf{curl}; Y)$ and $\mathbf{curl}\, \boldsymbol{h}_p \cdot \boldsymbol{n}\big|_{\partial Y} = 0$, then

$$\langle\, \boldsymbol{h}_p \,\rangle_{\partial Y_\parallel} = \langle\, \boldsymbol{h}_p \,\rangle_{\gamma_Y}. \tag{2.81}$$

The reason for this is the same as that for (2.77), but instead of considering the path integrals of $\boldsymbol{h}$ on any path crossing the cell, only those crossing the faces of the cell are considered.

In an insulated cell, there is $\mathbf{curl}\, \boldsymbol{h} \cdot \boldsymbol{n} = \boldsymbol{j} \cdot \boldsymbol{n} = 0$ on ∂Y. Also, $\boldsymbol{\nu} \cdot (\boldsymbol{B} + \mathbf{curl}\, \boldsymbol{a}_c)$ is weakly tangentially periodic on ∂Y. Although the periodicity is only weakly ensured due to the discretization, upscaling $\boldsymbol{H}$ using

$$\boldsymbol{H} = \langle\, \boldsymbol{\nu} \cdot (\boldsymbol{B} + \mathbf{curl}\, \boldsymbol{a}_c) \,\rangle_{\partial Y_\parallel} \tag{2.82}$$

worked in our experiments.

Similarly to the edge average, we first have to use an intermediate FEM projection to compute the tangential trace of the $\mathbf{curl}\, \boldsymbol{a}_c$ term. The weak form of this projection reads: find $\boldsymbol{h}_{\partial Y} \in \boldsymbol{H}_h(\mathbf{curl}; \partial Y)$ s.t.

$$\int_{\mathcal{K}(\partial Y_h)} (\boldsymbol{h}_{\partial Y} - \boldsymbol{\nu} \cdot (\boldsymbol{B} + \mathbf{curl}\, \boldsymbol{a}_c)) \cdot \boldsymbol{h}' = 0,$$

for all $\boldsymbol{h}' \in \boldsymbol{H}_h(\mathbf{curl}; \partial Y)$, where $\mathcal{K}(\partial Y_h)$ is the set of all the elements of Y_h that are adjacent to edges of $\mathcal{E}(\partial Y_h)$.

The tangential average is not very relevant in 2D, because the solution is only available on cell edges for in-plane magnetic field. And in case of normal magnetic field it is constant in Y_{N} (including ∂Y). Indeed, in 1D, a varying $\boldsymbol{h}$ is necessarily associated with currents, because it is not curl free. So normal $\boldsymbol{h}$ is constant in Y_{N}.

Computation of the magnetization using FEM projections and volume averages

The two previously presented methods have already been used in high-frequency electromagnetics, they are interesting but they do not allow using volume averages. In the next paragraphs, we show that it is possible to compute $\mathscr{M}_{\varepsilon\to\mathrm{H}}$, the part of the macroscopic magnetization created by the cell currents $\boldsymbol{j}_b = \boldsymbol{j} = \mathbf{curl}\,\boldsymbol{h}$[27], using some FEM projection filtering the magnetic field that $\boldsymbol{j}$ "creates". It allows to upscale $\boldsymbol{H}$ using the volume average $\boldsymbol{H} = \langle\, \boldsymbol{h}\,\rangle_Y - \mathscr{M}_{\varepsilon\to\mathrm{H}}$.

Assuming that the B and H-conforming formulations (2.65) and (2.72) of the cell problem are equivalent, the cell magnetic field is periodic and can be decomposed in $\boldsymbol{h} = \langle\, \boldsymbol{h}\,\rangle_{\gamma_Y} + \left(\, \boldsymbol{h} - \langle\, \boldsymbol{h}\,\rangle_{\gamma_Y}\right) = \boldsymbol{H} + \boldsymbol{h}_c$, so

$$\langle\, \boldsymbol{h}_c\,\rangle_Y = \langle\, \boldsymbol{h} - \boldsymbol{H}\,\rangle_Y = \langle\, \boldsymbol{h}\,\rangle_Y - \boldsymbol{H} = \mathscr{M}_{\varepsilon\to\mathrm{H}}$$

holds. The idea is to compute $\mathscr{M}_{\varepsilon\to\mathrm{H}}$ from $\boldsymbol{j}$ using the fact that $\boldsymbol{j} = \mathbf{curl}\,\boldsymbol{h} = \mathbf{curl}\,\boldsymbol{h}_c$ and that $\boldsymbol{h}_c$ has by definition a null edge average (see the splitting property (2.44)). It turns out that this information is sufficient to compute $\mathscr{M}_{\varepsilon\to\mathrm{H}}$. Indeed, the following theorem holds:

Theorem 2.1 *Let* $\boldsymbol{h} \in \boldsymbol{H}^{\#}(\boldsymbol{curl}; Y)$. *Let* $\boldsymbol{H} := \langle\, \boldsymbol{h}\,\rangle_{\gamma_Y}$ *be the macroscopic value of* $\boldsymbol{h}$ *and* $\mathscr{M}_{\varepsilon\to H} := \langle\, \boldsymbol{h} - \boldsymbol{H}\,\rangle_Y$ *the macroscopic magnetization due to the eddy currents in* Y.
If $\widetilde{\boldsymbol{h}_c} \in \boldsymbol{H}^{\#}(\boldsymbol{curl}; Y)$ *verifies*

$$\begin{cases} \boldsymbol{curl}\,\widetilde{\boldsymbol{h}_c} = \boldsymbol{curl}\,\boldsymbol{h} \quad \text{in } Y, & (2.83)\\ \left\langle\, \widetilde{\boldsymbol{h}_c}\,\right\rangle_{\gamma_Y} = \boldsymbol{0}, & (2.84) \end{cases}$$

then $\left\langle\, \widetilde{\boldsymbol{h}_c}\,\right\rangle_Y = \mathscr{M}_{\varepsilon\to H}$.

Any solution $\widetilde{\boldsymbol{h}_c}$ to the problem (2.83)-(2.84) is not pointwise equal to $\boldsymbol{h}_c$ because the formulation is not gauged. The choice of the gauge, an equation specifying $\operatorname{div}\widetilde{\boldsymbol{h}_c}$, is free here. Alternatively, it is possible to compute the exact $\boldsymbol{h}_c$ using the formulation in the following result:

Theorem 2.2 *Let* $\boldsymbol{h} \in \boldsymbol{H}^{\#}(\boldsymbol{curl}; Y)$. *Let* $\boldsymbol{h}_c := \boldsymbol{h} - \langle\, \boldsymbol{h}\,\rangle_{\gamma_Y}$ *be the periodic correction field of* $\boldsymbol{h}$. *A strength field* $\widetilde{\boldsymbol{h}_c} \in \boldsymbol{H}^{\#}(\boldsymbol{curl}; Y)$ *is equal to* $\boldsymbol{h}_c$ *if and only if*

$$\begin{cases} \boldsymbol{curl}\,\widetilde{\boldsymbol{h}_c} = \boldsymbol{curl}\,\boldsymbol{h} \quad \text{in } Y,\\ div\,\widetilde{\boldsymbol{h}_c} = div\,\boldsymbol{h} \quad \text{in } Y,\\ \left\langle\, \widetilde{\boldsymbol{h}_c}\,\right\rangle_{\gamma_Y} = \boldsymbol{0}. \end{cases} \tag{2.85}$$

---

[27] In the setting using insulated cells, there are no macroscopic currents, so all the cell current are confined at the cell scale: $\boldsymbol{j}_b = \boldsymbol{j}$.

The detailed proof of these theorems (and the next one) are given in Appendix A.4.3. But it is interesting to detail the two main properties on which the proofs rely.

The first is that the periodic strength fields $\boldsymbol{h}$ and $\boldsymbol{h}_c$ can be orthogonally decomposed in their volume averages plus a gradient field plus a curl fields using a Helmoltz-Hodge Decomposition (HHD). That is, if $\boldsymbol{h}_p \in \boldsymbol{H}^{\#}(\mathbf{curl}; Y)$ then there exist $\boldsymbol{\theta}_p \in \boldsymbol{H}^{\#}(\mathbf{curl}; Y)$ and $\varphi_p \in H^{\#}(\mathbf{grad}; Y)$ such that:

$$\boldsymbol{h}_p = \mathbf{grad}\, \varphi_p + \mathbf{curl}\, \boldsymbol{\theta}_p + \left\langle\, \boldsymbol{h}_p \,\right\rangle_Y, \tag{2.86}$$

where $\mathbf{grad}\, \varphi_p$ is curl free, $\mathbf{curl}\, \boldsymbol{\theta}_p$ is divergence free and $\left\langle\, \boldsymbol{h}_p \,\right\rangle_Y \in \mathbb{R}^D$ is a constant vector, both divergence and curl free. The decomposition is unique[28], deeper explanations can be found around (A.4) in Appendix A.4.1.

The orthogonality of the decomposition means that the $\boldsymbol{L}^2(Y)$ scalar product of any couple of terms from the decomposition - that is the integral of their dot product - is zero. It enables to prove that fixing the curl of $\boldsymbol{h}$ is equivalent to fixing its $\mathbf{curl}\, \boldsymbol{\theta}_p$ component, and that fixing the divergence of $\boldsymbol{h}$ is equivalent to fixing its $\mathbf{grad}\, \varphi_p$ component. Moreover, the edge average **and** volume average of any periodic gradient is zero (2.41). So the choice of gauge (or of divergence) for $\widetilde{\boldsymbol{h}}_c$ only affect its gradient part, which is independent of its edge average. In conclusion, the gauge choice does not affect its edge average, so

$$\left\langle\, \widetilde{\boldsymbol{h}}_c \,\right\rangle_{\gamma_Y} = \left\langle\, \boldsymbol{h}_c \,\right\rangle_{\gamma_Y} = \mathscr{M}_{\varepsilon\to\mathrm{H}}.$$

In practice, we decided to compute $\mathscr{M}_{\varepsilon\to\mathrm{H}}$ using Theorem 2.1 because it is more convenient to be able to choose the gauge. But we could not directly solve for $\widetilde{\boldsymbol{h}}_c$ using a weak form of (2.83) with first order Nedelec elements, the resolution does not work, probably due to the discrete operators used in the formulation, or their orders. Instead, what worked is solving for

$$\mathbf{curl}\,\mathbf{curl}\, \widetilde{\boldsymbol{h}}_c = \mathbf{curl}\,\mathbf{curl}\, \boldsymbol{h} \quad \text{ in } Y. \tag{2.87}$$

The discrete weak form of (2.87) writes as follows:
find $\widetilde{\boldsymbol{h}}_c \in \boldsymbol{H}^{\#}_{0\gamma_Y,h}(\mathbf{curl}; Y)$ and $\xi_p \in H^{\#}_{0\mathrm{P}_Y,h}(\mathbf{grad}; Y)$ such that

$$\begin{aligned} \int_{Y_h} \left(\mathbf{curl}\, \widetilde{\boldsymbol{h}}_c - \sigma\partial_t\Big(\boldsymbol{a}_c + \frac{1}{D-1}\boldsymbol{B}\times\boldsymbol{y}\Big)\right)\cdot \mathbf{curl}\, \boldsymbol{h}_p{}' + \int_{Y_h} \mathbf{grad}\, \xi_p \cdot \boldsymbol{h}_p{}' = 0,\\ \int_{Y_h} \widetilde{\boldsymbol{h}}_c \cdot \mathbf{grad}\, \xi_p{}' + \xi_p \xi_p{}' = 0, \end{aligned} \tag{2.88}$$

for all $\boldsymbol{h}_p{}' \in \boldsymbol{H}^{\#}_{0\gamma_Y,h}(\mathbf{curl}; Y)$ and $\xi_p{}' \in H^{\#}_{0\mathrm{P}_Y,h}(\mathbf{grad}; Y)$.

---

[28] $\mathbf{curl}\, \boldsymbol{\theta}_p$ and div φ_p are unique, but not the potentials $\boldsymbol{\theta}_p$ and φ_p (without additional gauging constraint). Fortunately, the value of these potentials is not interesting for our purpose.

The LHS of (2.66) $\sigma\partial_t\Big(\boldsymbol{a}_c + \frac{1}{D-1}\boldsymbol{B}\times\boldsymbol{y}\Big)$ is used as the expression for the current $\mathbf{curl}\,\boldsymbol{h}$, and $\widetilde{\boldsymbol{h}_c}$ is gauged using the Coulomb gauge. In (2.88), the constraint $\Big\langle\,\widetilde{\boldsymbol{h}_c}\,\Big\rangle_{\gamma_Y} = 0$ is strongly enforced in the functional space instead of weakly enforced via an integral constraint on γ_Y. It is worth mentioning because, otherwise, the precision of the final computation of $\mathscr{M}_{\varepsilon\to\mathrm{H}}$ would possibly not have better accuracy than a direct average of $\boldsymbol{h}$ on γ_Y.

The formulation (2.87) is similar to a *rotational component extraction* used to compute the curl term of Helmoltz-Hodge decompositions, studying works on the discrete HHD computation like [110] and [111] might help understanding why this formulation works.

In preliminary experiments on conducting cells with macroscopic current crossing the cell, we observed that the projection (2.88) can still extract $\boldsymbol{h}_p$ from $\boldsymbol{h}$ even if the anti-periodic term $\boldsymbol{h}_a$ is not zero. In this case, $\mathbf{curl}\,\boldsymbol{h} = \mathbf{curl}\,\boldsymbol{h}_p + \mathbf{curl}\,\boldsymbol{h}_a$. It seems that the formulation ignores the additional unwanted $\mathbf{curl}\,\boldsymbol{h}_a$ source, but a mathematical analysis of the formulation would be better to validate it.

A definition for the cell magnetization field

In Section 2.2, we made the hypothesis that $\boldsymbol{m}_\varepsilon$, the magnetization created by the cell eddy currents, could likely be defined as a potential for the eddy currents that is null outside the current loop. In our setting, it translates as follows: $\boldsymbol{m}_\varepsilon$ is a field such that $\boldsymbol{m}_\varepsilon = \boldsymbol{0}$ in Y_N and $\mathbf{curl}\,\boldsymbol{m}_\varepsilon = \boldsymbol{j}$ in Y_C[29]. But unlike $\boldsymbol{h}_c$, $\boldsymbol{m}_\varepsilon$ is to be computed in the conducting domain of the cell Y_C only, this can be cheaper if the latter is significantly smaller than the full cell.

The next result proves the consistency of this definition with the macroscopic magnetic field definition used in this work, and leads to another formulation usable to upscale $\boldsymbol{H}$.

Theorem 2.3 *Let $\boldsymbol{h}$ and $\mathscr{M}_{\varepsilon\to H}$ be defined as in Theorem 2.1, and suppose that $\mathbf{curl}\,\boldsymbol{h} = \boldsymbol{0}$ in Y_N.*
If there exist $\widetilde{\boldsymbol{m}_\varepsilon} \in \boldsymbol{H}_0(\mathbf{curl}; Y_\mathrm{C})$ verifying

$$\mathbf{curl}\,\widetilde{\boldsymbol{m}_\varepsilon} = \mathbf{curl}\,\boldsymbol{h} \quad \text{in } Y_\mathrm{C}, \tag{2.89}$$

then $\langle\,\widetilde{\boldsymbol{m}_\varepsilon}\,\rangle_Y = \mathscr{M}_{\varepsilon\to H}$ (where $\widetilde{\boldsymbol{m}_\varepsilon}$ is extended by $\boldsymbol{0}$ in Y_N).

For the same reasons used for the computation of $\widetilde{\boldsymbol{h}_c}$, we use a curl-curl equation to solve for (2.89):

$$\mathbf{curl}\,\mathbf{curl}\,\widetilde{\boldsymbol{m}_\varepsilon} = \mathbf{curl}\,\mathbf{curl}\,\boldsymbol{h} \quad \text{in } Y_\mathrm{C}. \tag{2.90}$$

---

[29] Such $\boldsymbol{m}_\varepsilon$ do not exist if the conducting domain is not simlply connected (if $\beta_1(Y_\mathrm{C}) \neq 0$). In this case, $\boldsymbol{m}_\varepsilon$ can be computed in a simply connected domain enclosing Y_C, e.g. inside the convex hull of Y_C.

The discrete weak form of (2.90) using the coulomb gauge for $\widetilde{\boldsymbol{m}_\varepsilon}$ is:
find $\widetilde{\boldsymbol{m}_\varepsilon} \in \boldsymbol{H}_{0,h}(\mathbf{curl}; Y_\mathrm{C})$ and $\xi \in H_{0,h}(\mathbf{grad}; Y_\mathrm{C})$ such that

$$\begin{aligned} \int_{Y_{\mathrm{C},h}} \big(\mathbf{curl}\, \widetilde{\boldsymbol{m}_\varepsilon} - \sigma \partial_t (\boldsymbol{a}_c + \boldsymbol{B} \times \boldsymbol{y})\big) \cdot \mathbf{curl}\, \boldsymbol{m}' + \int_{Y_{\mathrm{C},h}} \mathbf{grad}\, \xi \cdot \boldsymbol{m}' &= 0 \\ \int_{Y_{\mathrm{C},h}} \widetilde{\boldsymbol{m}_\varepsilon} \cdot \mathbf{grad}\, \xi' + \xi \xi' &= 0 \end{aligned} \tag{2.91}$$

where $\boldsymbol{m}' \in \boldsymbol{H}_{0,h}(\mathbf{curl}; Y_\mathrm{C})$ and $\xi' \in H_{0,h}(\mathbf{grad}; Y_\mathrm{C})$. Again, the RHS of the B-conforming formulation is used for the expression for the current in place of $\mathbf{curl}\, \boldsymbol{h}$.

Additionally, Theorem 2.3 can likely be extended on cells of macroscopically conducting domains as long as there is still a nonconducting outer domain in Y, that is if the corners of Y are not in Y_C ($\mathrm{P}_Y \cap \overline{Y_\mathrm{C}} = \emptyset$). This is because the boundary condition $\boldsymbol{m}_\varepsilon \times \boldsymbol{n}\big|_{\partial Y_\mathrm{C}} = \mathbf{0}$ is needed to fix the average of $\boldsymbol{m}_\varepsilon$ (it is necessary to have the information of where is the outside of the eddy current loops and put $\boldsymbol{m}_\varepsilon = 0$ there). An analysis of this case is made in [112], the new formulation is obtained by adding periodic boundary conditions on $\partial Y \cap Y_\mathrm{C}$ for all the field of the formulation (2.90). However, the formulation has not been validated in a multiscale HMM resolution.

Summary

To finish with this section on the magnetic field strength upscaling, a table is given to summarize the different methods with their advantages and drawbacks. The *Symbol* column contains the short name for the method, and the *Eq.* column contains the number of the equation of the discrete implementation of the method for the B-conforming formulation which is used in the numerical tests of Chapter 3.

Method name	Symbol	Eq.	Advantages	Drawbacks
Volume average	$\langle\, \boldsymbol{h} \,\rangle_Y$	(2.76)	Simple implementation	Limited to magnetostatic or when $\mathscr{M}_{\varepsilon\to\mathrm{H}}$ is negligible
Edge average	$\langle\, \boldsymbol{h} \,\rangle_{\gamma_Y}$	(2.79)	General	Numerical accuracy might be limited [109]
Tangential boundary average	$\langle\, \boldsymbol{h} \,\rangle_{\partial Y_\parallel}$	(2.82)	Surface integration (more accurate than path)	Limited to macroscopically nonconducting domains with $Y_\mathrm{C} \cap \partial Y = \emptyset$
Periodic correction volume average	$\langle\, \boldsymbol{h} - \boldsymbol{h}_c \,\rangle_Y$	(2.88)	Volume integration, may be generalized to any cell[30]	Cost of the FEM resolution for $\boldsymbol{h}_c$
Magnetization volume average	$\langle\, \boldsymbol{h} - \boldsymbol{m}_\varepsilon \rangle_Y$	(2.91)	Like $\langle\, \boldsymbol{h} - \boldsymbol{h}_c \,\rangle_Y$, but cheaper if Y_C is smaller than Y	Cost of the FEM resolution for $\boldsymbol{m}_\varepsilon$

Table 2.2: Summary for the different upscaling methods for the magnetic field strength $\boldsymbol{H}$ and their theoretical advantages and drawbacks.

---

[30] Preliminary experiments showed that the rotational component extraction (2.87) works even if the strength field is not periodic, that is if its curl is macroscopically nonzero (e.g. $\langle\, \mathbf{curl}\, \boldsymbol{h} \,\rangle_{\partial Y_\perp} = \boldsymbol{J} \neq \mathbf{0}$). So a variation of (2.88) may also be used to upscale the electric field $\boldsymbol{E}$, that almost always has a non-periodic

2.4.2 Flux fields upscaling

The usual electromagnetic flux fields are $\boldsymbol{b}$, $\boldsymbol{j}$, $\boldsymbol{d}$ and the Poynting vector $\boldsymbol{s}$. Only $\boldsymbol{B}$ and $\boldsymbol{S}$ are relevant to upscale in magnetoquasistatic with no macroscopic conductivity. We did not work on $\boldsymbol{S}$, so the upscaling formula are illustrated on the upscaling of $\boldsymbol{B}$ from the solutions of the H-conforming cell formulation (2.73). But the other fields cases are also briefly discuss.

Faces normal average

Following the definition of the macroscopic value of flux fields, the magnetic flux field can be upscaled using the faces normal average

$$\boldsymbol{B} = \left\langle \boldsymbol{\mu} \cdot \left(\boldsymbol{H} + \mathbf{grad}\, \varphi_p|_{Y_\mathrm{N}} + \boldsymbol{h}_\mathrm{C}|_{Y_\mathrm{C}}\right) \right\rangle_{\partial Y_\perp}. \tag{2.92}$$

Volume average

The divergence free fields $\boldsymbol{b}$ and $\boldsymbol{j}$ can also always be upscaled using the volume average, e.g.

$$\boldsymbol{B} = \left\langle \boldsymbol{\mu} \cdot \left(\boldsymbol{H} + \mathbf{grad}\, \varphi_p|_{Y_\mathrm{N}} + \boldsymbol{h}_\mathrm{C}|_{Y_\mathrm{C}}\right) \right\rangle_{Y}. \tag{2.93}$$

Indeed, it can be shown that if a periodic flux field is divergence free, that is $\boldsymbol{b}_p \in \boldsymbol{H}^\#(\mathrm{div}; Y)$ and $\mathrm{div}\, \boldsymbol{b}_p = 0$ in Y, then

$$\langle\, \boldsymbol{b}_p \,\rangle_Y = \langle\, \boldsymbol{b}_p \,\rangle_{\partial Y_\perp}. \tag{2.94}$$

This is due to the fact that the flux through any surface cutting the cell parallel to its faces of such $\boldsymbol{b}_p$ field is constant, due to the Gauss's law applied to the volume enclosed between the two surfaces and the flux periodicity of the sides. This is the very similar to the property on the circulations of periodic strength fields illustrated on Figure 2.12. The volume average shouldn't apply in general to $\boldsymbol{d}$ and $\boldsymbol{s}$, as they in can have nonzero macroscopic divergence.

Polarization computation using FEM projections and volume averages

Although the upscaling of the electric displacement is out of scope of our hypothesis and experiments, we would like to mention that the approach used to compute the magnetization $\boldsymbol{m}_\varepsilon$ in insulated cell can probably be transposed to the computation of the polarization $\boldsymbol{p}_\varepsilon$ when Y_C has an equal amount of positive and negative charges, that is when $\langle\, \mathrm{div}\, \boldsymbol{d} \,\rangle_Y = 0$.

---

component to account for the macroscopic $\partial_t \boldsymbol{B}$.

The analog of Theorems 2.1, 2.2 and 2.3 for the electric displacement and polarization are given in Section A.4.3. They could be used to upscale the electric displacement $\boldsymbol{D} = \langle\, \boldsymbol{d}\, \rangle_Y + \mathscr{P}_{\varepsilon \to \mathrm{H}}$ in electrostatic formulations (or rather the dielectric permittivity of the homogenized domain $\boldsymbol{\varepsilon}_\mathrm{H}$ using $\boldsymbol{D} = \boldsymbol{\varepsilon}_\mathrm{H}\boldsymbol{E}$) where the cell is insulated and Y_C has zero net charges, but is strongly polarized by charges bound in Y_C.

Summary

This chapter was dedicated to the derivation of our multiscale model and was divided into four sections. In the first one, we introduced different materials and contexts for which multiscale modeling is useful in electrical engineering, followed by the different general purpose numerical methods used to compute the electromagnetic fields in multiscale problems. Intuitive introduction of the scale separation hypothesis and HMM were proposed.

In a second part, the scale transition relation (STR) defining the macroscopic fields was studied using different perspectives, in order to understand how to define it for problems where dynamic hysteresis appears in the macroscopic magnetic law. A new STR applicable to periodic homogenization of media admitting an electrically insulated periodic cell was proposed. We detailed why our STR is consistent with the classical definition of Maxwell's equations in matter as well as the state of the art in the multiscale modeling of medium and high-frequency electromagnetic fields. We believe that this unified explanation of the different points of view is rather original, and quite useful for understanding the multiscale modeling of electromagnetic fields.

The third section built the B and H-conforming multiscale equations using the scale separation hypothesis, the new scale transition relation and the splitting of the cell fields that is commonly used in the literature. The reasons why this splitting implements the downscaling of macroscopic fields, that are rarely clearly explained, were also detailed.

Finally, four numerical implementations of the upscaling of the magnetic field strength were derived in the last section. The two last, that are based on FEM projections to compute the cell magnetization using volume averages, are original. Their consistency with the STR was justified mathematically.

In the next chapter, numerical experiments are conducted to validate the proposed formulation and uspcaling methods.

Chapter 3

Numerical validation

This chapter presents the main numerical experiments that were conducted to validate the formulation and theories presented in the previous chapter. The experiments are mostly performed on the geometry used in the example at the end of the first chapter, in Section 1.4, where the heterogeneous material is made of conducting and magnetic balls, periodically spaced in an insulating matrix. The balls have a diameter of 80μm, similar to the size of the iron inclusions in some soft magnetic materials.

The chapter is divided in two section. The first is dedicated to the study of the cell problem alone, independently of the multiscale resolution. In the second section, actual 3D magnetoquasistatic multiscale resolutions are implemented, with linear and nonlinear magnetic laws in the inclusions. Several properties of the method, such as accuracy and convergence with the decrease of the material spatial period are studied.

Metrics used to compare the numerical solutions

Different elements of comparison will be used to analyze the results. To qualitatively measure the results, integral quantities like the Joule losses power have to be compared.

They are scalar time signals that can be visualized by plotting their value over time. Let us consider $s_1(t)$ and $s_2(t)$. When the signals are visually identical, their *difference* $s_1 - s_2$ or their absolute difference $|s_1 - s_2|$ are plotted to enable finer comparison. Furthermore, the instantaneous (absolute) percentage of error of s_2 with respect to s_1 can be used to indicate the relative error, this is useful to understand the scale of the error when the actual value of the signal is not plotted. It is computed by $100 \left| \frac{s_1(t) - s_2(t)}{s_1(t)} \right|$ where a minimum threshold is applied to the denominator at time instant where it is too close to zero, to avoid potential division by zero. This quantity grows to infinity where the signals are nearly equal, but is meaningful at all times when the signals are the most different.

Additionally, two metrics will be used to quantitatively compare time dependent functions over a period of time.

If the time integral of the signals (e.g. $\int_{[0,T]} s_1(t)dt$) is of interest and if they are positive ($s_1, s_2 \geq 0$, the Joule losses power for example), the absolute percentage of difference of the time integral of s_2 with respect to that of s_1 can be computed. That is:

$$\mathrm{IPE}(s_1, s_2) = 100\frac{\left|\int_{[0,T]}(s_2 - s_1)dt\right|}{\int_{[0,T]} s_1 dt}, \tag{3.1}$$

where $[0, T]$ is the time interval over which the error is computed, usually one period of the source of the problem. This metric can only be used for quantities with constant sign, e.g. the Joule losses power, that is always positive.

We also use a metric that takes the instantaneous accuracy into account, the percentage of the $L^2([0, T])$ norm of $s_2 - s_1$ into that of s_1. It is defined by:

$$\mathrm{L2PE}(s_1, s_2) = 100\sqrt{\frac{\int_{[0,T]}(s_2 - s_1)^2 dt}{\int_{[0,T]} s_1^2\, dt}}. \tag{3.2}$$

This metric is sensible to the pointwise difference between the signals. All such errors are added thanks to the absolute value, unlike when comparing the time integrals where errors of opposite sign cancel out.

Software and computational resources

All the FEM and HMM implementation were made using the GetDP Software [22], and the meshes and visualizations were done using Gmsh [23].

Two HPC clusters were used to run the HMM resolutions in parallel. The first is the GRICAD cluster [113] from the Grenoble-Alpes University, to which we had access thanks to the PhD funding. The second is Nic5 [114], the cluster of Liège, to which we had access thanks to Christophe Geuzaine.

Finally, all the curve plots of the thesis were produced using the Julia library Makie.jl [115].

3.1 Cell problem validation

In this section, the numerical resolutions of the cell problem using H and B-conforming formulations is studied in detail. There are several objectives for doing this.

The first is to validate the cell problem independently of the multiscale machinery. In particular, it will be verified to which extent the $\boldsymbol{H}(\boldsymbol{B})$ law provided by the B-conforming cell problem is the inverse of the $\boldsymbol{B}(\boldsymbol{H})$ law provided by the H-conforming cell problem, and if the cell field maps obtained using each formulation correspond.

Also, studying the cell problem enables understanding better the physics of the cell solutions, and observe the sensitivity of the upscaled quantities with respect to the resolution parameters.

Finally, the cell solutions inform on consistence or difference between $\boldsymbol{H}$ and $\langle\, \boldsymbol{h} \,\rangle_Y$. So the validity and need for the proposed $\boldsymbol{H}$ upscaling formulas will be studied for different physical parameters.

These objectives are necessary steps in the validation of the multiscale model proposed in this thesis, but they would also be useful to validate the implementation of the cell problem when using the method on a new problem. There are numerous hyperparameters and sources of error in the implementation of HMM, so being able to validate the cell problem independently is very useful in practice.

Considered cell problem

One periodic cell is considered for all our tests. It is that of the problem introduced in Section 1.4, a conducting and magnetic ball surrounded by a nonmagnetic electric insulator. This cell respects the electric insulation hypothesis introduced on page 83, so all the previously introduced formulations apply.

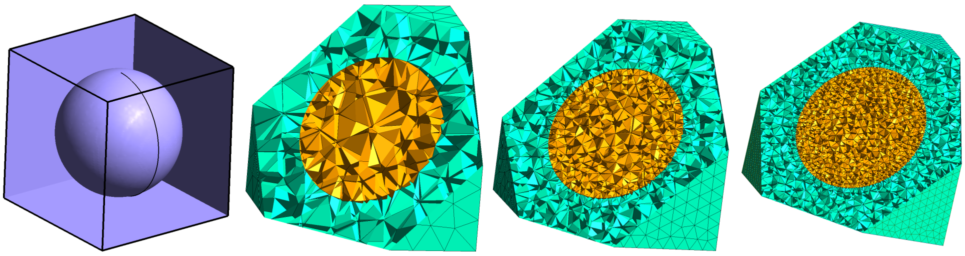

Figure 3.1: Geometry of the cell problem (left) and three meshes of the cell with respectively 4k, 37k and 140k tetrahedra (right).

In all the tests of Section 3.1, the sphere has a conductivity of $\sigma = 10 \times 10^6$ S.m^{-1} (close to that of Iron) and the insulator has the electromagnetic properties of the air, that is no conductivity and a relative permeability of $\mu_r = 1$. A linear magnetic law with $\mu_r = 10$ and a nonlinear magnetic law will be used in the sphere. The nonlinear law follows the Fröhlich-Kennelly law (1.82) with maximum relative permeability of $\mu_{r,\max} = 100$. The sphere has a diameter of 80 μm and the cell width is $\varepsilon = 100$ μm, so the volume fraction of magnetic material is approximately 27%.

3.1.1 Chained cell problems methodology

The validation of the solution of the cell problems is not easy because our multiscale model was not derived in a mathematically rigorous way, so there is no analytic formula to compute the macroscopic magnetic law and cell fields associated to a specific multiscale problem. It is thus necessary to use a numerical validation.

The only way that we found to solve the cell problems in the same physical state is to use the output of one formulation as the input of the other one. For example, a source magnetic flux density $\boldsymbol{B}_{\text{src}}(t)$ is chosen, then $\boldsymbol{H}(\boldsymbol{B}_{\text{src}}(t))$ is computed over the entire simulation period using the B-conforming formulation of the cell problem. Finally, $\boldsymbol{B}(\boldsymbol{H}(\boldsymbol{B}_{\text{src}}(t)))$ is computed using the H-conforming cell problem. The obtained $\boldsymbol{B}(t)$ can then be compared with the initial $\boldsymbol{B}_{\text{src}}(t)$ which serves as a reference. For shortness, this sequence of computations is called $\boldsymbol{B}_{\text{src}} \xrightarrow{\text{B-conf.}} \boldsymbol{H} \xrightarrow{\text{H-conf.}} \boldsymbol{B}$. The converse one, $\boldsymbol{H}_{\text{src}} \xrightarrow{\text{H-conf.}} \boldsymbol{B} \xrightarrow{\text{B-conf.}} \boldsymbol{H}$, is also studied. The steps of the method are summarized in Figure 3.2.

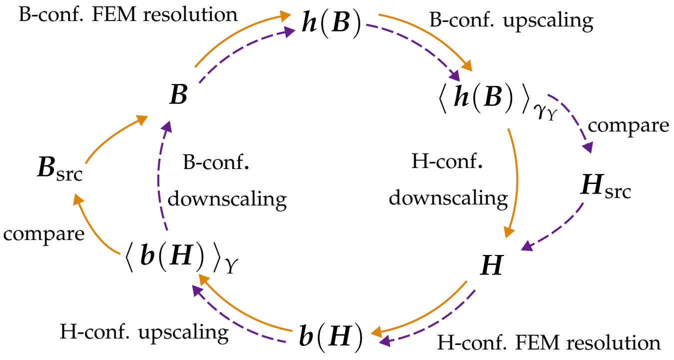

Figure 3.2: Diagram of the steps taken to chain the resolutions of the cell problems implemented with the two dual H and B conforming formulations. The method starts with a prescribed source $\boldsymbol{B}_{\text{src}}$ or $\boldsymbol{H}_{\text{src}}$, which serves as expected value to compare the results with after completing all the steps once.

We call this method the *chained cell problem* method. The idea originally comes from Janne Ruuskanen and was used in [39]. This method enables to validate that the cell problems are dual from each other, in terms of both the upscaled laws and the cell fields. If we assume that the H-conforming formulation is correct and reliable, which is the case according to [4], the methodology also enables to validate the B-conforming formulation of the cell problem. It is applicable on any cell geometry and with arbitrary direction and time variations of the sources.

One point worth highlighting is that the upscaled $\boldsymbol{H}(t)$ or $\boldsymbol{B}(t)$ fields are interpolated in **time** by smooth polynomials (over the entire simulation period) before downscaling it to the second cell problem. This is important to avoid additional error in the solution of the cell problems due to the non smoothness in time of the source. The Akima interpolation method [116] implemented in GetDP [22] (the `InterpolationAkima` function) is used for that. This method uses order three spline polynomials.

In the following, the actual validation of the aforementioned points is made on linear and nonlinear transient 3D cell problems.

3.1.2 Accuracy of the solutions of the cell problem

For the first experiment, the objective is to show the agreement between the H and B-conforming formulations, in terms of the upscaled magnetic field $\boldsymbol{H}$ or $\boldsymbol{B}$ and of the Joule losses density $\mathcal{P}_{\mathrm{JL}}$. The focus is made on these quantities because the first drives the convergence of the multiscale resolution, and the second is one of the main quantities interest in the simulation of magnetic materials and is usually difficult to accurately compute.

Reaching excellent accuracy with the chained cell problem test is not easy because the error committed in each resolution accumulate, so very fine discretization will be used. The cell mesh has around 160k tetrahedra, and 160 Time Steps per period (TSpp) are used for the time discretization.

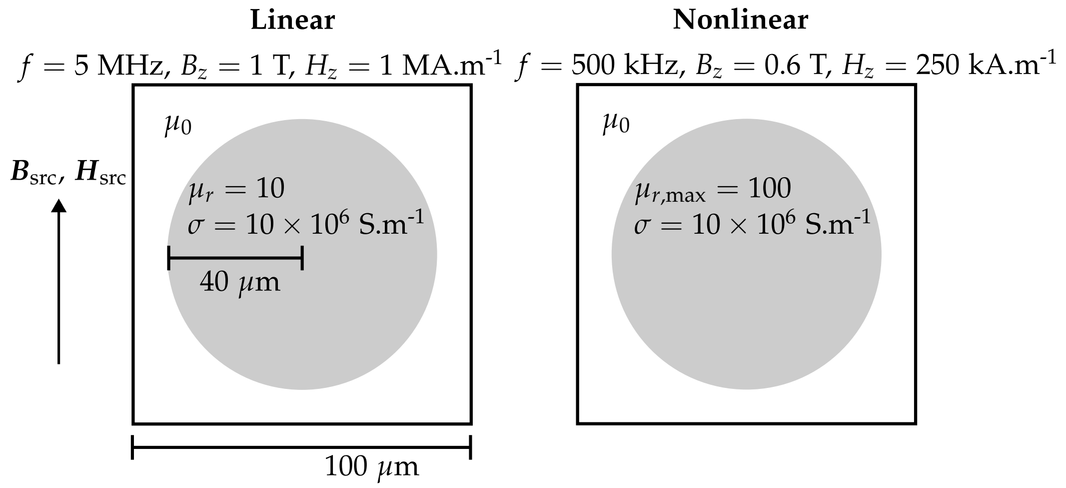

Figure 3.3: Parameters used for the validation of the accuracy of the cell formulations. The $\boldsymbol{B}_{\mathrm{src}}$ of magnitudes B_z are the sources for the B-conforming cell formulation in the sequence $\boldsymbol{B}_{\mathrm{src}} \xrightarrow{\text{B-conf.}} \boldsymbol{H} \xrightarrow{\text{H-conf.}} \boldsymbol{B}$, and the $\boldsymbol{H}_{\mathrm{src}}$ of magnitudes H_z are the sources of the H-conforming formulation in the sequence $\boldsymbol{H}_{\mathrm{src}} \xrightarrow{\text{H-conf.}} \boldsymbol{B} \xrightarrow{\text{B-conf.}} \boldsymbol{H}$.

The accuracy is measured with linear and nonlinear magnetic law in the ball, and with the cell problems chained with the H-conforming formulation first and then the B-conforming one first. Sine $\boldsymbol{B}_{\text{src}}$ and $\boldsymbol{H}_{\text{src}}$ sources oriented along $\boldsymbol{e}_z$ are used, that is

$$\boldsymbol{B}_{\text{src}}(t) = B_z \sin(2\pi f t)\boldsymbol{e}_z \quad \text{and} \quad \boldsymbol{H}_{\text{src}}(t) = H_z \sin(2\pi f t)\boldsymbol{e}_z. \tag{3.3}$$

The physical parameters used are given in the sketches in Figure 3.3. For linear magnetic law, the frequency is $f = 5$ MHz, the relative permeability of the sphere is $\mu_r = 10$ and the magnitudes of the sources are $B_z = 1$ T and $H_z = 1$ MA.m^{-1}. For the nonlinear law, we used $f = 500$ kHz, a maximum relative permeability of $\mu_{r,\max} = 100$ (used in the Fröhlich-Kennelly law) and the sources magnitudes are $B_z = 0.6$ T and $H_z = 250$ kA.m^{-1}. In both cases, the skin depth in the ball is approximately $\delta = 40$ μm, the radius of the ball, so there is no significant skin effect.

We will focus on the accuracy of the computation of the macroscopic magnetic field $\boldsymbol{H}$ or $\boldsymbol{B}$, and of the Joule losses power in the cell $\mathcal{P}_{\text{JL}}$, that is computed by:

$$\mathcal{P}_{\text{JL}} = \int_{Y_{\text{C}}} \boldsymbol{j} \cdot \boldsymbol{e}, \tag{3.4}$$

where the expression for $\boldsymbol{j}$ and $\boldsymbol{e}$ depend on the formulation.

For the order $\boldsymbol{H}_{\text{src}} \xrightarrow{\text{H-conf.}} \boldsymbol{B} \xrightarrow{\text{B-conf.}} \boldsymbol{H}$, the magnetic field and Joule losses are plotted over time in Figure 3.4, and the Table 3.1 contains the integrated percentage of errors of the upscaled magnetic field against the source, and the percentage of differences of the Joule losses computed by each formulation. The five possible $\boldsymbol{H}$ upscaling methods are tested, namely the volume average $\langle \boldsymbol{h} \rangle_Y$, the tangential boundary average $\langle \boldsymbol{h} \rangle_{\partial Y_\parallel}$, the tangential edge average $\langle \boldsymbol{h} \rangle_{\gamma_Y}$, the volume average using the computation of the cell magnetization $\langle \boldsymbol{h} - \boldsymbol{m}_\varepsilon \rangle_Y$ and the volume average using the computation of the magnetic field correction $\langle \boldsymbol{h} - \boldsymbol{h}_c \rangle_Y$. Some typical field maps of the solutions of the H and B-conforming problems are shown in Figure 3.6.

The curves show that there is an excellent accuracy and agreement between the two formulations. The L^2 percentages of error for the four methods proposed to upscale $\boldsymbol{H}$ are almost identical, 0.43% (linear) and 0.73% (nonlinear), and respectively better than the volume average $\langle \boldsymbol{h} \rangle_Y$, 4.62% (linear) and 0.91% (nonlinear). As expected, the volume average is not a correct upscaling method for $\boldsymbol{H}$.

The formulations also agree well on the estimation of the integrated Joule losses over the period, with differences of 0.93% (linear) and 1.41% (nonlinear).

The experiment was also conducted for the other sequence $\boldsymbol{B}_{\text{src}} \xrightarrow{\text{B-conf.}} \boldsymbol{H} \xrightarrow{\text{H-conf.}} \boldsymbol{B}$. The plots are given in Figure 3.5 and the integrated percentage of error in Table 3.2. The

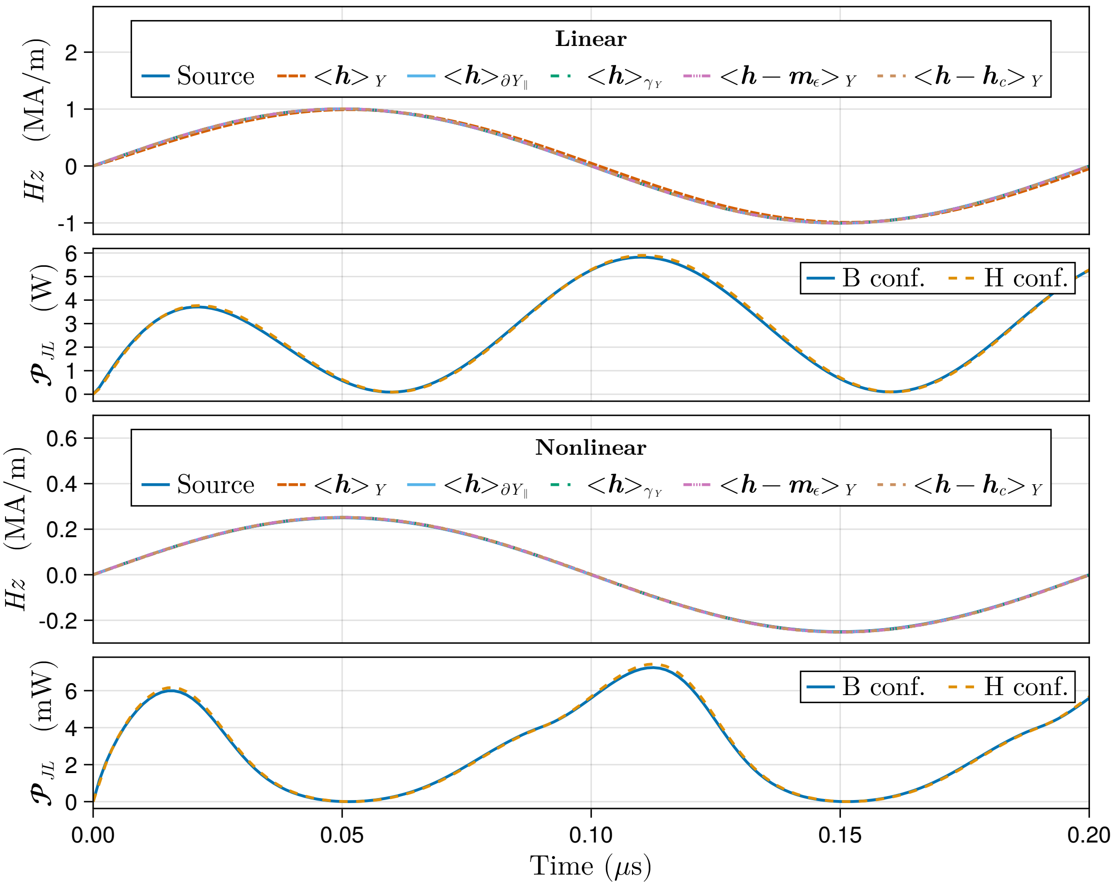

Figure 3.4: Upscaled magnetic field strength and total Joule losses power $\mathcal{P}_{\text{JL}}$ (3.4) for a finely discretized cell problem, using the sequence $\boldsymbol{H}_{\text{src}} \xrightarrow{\text{H-conf.}} \boldsymbol{B} \xrightarrow{\text{B-conf.}} \boldsymbol{H}$ with a source of magnitude $H_z = 1$ MA.m^{-1} and a frequency of 5 MHz for the linear case. For the nonlinear one, a magnitude of $H_z = 250$ kA.m^{-1} and a frequency of 500 kHz are set. The magnetic field curves qualitatively match perfectly, except the volume average in the linear case, but a difference is visible for the Joule losses. The larger error on $\mathcal{P}_{\text{JL}}$ is likely due to a too coarse time discretization.

Linear

	$\langle \boldsymbol{h} \rangle_Y$	$\langle \boldsymbol{h} \rangle_{\partial Y_{\parallel}}$	$\langle \boldsymbol{h} \rangle_{\gamma_Y}$	$\langle \boldsymbol{h} - \boldsymbol{m}_{\varepsilon} \rangle_Y$	$\langle \boldsymbol{h} - \boldsymbol{h}_c \rangle_Y$	$\mathcal{P}_{\text{JL}}$
L2PE (%)	4.62	0.42	0.42	0.43	0.43	2.08

	$\mathcal{P}_{\text{JL}}$
IPE (%)	0.93

Nonlinear

	$\langle \boldsymbol{h} \rangle_Y$	$\langle \boldsymbol{h} \rangle_{\partial Y_{\parallel}}$	$\langle \boldsymbol{h} \rangle_{\gamma_Y}$	$\langle \boldsymbol{h} - \boldsymbol{m}_{\varepsilon} \rangle_Y$	$\langle \boldsymbol{h} - \boldsymbol{h}_c \rangle_Y$	$\mathcal{P}_{\text{JL}}$
L2PE (%)	0.91	0.72	0.72	0.73	0.73	2.42

	$\mathcal{P}_{\text{JL}}$
IPE (%)	1.41

Table 3.1: L^2 percentages of error (see (3.2)) of the upscaled magnetic field with respect to $\boldsymbol{H}_{\text{src}}$, computed from solution presented in Figure 3.4, and the integral percentage of difference (3.1) between the total joule losses over the period given by H and B-conforming solution (rightmost column).

results are similar to the previous, the L^2 percentage of error of the upscaled $\boldsymbol{B}$ with the

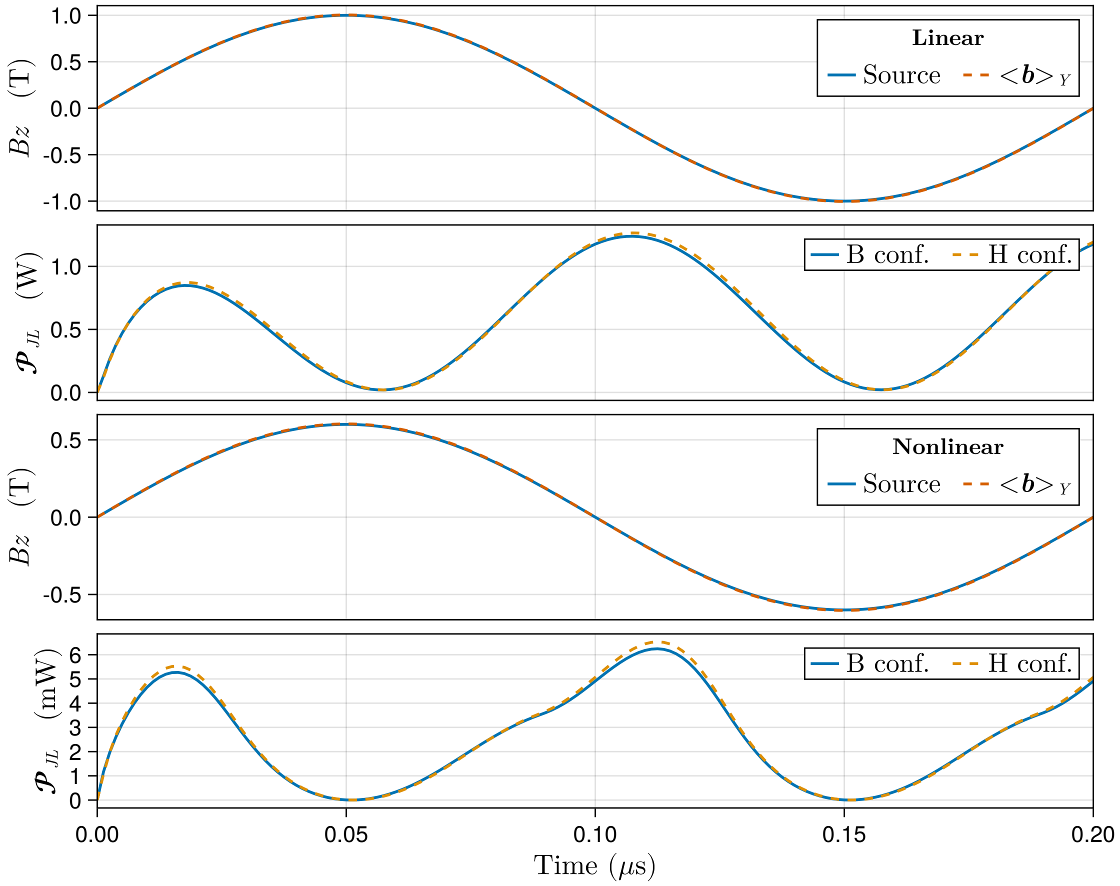

Figure 3.5: Upscaled magnetic flux density and total Joule losses power $\mathcal{P}_{\mathrm{JL}}$ (3.4) for a finely discretized cell problem, using the sequence $\boldsymbol{B}_{\mathrm{src}} \xrightarrow{\text{B-conf.}} \boldsymbol{H} \xrightarrow{\text{H-conf.}} \boldsymbol{B}$ with a source of magnitude $B_z = 1$ T and of frequency 5 MHz for the linear case, and with a source of magnitude $B_z = 0.6$ T and of frequency 500 kHz for the nonlinear case. The error on the Joule losses is slightly greater than when the problems are solved in the other sequence (H-conf. then B-conf.).

reference of 0.42% (linear) and 0.67% (nonlinear).

Linear

	$\langle \boldsymbol{b} \rangle_Y$	$\mathcal{P}_{\mathrm{JL}}$
L2PE (%)	0.42	2.71

	$\mathcal{P}_{\mathrm{JL}}$
IPE (%)	1.90

Nonlinear

	$\langle \boldsymbol{b} \rangle_Y$	$\mathcal{P}_{\mathrm{JL}}$
L2PE (%)	0.67	3.84

	$\mathcal{P}_{\mathrm{JL}}$
IPE (%)	2.80

Table 3.2: L^2 percentages of error (see (3.2)) of the upscaled magnetic field with respect to $\boldsymbol{B}_{\mathrm{src}}$, computed from solution presented in Figure 3.5, and the percentage of difference between the total joule losses over the period given by H and B conforming solution (rightmost column).

There is a lower agreement on the error of the Joule losses integrated over the period, while the L^2 error is similar. This likely means that in the previous experiment, the relative difference between both $\mathcal{P}_{\mathrm{JL}}$ curves changes sign such that the error compensate, and that it does not change sign and cumulate in the latter experiment.

From these results, we can safely conclude that the proposed formulation are inverse of each other. This ensures that the upscaling of $\boldsymbol{B}$ from the H-conforming solution is consistent with its downscaling in the B-conforming formulation. And vice versa for $\boldsymbol{H}$, as long as one of the correct methods is used (all except the volume average). It seems that the four proposed $\boldsymbol{H}$ upscaling methods have the same accuracy on fine meshes. These results also confirm that the formulation accurately model the transient regime happening in the beginning of the period.

We can also visualize the macroscopic material law that the cell problems implement. For that, the B-H curve of the upscaled law for linear and nonlinear problems are plotted in Figure 3.7, for the $\langle \boldsymbol{h} \rangle_{\partial Y_{\|}}$ proposed upscaling methods for $\boldsymbol{H}$, and also for the volume average $\langle \boldsymbol{h} \rangle_{Y}$.

We see that the macroscopic magnetic laws are hysteretic, and we observe greater difference between $\langle \boldsymbol{h} \rangle_{Y}$ and $\boldsymbol{H}$ for the linear case than in the nonlinear one, which is consistent with the percentages of error of Tables 3.1 and 3.2. The hysteresis effect is not very strong because it is only due to the microscale eddy currents, the ferromagnetic hysteresis is not considered here with the choice of magnetic material law in the inclusion. But it is strong enough for the macroscopic problem to require a nonlinear resolution even if the material law in the cell is linear.

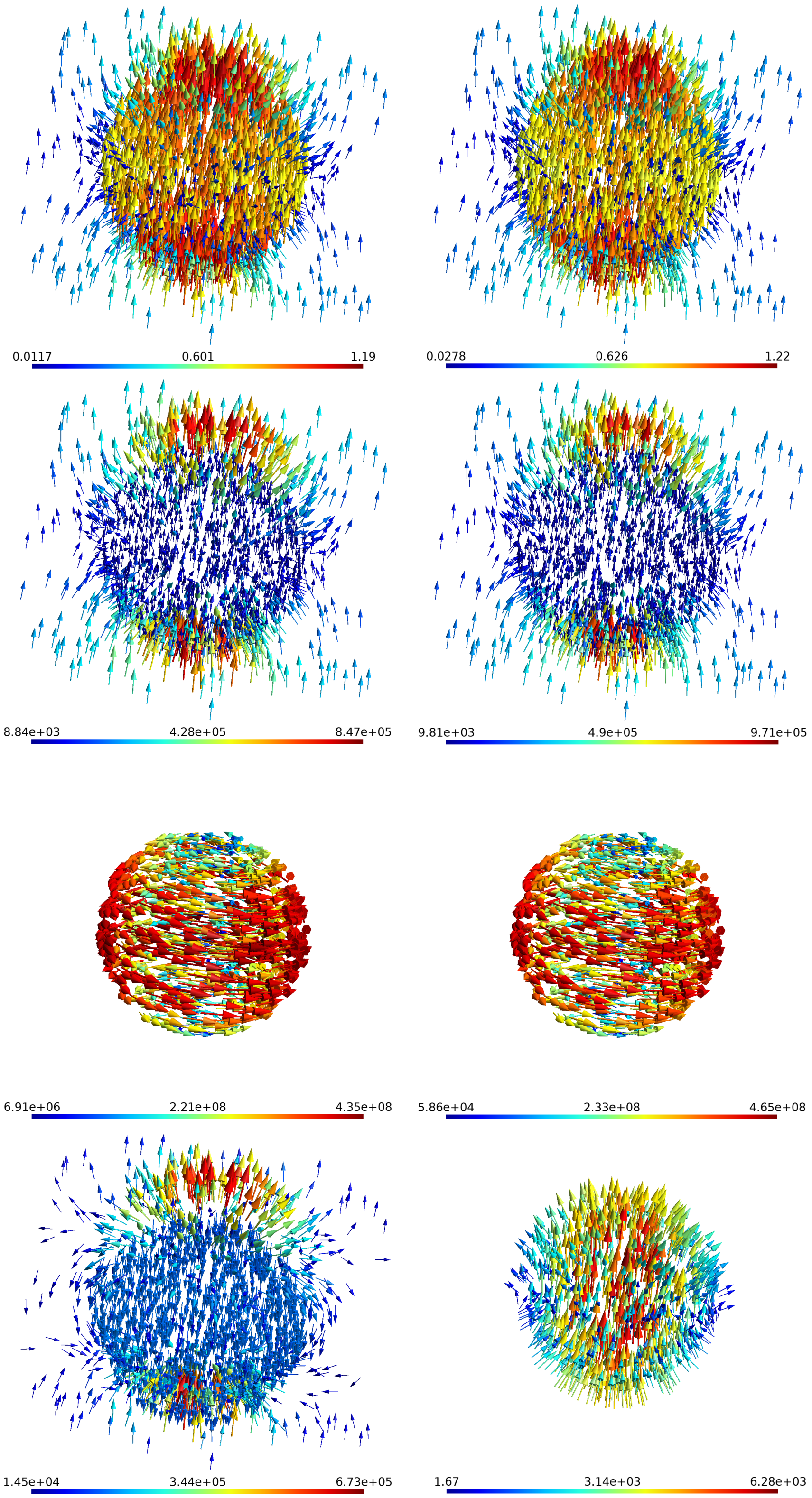

Figure 3.6: Field maps obtained from the solutions of the cell problem discretized with 21k tetrahedra, using the H-conforming formulation (left) and the B-conforming formulation (right). The plotted fields are, from top to bottom: $\boldsymbol{b}$, $\boldsymbol{h}$, $\boldsymbol{j}$, and $\boldsymbol{h}_c$-$\boldsymbol{m}_\varepsilon$ on the last row. For better visibility, the arrows are only plotted in $1/12^{\text{th}}$ of the elements, the chosen time step is TS $= 60$ over the 160 of the total period.

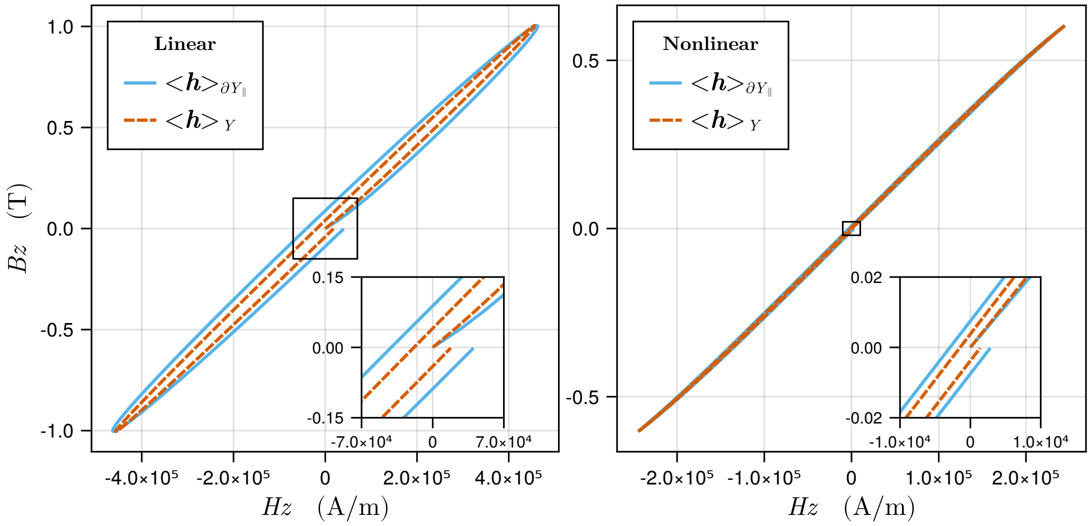

Figure 3.7: The upscaled B_z-H_z curve of the macroscopic field provided by the cell problem for linear (left) and nonlinear (right) magnetic laws. The curves are plotted for two magnetic field upscaling methods, the boundary tangential average $\langle \boldsymbol{h} \rangle_{\partial Y_{\parallel}}$ and the volume average $\langle \boldsymbol{h} \rangle_{Y}$. The linear curve is an ellipse, with a quite large width because there are strong Joule losses due to the high frequency. A small saturation effect is visible on the nonlinear curve ends, it is not very visible due to the small volume fraction of iron in the cell ($\approx 27\%$) even if the nonlinear magnetic law is locally saturated in the ball.

Although all the tests from this section are performed using a source with constant direction, the z axis, additional tests not presented and the latter experiment of the HMM confirm that the formulation works with sources in any direction.

3.1.3 Sensitivity to the discretization and the choice of upscaling method

The next experiments aim at helping to understand what resolution parameters influence the quality of the upscaled quantities for the B-conforming formulation. We would like to study the influence of the spatial and temporal discretization on the upscaled magnetic field and Joule losses, and compare the values given by the different upscaling methods.

Once again, we have no access to the analytic solutions for either the B or H-conforming formulations of the cell problem, but we want reference solution for the B-conforming one, so the $\boldsymbol{H}_{\mathrm{src}} \xrightarrow{\text{H-conf.}} \boldsymbol{B} \xrightarrow{\text{B-conf.}} \boldsymbol{H}$ chained cell problem method is used.

But in order to only measure the error due to the B-conforming formulation, fine discretizations are used for the H-conforming resolution (160k elements and 160 TSpp like last experiments), and very coarse discretizations are used for the B-conforming resolution with 4k or 1.5k elements and 40 or 20 TSpp. This way, the error at the end of the pipeline should be mainly due to the B-conforming problem.

Comparison of the different upscaling methods for $\boldsymbol{H}$

First, the upscaled $\boldsymbol{H}$ using the five studied methods are compared with $\boldsymbol{H}_{\mathrm{src}}$ for the discretization with 4k elements and 40 TSpp, in Figure 3.8 for the linear magnetic law and in Figure 3.9 for the nonlinear one.

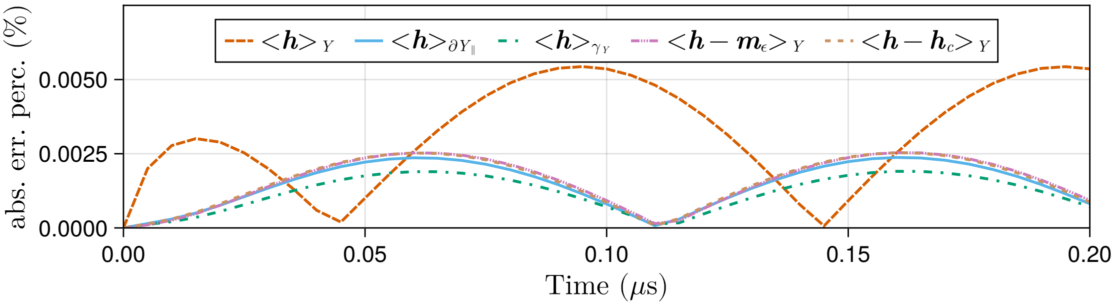

Figure 3.8: Absolute error in percentage of the maximum reference value $\boldsymbol{H}_{\mathrm{src}}\cdot\boldsymbol{e}_z = 1$ MA.m^{-1}, between the z components of the source $\boldsymbol{H}_{\mathrm{src}}\cdot\boldsymbol{e}_z$ and the five possible upscaling formulas for $\boldsymbol{H}$ using the sequence $\boldsymbol{H}_{\mathrm{src}} \xrightarrow{\text{H-conf.}} \boldsymbol{B} \xrightarrow{\text{B-conf.}} \boldsymbol{H}$ with **linear magnetic law**, and a coarse discretization of the B-conforming problem (4k elements and 40 TSpp).

For the linear case, there are significant differences between the volume average $\langle\, \boldsymbol{h}\,\rangle_Y$ and the other methods. The error with the reference is larger, and it has a phase offset, unlike the other methods. This phase offset is consistent with our theory that the error is due to the magnetization field generated by the eddy currents, because the latter are in quadrature with the source magnetic field.

Also, this experiment suggests that the four proposed $\boldsymbol{H}$ upscaling methods are equivalent in terms of accuracy, the discretization parameters influence more the accuracy than the choice of the upscaling method.

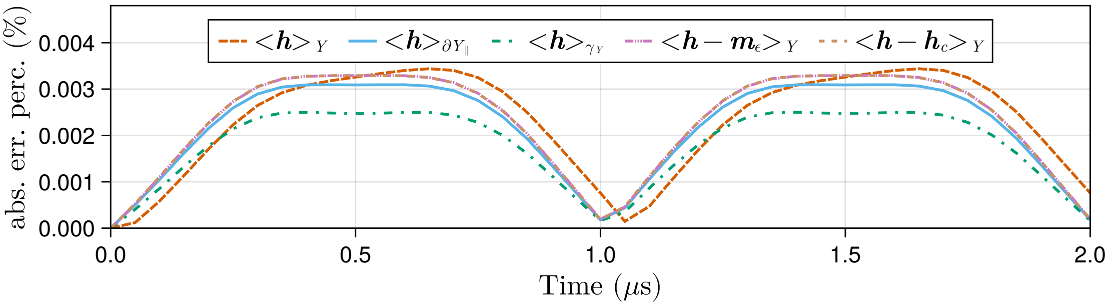

Figure 3.9: Absolute error in percentage of the maximum reference value $\boldsymbol{H}_{\text{src}}\cdot\boldsymbol{e}_z = 250$ kA.m^{-1}, between the z components of the source $\boldsymbol{H}_{\text{src}}\cdot\boldsymbol{e}_z$ and the five possible upscaling formulas for $\boldsymbol{H}$ using the sequence $\boldsymbol{H}_{\text{src}} \xrightarrow{\text{H-conf.}} \boldsymbol{B} \xrightarrow{\text{B-conf.}} \boldsymbol{H}$ with **nonlinear magnetic law**, and a coarse discretization of the B-conforming problem (4k elements and 40 TSpp).

For the nonlinear case, shown in Figure 3.9, the eddy currents are sufficiently negligible that there is no significant difference between all the methods.

Error on $\boldsymbol{H}$ and $\mathcal{P}_{\text{JL}}$ with the coarsening of the discretization in space and time

In a second time, the degradation of the accuracy with the coarsening of either the mesh or the time step is studied, in order to give recommendations on how to refine the cell problem in case the solutions are not accurate enough. This experiment is made on the upscaled magnetic field and Joule losses, using only the tangential average upscaling method $\langle\, \boldsymbol{h}\,\rangle_{\partial Y_\parallel}$ because all methods follow the same trend.

The errors measured using the linear law are plotted in Figure 3.10 for three discretizations: 4k elements and 40 TSpp, 4k elements and 20 TSpp, and 1.5k elements and 40 TSpp. The error using the nonlinear law and the same discretization is plotted in Figure 3.11.

The main take-away of this experiment is that the error on the magnetic field is influenced by the spatial discretization, but not really by the time one. Conversely, the error on Joule losses is strongly affected by the time discretization, but less by the spatial one. In our experience, this effect is amplified once the mesh is decently refined (10-20k elements), then, only the time refinement improves the accuracy of $\mathcal{P}_{\text{JL}}$.

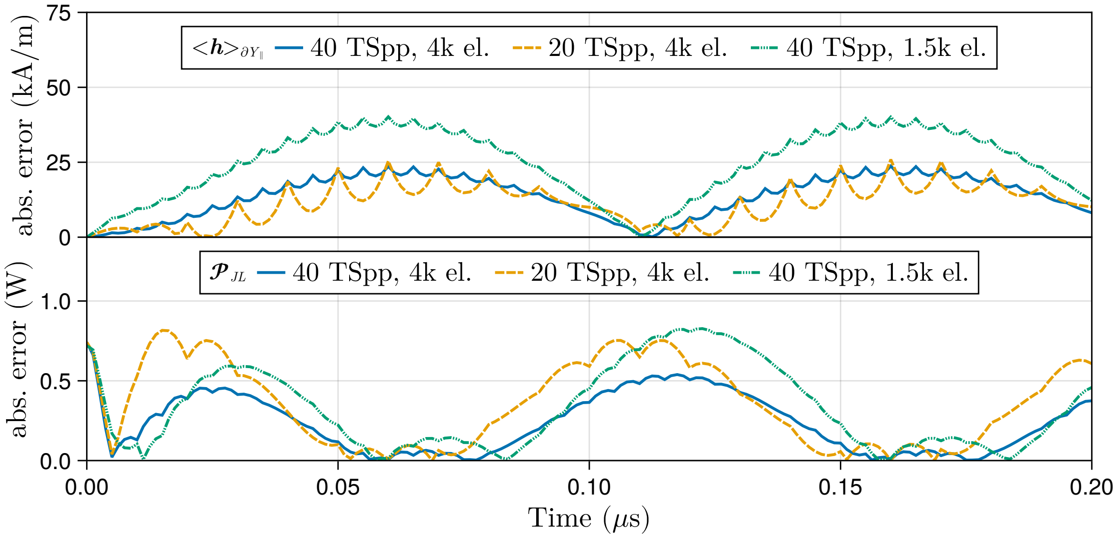

Figure 3.10: Absolute difference between $\boldsymbol{H}$ and $\mathcal{P}_{\mathrm{JL}}$ computed with a finely discretized cell problem (160k tets. and 160 TSpp) and a coarsely discretized cell problems (4/1.5k tets. and 40/20 TSpp). The reference are the upscale quantities from Figure 3.4 with linear laws. The jumps effects are due to the comparison of the linear interpolation between the points with different sampling rates (different TSpp). The accuracy for H is strongly affected by the spatial discretization but not really by the time one. Conversely, the accuracy for $\mathcal{P}_{\mathrm{JL}}$ is very impacted by the time discretization. Once the spatial discretization is decent (10-15k elements), it does not affect the Joule losses accuracy anymore.

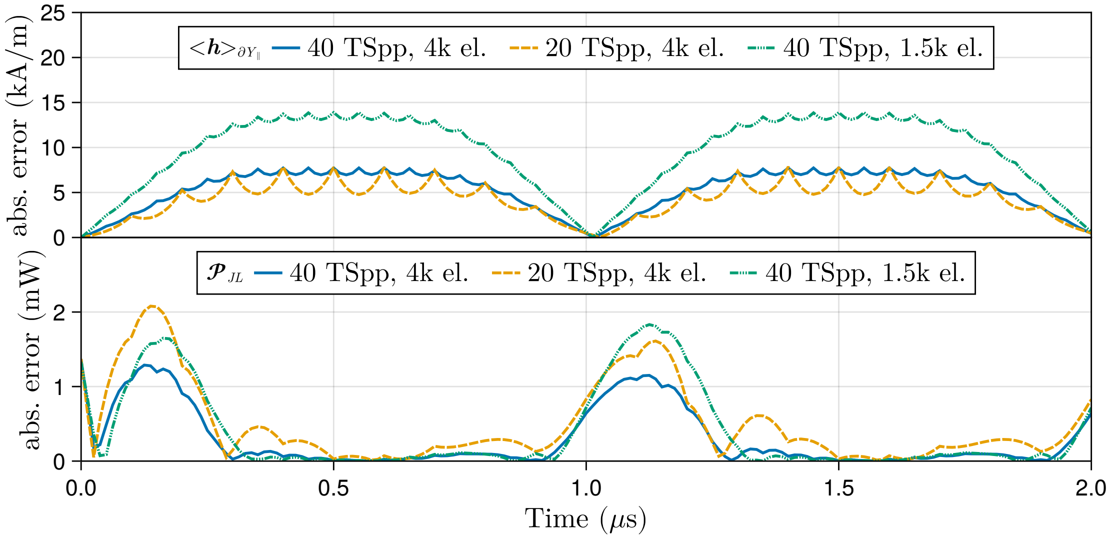

Figure 3.11: Same comparison as in Figure 3.10, but for the nonlinear cell problem with solution of Figure 3.4 as reference. The behavior is the same as in the linear case, except that the error on $\mathcal{P}_{\mathrm{JL}}$ happen when the magnetic field is growing fast (first quarter of the half-periods), probably before the magnetic material saturates.

3.1.4 Parametric study of the validity of the magnetic field strength upscaling

The results presented previously show that there might be a significant difference between $\boldsymbol{H}$ and the volume average $\langle\, \boldsymbol{h} \,\rangle_Y$ in the presence of strong eddy currents, but not always.

In order to have a clearer vision of which scenarios lead to a wrong upscaling of $\boldsymbol{H}$ using the volume average, we conducted a parametric study to show when $\langle\, \boldsymbol{h} \,\rangle_Y$ diverges from $\boldsymbol{H}$. The cell problem was solved for different frequencies and relative permeabilities in the magnetic balls. For each, two quantities are computed, the discrepancy between $\boldsymbol{H}$ and $\langle\, \boldsymbol{h} \,\rangle_Y$ denoted H_{err} and the ratio of the Joule losses in the total absolute electromagnetic power $\mathcal{P}_{\text{rat}}$.

The error H_{err} between $\boldsymbol{H}$ and $\langle\, \boldsymbol{h} \,\rangle_Y$ is computed as follows:

$$H_{\text{err}} = 100 \frac{\int_{[0,T]} \|\boldsymbol{H}(t) - \langle\, \boldsymbol{h}(t) \,\rangle_Y\|^2 dt}{\int_{[0,T]} \|\boldsymbol{H}(t)\|^2 dt}, \tag{3.5}$$

it is the percentage of difference between the $L^2([0,T])$ norm of $\|\boldsymbol{H} - \langle\, \boldsymbol{h} \,\rangle_Y\|(t)$ and that of $\|\boldsymbol{H}\|(t)$.

The power ratio $\mathcal{P}_{\text{rat}}$ is computed with:

$$\mathcal{P}_{\text{rat}} = 100 \frac{\int_{[0,T]} \mathcal{P}_{\text{JL}}^2 dt}{\int_{[0,T]} \mathcal{P}_{\text{em}}^2 dt}, \tag{3.6}$$

that is the percentage of the $L^2([0,T])$ norm of $\mathcal{P}_{\text{JL}}$ into the $L^2([0,T])$ norm of $\mathcal{P}_{\text{em}}$. The latter is the electromagnetic power in the cell, computed using:

$$\mathcal{P}_{\text{em}} = \int_{Y_h} \boldsymbol{h} \cdot \partial_t \boldsymbol{b} \; + \; \boldsymbol{j} \cdot \boldsymbol{e}.$$

The reason to monitor this quantity is that it might inform on how much $\boldsymbol{H}$ differs from $\langle\, \boldsymbol{h} \,\rangle_Y$. Indeed, as the eddy currents cannot flow at the macroscopic scale, their power is transferred to the macroscopic magnetic law. As explained before, we believe that this comes with additional magnetization that is created by the eddy current loop, and that is responsible for the difference between $\langle\, \boldsymbol{h} \,\rangle_Y$ and $\boldsymbol{H}$. This magnetization has a phase offset of $\pi/2$ with the magnetic field (it is in phase with $\partial_t \boldsymbol{B}$ and the eddy currents), which explains why the error of $\langle\, \boldsymbol{h} \,\rangle_Y$ has a phase offset (e.g. in Figure 3.8).

Also, the magnetization created by induced current loops goes "against" (decreases) the magnetic field that creates it. So we believe that removing such additional magnetization from $\langle\, \boldsymbol{h} \,\rangle_Y$ to obtain $\boldsymbol{H}$ increases the latter, which explains why the macroscopic $\boldsymbol{B}/\boldsymbol{H}$-loop is wider than the $\boldsymbol{B}/\langle\, \boldsymbol{h} \,\rangle_Y$-loop (e.g. in Figure 3.7).

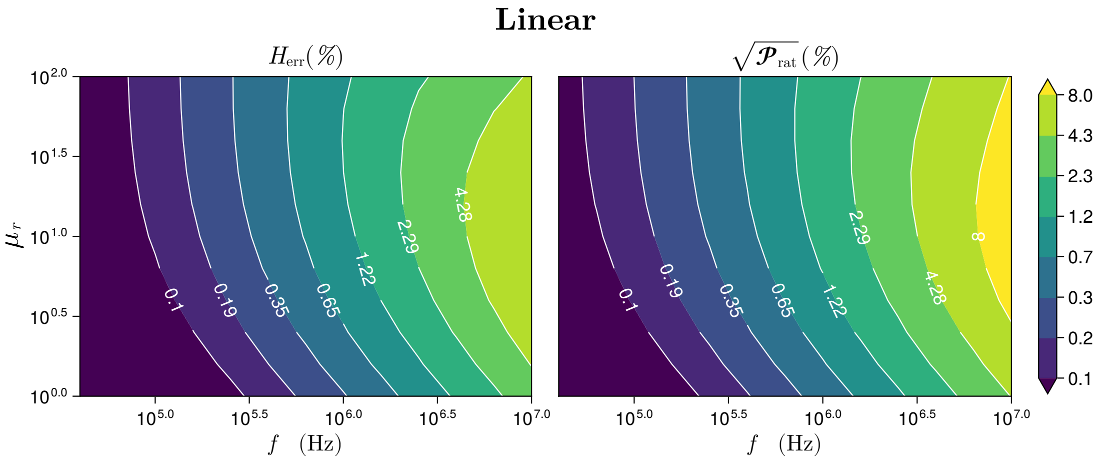

Figure 3.12: Log-log error maps at different frequencies and at different sphere relative permeabilities, ranging from 46kHz to 10MHz, and from $\mu_r = 1$ to $\mu_r = 100$, for the **magnetically linear** cell problem. Left : H_{err}, the percentage of discrepancy between $\boldsymbol{H}$ and $\langle \boldsymbol{h} \rangle_Y$ computed using (3.5). Right : $\sqrt{\mathcal{P}_{\mathrm{rat}}}$, square root of the ratio of the eddy currents power into the total electromagnetic power, computed using (3.6). We chose to plot the square root of the power error because the Joule losses typically grow with the square of the fields, and it shows better the correlation between the two quantities.

The contour maps for (3.5) and (3.6) were computed using a linear magnetic law (Figure 3.12) and using a nonlinear one (Figure 3.13). The H-conforming formulation of the cell problem with sources $\boldsymbol{H}_{\mathrm{src}}$ from (3.3) was used, on a cell mesh of 37k elements and with 160TSpp.

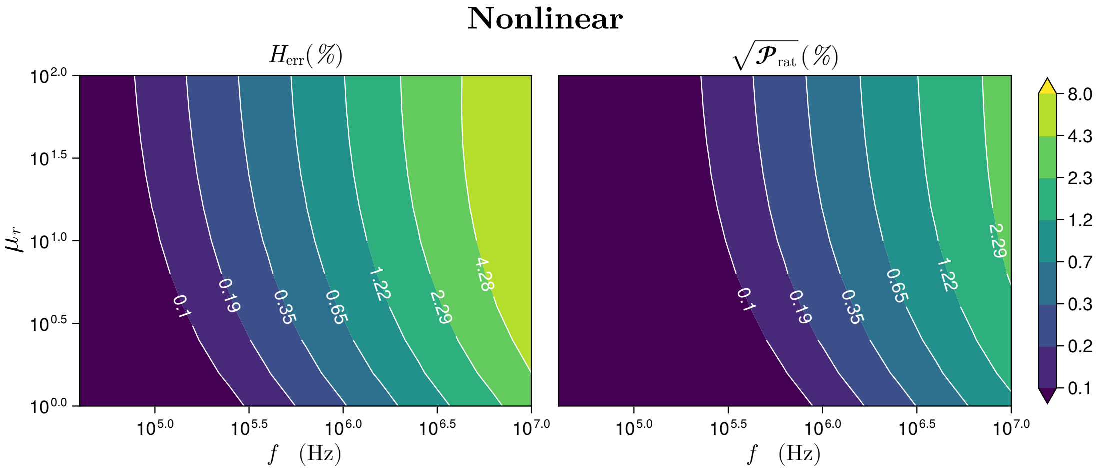

Figure 3.13: Log-log error maps of the same quantities as Figure 3.12, but with **nonlinear magnetic** law in the balls. Here, μ_r is the nonlinear law parameter of the maximum/unsaturated permeability, so the effective permeability is actually inferior to the y-axis value. There is still a correlation between the two maps, but the values match less than in the linear case, the share of Joule losses in the electromagnetic power is lower than the upscaling error.

In both linear and nonlinear cases, both quantities strictly increase with the frequency, but not with the permeability. This means that although the error is correlated with the skin depth, the latter is not always a good predictor of the discrepancy between $\boldsymbol{H}$ and $\langle\, \boldsymbol{h} \,\rangle_Y$.

Also, the ratio of the Joule losses into the total electromagnetic power in the cell seems to be a great indicator of the discrepancy between $\boldsymbol{H}$ and $\langle\, \boldsymbol{h} \,\rangle_Y$ for magnetically linear problems, but not for nonlinear ones.

The most important take-away of this experiment is that the necessity to avoid using $\langle\, \boldsymbol{h} \,\rangle_Y$ seems quite limited in the simulation of magnetic cores, except maybe at very high frequencies. However, implementing one of the proposed $\boldsymbol{H}$ upscaling methods is a good idea when working with B-conforming formulation at high frequencies, at least to compare it to $\langle\, \boldsymbol{h} \,\rangle_Y$, as it is currently the only reliable way to guaranty that $\boldsymbol{H}$ is correctly upscaled.

3.2 Multiscale validation on magnetoquasistatic 3D problems

This section is devoted to the validation of the accuracy and properties of the proposed multiscale method. Although the development of our implementation went through many intermediate steps, including static and low-frequency resolutions of 2D and 3D problems, we present the results corresponding to two of the more challenging settings that we could successfully solve for. The emphasis is made on the precise description of the results and the in-depth study of the behavior of the multiscale method in order to show its capabilities and limits, rather than the multiplication of the settings examples.

The settings used are 3D magnetoquasistatic problems in time transient regime, using linear and nonlinear magnetic material laws in the heterogeneous material. The geometry used is that from the example in the first chapter (see Section 1.4), the geometry of the reference problem and an example of mesh for the macroscopic problem are shown in Figure 3.14. The tests are preformed with the B-conforming formulation at relatively high frequencies, between 100 kHz and 10 MHz, in order to validate our theory related to the upscaling of the magnetic field strength.

The section is organized as follows. First, the accuracy of HMM is validated for the two aforementioned settings. Then, the convergence properties of the multiscale method with the macroscopic field discretization and the decrease of the cell size are studied. Finally, the power of the method is illustrated on two problems impossible to solve with single scale FEM and some conclusions are drawn.

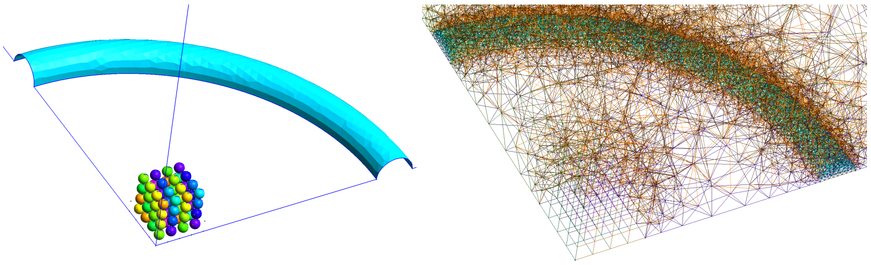

Figure 3.14: One eighth of the geometry used for the multiscale accuracy validation (left), and the mesh for the macroscopic problem (left). The problem is the same as the example resolution in Section 1.4, the magnetic core is made of 512 magnetic and conducting balls, but 64 are meshed thanks to the symmetries of the geometry. The heterogeneous domain has a real width of 800 μm, the cell size is 100 μm and torus stranded coil with circular section of radius 100 μm is fed with an imposed sinusoidal current source. The big radius of the inductor is 1.5 mm. The homogenized core is generally meshed with 64 hexahedric elements (like in the figure), although any type and size of element could be used.

Integral quantities of interest

Mainly two quantities will be used to monitor the behavior of the solution. The first is the Joule losses power in the magnetic core. On the reference problem, it is computed as:

$$\mathcal{P}_{\text{JL,ref}} = \int_{\Omega_{\varepsilon,h}} \boldsymbol{j} \cdot \boldsymbol{e}. \tag{3.7}$$

On the multiscale problem, it is computed using the upscaled Joule losses density as:

$$\mathcal{P}_{\text{JL,HMM}} = \int_{\Omega_{\text{H},h}} \langle \boldsymbol{j} \cdot \boldsymbol{e} \rangle_Y, \tag{3.8}$$

where $\langle \boldsymbol{j} \cdot \boldsymbol{e} \rangle_Y$ is the Joule losses density in the cell.

The second is the total electromagnetic power in the magnetic core $\mathcal{P}_{\text{em}}$, with expressions slightly different in the reference and multiscale problem. For the reference problem, it is written

$$\mathcal{P}_{\text{em,ref}} = \int_{\Omega_{\varepsilon,h}} \boldsymbol{h} \cdot \partial_t \boldsymbol{b} \; + \; \boldsymbol{j} \cdot \boldsymbol{e}. \tag{3.9}$$

But in the homogenized domain, there are no currents, so the electric term disappears, and the expression is

$$\mathcal{P}_{\text{em,HMM}} = \int_{\Omega_{\text{H},h}} \boldsymbol{H} \cdot \partial_t \boldsymbol{B}. \tag{3.10}$$

The Joule losses are naturally taken into account in the homogenized magnetic law via some dynamic hysteresis. But this can only be noticed when it is not negligible in comparison to the magnetic term.

To note, the accuracies numbers given in the next sections are computed using a reference with the same type of formulation as the multiscale one, the B-conforming formulation[1].

---

[1] There is actually a large difference ($\approx$ 30%) between the Joule losses predicted by our implementatio of

The results will show the accuracy of the multiscale method compared to using the state-of-the-art single scale formulation.

3.2.1 Transient linear results

The goal of the first test is to prove numerically that the 3D multiscale formulation requires using the proposed $\boldsymbol{H}$ upscaling methods when there are strong eddy currents loops in the conducting inclusions, as described in Chapter 2. This hypothesis has already been validated in 2D in the course of this thesis, the results are available in [112].

We observed that the responsible phenomenon increases with the frequency, with the diameter and volume fraction of the inclusion in the cell, and with the conductivity. So in order to demonstrate a large difference between using the volume average and the other upscaling methods, the following test is conducted on copper inclusions of conductivity 59.7×10^6 S.m^{-1} and of linear magnetic permeability $\boldsymbol{\mu} = \mu_0$. Additionally, the radius of the sphere is set to 45 μm, making the volume fraction of the inclusion increase from $\simeq 27\%$ to $\simeq 38\%$ compared to the other tests.

Finally, the source is an imposed current in the stranded inductor following the definition (1.85), with the frequency set to $f = 10$ MHz and a total current set to $I(t) = 1000\sin(2\pi f t)$ A. The skin depth δ is approximately 21 μm, so the skin effect is significant (the ball radius is 45 μm). The macroscopic mesh has 29k elements, the cell meshes have 19k elements, and the simulation is run during 225 ns (2.25 periods) with 160 TS per period.

Linear, $\mathcal{P}_{\text{JL}}$

Upscale method	$\langle \boldsymbol{h} \rangle_Y$	$\langle \boldsymbol{h} \rangle_{\partial Y_\parallel}$	$\langle \boldsymbol{h} \rangle_{\gamma_Y}$	$\langle \boldsymbol{h} - \boldsymbol{m}_\varepsilon \rangle_Y$	$\langle \boldsymbol{h} - \boldsymbol{h}_c \rangle_Y$
L2PE (%)	31.1	0.67	0.97	1.13	0.48
IPE (%)	26.1	0.68	0.98	1.11	0.45

Linear, $\mathcal{P}_{\text{em}}$

Upscale method	$\langle \boldsymbol{h} \rangle_Y$	$\langle \boldsymbol{h} \rangle_{\partial Y_\parallel}$	$\langle \boldsymbol{h} \rangle_{\gamma_Y}$	$\langle \boldsymbol{h} - \boldsymbol{m}_\varepsilon \rangle_Y$	$\langle \boldsymbol{h} - \boldsymbol{h}_c \rangle_Y$
L2PE (%)	28.0	0.66	1.08	1.90	1.29

Table 3.3: Integrated percentages of error ($L^2([0, T])$ (3.2) and integral (3.1)) on Joule losses and total electromagnetic power of the homogenized domain, computed from the solutions presented in Figures 3.15 and 3.16.

The computation of the reference solution took 15h on a personal computer[2]. The HMM resolutions were made using 48 cores on the GRICAD cluster, it took around 20h for

---

the B-conforming and H-conforming references on this problem. But this does not impact our validation, because this error is presumably not associated with the homogenization process.

[2] The PC had 16 Go of RAM and the CPU model is Intel(R) Core(TM) i5-10500 CPU @ 3.10GHz.

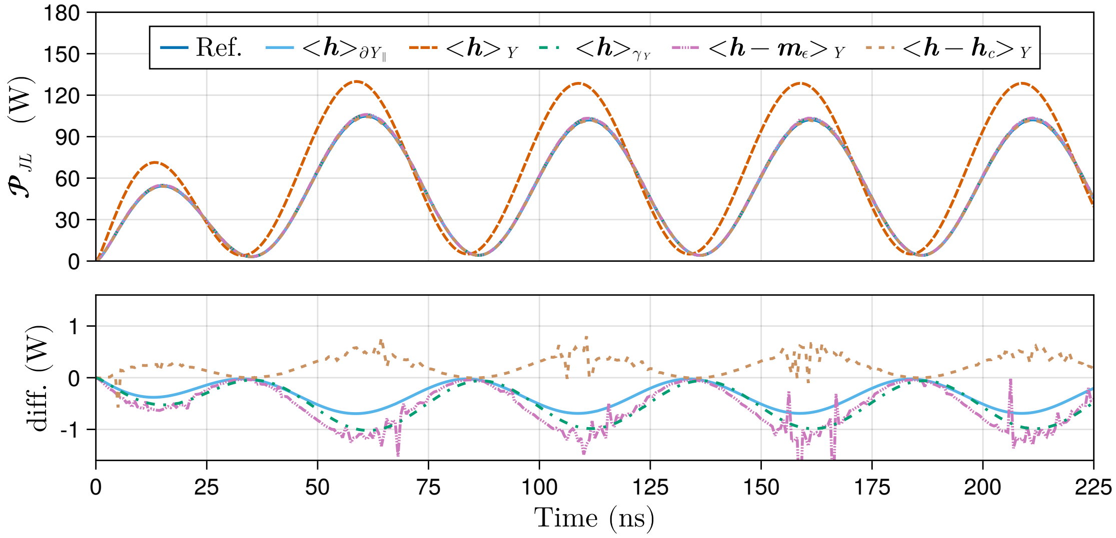

Figure 3.15: Comparison of the Joule losses power in the homogenized domain predicted by the HMM resolution, using different upscaling methods for $\boldsymbol{H}$ and using **magnetically linear** copper inclusions. The difference with respect to the reference is given for the correct upscaling methods in the bottom plot. All methods have an excellent accuracy, except the volume average $\langle\, \boldsymbol{h} \,\rangle_Y$, which has significant phase and magnitude offsets with the reference (it is thus not plotted in the bottom axis). The upscaling methods using FEM projections ($\langle\, \boldsymbol{h} - \boldsymbol{m}_\varepsilon \,\rangle_Y$ and $\langle\, \boldsymbol{h} - \boldsymbol{h}_c \,\rangle_Y$) result in poorer convergence of the multiscale problem.

the upscaling techniques without FEM projections, 30h using $\langle\, \boldsymbol{h} - \boldsymbol{m}_\varepsilon \,\rangle_Y$ and 44h using $\langle\, \boldsymbol{h} - \boldsymbol{h}_c \,\rangle_Y$. The multiscale resolution were slower than the reference on this problem due to the fairly small amount of balls. HMM is not necessary here, but using such reference problem is necessary for validation purpose. The upscaling methods using FEM projections are significantly slower than the others here, respectively 50% slower for $\langle\, \boldsymbol{h} - \boldsymbol{m}_\varepsilon \,\rangle_Y$ and 120% slower for $\langle\, \boldsymbol{h} - \boldsymbol{h}_c \,\rangle_Y$.

Several field maps of the solutions are shown in Figure 3.19. The Joule losses dissipated in the homogenized domain and its total electromagnetic power are respectively plotted in Figures 3.15 and 3.16, and the associated integrated percentages of error are given in Table 3.3.

The results demonstrate an excellent accuracy of HMM when one of the four proposed upscaling method is used. Indeed, the error on Joule losses over the two first periods reaches 26.1% using the volume average, while it is between 0.45% and 1.11% for the others methods. These results are similar to that given in [112] in 2D. In our experience, the differences between the correct methods are not representative of a general behavior: the volume average with correction projection $\langle\, \boldsymbol{h} - \boldsymbol{h}_c \,\rangle_Y$ is the most accurate here, but this is not true in general.

Six B-H curves of the upscaled law are displayed in Figure 3.17, three with a correct upscaling method and three with the volume average method. When using the latter, the upscaled law is actually $\boldsymbol{H}(\boldsymbol{B}) = \nu_0 \boldsymbol{B}$. Indeed, there is $\boldsymbol{\nu} = \nu_0$ everywhere in Y,

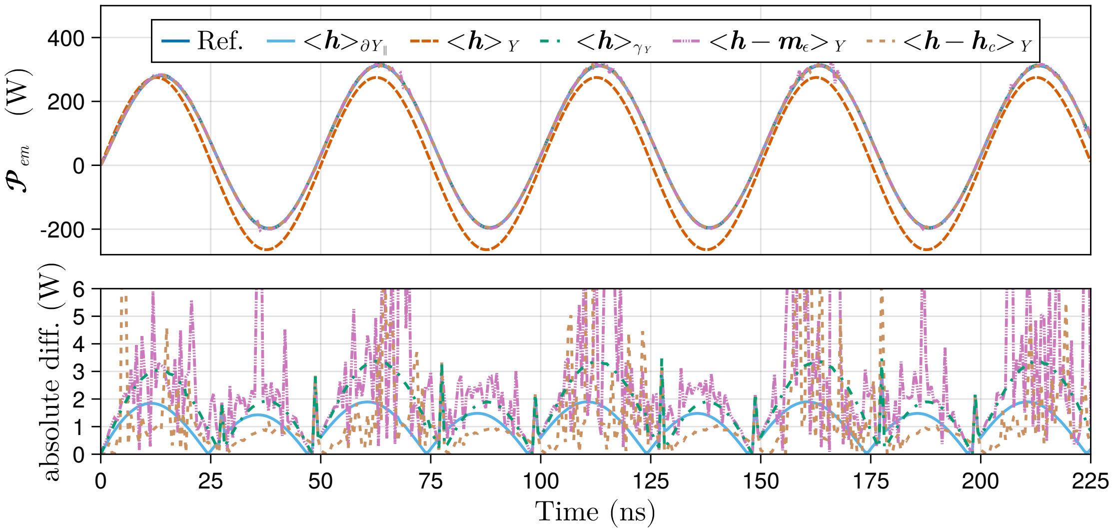

Figure 3.16: Comparison of the electromagnetic power in the homogenized domain predicted by the HMM resolution, using different upscaling methods for $\boldsymbol{H}$, with linear magnetic law in the balls. The observations are similar to that on Joule losses in Figure 3.15. The difference of the volume average is too large compared with the others, so it is not plotted in the bottom axis.

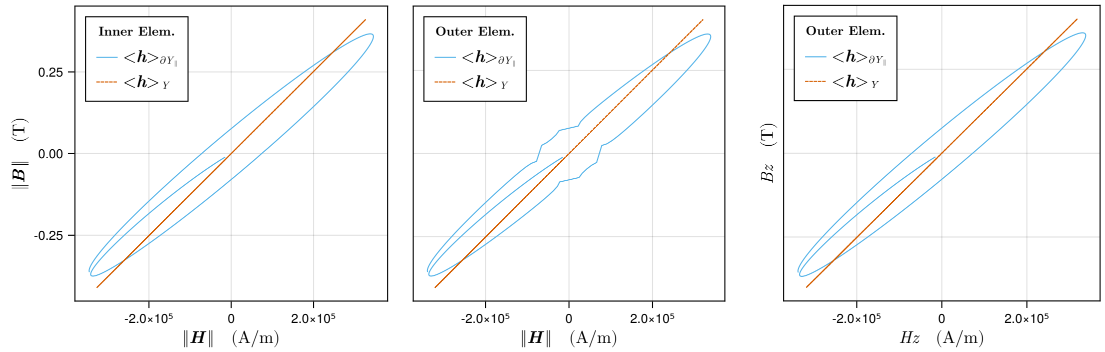

Figure 3.17: B-H curves of two cell problems in HMM with linear magnetic law in the cell. There are two $\|\boldsymbol{B}\|$-$\|\boldsymbol{H}\|$ on the left, and one H_z-B_z curve on the right. The curves with the norms are multiplied by the sign of the z component (because the homogenized domain is exited by a field of direction close to $\boldsymbol{e}_z$, as the inductor is in the $z = 0$ plane). The "Inner" cell problem is that of the element the closer to the center of Ω_H, and the "Outer" one is the corner of Ω_H. The curve in the middle is not smooth, due to a slight rotation of the field when changing direction and to the phase offset between $\boldsymbol{B}$ and $\boldsymbol{H}$. But each field component evolves smoothly in time, e.g. the H_z and B_z components plotted in the right curve.

so $\langle\, \boldsymbol{h}\, \rangle_Y = \langle\, \nu_0 \boldsymbol{b}\, \rangle_Y = \nu_0 \langle\, \boldsymbol{b}\, \rangle_Y = \nu_0 \boldsymbol{B}$. When using the correct definition for $\boldsymbol{H}$, the curve becomes ellipse, meaning that strong dynamic hysteresis appears. In average, the magnetic reluctivity is increases due to high self-inductance of the inclusions which creates a magnetization opposed to the imposed magnetic field.

Finally, the convergence criteria for the multiscale resolutions are shown in Figure 3.18. As already mentioned, the macroscopic problem must be iteratively solved even if the

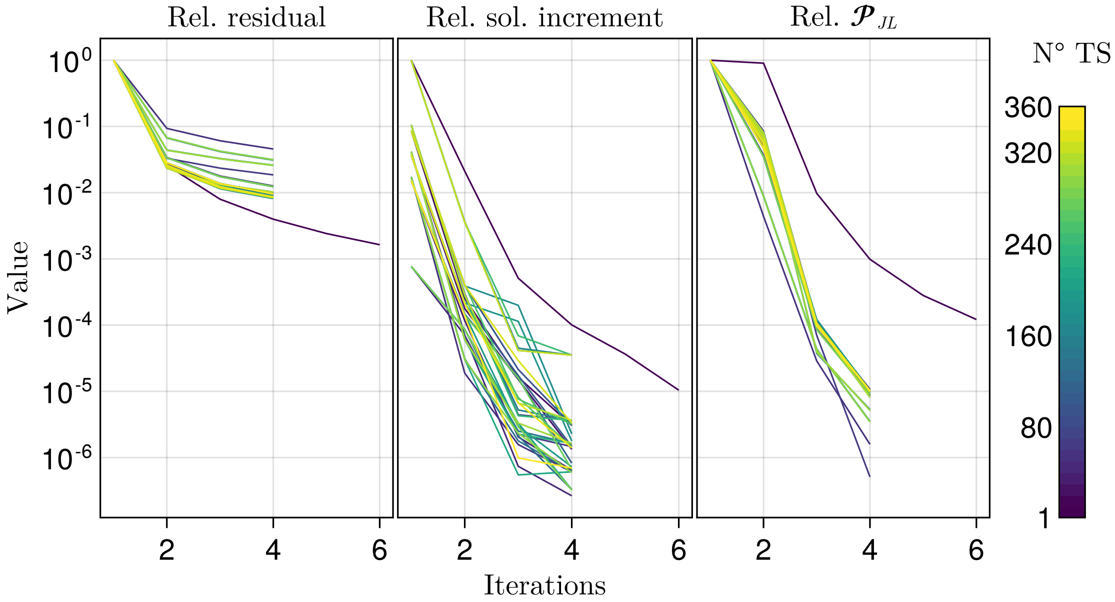

Figure 3.18: Convergence of the macroscopic problem of HMM with linear cell magnetic law. The macroscopic relative residual, the relative increment of the macroscopic solution and the relative increment of the Joule losses are plotted over the iteration index, for one tenth of the time steps (one every ten). The stopping criteria effectively used is Rel $\mathcal{P}_{\mathrm{JL}} < 2.5 \times 10^{-5}$ during the first 5 time steps (fast convergence stop), and Rel $\mathcal{P}_{\mathrm{JL}} < 5.0 \times 10^{-4}$ from the sixth time step (slow convergence stop). The graph shows that it is impossible to find a stopping threshold valid far all the time steps on the relative macroscopic residual or relative increment of the macroscopic solution. The stopping criteria using $\mathcal{P}_{\mathrm{JL}}$ relates to the convergence of the losses in the cell problems averaged over all the homogenized domain, it is a multiscale stopping criterium.

cell constitutive laws are linear, because the macroscopic law depends on the eddy currents, which depend on the downscaled $\partial_t \boldsymbol{B}$ and previous time step cell solution $\boldsymbol{a}^n$. From our observations, the relative variation of the Joule losses power $\mathcal{P}_{\mathrm{JL}}$ is the best convergence criterion for the multiscale problem. Indeed, the macroscopic residual and relative solution increment converge to different values depending on the time step and difficulty of convergence, so it is hard or even impossible to find a threshold indicating convergence based on these quantities. On the other hand, the relative variation of $\mathcal{P}_{\mathrm{JL}}$ is a sensitive indicator, which usually steadily decreases when the iterations converge. It can be set depending on the desired accuracy on $\mathcal{P}_{\mathrm{JL}}$. Indeed, choosing the threshold on the relative increment of $\mathcal{P}_{\mathrm{JL}}$ between $1e^{-4}$ to $1e^{-5}$ will likely lead to commit an error smaller than $\approx 1e^{-3}$ on $\mathcal{P}_{\mathrm{JL}}$ if the convergence is not too slow.

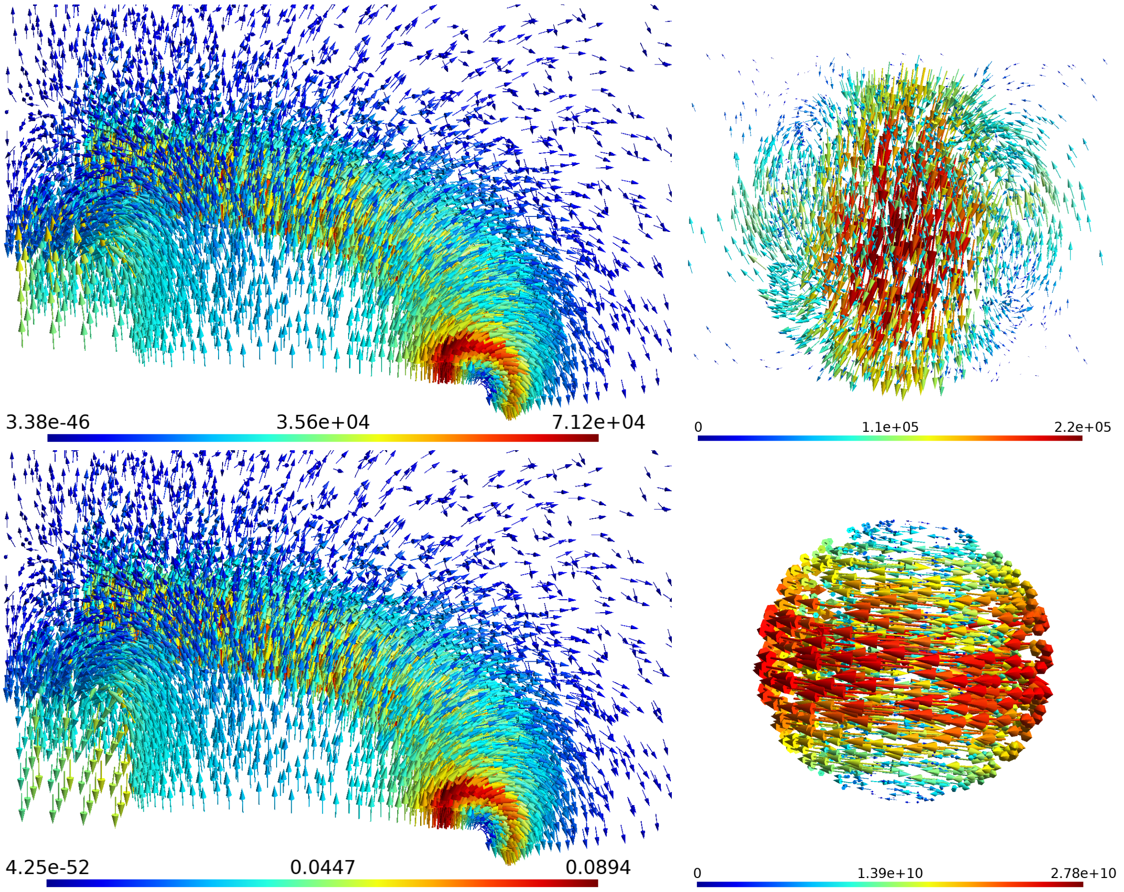

Figure 3.19: Fields maps at time step TS$= 81$, just after the source magnetic field changed direction, $\partial_t \boldsymbol{B}$ is directed upward. There are the macroscopic $\boldsymbol{H}$ (top left) and $\boldsymbol{B}$ (bottom left) plotted in Ω (all the outer air is not displayed, but Ω_{H} and Ω_s are visible). On the right, there are the maps of $\boldsymbol{h}$ (top) and $\boldsymbol{j}$ (bottom). The map of $\boldsymbol{b}$ is the same as $\boldsymbol{h}$, they only differ by μ_0. Macroscopically, the phase delay of $\boldsymbol{B}$ with respect to $\boldsymbol{H}$ make them point in opposite direction in Ω_{H}. In the cell, $\boldsymbol{h}$ points upward out of the ball, even if in volume average, $\boldsymbol{b} = \frac{1}{\mu_0}\boldsymbol{h}$ points downwards due to the remaining field in the ball, resulting from the confined currents created by the strong $\partial_t \boldsymbol{B}$.

3.2.2 Transient nonlinear results

The goal of the next test is to prove numerically the capability of HMM to solve a hard magnetoquasistatic problem which cumulates most of the difficulties encountered in the simulation of magnetic cores. We solve a transient 3D problem on a heterogeneous material featuring nonlinear magnetic laws in the inclusions with the objective to accurately predict the Joule losses in the core. The simulation parameters are chosen to see some skin effect and magnetic saturation in the inclusions. This will also push our numerical implementation to the limits in terms of difficulty of multiscale nonlinear convergence.

The magnetic core is made of conducting metal balls with a conductivity of 10×10^6 S.m^{-1}. The magnetic law in the ball follows the Fröhlich-Kennelly law (1.82) (the $\boldsymbol{h}(\boldsymbol{b})$ law is given in equation (A.1)) with maximum permeability of $\mu_{r,\max} = 100$ and saturation induction of $B_s = 1.5$ T. The radius of the sphere is set to 40 μm, so the volume fraction of the inclusion is $\simeq$ 27%. The source frequency is set to $f = 10$ MHz and its total intensity to $I(t) = 1000 \sin(2\pi f t)$ A. The skin depth δ varies between 29.1 μm and 291 μm depending on the saturation of the magnetic law, so the skin effect is noticeable but not always significant. The macroscopic mesh has 29k elements, the cell meshes have 18k elements, and the simulation is run during $4.1\overline{6}$ μs (1.25 periods) at minimum 160 TS per period, the time step can be refined via adaptive time stepping.

Adaptive time stepping and relaxation factor research are implemented on the macroscopic problem, as follows. If the nonlinear loop diverges at a TS, it is reset (the simulation restarts at the previous TS) and the time delta Δt is refined (divided by two), but not below one fourth of the initial Δt. If a NL loop converged easily, in the minimum number of iterations, Δt is multiplied by 1.1 to coarsen the time discretization at the next time step, but Δt cannot get bigger than the initially prescribed value.

The relaxation of the NL loop is activated if the macroscopic residual increases at an iteration, for all iteration of the current time instant, but not the next ones. Up to five relaxation factors are tested, $\omega = 1$, 0.75, 0.5, 0.25 and 0.005, in this order. If a relaxation factor increases the macroscopic residual, the relaxation research is stopped, as smaller ω won't yield smaller residual in our experience. To note, this method is quite costly. Indeed, it is necessary to downscale $\boldsymbol{B}$ and upscale $\boldsymbol{H}$ for each relaxation factor to test, because the macroscopic residual is computed using $\boldsymbol{H}$, that can only be updated using the cell problems.

The following results were obtained. The computation of the reference solution took 55h on a personal computer. The information of the resolutions with the Different $\boldsymbol{H}$ upscaling methods are given in the following table:

Method	Cluster	T_f (μs)	TSs	WallTime (hours)
$\langle \boldsymbol{h} \rangle_{\partial Y_\parallel}$	GRICAD	4.17	200	40
$\langle \boldsymbol{h} \rangle_{Y}$	GRICAD	1.15	99	48
$\langle \boldsymbol{h} \rangle_{\gamma_Y}$	GRICAD	0.19	31	8
$\langle \boldsymbol{h} - \boldsymbol{m}_\varepsilon \rangle_{Y}$	Nic5	4.17	200	21
$\langle \boldsymbol{h} - \boldsymbol{h}_c \rangle_{Y}$	Nic5	2.47	212	48

The expected number of time steps (without adaptive time stepping) is 200, and the final time was $T_f = 4.1\overline{6}\ \mu$s. The resolutions were made using 48 cores on the GRICAD cluster and 32 cores on Nic5, the maximum WallTime (maximum human time over which the program can run) was 48h for both, but these are not comparable between the two clusters because the hardwares are different.

We present these results as is, even if all the methods did not converge properly, because we had not enough time to investigate and fix the issues. The resolution using $\langle \boldsymbol{h} \rangle_{\gamma_Y}$ crashed after only few time steps, the macroscopic nonlinear loop diverges in few iterations, and ends with NaN in the macroscopic solution. The resolutions using $\langle \boldsymbol{h} \rangle_{Y}$ and $\langle \boldsymbol{h} - \boldsymbol{h}_c \rangle_{Y}$ did not finish due to the bad convergence, the use of adaptive relaxation and adaptive time stepping slowed them too much. But the simulations using the $\langle \boldsymbol{h} \rangle_{\partial Y_\parallel}$ and $\langle \boldsymbol{h} - \boldsymbol{m}_\varepsilon \rangle_{Y}$ methods worked fine and gave usable results.

Nonlinear, $\mathcal{P}_{\mathrm{JL}}$

Upscale method	$\langle \boldsymbol{h} \rangle_{\partial Y_\parallel}$	$\langle \boldsymbol{h} - \boldsymbol{m}_\varepsilon \rangle_{Y}$
L2PE (%)	0.23	0.88
IPE (%)	0.19	0.81

Nonlinear, $\mathcal{P}_{\mathrm{em}}$

Upscale method	$\langle \boldsymbol{h} \rangle_{\partial Y_\parallel}$	$\langle \boldsymbol{h} - \boldsymbol{m}_\varepsilon \rangle_{Y}$
L2PE (%)	0.44	0.60

Table 3.4: Integrated percentage of error on Joule losses power and electromagnetic power of the homogenized domain, computed from solution presented in Figures 3.20 and 3.21. The methods that converged, the boundary tangential average $\langle \boldsymbol{h} \rangle_{\partial Y_\parallel}$ and volume average with computation of the magnetization $\langle \boldsymbol{h} - \boldsymbol{m}_\varepsilon \rangle_{Y}$, result in excellent accuracy.

Several field maps of the solutions are shown in Figure 3.24. The Joule losses dissipated in the homogenized domain and its total electromagnetic power are respectively plotted in Figures 3.20 and 3.21, and the associated integrated percentages of error are given in Table 3.4.

The results demonstrate an excellent accuracy of HMM when it converges, the error on $\mathcal{P}_{\mathrm{JL}}$ and $\mathcal{P}_{\mathrm{em}}$ is below 1% then. But the multiscale nonlinear convergence is very challenging here, three methods did not work. To note, our algorithm focuses on not crashing: adaptive time stepping and possible strong relaxation are used to maximize the chances of convergence, but they may slow the resolution a lot.

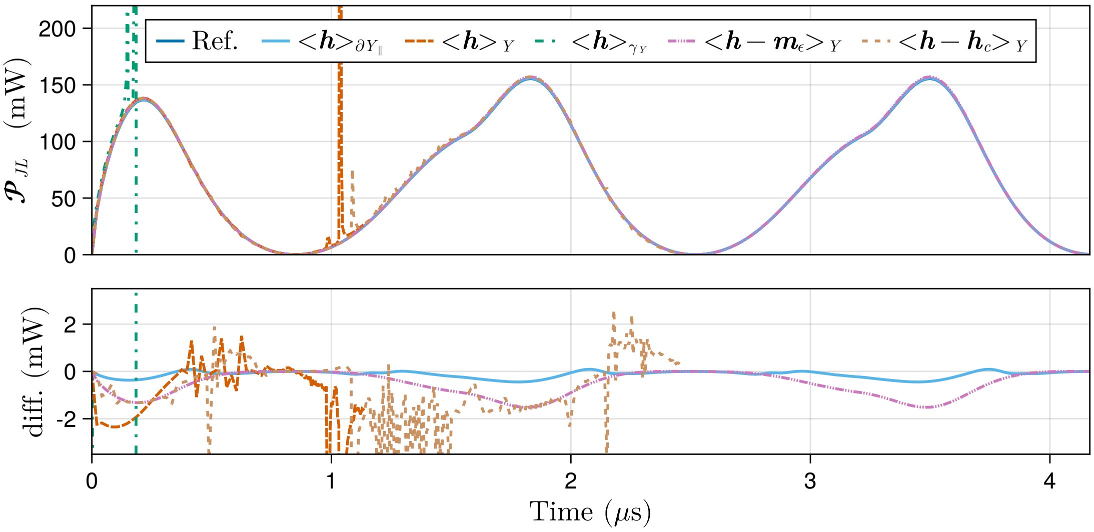

Figure 3.20: Comparison of the Joule losses power in the magnetic core predicted by the HMM resolution, using different upscaling methods for $\boldsymbol{H}$, using **nonlinear magnetic law** in the balls. The $\langle \boldsymbol{h} \rangle_{\gamma_Y}$ method crashed after few time steps, and the $\langle \boldsymbol{h} \rangle_Y$ and $\langle \boldsymbol{h} - \boldsymbol{h}_c \rangle_Y$ were slow due to bad multiscale nonlinear convergence and did not complete the simulation. The two working methods provide smooth and small errors.

The adaptive relaxation of the macroscopic problem is activated when the convergence is bad, and we notice than the lower possible relaxation factor, $\omega = 0.005$, was nearly always chosen. It means that the better residual is obtained by not updating the macroscopic solution to a new value. For this reason, we suspect that the bad convergence is due to errors in the macroscopic problem, probably the accuracy of the numerical computation of the upscaled Jacobian using finite differences on the cell problem.

Four B-H curves of the upscaled law are displayed in Figure 3.22, with the boundary average upscaling method and the volume average method. We notice that the volume average gives relatively correct values, the cell magnetization is not a problem here. There is a saturation of the macroscopic magnetic law due to that of the inclusion one, but it is not very strong because the volume fraction of the inclusion is only $\approx 27\%$.

Finally, the possible convergence indicator for the simulation using the tangential boundary average for the multiscale resolutions are shown in Figure 3.23. Again, the relative variation of the Joule losses power $\mathcal{P}_{\text{JL}}$ is the best convergence criterion for the multiscale problem. Indeed, it is the only one that steadily and monotonously decreases when the iterations converge.

Also, few validation tests were conducted on 2D nonlinear multiscale problems corresponding to the 3D setting above. Only the boundary tangential average was used. Although no clean results are presented here due to time limitations, we can mention that preliminary results indicated good accuracy and similar or better multiscale convergence

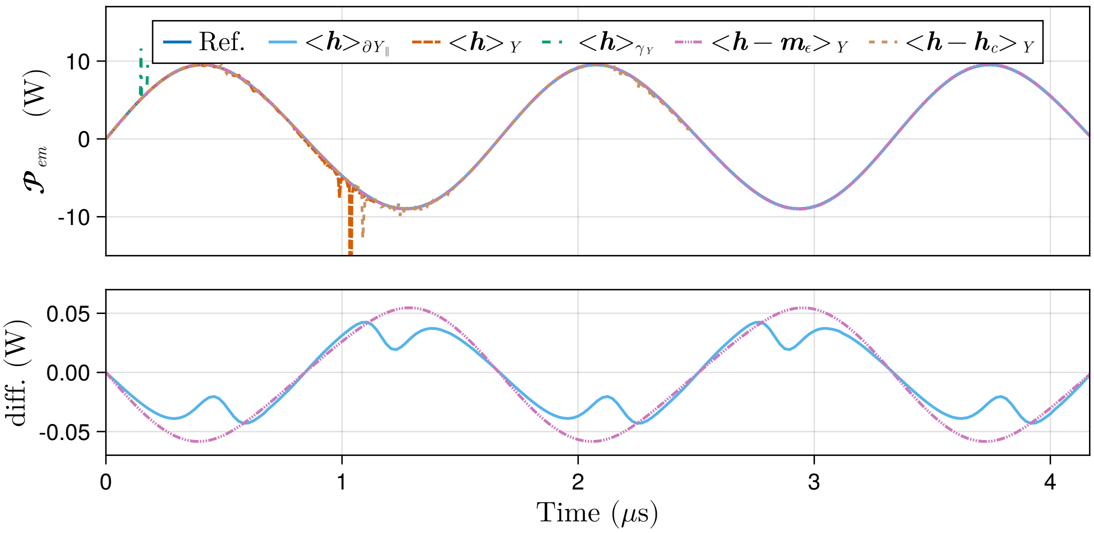

Figure 3.21: Comparison of the electromagnetic power in the magnetic core predicted by the HMM resolution, using different upscaling methods for $\boldsymbol{H}$, with nonlinear magnetic law in the balls. The analysis is the same as that in Figure 3.20.

behavior than in 3D.

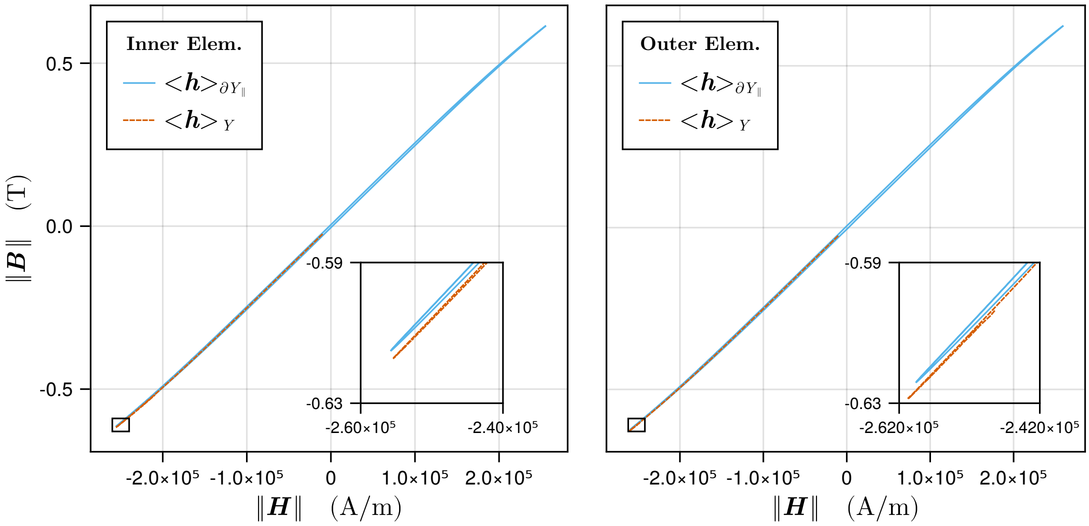

Figure 3.22: B-H curve of two cell problems in HMM with nonlinear cell magnetic law. The "Inner" cell problem is that of the element the closer to the center of Ω_H, and the "Outer" one is the corner of Ω_H. The curve is plotted between the norms of $\boldsymbol{B}$ and $\boldsymbol{H}$, multiplied by the sign of the z component (because the homogenized domain is exited by a field of direction close to $\boldsymbol{e}_z$, as the inductor is in the $z=0$ plane). The curve for $\langle\,\boldsymbol{h}\,\rangle_Y$ is only plotted on the few time steps were it was stable enough.

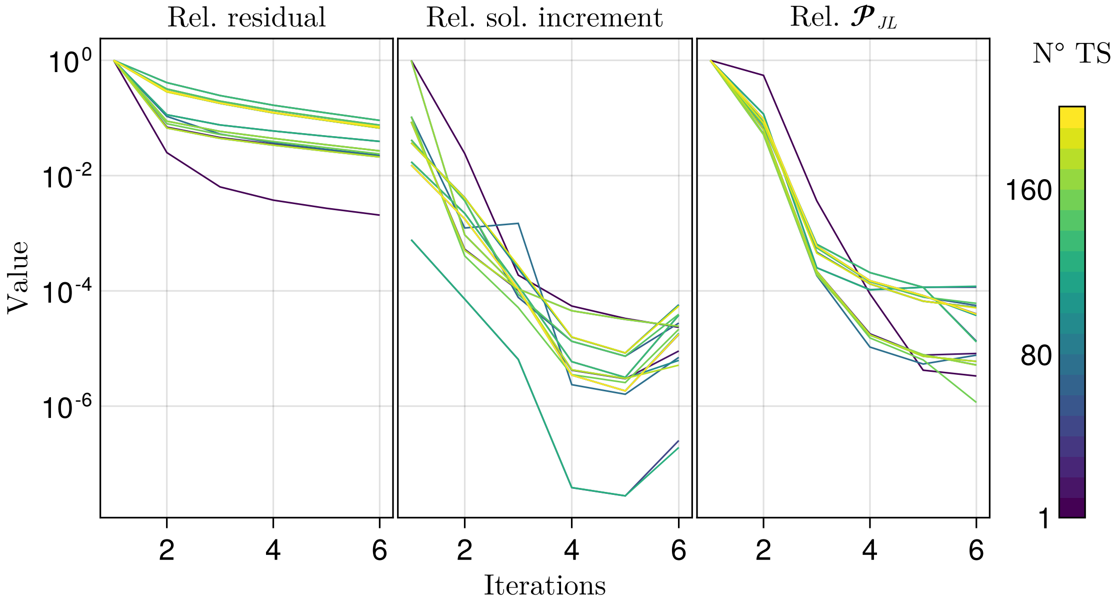

Figure 3.23: Macroscopic Newton-Raphson convergence of HMM with a nonlinear magnetic law in the cell. The relative residual, the relative increment of the solution and the relative increment of the Joule losses power are plotted against the iteration index, for every one time step over ten. The relative increment of the solution goes up between the 5th and the 6th iteration because the Jacobian is computed at iterations 1, 2 and 5, but we observed that it is not a problem. And the residual would decrease again at the iterations 7 and 8 (if the loop was continued, according to other experiments).

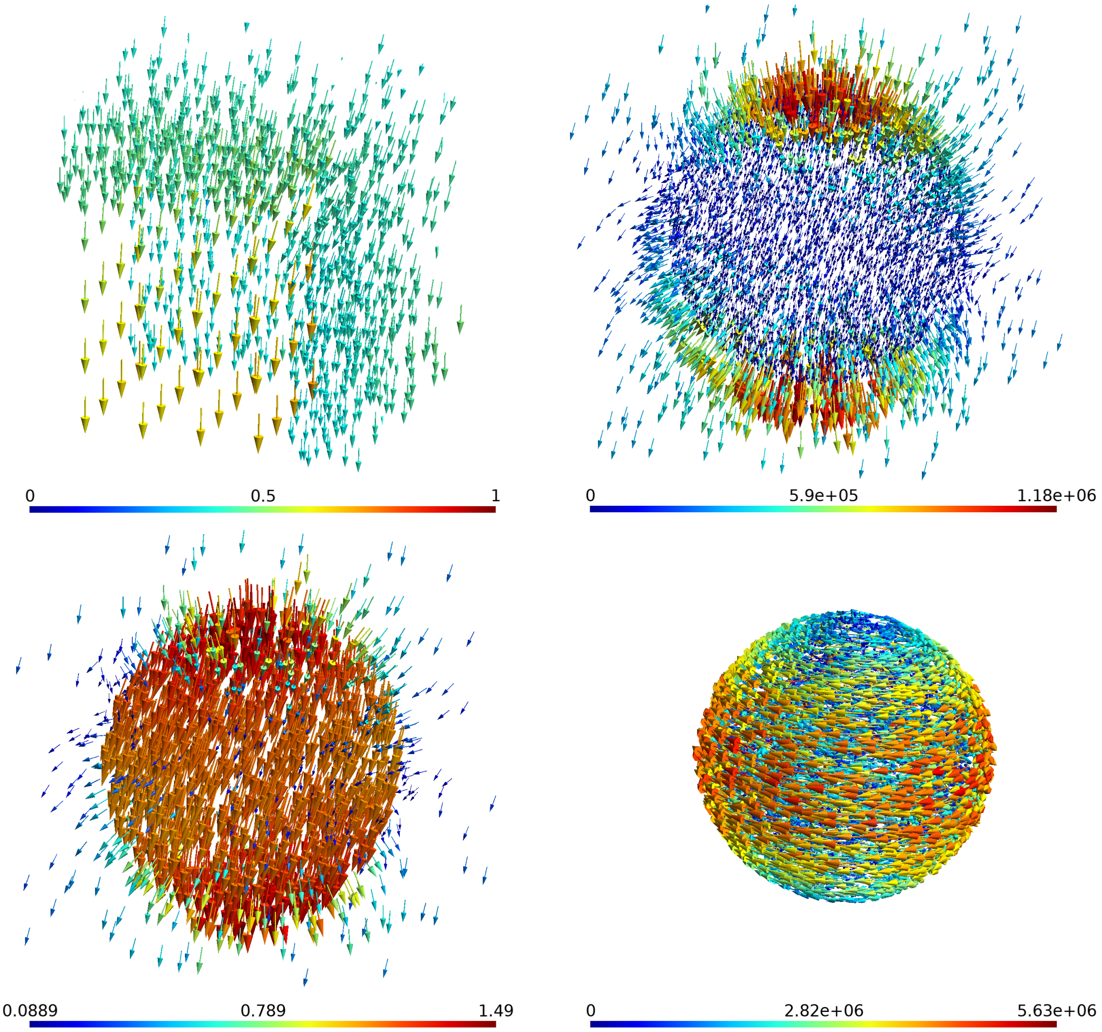

Figure 3.24: Fields maps at time step TS$= 40$, when the saturation is maximal, in Ω_{H} and in the outer cell. There are the macroscopic $\boldsymbol{B}$ (top left), $\boldsymbol{h}$ (top right), $\boldsymbol{b}$ (bottom left) and $\boldsymbol{j}$ (bottom right).

3.2.3 Accuracy convergence of the multiscale method

In the previous section, several HMM resolutions showing the good accuracy of the method were presented. But it is also interesting to validate that the multiscale method has the expected good property of convergence, in order to validate the reliability of the method for latter use on problems without possibility of secondary validation. Only the boundary tangential average $\langle \boldsymbol{h} \rangle_{\partial Y_{\parallel}}$ upscaling method is used in this section.

There are several sources of error in the multiscale numerical modeling, they include:

- the time discretization approximation (theta schema)
- the scale separation approximation
- the spatial discretization of the macroscopic fields (FEM)
- the discretization of the macroscopic material law, which depends on the definition of the cell problem, its temporal and spatial discretization and the upscaling method.

In comparison with the reference FEM model, the multiscale model with HMM adds the scale separation approximation, the space discretization of the points at which the macroscopic material law is estimated (with cell problems), and the accuracy of cell problems.

As explained in Section 3.1, the cell problem accuracy can be validated independently of the multiscale resolution (once the formulation are validated, which we did). But the two other sources of error should be studied to validate the method. This is the goal of this section.

The first source of error is the meshing of the homogenized domain. With our implementation, it is also the number of cell problems, i.e. of computation points of the macroscopic law. It is a parameter of the HMM method, and should be fine-tuned for each problem.

The second, the scale separation approximation, is not really a parameter. Indeed, it is closely related to the smoothness of the macroscopic field relatively to the cell size, so it is fixed for a studied problem. However, it will be treated as a parameter to have an idea of the sensitivity of HMM's accuracy to this source of error.

In order to study the effect of these parameters independently of the others, the previously used problems and parameters will be re-used, such that only the studied parameter varies and the others source of error can be assumed negligible.

Convergence with the refinement of the macroscopic mesh

In theory, the mesh of the homogenized domain should be just fine enough to accurately represent the discretized macroscopic field. Adding unnecessary elements implies solving for more cell problems than needed, which is quite costly.

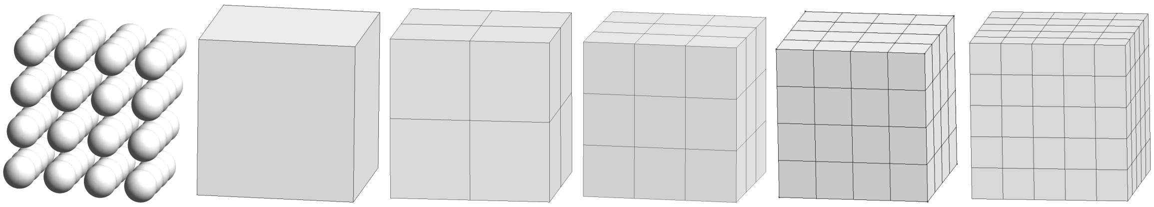

Figure 3.25: Core geometry (leftmost) and homogenized core meshes (right) used to validate the convergence of HMM with the refinement of the macrosocpic mesh. This also illustrate that the number of macroscopic elements is independent of the number of periods of the real geometry.

The impact of the macroscopic mesh density is tested using the geometry and parameters of the nonlinear problem from Section 3.2.2, except that the frequency is decreased to $f = 100$ kHz and the amplitude of the current source to $I = 800$ A (instead of 1000 A before) in order to have better convergence of the multiscale resolution. The macroscopic problem is solved on the meshes shown in Figure 3.25, that contain $N_{Mac} = 1, 8, 27, 64$ and 125 elements in the homogenized domain.

The different Joule losses curves are plotted in Figure 3.26, those of the electromagnetic power in the core are plotted in Figure 3.27, and the integrated percentages of error are given in Table 3.5.

Nonlinear $\mathcal{P}_{\text{JL}}$

N_{Mac}	1	8	27	64	125
L2PE (%)	6.09	1.79	0.32	0.26	2.26
IPE (%)	5.74	1.57	0.29	0.17	1.87

Nonlinear $\mathcal{P}_{\text{em}}$

N_{Mac}	1	8	27	64	125
L2PE (%)	5.58	0.74	0.04	0.40	1.38

Table 3.5: Integrated percentages of error on Joule losses and the total electromagnetic power in the homogenized core, for different number of elements of its macroscopic mesh N_{Mac}. They are computed using the solutions displayed in Figures 3.26 and 3.27. The errors for $N_{Mac} = 125$ are significantly amplified due to the poor multiscale convergence, but they could be greater than for $N_{Mac} = 64$ even with good convergence.

The results demonstrate a pretty good convergence of the multiscale method with the refinement of the macroscopic mesh. Generally, the errors on $\mathcal{P}_{\text{JL}}$ and $\mathcal{P}_{\text{em}}$ are in phase with the estimated signal, and they stay relatively close to zero ($< 2\%$) when the mesh is refined.

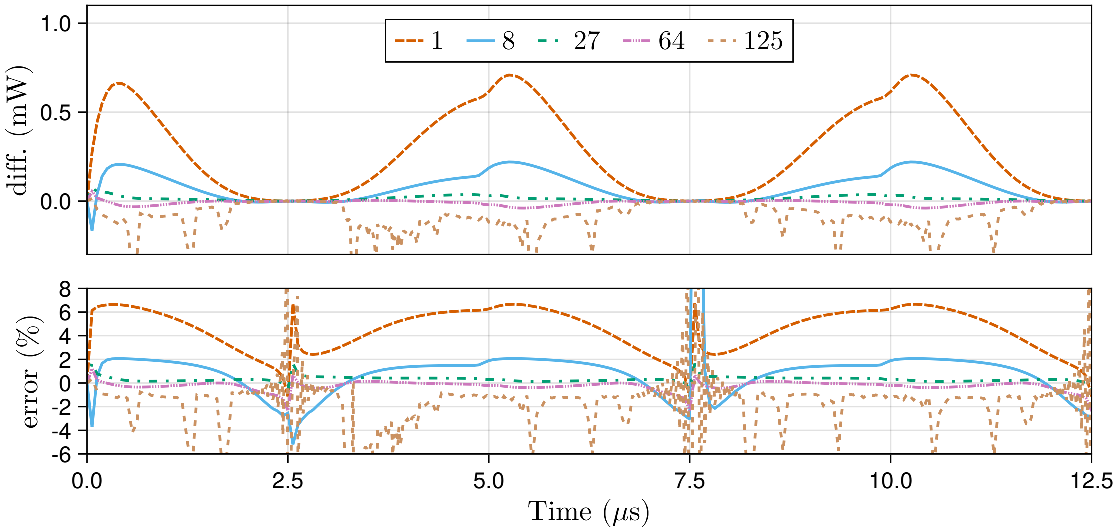

Figure 3.26: Comparison of the Joule losses in the magnetic core predicted by HMM for the different meshes of the homogenized domain displayed in Figure 3.25. The tangential boundary average is used to upscale $\boldsymbol{H}$ and a **nonlinear magnetic law** is considered in the balls. The relative difference decreases with the number of macroscopic elements. It crosses zero between 27 and 64 elements. Although the multiscale nonlinear convergence of the resolution with 125 elements is not as good as the others, the losses values seem to continue to decrease beyond $N_{Mac} = 64$, we cannot affirm that the convergence with the mesh refinement is reached.

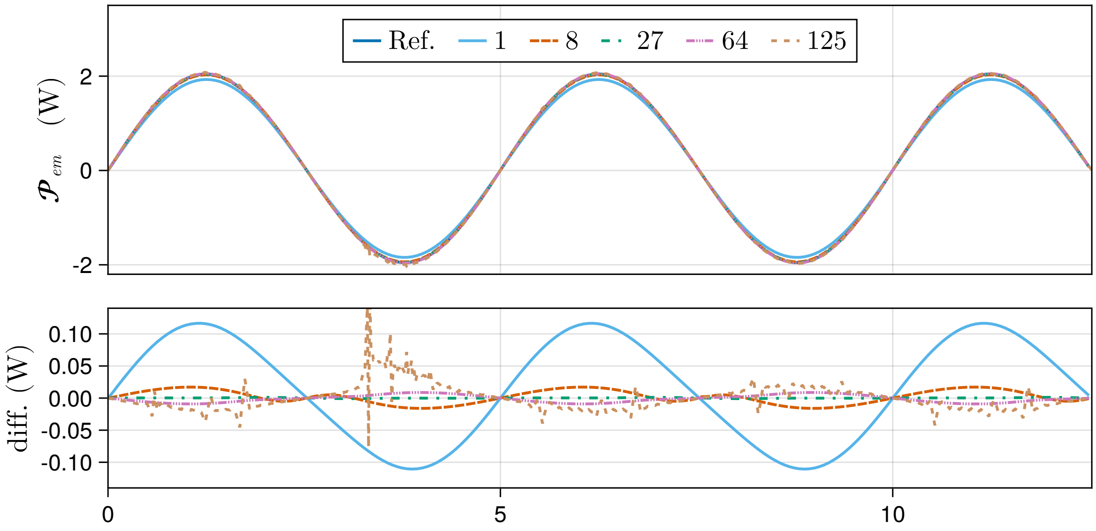

Figure 3.27: Comparison of the core electromagnetic power predicted by the HMM resolution for the different meshes of the homogenized domain presented in Figure 3.25, and the relative differences with the reference solutions. The analysis of the plot is the same as for the Joule losses in Figure 3.26.

Also, we noticed that the convergence of the multiscale problem gets harder when the number of macroscopic elements increases. We think that this is inherent to the resolution algorithm of HMM with the alternated resolution at each scale. As there is a weak coupling of the equations of each scale, it gets harder for all problems to converge together to the multiscale solution, especially when the number of cell problems increases, as they are solved independently. We also noticed that the convergence is sensible to the quality of the upscaled Jacobians.

Convergence with respect to the size of the cell

The accuracy of homogenization methods should increase with the redundancy in the solution. For HMM, it means with better compliance with the scale separation hypothesis, which is the augmentation of the number of spatial period of the solution for a fixed macroscopic variation. Indeed, the slower the macroscopic field varies from cell to cell, the better the scale separation is. In practice, the hypothesis is better satisfied if a larger number of periodic cells fit in a macroscopic element.

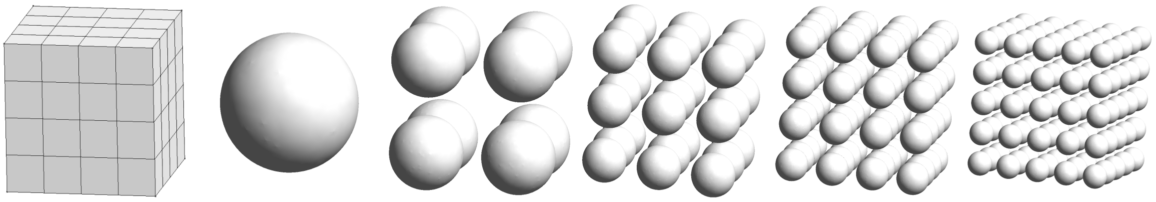

Figure 3.28: One eighth of the homogenized core mesh (leftmost) and core geometries (right) used to validate the convergence of HMM with ε, the size of the spatial period of the material. All cores have a total width of 800 μm. The cell sizes are 400, 200, 133, 100 and 80 μm, so there are respectively 8, 64, 216, 512 and 1000 balls in total in the core (only one eighth are meshed). This also illustrates that the size of the macroscopic elements is independent of the cell size ε, it can be bigger or smaller (HMM is only useful and likely to be accurate if ε is smaller than the macroscopic elements size).

So, what one has to do to validate this convergence is decreasing the cell size ε for a fixed macroscopic domain. Indeed, in our problem, if the size and shape of the magnetic core do not change, the amount of magnetic material do not either because the volume fraction of the inclusion does not change with the cell size. So the macroscopic field map should not vary much. Only the cell solutions and Joule losses will.

We conducted an experiment of convergence of the HMM method with the cell size using a linear magnetic law in the inclusions with a relative permeability of $\mu_r = 100$. The frequency is $f = 500$ kHz and the conductivity is $\sigma = 10 \times 10^6$ S.m^{-1}. The size of the magnetic core is fixed to 800 μm and its macroscopic mesh is fixed with 64 elements. The reference and HMM problems were solved for the five magnetic cores shown in Figure 3.28, with the cell sizes $\varepsilon = 400, 200, 133, 100$ and 80 μm respectively.

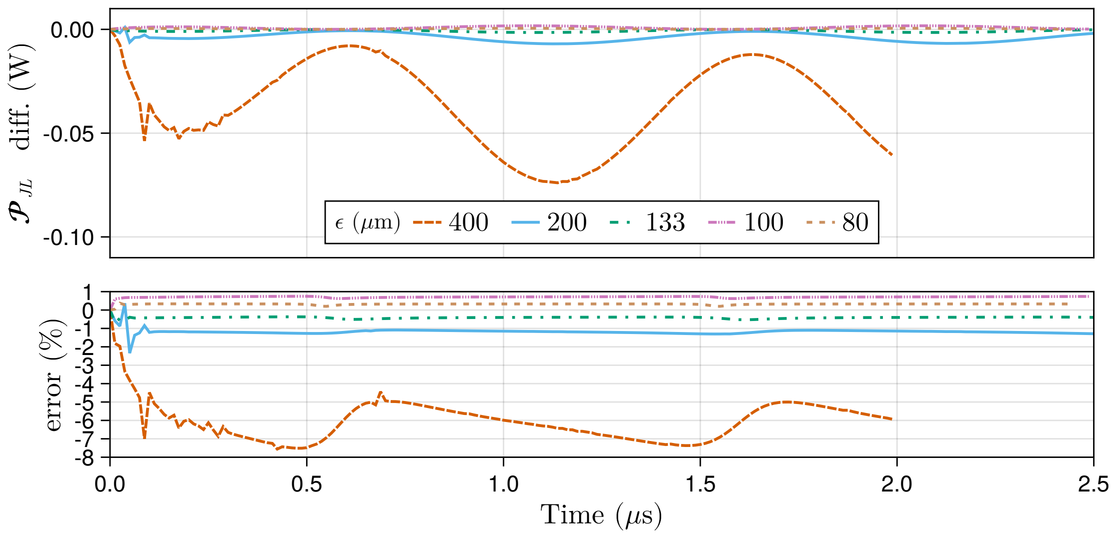

Figure 3.29: Comparison of the Joule losses in the magnetic core predicted by HMM for different cell sizes ε. The boundary tangential average is used to upscale $\boldsymbol{H}$, and the **linear magnetic law** is used in the balls. The convergence with ε is excellent with an error which is below 0.3% for ten periods of the periodic material (in each direction), that is $\varepsilon = 80\mu$m. Some instability in the multiscale problem convergence is visible on two curves, it would probably be possible to fix it by changing the NR parameters, but it would not significantly change the result because the problem is driven by the magnetic field, which is correctly computed.

The error and the instantaneous percentage of error on Joule losses in the magnetic core are shown in Figure 3.29, those on the total electromagnetic power are shown in Figure 3.30, and associated the integral percentages of error are given in Table 3.6.

Linear $\mathcal{P}_{\mathrm{JL}}$

ε (μm)	400	200	133	100	80
L2PE (%)	6.14	1.18	0.40	0.71	0.33
IPE (%)	6.08	1.18	0.40	0.71	0.33

Linear $\mathcal{P}_{\mathrm{em}}$

ε (μm)	400	200	133	100	80
L2PE (%)	3.22	0.27	0.07	0.50	0.56

Table 3.6: Integrated percentage of error on Joule losses and total electromagnetic power in the homogenized domain, computed from solution presented in Figures 3.29 and 3.30. The errors do not monotonously converge to zero when ε goes to 0, but it stays small for smaller ε and the variation decreases with ε. $\mathcal{P}_{\mathrm{JL}}$ seems to converge to zero, and $\mathcal{P}_{\mathrm{em}}$ close to zero ($\approx 0.6\%$ of L^2 percentage error).

The results demonstrate the good convergence of the multiscale method with ε, the size of the cell. Overall, the errors on $\mathcal{P}_{\mathrm{JL}}$ and $\mathcal{P}_{\mathrm{em}}$ are in phase with the estimated signal, and they converge close to zero when ε decreases.

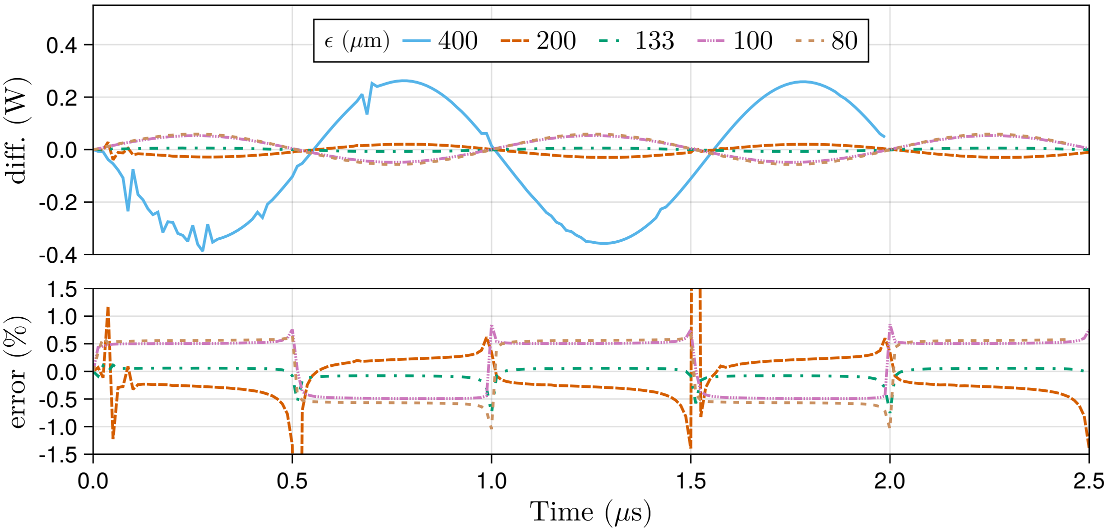

Figure 3.30: Comparison of the electromagnetic power in the magnetic core predicted by the HMM resolution for different cell sizes. The relative difference increases with the decrease of ε. It crosses zero between $\varepsilon = 200$ and 133 μm, and is stabilized close to zero from $\varepsilon = 100$ to 80 μm.

3.2.4 Extrapolation of the results beyond FEM capabilities

In all the previously presented experiments, the accuracy of HMM has been validated using FEM on the complete fine scale geometry as a reference. It thus seems reasonable to use the method on problems for which no FEM reference can be solved, and be confident that the results are still correct.

To illustrate the power of the method to simulate nonlinear heterogeneous periodic domains with numerous periods without convergence problems, simulations were performed with the parameters used in the nonlinear experiments in Section 3.2.3. That is, the frequency is set to $f = 100$ kHz and the amplitude of the current source is set to $I = 800$ A. The cell sizes used are 100 μm, 10 μm and $6.6\overline{6}$ μm. They correspond to respectively 512, 512.000 and 1.728.000 balls in the magnetic core, and full fine scale meshes of approximately 1.8M, 1.8G and 6.2G elements, respectively. The two last problems are thus impossible to solve using FEM.

All three HMM resolutions converged well. The Joule losses power dissipated in the homogenized domain are plotted in Figure 3.31. The losses decrease with the square of the size of the cell, this is expected because the area of the eddy current loops (the section of the inclusions) is divided by the square of the number of inclusions in the plane orthogonal to the magnetic field.

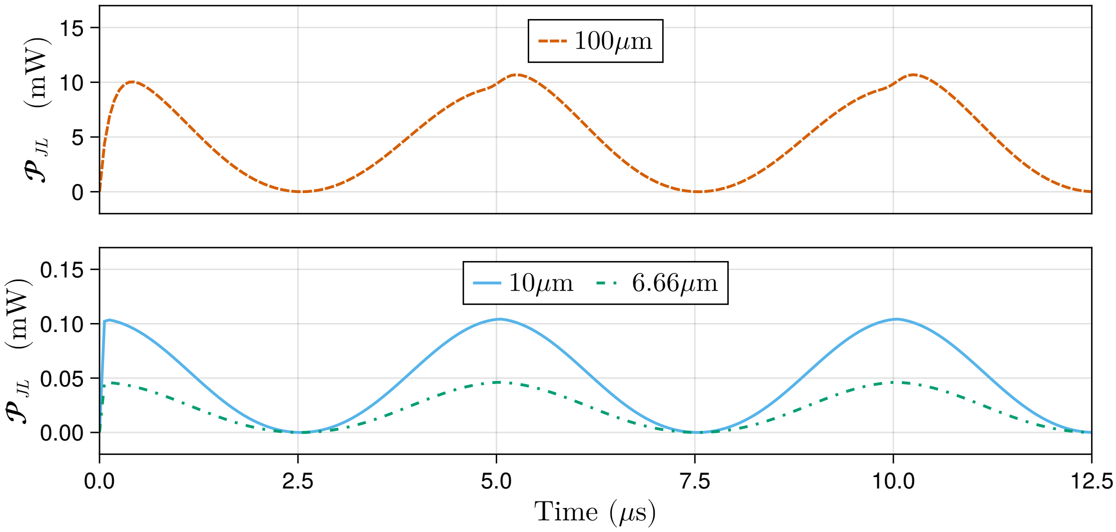

Figure 3.31: Joule losses power in the magnetic core predicted by HMM for cores of total width of 800 μm and cell size of 100, 10 and $6.\overline{66}$ μm. The first case was validated against single scale FEM in Table 3.5 (column 64 elements), but the two others are impossible to solve without a multiscale method. It seems that the steady state regime is reached in few time steps and the losses curve is closer to a pure sinus for $\varepsilon = 10$ and $6.\overline{66}$ μm, this is due to lower self-inductance of the inclusions.

Summary

In this chapter, several numerical experiments were conducted to validate the formulations and upscaling techniques introduced in the previous chapter.

In the first part, the accuracy of both the H and B-conforming formulations of the cell problem were validated using the chained cell problems method. Additionally, the comparisons of the different methods to upscale the magnetic field strength demonstrated the possible discrepancy between the volume average and the other four proposed methods, which take into account the macroscopic magnetization created by the eddy current in the cell. A parametric study of the discrepancy between the macroscopic magnetic field and the volume average of the cell one was made, helping to understand when the volume average should be avoided. To note, the computed error maps would highly depend on the geometry of the cell problem, especially the size of the inclusions.

In the second part, the behavior of the multiscale modeling using HMM implemented with the proposed B-conforming formulation has been studied. The accuracy of the method, as well as other key properties of HMM, were demonstrated on 3D transient problems with linear and nonlinear magnetic laws. It was observed that avoiding using the volume average upscaling method is not always necessary, especially in the simulation of magnetic cores with small Joule losses. The tests shown a difficult multiscale convergence of HMM when there is a nonlinear magnetic law in the inclusions. It was observed that the different upscaling methods provide different convergence behaviors, but this could change if the instabilities are due to an unstable computation of the Jacobian of the upscaled law with finite differences. In this case, formal derivation techniques, implemented using the adjoint state method on the cell problem resolution, could lead to other convergence behavior for the different upscaling methods. But in the meantime, the results of this thesis suggest that the tangential boundary average offers the best compromise between correctness, cost of computations and stability of the multiscale convergence.

General conclusions

This thesis is dedicated to the improvement of multiscale modeling techniques for magnetoquasistatic problems. These techniques are often used to simulate electrical engineering devices involving heterogeneous materials such as coils and magnetic cores. Our two main objectives were to demonstrate the capabilities of the existing HMM method to handle 3D nonlinear transient problems, and to find a reliable way of upscaling the magnetic field strength to enable the use of B-conforming formulations.

In the first chapter, we recalled the standard model of electromagnetism in the magnetoquasistatic regime, which is used to model devices up to medium frequencies in electrical engineering. We detailed how the different formulations of the equations can be implemented numerically using the finite element method. The method was applied for the simulation of a periodic magnetic core to show its capabilities, and its limitations on geometries featuring heterogeneous materials.

In the second chapter, a magnetoquasistatic multiscale framework is derived step by step assuming the scale separation between the macroscopic and fine scale variations of the electromagnetic fields, and assuming that the heterogeneous domain is periodic and admits an electrically insulated periodic cell. There are three original contributions improving the model. The first is a new definition for the scale transition relation which is consistent with the classic definition of Maxwell's equations in matter, and with the literature in computational electromagnetics. The second is a detailed derivation of the cell formulations to explain why they correctly implement the downscaling of the macroscopic fields. The third and last is the presentation of four different numerical implementations of the upscaling of the magnetic field strength, including two original ones using FEM projections to compute the magnetization created by the eddy current at the fine scale. These developments extend the use of B-conforming multiscale formulation to problems where fine scale eddy currents result in dynamic hysteresis in the macroscopic magnetic material law.

In the last chapter, we performed numerical experiments to validate the components and expected behaviors of the multiscale formulation. We validated the B-conforming formulation on 3D multiscale transient linear and nonlinear magnetoquasistatic problems. We showed that the accuracy of the method is robust to strong skin effects in the cell and to dynamic hysteresis in the macroscopic magnetic law.

There are numerous open question left for future research. Several perspectives of the second and third chapters followed by general perspectives are given next.

Perspectives on the theoretical multiscale model

The scale transition relation should be extended to non hexahedric and non electrically insulated cells. The further extension to fully conducting periodic media featuring a high conductivity contrast between the interior and exterior of the cell is challenging, it would likely require a new definition for the splitting of the field in the cell giving more freedom to its non-periodic term.

Also, it should be studied how and under which hypothesis the proposed scale transition relation can be reconciled with the existing asymptotic multiscale models. The work of Bouchitté *et al.* on high-frequency problems should be a good starting point. Such study would also likely involve a dimensionless transformation of the cell problem as in Amirat *et al.*, in order to prevent the Joule losses to go to zero when the scale separation parameter ε goes to zero, because the magnetoquasistatic solutions of the cell problem depend on the size of the cell.

Perspectives for the numerical model

The numerical convergence of the multiscale model needs to be improved. It is necessary to study deeper what is the best method to compute the Jacobian of the upscaled laws. Possible fix for this issue include computing the upscaled Jacobians with formal derivation instead of numerical one, possibly implemented with an adjoint state method to differentiate the FEM resolution of the cell problem. It is also possible to use alternatives to the Newton-Raphson method featuring approximation of the Jacobians to stabilize the convergence.

General perspectives

There are other general perspectives which have not been studied at all in this work. Firstly, model order reduction methods should be developed to reduce the computational burden of repeatedly solving all the cell problems, most of which have very similar solutions. Once the method is accelerated enough to scale on macroscopic meshes containing thousands of macroscopic elements, the method can be tested on real world applications. It could be used to model problems with 3D printed materials that have heterogeneous but relatively predictable geometry.

Bibliography

[1] A. Bossavit, “On the homogenization of Maxwell equations,” *COMPEL-The international journal for computation and mathematics in electrical and electronic engineering*, vol. 14, no. 4, pp. 23–26, 1995, Publisher: MCB UP Ltd. [Online]. Available: https://www-emerald-com.sid2nomade-1.grenet.fr/insight/content/doi/10.1108/eb051906/full/html (visited on 02/05/2024).

[2] M. El Feddi, Z. Ren, A. Razek, and A. Bossavit, “Homogenization technique for Maxwell equations in periodic structures,” *IEEE Transactions on Magnetics*, vol. 33, no. 2, pp. 1382–1385, Mar. 1997, Conference Name: IEEE Transactions on Magnetics, ISSN: 1941-0069. DOI: 10.1109/20.582514.

[3] O. Ouchetto, C.-W. Qiu, S. Zouhdi, L.-W. Li, and A. Razek, “Homogenization of 3-D Periodic Bianisotropic Metamaterials,” *IEEE Transactions on Microwave Theory and Techniques*, vol. 54, no. 11, pp. 3893–3898, Nov. 2006, Conference Name: IEEE Transactions on Microwave Theory and Techniques, ISSN: 1557-9670. DOI: 10.1109/TMTT.2006.885082.

[4] G. Meunier, V. Charmoille, C. Guerin, P. Labie, and Y. Marechal, “Homogenization for Periodical Electromagnetic Structure: Which Formulation?” *IEEE Transactions on Magnetics*, vol. 46, no. 8, pp. 3409–3412, Aug. 2010, Conference Name: IEEE Transactions on Magnetics, ISSN: 1941-0069. DOI: 10.1109/TMAG.2010.2044386.

[5] O. Bottauscio and A. Manzin, “Comparison of multiscale models for eddy current computation in granular magnetic materials,” *Journal of Computational Physics*, vol. 253, pp. 1–17, Nov. 2013, ISSN: 0021-9991. DOI: 10.1016/j.jcp.2013.06.037. [Online]. Available: https://www.sciencedirect.com/science/article/pii/S0021999113004671 (visited on 11/29/2021).

[6] O. Bottauscio, V. C. Piat, M. Chiampi, M. Codegone, and A. Manzin, “Nonlinear Homogenization Technique for Saturable Soft Magnetic Composites,” *IEEE Transactions on Magnetics*, vol. 44, no. 11, pp. 2955–2958, Nov. 2008, Conference

Name: IEEE Transactions on Magnetics, ISSN: 1941-0069. DOI: 10.1109/TMAG.2008.2001341.

[7] G. Meunier, A.-T. Phung, O. Chadebec, X. Margueron, and J.-P. Keradec, "Propriétés macroscopiques équivalentes pour représenter les pertes dans les bobines conductrices," *Revue internationale de génie électrique*, vol. 10, no. 6, pp. 675–694, Dec. 2008, ISSN: 1295490X. DOI: 10.3166/rige.11.675-694. [Online]. Available: http://rige.revuesonline.com/article.jsp?articleId=12499 (visited on 01/24/2023).

[8] O. Bottauscio, M. Chiampi, and A. Manzin, "Multiscale modeling of heterogeneous magnetic materials," *International Journal of Numerical Modelling: Electronic Networks, Devices and Fields*, vol. 27, no. 3, pp. 373–384, 2014, ISSN: 1099-1204. DOI: 10.1002/jnm.1937. [Online]. Available: https://onlinelibrary.wiley.com/doi/abs/10.1002/jnm.1937 (visited on 01/16/2023).

[9] I. Niyonzima, R. V. Sabariego, P. Dular, and C. Geuzaine, "Nonlinear Computational Homogenization Method for the Evaluation of Eddy Currents in Soft Magnetic Composites," *IEEE Transactions on Magnetics*, vol. 50, no. 2, pp. 61–64, Feb. 2014, Conference Name: IEEE Transactions on Magnetics, ISSN: 1941-0069. DOI: 10.1109/TMAG.2013.2286413.

[10] I. Niyonzima, "Multiscale Finite Element Modeling of Nonlinear Quasistatic Electromagnetic Problems," English, Publisher: ULiège - Université de Liège, Ph.D. dissertation, Sep. 2014. [Online]. Available: https://orbi.uliege.be/handle/2268/171929 (visited on 01/16/2023).

[11] I. Niyonzima, R. V. Sabariego, P. Dular, K. Jacques, and C. Geuzaine, "Multiscale Finite Element Modeling of Nonlinear Magnetoquasistatic Problems using Magnetic Induction Conforming Formulations," *Multiscale Modeling & Simulation*, vol. 16, no. 1, pp. 300–326, Jan. 2018, ISSN: 1540-3459, 1540-3467. DOI: 10.1137/16M1081609. [Online]. Available: https://epubs.siam.org/doi/10.1137/16M1081609 (visited on 01/23/2024).

[12] P. Dular, J. Gyselinck, C. Geuzaine, N. Sadowski, and J. Bastos, "A 3-d magnetic vector potential formulation taking eddy currents in lamination stacks into account," *IEEE Transactions on Magnetics*, vol. 39, no. 3, pp. 1424–1427, May 2003, ISSN: 0018-9464. DOI: 10.1109/TMAG.2003.810386. [Online]. Available: http://ieeexplore.ieee.org/document/1198490/ (visited on 01/14/2024).

[13] J. Gyselinck, R. Sabariego, and P. Dular, "A nonlinear time-domain homogenization technique for laminated iron cores in three-dimensional finite-element models," *IEEE Transactions on Magnetics*, vol. 42, no. 4, pp. 763–766, Apr. 2006,

ISSN: 0018-9464. DOI: 10.1109/TMAG.2006.872034. [Online]. Available: http://ieeexplore.ieee.org/document/1608318/ (visited on 01/14/2024).

[14] K. Hollaus and J. Schöberl, "Some 2-D multiscale finite-element formulations for the eddy current problem in iron laminates," *IEEE Transactions on Magnetics*, vol. 54, no. 4, pp. 1–16, 2018, Publisher: IEEE.

[15] K. Hollaus, "A MSFEM to simulate the eddy current problem in laminated iron cores in 3D," *COMPEL - The international journal for computation and mathematics in electrical and electronic engineering*, vol. 38, no. 5, pp. 1667–1682, Jan. 2019, Publisher: Emerald Publishing Limited, ISSN: 0332-1649. DOI: 10.1108/COMPEL-12-2018-0538. [Online]. Available: https://doi.org/10.1108/COMPEL-12-2018-0538 (visited on 07/10/2023).

[16] A. Abdulle, E. Weinan, B. Engquist, and E. Vanden-Eijnden, "The heterogeneous multiscale method," *Acta Numerica*, vol. 21, pp. 1–87, 2012, Publisher: Cambridge University Press.

[17] W. Ee, B. Engquist, X. Li, W. Ren, and E. Vanden-Eijnden, "Heterogeneous multiscale methods: A review," *Communications in Computational Physics*, vol. 2, Jun. 2007.

[18] J. Pendry, A. Holden, D. Robbins, and W. Stewart, "Magnetism from conductors and enhanced nonlinear phenomena," *IEEE Transactions on Microwave Theory and Techniques*, vol. 47, no. 11, pp. 2075–2084, Nov. 1999, Conference Name: IEEE Transactions on Microwave Theory and Techniques, ISSN: 1557-9670. DOI: 10.1109/22.798002.

[19] G. Bouchitté and D. Felbacq, "Homogenization near resonances and artificial magnetism from dielectrics," *Comptes Rendus Mathematique*, vol. 339, no. 5, pp. 377–382, Sep. 2004, ISSN: 1631-073X. DOI: 10.1016/j.crma.2004.06.018. [Online]. Available: https://www.sciencedirect.com/science/article/pii/S1631073X0400319X (visited on 04/11/2023).

[20] R. V. Kohn and S. P. Shipman, *Magnetism and homogenization of micro-resonators*, arXiv:0712.2210 [math-ph], Dec. 2007. [Online]. Available: http://arxiv.org/abs/0712.2210 (visited on 08/19/2023).

[21] B. Schweizer and M. Urban, "Effective Maxwell's equations in general periodic microstructures," *Applicable Analysis*, vol. 97, no. 13, pp. 2210–2230, 2018, Publisher: Taylor & Francis.

[22] C. Geuzaine and P. Dular, *GetDP*. [Online]. Available: https://getdp.info/.

[23] C. Geuzaine and J.-F. Remacle, *Gmsh*. [Online]. Available: https://gmsh.info/.

[24] A. Bossavit, "Whitney forms: A class of finite elements for three-dimensional computations in electromagnetism," *IEE Proceedings A (Physical Science, Measurement and Instrumentation, Management and Education, Reviews)*, vol. 135, no. 8, pp. 493–500, Nov. 1988, Publisher: IET Digital Library, ISSN: 2053-7905. DOI: `10.1049/ip-a-1.1988.0077`. [Online]. Available: `https://digital-library.theiet.org/content/journals/10.1049/ip-a-1.1988.0077` (visited on 05/03/2023).

[25] R. Zhao, M. Desbrun, G.-W. Wei, and Y. Tong, "3D hodge decompositions of edge- and face-based vector fields," *ACM Transactions on Graphics*, vol. 38, no. 6, pp. 1–13, Nov. 2019, ISSN: 0730-0301, 1557-7368. DOI: `10.1145/3355089.3356546`. [Online]. Available: `https://dl.acm.org/doi/10.1145/3355089.3356546` (visited on 01/27/2022).

[26] J. Chen, R. Zhao, Y. Tong, and G.-W. Wei, *Evolutionary de Rham-Hodge method*, arXiv:1912.12388 [math], Dec. 2019. [Online]. Available: `http://arxiv.org/abs/1912.12388` (visited on 09/13/2023).

[27] H. Bhatia, G. Norgard, V. Pascucci, and P.-T. Bremer, "The Helmholtz-Hodge Decomposition—A Survey," *IEEE Transactions on Visualization and Computer Graphics*, vol. 19, no. 8, pp. 1386–1404, Aug. 2013, Conference Name: IEEE Transactions on Visualization and Computer Graphics, ISSN: 1941-0506. DOI: `10.1109/TVCG.2012.316`.

[28] A. Journeaux, "Modélisation multi-physique en génie électrique. Application au couplage magnéto-thermo-mécanique," Ph.D. dissertation, Université Paris Sud - Paris XI, Nov. 2013. [Online]. Available: `https://tel.archives-ouvertes.fr/tel-00920289` (visited on 03/29/2021).

[29] E. Tonti, "On the Mathematical Structure of a Large Class of Physical Theories," Tech. Rep., Section: Technical Reports. [Online]. Available: `https://apps.dtic.mil/sti/citations/AD0766983` (visited on 06/14/2023).

[30] P. Dular, "Modélisation du champ magnétique et des courants induits dans des systèmes tridimensionnels non linéaires," Publisher: ULiège-Université de Liège, Ph.D. dissertation, Liège, 1994.

[31] A. Bossavit, *Computational electromagnetism: variational formulations, complementarity, edge elements*. Academic Press, 1998.

[32] P. Dular, W. Legros, and A. Nicolet, "Coupling of local and global quantities in various finite element formulations and its application to electrostatics, magnetostatics and magnetodynamics," *IEEE Transactions on Magnetics*, vol. 34, no. 5, pp. 3078–3081, Sep. 1998, Conference Name: IEEE Transactions on Magnetics, ISSN: 1941-0069. DOI: `10.1109/20.717720`.

[33] Q. V. Dang, "Modeling of Electromagnetic Systems by Coupling of Subproblems – Application to Thin Shell Finite Element Magnetic Models," English, Jun. 2013, Publisher: ULiège - Université de Liège. [Online]. Available: https://orbi.uliege.be/handle/2268/147407 (visited on 06/14/2023).

[34] G. Meunier, Ed., *The Finite Element Method for Electromagnetic Modeling*, English, 1st edition. London: Wiley-ISTE, Nov. 2008, ISBN: 978-1-84821-030-1.

[35] O. Biro, C. Paul, K. Preis, and S. Russenschuck, "Ar formulation using edge elements, for the calculation of 3-D fields in superconducting magnets," *IEEE transactions on magnetics*, vol. 35, no. 3, pp. 1391–1393, 1999, Publisher: IEEE. [Online]. Available: https://ieeexplore-ieee-org.sid2nomade-1.grenet.fr/abstract/document/767223/ (visited on 01/03/2024).

[36] P. Ferrouillat, "Développement de formulations éléments finis 3D en potentiel vecteur magnétique : Application aux machines asynchrones en mouvement," Ph.D. dissertation, Université Grenoble Alpes, Dec. 2015. [Online]. Available: https://tel.archives-ouvertes.fr/tel-01273012 (visited on 03/10/2021).

[37] J.-F. Remacle, P. Dular, F. Henrotte, A. Genon, and W. Legros, "On the resolution of magnetostatic and magnetodynamic mixed formulations," *IEEE Transactions on Magnetics*, vol. 33, no. 2, pp. 1768–1771, Mar. 1997, ISSN: 00189464. DOI: 10.1109/20.582616. [Online]. Available: http://ieeexplore.ieee.org/document/582616/ (visited on 01/23/2024).

[38] M. Ohlberger, B. Schweizer, M. Urban, and B. Verfürth, *Mathematical analysis of transmission properties of electromagnetic meta-materials*, arXiv:1809.08824 [math], Sep. 2018. DOI: 10.48550/arXiv.1809.08824. [Online]. Available: http://arxiv.org/abs/1809.08824 (visited on 01/16/2023).

[39] J. Ruuskanen *et al.*, "Multiharmonic Multiscale Modeling in 3-D Nonlinear Magnetoquasistatics: Composite Material Made of Insulated Particles," in *Computer Methods in Applied Mechanics and Engineering*, submitted.

[40] P. Monk and D. o. M. S. P. M. PH, *Finite Element Methods for Maxwell's Equations*. Clarendon Press, Apr. 2003, Google-Books-ID: zI7Y1jT9pCwC, ISBN: 978-0-19-850888-5.

[41] A. A. Rodríguez and A. Valli, *Eddy Current Approximation of Maxwell Equations_ Theory, Algorithms and Applications*, Springer-Verlag Italia. 2010, ISBN: 978-88-470-1505-0.

[42] Z. Tang, "Estimateurs d'erreur a posteriori résiduels en éléments finis pour la résolution de problèmes d'électromagnétisme en formulations potentielles," These de doctorat, Lille 1, Nov. 2012. [Online]. Available: http://www.theses.fr/2012LIL10136 (visited on 02/26/2021).

[43] M. Desbrun, E. Kanso, and Y. Tong, “Discrete Differential Forms for Computational Modeling,” in *Discrete Differential Geometry*, ser. Oberwolfach Seminars, A. I. Bobenko, J. M. Sullivan, P. Schröder, and G. M. Ziegler, Eds., Basel: Birkhäuser, 2008, pp. 287–324, isbn: 978-3-7643-8621-4. doi: `10.1007/978-3-7643-8621-4_16`. [Online]. Available: `https://doi.org/10.1007/978-3-7643-8621-4_16` (visited on 02/02/2022).

[44] J. C. Nedelec, “Mixed finite elements in ?3,” *Numerische Mathematik*, vol. 35, no. 3, pp. 315–341, Sep. 1980, issn: 0029-599X, 0945-3245. doi: `10.1007/BF01396415`. [Online]. Available: `http://link.springer.com/10.1007/BF01396415` (visited on 11/09/2023).

[45] J. Webb, “Hierarchal vector basis functions of arbitrary order for triangular and tetrahedral finite elements,” *IEEE Transactions on Antennas and Propagation*, vol. 47, no. 8, pp. 1244–1253, Aug. 1999, Conference Name: IEEE Transactions on Antennas and Propagation, issn: 1558-2221. doi: `10.1109/8.791939`.

[46] P. Raviart and J. Thomas, “A mixed finite element method for 2-nd order elliptic problems,” *Mathematical Aspects of Finite Element Methods*, pp. 292–315, 1977, Publisher: Springer.

[47] F. Moukalled, L. Mangani, and M. Darwish, “The Finite Volume Method,” in *The Finite Volume Method in Computational Fluid Dynamics*, vol. 113, Series Title: Fluid Mechanics and Its Applications, Cham: Springer International Publishing, 2016, pp. 103–135, isbn: 978-3-319-16873-9 978-3-319-16874-6. doi: `10.1007/978-3-319-16874-6_5`. [Online]. Available: `https://link.springer.com/10.1007/978-3-319-16874-6_5` (visited on 11/09/2023).

[48] D. M. Copeland and U. Langer, “Domain decomposition solvers for nonlinear multiharmonic finite element equations,” *Journal of Numerical Mathematics*, vol. 18, no. 3, Jan. 2010, issn: 1570-2820, 1569-3953. doi: `10.1515/jnum.2010.008`. [Online]. Available: `https://www.degruyter.com/document/doi/10.1515/jnum.2010.008/html` (visited on 01/26/2024).

[49] E. Hairer and G. Wanner, *Solving Ordinary Differential Equations II: Stiff and Differential-Algebraic Problems*. 1996, vol. 14, isbn: 978-3-642-05220-0. doi: `10.1007/978-3-540-78862-1`.

[50] R. Lamour, R. März, and C. Tischendorf, *Differential-Algebraic Equations: A Projector Based Analysis*. Springer Science & Business Media, Jan. 2013, Google-Books-ID: Ca1AAAAAQBAJ, isbn: 978-3-642-27555-5.

[51] J. Verbeke and R. Cools, “The Newton-Raphson method,” *International Journal of Mathematical Education in Science and Technology*, vol. 26, no. 2, pp. 177–193, Mar. 1995, ISSN: 0020-739X, 1464-5211. DOI: 10.1080/0020739950260202. [Online]. Available: http://www.tandfonline.com/doi/abs/10.1080/0020739950260202 (visited on 11/09/2023).

[52] Y. Okamoto, K. Fujiwara, and R. Himeno, “Exact Minimization of Energy Functional for NR Method With Line-Search Technique,” *IEEE Transactions on Magnetics*, vol. 45, no. 3, pp. 1288–1291, Mar. 2009, Conference Name: IEEE Transactions on Magnetics, ISSN: 1941-0069. DOI: 10.1109/TMAG.2009.2012599.

[53] V. Pellissier, E. Rodriguez, and G. Meunier, “Method for determining relaxation factor for modified Newton-Raphson method for non-linear systems,” in *Proc. COMPUMAG Conf.*, 2011, pp. 826–827.

[54] C. Geuzaine, B. Meys, F. Henrotte, P. Dular, and W. Legros, “A Galerkin projection method for mixed finite elements,” *IEEE Transactions on Magnetics*, vol. 35, no. 3, pp. 1438–1441, May 1999, Conference Name: IEEE Transactions on Magnetics, ISSN: 1941-0069. DOI: 10.1109/20.767236.

[55] Zhuoxiang Ren, “Influence of the RHS on the convergence behaviour of the curl-curl equation,” *IEEE Transactions on Magnetics*, vol. 32, no. 3, pp. 655–658, May 1996, Conference Name: IEEE Transactions on Magnetics, ISSN: 1941-0069. DOI: 10.1109/20.497323.

[56] F. Bachinger, U. Langer, and J. Schöberl, “Numerical analysis of nonlinear multiharmonic eddy current problems,” *Numerische Mathematik*, vol. 100, no. 4, pp. 593–616, Jun. 2005, ISSN: 0945-3245. DOI: 10.1007/s00211-005-0597-2. [Online]. Available: https://doi.org/10.1007/s00211-005-0597-2 (visited on 06/02/2023).

[57] E. Creusé, P. Dular, and S. Nicaise, “About the gauge conditions arising in Finite Element magnetostatic problems,” *Computers & Mathematics with Applications*, vol. 77, no. 6, pp. 1563–1582, Mar. 2019, ISSN: 08981221. DOI: 10.1016/j.camwa.2018.06.030. [Online]. Available: https://linkinghub.elsevier.com/retrieve/pii/S0898122118303547 (visited on 01/27/2021).

[58] P. Ferrouillat, C. Guérin, G. Meunier, B. Ramdane, and A. Carpentier, “Direct computation of current density to solve 3D electric conduction problems using facet elements with FEM,” *International Journal of Numerical Modelling: Electronic Networks, Devices and Fields*, vol. 27, no. 3, pp. 400–417, 2014, _eprint: https://onlinelibrary.wiley.com/doi/pdf/10.1002/jnm.1952, ISSN: 1099-1204. DOI: 10.1002/jnm.1952. [Online]. Available: https://onlinelibrary.wiley.com/doi/abs/10.1002/jnm.1952 (visited on 06/05/2023).

[59] M. Darbas, J. Heleine, and S. Lohrengel, "A Method With Penalized Right Hand Side For The Numerical Resolution Of The Curl Curl Equation," working paper or preprint, Jan. 2018. [Online]. Available: https://hal.archives-ouvertes.fr/hal-01681590 (visited on 03/04/2021).

[60] Y. Saad, *Iterative methods for sparse linear systems*. SIAM, 2003.

[61] A. Quarteroni and A. Valli, *Numerical Approximation of Partial Differential Equations*. Springer Science & Business Media, Sep. 2008, Google-Books-ID: UdLr_sttd4QC, ISBN: 978-3-540-85267-4.

[62] Z. Tang, Y. Zhao, and Z. Ren, "Auto-Gauging of Vector Potential by Parallel Sparse Direct Solvers—Numerical Observations," *IEEE Transactions on Magnetics*, vol. 55, no. 6, pp. 1–5, Jun. 2019, Conference Name: IEEE Transactions on Magnetics, ISSN: 1941-0069. DOI: 10.1109/TMAG.2019.2892868.

[63] F. Rapetti, F. Dubois, and A. Bossavit, "Discrete Vector Potentials for Nonsimply Connected Three-Dimensional Domains," *SIAM Journal on Numerical Analysis*, vol. 41, no. 4, pp. 1505–1527, Jan. 2003, Publisher: Society for Industrial and Applied Mathematics, ISSN: 0036-1429. DOI: 10.1137/S0036142902412646. [Online]. Available: https://epubs.siam.org/doi/10.1137/S0036142902412646 (visited on 03/04/2021).

[64] O. Bíró and A. Valli, "The Coulomb gauged vector potential formulation for the eddy-current problem in general geometry: Well-posedness and numerical approximation," *Computer Methods in Applied Mechanics and Engineering*, vol. 196, no. 13, pp. 1890–1904, Mar. 2007, ISSN: 0045-7825. DOI: 10.1016/j.cma.2006.10.008. [Online]. Available: https://www.sciencedirect.com/science/article/pii/S0045782506003422 (visited on 06/02/2023).

[65] R. M. Bozorth, *Ferromagnetism* (Bell Telephone Laboratories series), eng. New York: Van Nostrand, 1951, OCLC: 1540975.

[66] P. R. Amestoy, I. S. Duff, J.-Y. L'Excellent, and J. Koster, "MUMPS: A general purpose distributed memory sparse solver," in *International Workshop on Applied Parallel Computing*, Springer, 2000, pp. 121–130.

[67] J. Hagedorn, F. S.-L. Blanc, and J. Fleischer, Eds., *Handbook of Coil Winding*. Berlin, Heidelberg: Springer Berlin Heidelberg, 2018, ISBN: 978-3-662-54401-3 978-3-662-54402-0. DOI: 10.1007/978-3-662-54402-0. [Online]. Available: http://link.springer.com/10.1007/978-3-662-54402-0 (visited on 01/29/2024).

[68] O. Garcia, *Winding image*, en. [Online]. Available: https://pixabay.com/photos/magneto-stator-coil-coil-electrical-6374434/ (visited on 02/01/2024).

[69] D. DeMaw, *Ferromagnetic-core design and application handbook*. Prentice-Hall, 1981, ISBN: 0-13-314088-1. [Online]. Available: https://cir.nii.ac.jp/crid/1130282269312670592 (visited on 01/29/2024).

[70] *Transformer image*. [Online]. Available: https://www.desertcart.com.py/products/174914490-electronic-spices-220-v-ac-to-24-0-24-12-ac-current-5-a-step-down-vertical-mount-electric-power-transformer-5000-m-a (visited on 02/01/2024).

[71] C. Oikonomou, "Surface Characterization of Soft Magnetic Composite Powder and Compacts," Chalmers Tekniska Hogskola (Sweden), 2014.

[72] J. Vesa and P. Rasilo, "Producing 3-D Imitations of Soft Magnetic Composite Material Geometries," *IEEE Transactions on Magnetics*, Jul. 2019. DOI: 10.1109/TMAG.2019.2925580.

[73] L. A. Caudillo-Mata, "Multiscale and upscaling methods for geophysical electromagnetic forward modeling," eng, Ph.D. dissertation, University of British Columbia, 2017. DOI: 10.14288/1.0357172. [Online]. Available: https://open.library.ubc.ca/soa/cIRcle/collections/ubctheses/24/items/1.0357172 (visited on 01/16/2023).

[74] X. Ren, "Modélisation semi-analytique des pertes par courants de Foucault dans les matériaux composites," PhD Thesis, Université Paris-Saclay (ComUE), 2017. [Online]. Available: https://www.theses.fr/2017SACLS159 (visited on 02/05/2024).

[75] A. H. Sihvola, *Electromagnetic mixing formulas and applications*. Iet, 1999. [Online]. Available: https://books.google.com/books?hl=fr&lr=&id=uIHSNwxBxjgC&oi=fnd&pg=IA3&dq=A.+Sihvola,+Electromagnetic+mixing+formulas+and+applications,+IEEE+Electromagnetic+Waves+Series,+47),+1999.&ots=0fXzVzH09j&sig=YR8N85AeJuoNmBAr-zOFqMfUw2U (visited on 02/05/2024).

[76] P. Queffelec, D. Bariou, and P. Gelin, "A predictive model for the permeability tensor of magnetized heterogeneous materials," en, *IEEE Transactions on Magnetics*, vol. 41, no. 1, pp. 17–23, Jan. 2005, ISSN: 0018-9464. DOI: 10.1109/TMAG.2004.837755. [Online]. Available: http://ieeexplore.ieee.org/document/1381502/ (visited on 02/05/2024).

[77] L. Daniel and R. Corcolle, "A Note on the Effective Magnetic Permeability of Polycrystals," en, *IEEE Transactions on Magnetics*, vol. 43, no. 7, pp. 3153–3158, Jul. 2007, ISSN: 0018-9464. DOI: 10.1109/TMAG.2007.896228. [Online]. Available: http://ieeexplore.ieee.org/document/4252285/ (visited on 02/05/2024).

[78] L. Daniel, O. Hubert, and R. Billardon, "Homogenisation of magneto-elastic behaviour: From the grain to the macro scale," *Computational & Applied Mathematics*, vol. 23, pp. 285–308, 2004, Publisher: SciELO Brasil. [Online]. Available: https://www.scielo.br/j/cam/a/M7kp44x67bJVYNVbMyCwgQR/?lang=en&format=html (visited on 02/05/2024).

[79] J. Gyselinck, P. Dular, L. Krähenbühl, and R. V. Sabariego, "Finite-Element Homogenization of Laminated Iron Cores With Inclusion of Net Circulating Currents Due to Imperfect Insulation," *IEEE Transactions on Magnetics*, vol. 52, no. 3, pp. 1–4, Mar. 2016, Conference Name: IEEE Transactions on Magnetics, ISSN: 1941-0069. DOI: 10.1109/TMAG.2015.2488038. [Online]. Available: https://ieeexplore.ieee.org/abstract/document/7293636 (visited on 01/29/2024).

[80] F. Purnode, F. Henrotte, F. Caire, J. D. Silva, G. Louppe, and C. Geuzaine, "A Material Law Based on Neural Networks and Homogenization for the Accurate Finite Element Simulation of Laminated Ferromagnetic Cores in the Periodic Regime," *IEEE Transactions on Magnetics*, vol. 58, no. 9, pp. 1–4, Sep. 2022, ISSN: 0018-9464, 1941-0069. DOI: 10.1109/TMAG.2022.3160651. [Online]. Available: https://ieeexplore.ieee.org/document/9743882/ (visited on 01/29/2024).

[81] M. Schöbinger and K. Hollaus, "A Novel MSFEM Approach Based on the A-Formulation for Eddy Currents in Iron Sheets," *IEEE Transactions on Magnetics*, vol. 59, no. 5, pp. 1–4, May 2023, ISSN: 0018-9464, 1941-0069. DOI: 10.1109/TMAG.2023.3238121. [Online]. Available: https://ieeexplore.ieee.org/document/10024987/ (visited on 01/29/2024).

[82] T. Matsuo, "Hysteretic magnetic field analysis with Second-Order homogenization," *Journal of Magnetism and Magnetic Materials*, vol. 591, p. 171 713, Feb. 2024, ISSN: 0304-8853. DOI: 10.1016/j.jmmm.2024.171713. [Online]. Available: https://www.sciencedirect.com/science/article/pii/S0304885324000027 (visited on 01/29/2024).

[83] J. Gyselinck and P. Dular, "Frequency-domain homogenization of bundles of wires in 2-D magnetodynamic FE calculations," *IEEE transactions on magnetics*, vol. 41, no. 5, pp. 1416–1419, 2005, Publisher: IEEE. [Online]. Available: https://ieeexplore-ieee-org.sid2nomade-1.grenet.fr/abstract/document/1430873/ (visited on 01/29/2024).

[84] J. Gyselinck, R. V. Sabariego, and P. Dular, "Time-domain homogenization of windings in 2-D finite element models," *IEEE transactions on magnetics*, vol. 43, no. 4, pp. 1297–1300, 2007, Publisher: IEEE. [Online]. Available: https://ieeexplore-ieee-org.sid2nomade-1.grenet.fr/abstract/document/4137727/ (visited on 01/29/2024).

[85] T. Y. Hou and X.-H. Wu, “A multiscale finite element method for elliptic problems in composite materials and porous media,” *Journal of computational physics*, vol. 134, no. 1, pp. 169–189, 1997, Publisher: Elsevier.

[86] J. Fish, *Practical Multiscaling*. John Wiley & Sons, Sep. 2013, Google-Books-ID: sXuwAAAAQBAJ, ISBN: 978-1-118-53485-4.

[87] T. J. R. Hughes, “Multiscale phenomena: Green’s functions, the Dirichlet-to-Neumann formulation, subgrid scale models, bubbles and the origins of stabilized methods,” *Computer Methods in Applied Mechanics and Engineering*, vol. 127, no. 1, pp. 387–401, Nov. 1995, ISSN: 0045-7825. DOI: 10.1016/0045-7825(95)00844-9. [Online]. Available: https://www.sciencedirect.com/science/article/pii/0045782595008449 (visited on 08/09/2023).

[88] G. Allaire, “Introduction To Homogenization Theory,” 2010. [Online]. Available: https://www.semanticscholar.org/paper/INTRODUCTION-TO-HOMOGENIZATION-THEORY-Allaire/17ac3fa1ca448eb5febf1f9a7899c8cbb5c20193 (visited on 10/04/2023).

[89] Y. Amirat and V. Shelukhin, “Homogenization of time harmonic Maxwell equations and the frequency dispersion effect,” *Journal de Mathématiques Pures et Appliquées*, vol. 95, no. 4, pp. 420–443, Apr. 2011, ISSN: 0021-7824. DOI: 10.1016/j.matpur.2010.10.007. [Online]. Available: https://www.sciencedirect.com/science/article/pii/S0021782410001248 (visited on 01/05/2022).

[90] A. Bensoussan, J.-L. Lions, and G. Papanicolaou, *Asymptotic analysis for periodic structures*. American Mathematical Soc., 2011, vol. 374.

[91] J. Ruuskanen *et al.*, “Multiharmonic Multiscale Modeling in 3-D Nonlinear Magnetoquasistatics,” in *EMF’2023-The 13th International Symposium on Electric and Magnetic Fields*, Marseille, 2023.

[92] C. Vassallo, *Electromagnétisme classique dans la matiere*. Dunod, 1980.

[93] S. Chikazumi, *Physics of ferromagnetism*. Oxford university press, 1997, ISBN: 978-0-19-956481-1. [Online]. Available: https://books.google.com/books?hl=fr&lr=&id=PMURDAAAQBAJ&oi=fnd&pg=PR7&dq=Chikazumi,+Physics+of+Magnetism&ots=sMggK07nQy&sig=0wRi6EkEZ4xnmAEo0fPHzKVVbfw (visited on 01/14/2024).

[94] G. Russakoff, “A Derivation of the Macroscopic Maxwell Equations,” *American Journal of Physics*, vol. 38, no. 10, pp. 1188–1195, Oct. 1970, ISSN: 0002-9505. DOI: 10.1119/1.1976000. [Online]. Available: https://doi.org/10.1119/1.1976000 (visited on 07/20/2023).

[95] D. J. Griffiths, *Introduction to Electrodynamics*, English, 4th edition. Cambridge: Cambridge University Press, Jul. 2017, ISBN: 978-1-108-42041-9.

[96] E. M. Purcell and D. J. Morin, *Electricity and magnetism*. Cambridge university press, 2013.

[97] I. Bardi, J. Tharp, and R. Petersson, "Homogenization of Periodic Structures Using the FEM," *IEEE Transactions on Magnetics*, vol. 50, no. 2, pp. 157–160, Feb. 2014, Conference Name: IEEE Transactions on Magnetics, ISSN: 1941-0069. DOI: `10.1109/TMAG.2013.2282532`.

[98] G. Bouchitté, C. Bourel, and D. Felbacq, "Homogenization of the 3D Maxwell system near resonances and artificial magnetism," *Comptes Rendus Mathematique*, vol. 347, no. 9-10, pp. 571–576, 2009, Publisher: Elsevier.

[99] G. Bouchitté and B. Schweizer, "Homogenization of Maxwell's Equations in a Split Ring Geometry," *Multiscale Modeling & Simulation*, vol. 8, pp. 717–750, Jan. 2010. DOI: `10.1137/09074557X`.

[100] G. Bouchitté, C. Bourel, and D. Felbacq, "Homogenization Near Resonances and Artificial Magnetism in Three Dimensional Dielectric Metamaterials," *Archive for Rational Mechanics and Analysis*, vol. 225, no. 3, pp. 1233–1277, Sep. 2017, ISSN: 0003-9527, 1432-0673. DOI: `10.1007/s00205-017-1132-1`. [Online]. Available: `http://link.springer.com/10.1007/s00205-017-1132-1` (visited on 09/26/2023).

[101] B. Schweizer, "Resonance Meets Homogenization: Construction of Meta-Materials with Astonishing Properties," *Jahresbericht der Deutschen Mathematiker-Vereinigung*, vol. 119, no. 1, pp. 31–51, Mar. 2017, ISSN: 0012-0456, 1869-7135. DOI: `10.1365/s13291-016-0153-2`. [Online]. Available: `http://link.springer.com/10.1365/s13291-016-0153-2` (visited on 09/26/2023).

[102] R. Lipton and B. Schweizer, "Effective Maxwell's equations for perfectly conducting split ring resonators," *Archive for Rational Mechanics and Analysis*, vol. 229, pp. 1197–1221, 2018, Publisher: Springer.

[103] D. Felbacq and G. Bouchitté, "Homogenization of a set of parallel fibres," *Waves in Random Media*, vol. 7, no. 2, p. 245, Apr. 1997, ISSN: 0959-7174. DOI: `10.1088/0959-7174/7/2/006`. [Online]. Available: `https://dx.doi.org/10.1088/0959-7174/7/2/006` (visited on 09/26/2023).

[104] D. Felbacq, "Anomalous homogeneous behaviour of metallic photonic crystals," *Journal of Physics A: Mathematical and General*, vol. 33, no. 4, pp. 815–821, Feb. 2000, ISSN: 0305-4470, 1361-6447. DOI: `10.1088/0305-4470/33/4/314`. [Online]. Available: `https://iopscience.iop.org/article/10.1088/0305-4470/33/4/314` (visited on 10/04/2023).

[105] G. Meunier, O. Maloberti, and A. Kedous-Lebouc, "Pertes dynamiques dans les matériaux magnétiques," *Revue internationale de génie électrique*, vol. 10, no. 2-3, pp. 303–332, Jun. 2008, ISSN: 1295490X. DOI: 10.3166/rige.11.303-332. [Online]. Available: http://rige.revuesonline.com/article.jsp?articleId=11941 (visited on 04/25/2022).

[106] C. A. Gonano, R. E. Zich, and M. Mussetta, "Definition For Polarization P And Magnetization M Fully Consistent With Maxwell's Equations," *Progress In Electromagnetics Research B*, vol. 64, pp. 83–101, 2015, ISSN: 1937-6472. DOI: 10.2528/PIERB15100606. [Online]. Available: http://www.jpier.org/PIERB/pier.php?paper=15100606 (visited on 06/08/2023).

[107] A. Quarteroni, R. Sacco, and F. Saleri, *Numerical mathematics*. Springer Science & Business Media, 2006, vol. 37, ISBN: 978-0-387-98959-4. [Online]. Available: https://books.google.com/books?hl=en&lr=&id=31m4ahn_KfkC&oi=fnd&pg=PA3&dq=info:Ile_kLLWtuIJ:scholar.google.com&ots=MOUXKFDmeB&sig=DEIKaC_RE_ElNLSnRt-LFBWRC7Y (visited on 01/11/2024).

[108] I. Niyonzima, R. V. Sabariego, P. Dular, F. Henrotte, and C. Geuzaine, "Computational Homogenization for Laminated Ferromagnetic Cores in Magnetodynamics," *IEEE Transactions on Magnetics*, vol. 49, no. 5, pp. 2049–2052, May 2013, Conference Name: IEEE Transactions on Magnetics, ISSN: 1941-0069. DOI: 10.1109/TMAG.2012.2237546.

[109] A. K. Amert, V. V. Gozhenko, and K. W. Whites, "Calculation of effective material parameters by field averaging over lattices with non-negligible unit cell size," *Applied Physics A*, vol. 109, no. 4, pp. 1007–1013, Dec. 2012, ISSN: 0947-8396, 1432-0630. DOI: 10.1007/s00339-012-7382-8. [Online]. Available: http://link.springer.com/10.1007/s00339-012-7382-8 (visited on 01/23/2024).

[110] P. Angot, J.-P. Caltagirone, and P. Fabrie, "Fast discrete Helmholtz–Hodge decompositions in bounded domains," *Applied Mathematics Letters*, vol. 26, no. 4, pp. 445–451, 2013, Publisher: Elsevier.

[111] A. Lemoine, "Décomposition de Hodge-Helmholtz discrète," Ph.D. dissertation, Université de Bordeaux, 2014.

[112] A. Marteau *et al.*, "Magnetic Field Upscaling and B-Conforming Magnetoquasistatic Multiscale Formulation," *IEEE Transactions on Magnetics*, vol. 59, no. 5, pp. 1–4, May 2023, Conference Name: IEEE Transactions on Magnetics, ISSN: 1941-0069. DOI: 10.1109/TMAG.2023.3235208.

[113] *GRICAD*. [Online]. Available: https://gricad.univ-grenoble-alpes.fr/index.html (visited on 12/06/2023).

[114] *Nic5*. [Online]. Available: https://www.ceci-hpc.be/clusters.html#nic5 (visited on 12/06/2023).

[115] S. Danisch and J. Krumbiegel, "Makie.jl: Flexible high-performance data visualization for Julia," *Journal of Open Source Software*, vol. 6, no. 65, p. 3349, Sep. 2021, ISSN: 2475-9066. DOI: 10.21105/joss.03349. [Online]. Available: https://joss.theoj.org/papers/10.21105/joss.03349 (visited on 12/06/2023).

[116] H. Akima, "A New Method of Interpolation and Smooth Curve Fitting Based on Local Procedures," *Journal of the ACM*, vol. 17, no. 4, pp. 589–602, Oct. 1970, ISSN: 0004-5411, 1557-735X. DOI: 10.1145/321607.321609. [Online]. Available: https://dl.acm.org/doi/10.1145/321607.321609 (visited on 12/08/2023).

[117] A. Visintin, "Electromagnetic processes in doubly-nonlinear composites," *Communications in Partial Differential Equations*, vol. 33, pp. 808–841, 2008.

[118] G. Schwarz, *Hodge Decomposition - A Method for Solving Boundary Value Problems*, en. Springer, Nov. 2006, ISBN: 978-3-540-49403-4.

[119] S. Wang and A. Chern, "Computing minimal surfaces with differential forms," en, *ACM Transactions on Graphics*, vol. 40, no. 4, pp. 1–14, Aug. 2021, ISSN: 0730-0301, 1557-7368. DOI: 10.1145/3450626.3459781. [Online]. Available: https://dl.acm.org/doi/10.1145/3450626.3459781 (visited on 09/14/2023).

Appendix A

Appendix

A.1 Electromagnetism quantities and their SI unit.

The following table summarizes up the main quantities used in electromagnetism along with their symbols, SI units and names.

Name	Symbol	SI unit	SI name	SI base unit	Other SI unit
Physical quantities					
Current	I	A	Ampere	A	-
Charge	q	C	Coulomb	s.A	-
Voltage	U	V	Volt	$kg.m^2.s^{-3}.A^{-1}$	$W.A^{-1}$ or $J.C^{-1}$
Magnitec flux	Φ	Wb	Weber	$kg.m^2.s^{-2}.A^{-1}$	$V.S^{-1}$
Resistance	R	Ω	Ohm	$kg^1.m^2.s^{-3}.A^{-2}$	$V.A^{-1}$ or $J.S.C^{-2}$
Conductance	G	S	Siemens	$kg^{-1}.m^{-2}.s^3.A^2$	Ω^{-1}
Inductance	L	H	Henry	$kg.m^2.s^{-2}.A^{-2}$	$Wb.A^{-1}$
Capacitance	C	F	Farad	$kg^{-1}.m^{-2}.s^4.A^2$	$C.V^{-1}$ or $C^2.J^{-1}$
Local fields					
Magnetic flux density	$\boldsymbol{b}$	T	Tesla	$kg.s^{-2}.A^{-1}$	$Wb.m^{-2}$
Magnetic field strength	$\boldsymbol{h}$	$A.m^{-1}$	-	$m^{-1}.A$	-
Electric field strength	$\boldsymbol{e}$	$V.m^{-1}$	-	$kg.m.s^{-3}.A^{-1}$	-
Electric displacement	$\boldsymbol{d}$	$C.m^{-2}$	-	$m^{-2}.s.A$	-
Free current density	$\boldsymbol{j}$	$A.m^{-2}$	-	$m^{-2}.A$	-
Electric charge density	ρ	$C.m^{-3}$	-	$m^{-3}.s.A$	-
Magnetization	$\boldsymbol{m}$	$A.m^{-1}$	-	$m^{-1}.A$	-
Polarization	$\boldsymbol{p}$	$C.m^{-2}$	-	$m^{-2}.s.A$	-
Electric vector potential	$\boldsymbol{t}$	$V.m^{-1}$	-	$kg.m.s^{-3}.A^{-1}$	-
Magnetic vector potential	$\boldsymbol{a}$	T.m	-	$kg.m.s^{-2}.A^{-1}$	$Wb.m^{-1}$
Electric scalar potential	v	V	-	$kg.m^2.s^{-3}.A^{-1}$	-
Magnetic scalar potential	φ	A	-	A	-
Poynting vector	$\boldsymbol{s}$	$w.m^{-2}$	-	$kg.s^{-3}$	-
Material law tensors					
(Vacuum) Permeability	$\mu_0, \boldsymbol{\mu}$	$H.m^{-1}$	-	$kg.m.s^{-2}.A^{-2}$	$N.A^{-2}$
(Vacuum) Reluctivity	$\nu_0, \boldsymbol{\nu}$	$m.H^{-1}$	-	$kg^{-1}.m^{-1}.s^2.A^2$	$A^2.N^{-1}$
(Vacuum) Permittivity	$\varepsilon_0, \boldsymbol{\varepsilon}$	$F.m^{-1}$	-	$kg^{-1}.m^{-3}.s^4.A^2$	$C.V^{-1}.m^{-1}$
Conductivity	σ	$S.m^{-1}$	-	$kg^{-1}.m^{-3}.s^3.A^2$	$\Omega^{-1}.m^{-1}$
Resistivity	ρ	$\Omega.m$	-	$kg.m^3.s^{-3}.A^{-2}$	$m.S^{-1}$

Table A.1: Summary table of electromagnetism quantities and their SI unit.

A.2 Inverse Fröhlich-Kennelly nonlinear magnetic law

The analytic Fröhlich-Kennelly nonlinear magnetic $\boldsymbol{b}(\boldsymbol{h})$ law was introduced in 1.3.4. The analytic inverse law, that is the associated $\boldsymbol{h}(\boldsymbol{b})$ law, is defined by the reluctivity

$$\nu(\boldsymbol{b}) = \frac{2B_s}{c_1(\|\boldsymbol{b}\|) + c_2(\|\boldsymbol{b}\|)} \tag{A.1}$$

with

$$\begin{aligned} c_1(\|\boldsymbol{b}\|) &= \mu_0\mu_{r,\max}B_s - \mu_0(\mu_{r,\max} - 1)\|\boldsymbol{b}\|, \\ c_2(\|\boldsymbol{b}\|) &= \sqrt{c_1(\|\boldsymbol{b}\|)^2 + c_3\|\boldsymbol{b}\|}, \\ c_3 &= 4B_s\mu_0^2(\mu_{r,\max} - 1). \end{aligned}$$

The Jacobian matrix of the law is given by

$$\frac{\partial \boldsymbol{h}}{\partial \boldsymbol{b}}(\boldsymbol{b}) = \nu(\boldsymbol{b})I_3 + \frac{1}{\|\boldsymbol{b}\|}\frac{\partial \nu(\boldsymbol{b})}{\partial \|\boldsymbol{b}\|}\boldsymbol{b} \otimes \boldsymbol{b} \tag{A.2}$$

where

$$\frac{\partial \nu(\boldsymbol{b})}{\partial \|\boldsymbol{b}\|} = \frac{\mu_0}{2}(\mu_{r,\max} - 1)\nu(\boldsymbol{b})^2 + \frac{1}{B_s}\left(1 + \frac{c_1(\|\boldsymbol{b}\|) - 4B_s\mu_0}{c_2(\|\boldsymbol{b}\|)}\right). \tag{A.3}$$

It can be verified that $\boldsymbol{h}(\boldsymbol{b})$ is equivalent to $\frac{1}{\mu_0\mu_{r,\max}}\boldsymbol{b}$ near $\|\boldsymbol{b}\| = 0$ and to $\frac{1}{\mu_0}\boldsymbol{b}$ for $\|\boldsymbol{b}\| \gg B_s$.

A.3 On the choice of smoothing kernel for spatial homogenization

The macroscopic homogenized fields are classically defined as the spatial average of the fine scale fields by a convolution with a smoothing kernel [94, 92, 1]. The choice of kernel is not necessarily obvious. To be considered a smoothing or averaging kernel, it should be a function that is:

- positive,
- symmetric around zero (to be anisotropic),
- of integral 1 (to just average without "increasing the amount of field").

Still, there is a lot of choice of smoothing kernels. Two examples of smoothing kernels are the *constant* kernel (shown in Figure A.1) and the Gaussian kernel (Figure A.3. In 1D, the constant kernel is a rectangle of width L, its support, and height $\frac{1}{L}$ (so its area is 1). This corresponds to the cell volume average classically used in periodic homogenization.

The point of this section is to show the difference between possible kernels, and to show that when there is enough scale separation between the fine and macroscopic scales, all

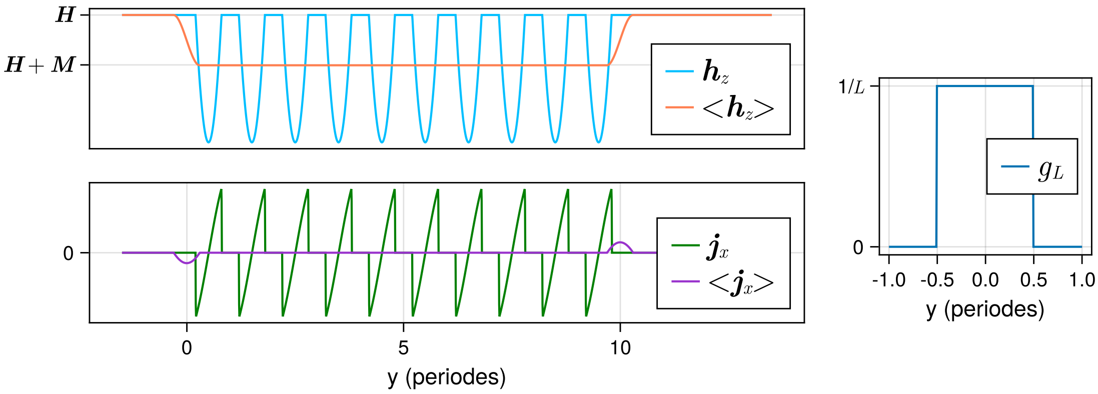

Figure A.1: Fine-scale periodic fields (left) smoothed using a kernel g_L constant on its support (on the right), the physical meaning of this example is described in Section 2.2.2. This kernel corresponds to the cell average used in periodic homogenization, it is efficient on perfectly periodic functions.

averaging kernels lead to equivalent macroscopic fields, as long as they produce smooth fields. Indeed, a smoothing can only define a macroscopic field if the result has very slow and smooth variation at the fine scale. Otherwise, the macroscopic value of the field is ambiguous or noisy, as the field should be studied at the fine scale to define its value.

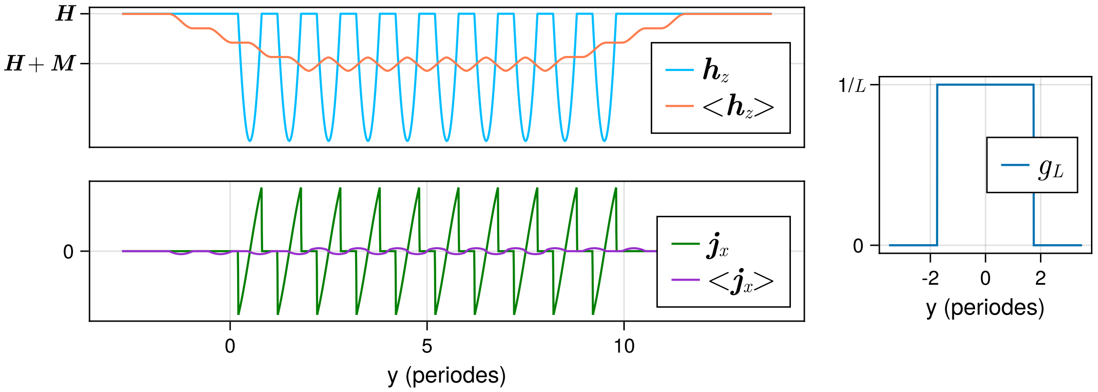

Figure A.2: Fine-scale periodic fields (left) smoothed using a constant kernel g_L of support width different from that of the period of the signal (on the right). The result is not smooth because this kernel does not filter the variations of spatial period different from its support (or higher harmonics). For this reason, this kernel cannot be used on arbitrary fine-scale fields, except if they are arbitrarily periodized in a RVE containing a representative portion of material.

For example, usage of the constant kernel of support different from the spatial period of the field is shown in Figure A.2. This behavior would also happen if the material has a stochastic fine scale structure. A solution to this is using a smoothing kernel that filters more spatial frequencies, like the Gaussian kernel used in Figure A.3.

It is important to note that the constant kernel of correct support and the Gaussian kernel lead to the same macroscopic fields. Indeed, the only difference between the smoothed fields in Figures A.2 and A.3 is how "diluted" the variations of the fields are. But when zooming out at the macroscopic scale, those variations are not possible to distinguish (the dilution spread the result on a distance not larger than the kernel support, which should be chosen smaller than the macroscopic resolution). Also, the field $\boldsymbol{h}_z$ in the material and the surface field $\langle \boldsymbol{j}_x \rangle$ at the material boundary have the same value independently of the choice of kernel.

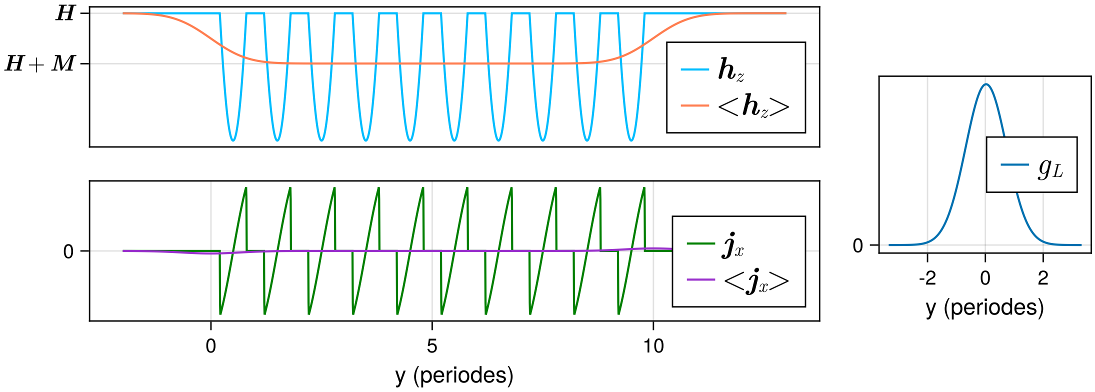

Figure A.3: Fine-scale periodic fields (left) smoothed using a Gaussian kernel g_L (on the right). This kernel efficiently smoothes all spatial frequencies, field Looked at the fine scale, the smoothed fields are less precisely defined than when using the cell average because the Gaussian has a wider support. But it leads to the same macroscopic fields, because the strength of the magnetization, that is the magnetic field discontinuity at the material boundary, is the same.

The smoother the smoothing kernel is near its support boundary, the better it is at handling various frequencies of the fine scale variation of the field. The ultimate kernel for that is the Gaussian kernel, because its smoothing ability is equivalent for on all frequencies, this is because its Fourier transform is very smooth (it is itself). This point is detailed in [92], but this is standard signal processing theory.

Also, the Gaussian kernel has the following remarkable property: repeatedly smoothing a function with any kernel tends to be equivalent to doing a smoothing by a Gaussian kernel, when the number of smoothing tends to infinity[1]. So even if it is tempting to repeat the smoothing operation if a first smoothing was not effective enough, like in Figure A.2, it might just be better to use an adapted smoothing kernel from the start, the default choice being the Gaussian kernel.

In general, choosing another kernel than the Gaussian one requires having knowledge on the frequency content of the fine scale variation of the field, e.g. periodicity.

---

[1] This is the central limit theorem from statistics, considering that the composition of the convolutions is the characteristic function of the sum of random variables following the same probabilistic law, and one of the kernels is the characteristics function of the aforementioned law.

A.4 Mathematic tools for the study of the cell fields

A.4.1 Helmoltz-Hodge decomposition of periodic cell fields

A periodic field $\boldsymbol{h}_p \in \boldsymbol{L}^{2,\#}(Y)$ can be uniquely decomposed[2] in

$$\boldsymbol{h}_p = \mathbf{grad}\, \varphi_p + \mathbf{curl}\, \boldsymbol{\theta}_p + \langle\, \boldsymbol{h}_p \,\rangle_Y \tag{A.4}$$

where $\varphi_p \in H^{\#}(\mathbf{grad}; Y)$, $\boldsymbol{\theta}_p \in \boldsymbol{H}^{\#}(\mathbf{curl}; Y)$ and$\langle\, \boldsymbol{h}_p \,\rangle_Y \in \mathbb{R}^3$. Morover, the decomposition is orthogonal for the $\boldsymbol{L}^{2,\#}(Y)$-norm, that is:

$$\begin{aligned}
&\int_Y \mathbf{grad}\, \varphi_p \cdot \mathbf{curl}\, \boldsymbol{\theta}_p{}' = 0, && \int_Y \mathbf{grad}\, \varphi_p \cdot \boldsymbol{C} = 0,\\
&\int_Y \mathbf{curl}\, \boldsymbol{\theta}_p \cdot \mathbf{grad}\, \varphi_p{}' = 0, && \int_Y \mathbf{curl}\, \boldsymbol{\theta}_p \cdot \boldsymbol{C} = 0,\\
&\int_Y \langle\, \boldsymbol{h}_p \,\rangle_Y \cdot \mathbf{curl}\, \boldsymbol{\theta}_p{}' = 0, && \int_Y \langle\, \boldsymbol{h}_p \,\rangle_Y \cdot \mathbf{grad}\, \varphi_p{}' = 0,
\end{aligned} \tag{A.5}$$

for all $\boldsymbol{\theta}_p{}' \in \boldsymbol{H}^{\#}(\mathbf{curl}; Y)$, $\varphi_p{}' \in H^{\#}(\mathbf{grad}; Y)$ and $\boldsymbol{C} \in \mathbb{R}^3$ (including $\boldsymbol{\theta}_p$, φ_p and $\langle\, \boldsymbol{h}_p \,\rangle_Y$ respectively).

The decomposition can be applied to fields $\boldsymbol{h}_p \in \boldsymbol{H}^{\#}(\mathbf{curl}; Y)$ or $\boldsymbol{b}_p \in \boldsymbol{H}^{\#}(\mathrm{div}; Y)$ because these two spaces are subspaces of $\boldsymbol{L}^{2,\#}(Y)$, so such $\boldsymbol{h}_p$ and $\boldsymbol{b}_p$ are in $\boldsymbol{L}^{2,\#}(Y)$.

This decomposition is obtained using to the one to one pairing between the periodic fields in Y and the fields in the periodized cell $\mathcal{Y}$, which has the topology of the torus $\mathbb{T}^3$. Indeed, $\mathcal{Y}$ is defined by setting identical the opposite faces of ∂Y, as described in [117, Section 3]. As a result, $\mathcal{Y}$ has no boundary and any field defined on $\mathcal{Y}$ can be identified with a periodic field in Y, as described in [21, Section 2.1]. The decomposition (A.4) results from taking in $\boldsymbol{L}^{2,\#}(Y)$ the usual three term HHD of vector fields [118, Corolary 3.5.2][3] written for fields in $\boldsymbol{L}^2(\mathcal{Y})$.

Furthermore, we should detail why the third term of (A.4) is a constant field in Y, and why it is the volume average of the decomposed field $\boldsymbol{h}_p$. This third term is the harmonic part of the decomposition, meaning it has a null curl and divergence. In general, there are two kinds of harmonic field: the cohomology harmonic fields that exist due to the topology of the domain, and those that are due to field entering the domain via its boundary [25].

The latter can always be expressed both as the gradient of a scalar potential φ_H and as the curl of a vector potential $\boldsymbol{\theta}_H$ that are respectively solution of scalar and vector Laplace problems $\Delta\varphi_H = 0$ and $\boldsymbol{\Delta\theta}_H = \boldsymbol{0}$ in $\mathcal{Y}$ [25]. But these fields cannot exist if the domain

---

[2] The decomposition is unique, but the potentials φ_p and $\boldsymbol{\theta}_p$ are not unique unless appropriate gauge conditions are applied.

[3] As the author mentions, the regularity can be chosen as $\boldsymbol{L}^2(\mathcal{Y})$ like in [118, Theorem 2.4.2].

has no boundary. For example, there is:

$$0 = \int_{\mathcal{Y}} \Delta\varphi_H \, \varphi' = \int_{\mathcal{Y}} \mathbf{grad}\,\varphi_H \cdot \mathbf{grad}\,\varphi' + \int_{\partial\mathcal{Y}} \mathbf{grad}\,\varphi_H \cdot \boldsymbol{n}\varphi'$$

for all $\varphi' \in H(\mathbf{grad};\mathcal{Y})$. But as $\partial\mathcal{Y} = \emptyset$, the boundary integral vanishes and there is $\int_{\mathcal{Y}} \mathbf{grad}\,\varphi_H \cdot \mathbf{grad}\,\varphi' = 0$, which implies $\|\mathbf{grad}\,\varphi_H\|_{\boldsymbol{L}^2(\mathcal{Y})} = 0$ if choosing $\varphi' = \varphi_H$. As a consequence, any such harmonic field $\mathbf{grad}\,\varphi_H$ is zero. The same computation can be made if the harmonic field is written $\mathbf{curl}\,\boldsymbol{\theta}_H$.

In summary, the space in which lives the third term in (A.4) is the unique space such that:

- its fields are harmonic (null curl and divergence),
- its fields are $\boldsymbol{L}^2(\mathcal{Y})$ orthogonal to the curls and gradients,
- is of dimension $3 = \beta_1(\mathcal{Y}) = \beta_2(\mathcal{Y})$, the Betti numbers of $\mathbb{T}^3$ (see [119, Section 2.6]).

But as the space of constant fields in $\mathcal{Y}$ (i.e. $\{\boldsymbol{C}(y) = \boldsymbol{C} \in \mathbb{R}^3 \mid \boldsymbol{y} \in \mathcal{Y}\}$) fulfills all the properties, it is the correct harmonic space of (A.4). Finally, using the Y volume average on both sides of

$$\boldsymbol{h}_p = \mathbf{grad}\,\varphi_p + \mathbf{curl}\,\boldsymbol{\theta}_p + \boldsymbol{C}$$

yields $\langle\, \boldsymbol{h}_p \,\rangle_Y = \boldsymbol{C}$, explaining why the harmonic term in (A.4) is written $\langle\, \boldsymbol{h}_p \,\rangle_Y$.

A.4.2 Proofs of properties of the cell fields

Proof of equation (2.41)

The edge average (2.25) uses path integrals over the twelve edges of Y. But via the gradient theorem for path integrals (1.29), the path integrals of gradients of potential fields can be computed using the difference of the value of the potential field at the boundary of the path. For cell edges, those are the corners of the cell. But due to the periodicity, this difference vanishes for periodic potentials, hence $\langle\, \mathbf{grad}\,\varphi_p \,\rangle_{\gamma_Y} = \mathbf{0}$ in (2.41).

Similarly, the face normal average (2.26) uses flux integral through the six faces of Y. Using the Stokes theorem (1.30), the flux integrals through a surface of the curls of strength fields can be computed using the path integral of the field itself on the boundary of the surface. For the faces of the cell, the boundary is the set of four bounding edges. But due to the periodicity, the path integral over these edges cancel for periodic strength fields, hence $\langle\, \mathbf{curl}\,\boldsymbol{h}_p \,\rangle_{\partial Y_\perp} = \mathbf{0}$ in (2.41).

A.4.3 Theorems on the cell distribution of magnetization and polarization

Theorems 2.1, 2.2 and 2.3 on the distribution of $\mathscr{M}_{\varepsilon\to\mathrm{H}}$ in the cell

In the following proofs, $\boldsymbol{h} \in \boldsymbol{H}^{\#}(\mathbf{curl}; Y)$ is a periodic strength field split in $\boldsymbol{h} = \boldsymbol{H} + \boldsymbol{h}_c$, where $\boldsymbol{H} := \langle \boldsymbol{h} \rangle_{\gamma_Y}$ and $\langle \boldsymbol{h}_c \rangle_{\gamma_Y} = \mathbf{0}$. We are interested in proving some formulation that help computing the macroscopic magnetization $\mathscr{M}_{\varepsilon\to\mathrm{H}} := \langle \boldsymbol{h}_c \rangle_Y$ using the local currents $\mathbf{curl}\,\boldsymbol{h}$, in order to compute $\boldsymbol{H} = \langle \boldsymbol{h} \rangle_Y - \mathscr{M}_{\varepsilon\to\mathrm{H}}$. The following proofs show why $\mathscr{M}_{\varepsilon\to\mathrm{H}}$ depends on $\mathbf{curl}\,\boldsymbol{h}$ but not on $\operatorname{div}\boldsymbol{h}$. This is due to the fact that a change of the divergence of a periodic strength field $\boldsymbol{h}_c$ is equivalent to a change of its gradient component in its HHD (A.4), but as the edge average of a periodic gradient is zero (2.41), such a change does not affect the edge average of $\boldsymbol{h}_c$.

Proof of Theorem 2.1
Let $\widetilde{\boldsymbol{h}_c} \in \boldsymbol{H}^{\#}(\mathbf{curl}; Y)$ be a solution of

$$\begin{cases} \mathbf{curl}\,\widetilde{\boldsymbol{h}_c} = \mathbf{curl}\,\boldsymbol{h} \quad \text{in } Y, & \text{(A.6)} \\ \left\langle \widetilde{\boldsymbol{h}_c} \right\rangle_{\gamma_Y} = \mathbf{0}. & \text{(A.7)} \end{cases}$$

The HHD (A.4) applied to $\boldsymbol{h}$ and $\widetilde{\boldsymbol{h}_c}$ yields

$$\boldsymbol{h} = \mathbf{grad}\,\varphi_p + \mathbf{curl}\,\boldsymbol{\theta}_p + \langle \boldsymbol{h} \rangle_Y , \tag{A.8}$$

$$\widetilde{\boldsymbol{h}_c} = \mathbf{grad}\,\widetilde{\varphi_p} + \mathbf{curl}\,\widetilde{\boldsymbol{\theta}_p} + \left\langle \widetilde{\boldsymbol{h}_c} \right\rangle_Y , \tag{A.9}$$

where $\boldsymbol{\theta}_p, \widetilde{\boldsymbol{\theta}_p} \in \boldsymbol{H}^{\#}(\mathbf{curl}; Y)$ and $\varphi_p, \widetilde{\varphi_p} \in H^{\#}(\mathbf{grad}; Y)$.

Let us show that $\mathbf{curl}\,\boldsymbol{\theta}_p = \mathbf{curl}\,\widetilde{\boldsymbol{\theta}_p}$. Plugging the decompositions (A.8)-(A.9) into (A.6) gives

$$\mathbf{curl}\,\mathbf{curl}\,\boldsymbol{\theta}_p = \mathbf{curl}\,\mathbf{curl}\,\widetilde{\boldsymbol{\theta}_p} \quad \text{in } Y$$

because the other HHD terms are curl free. If we multiply this equation by test functions $\boldsymbol{\theta}_p{}' \in \boldsymbol{H}^{\#}(\mathbf{curl}; Y)$ and integrate it over Y, there is

$$\int_Y \mathbf{curl}\left(\mathbf{curl}\,\boldsymbol{\theta}_p\right) \cdot \boldsymbol{\theta}_p{}' = \int_Y \mathbf{curl}\left(\mathbf{curl}\,\widetilde{\boldsymbol{\theta}_p}\right) \cdot \boldsymbol{\theta}_p{}'.$$

Then, performing an integration by part and regrouping the terms give

$$\int_Y \mathbf{curl}\left(\boldsymbol{\theta}_p - \widetilde{\boldsymbol{\theta}_p}\right) \cdot \mathbf{curl}\,\widetilde{\boldsymbol{\theta}_p}{}' = 0 \tag{A.10}$$

where the boundary terms disappear due to the periodic boundary conditions. Indeed, $\int_{\partial Y} (\mathbf{curl}\,\boldsymbol{\theta}_p \times \boldsymbol{n}) \cdot \boldsymbol{\theta}_p{}' = \int_{\partial Y} (\boldsymbol{\theta}_p{}' \times \mathbf{curl}\,\boldsymbol{\theta}_p) \cdot \boldsymbol{n} = 0$, because $\boldsymbol{\theta}_p{}' \times \mathbf{curl}\,\boldsymbol{\theta}_p$ is ∂Y-periodic, so its normal trace is zero. Both curls are in the Hilbert space $\mathcal{V} = \mathbf{curl}\,\boldsymbol{H}^{\#}(\mathbf{curl}; Y)$ and the equation (A.10) holds for all $\mathbf{curl}\,\boldsymbol{\theta}_p{}' \in \mathcal{V}$. So by choosing $\widetilde{\boldsymbol{\theta}_p}{}' = (\boldsymbol{\theta}_p - \widetilde{\boldsymbol{\theta}_p})$ we get $\mathbf{curl}\left(\boldsymbol{\theta}_p - \widetilde{\boldsymbol{\theta}_p}\right) = \mathbf{0}|_{\mathcal{V}}$, that is

$$\mathbf{curl}\,\boldsymbol{\theta}_p = \mathbf{curl}\,\widetilde{\boldsymbol{\theta}_p}. \tag{A.11}$$

We can now compute $\left\langle \widetilde{\boldsymbol{h}_c} \right\rangle_{\gamma_Y}$ and $\langle \boldsymbol{h} \rangle_{\gamma_Y}$ to conclude, the former is:

$$\begin{aligned}
\mathbf{0} \overset{(A.7)}{=} \left\langle \widetilde{\boldsymbol{h}_c} \right\rangle_{\gamma_Y} &\overset{(A.9)}{=} \left\langle \mathbf{curl}\,\widetilde{\boldsymbol{\theta}_p} + \mathbf{grad}\,\widetilde{\varphi_p} + \left\langle \widetilde{\boldsymbol{h}_c} \right\rangle_Y \right\rangle_{\gamma_Y} \\
&\overset{(2.41)}{=} \left\langle \mathbf{curl}\,\widetilde{\boldsymbol{\theta}_p} \right\rangle_{\gamma_Y} + \left\langle \widetilde{\boldsymbol{h}_c} \right\rangle_Y \\
\mathbf{0} &\overset{(A.11)}{=} \left\langle \mathbf{curl}\,\boldsymbol{\theta}_p \right\rangle_{\gamma_Y} + \left\langle \widetilde{\boldsymbol{h}_c} \right\rangle_Y
\end{aligned} \tag{A.12}$$

and the latter is:

$$\begin{aligned}
\boldsymbol{H} \overset{\text{def.}}{=} \langle \boldsymbol{h} \rangle_{\gamma_Y} &\overset{(A.8)}{=} \left\langle \mathbf{curl}\,\boldsymbol{\theta}_p + \mathbf{grad}\,\varphi_p + \langle \boldsymbol{h} \rangle_Y \right\rangle_{\gamma_Y} \\
\boldsymbol{H} &\overset{(2.41)}{=} \left\langle \mathbf{curl}\,\boldsymbol{\theta}_p \right\rangle_{\gamma_Y} + \langle \boldsymbol{h} \rangle_Y.
\end{aligned} \tag{A.13}$$

Finally, plugging (A.13) into (A.12) to eliminate $\mathbf{curl}\,\boldsymbol{\theta}_p$ yields

$$\left\langle \widetilde{\boldsymbol{h}_c} \right\rangle_Y = \langle \boldsymbol{h} - \boldsymbol{H} \rangle_Y = \langle \boldsymbol{h} \rangle_Y - \boldsymbol{H} = \langle \boldsymbol{h}_c \rangle_Y = \mathscr{M}_{\varepsilon\to\mathrm{H}}. \tag{A.14}$$

□

Proof of Theorem 2.2
Direct implication ⇒ :
If $\widetilde{\boldsymbol{h}_c} = \boldsymbol{h}_c$, their curl, divergence and edge averages are equal, so

$$\begin{cases}
\mathbf{curl}\,\widetilde{\boldsymbol{h}_c} = \mathbf{curl}\,\boldsymbol{h}_c = \mathbf{curl}\,(\boldsymbol{h}_c + \boldsymbol{H}) = \mathbf{curl}\,\boldsymbol{h} & \text{in } Y, \\
\operatorname{div}\widetilde{\boldsymbol{h}_c} = \operatorname{div}\boldsymbol{h}_c = \operatorname{div}(\boldsymbol{h}_c + \boldsymbol{H}) = \operatorname{div}\boldsymbol{h} & \text{in } Y, \\
\left\langle \widetilde{\boldsymbol{h}_c} \right\rangle_{\gamma_Y} = \langle \boldsymbol{h}_c \rangle_{\gamma_Y} = \mathbf{0}.
\end{cases}$$

so $\widetilde{\boldsymbol{h}_c}$ is solution of (2.85).

Converse ⇐ :
Let $\widetilde{\boldsymbol{h}_c} \in \boldsymbol{H}^{\#}(\mathbf{curl}; Y)$ be solution of (2.85). As $\widetilde{\boldsymbol{h}_c}$ respects the hypothesis of Theorem 2.1, we can follow the proof of Theorem 2.1 and take the same HHDs (A.8)-(A.9) of $\widetilde{\boldsymbol{h}_c}$ and $\boldsymbol{h}$. We already know that

$$\begin{aligned}
\mathbf{curl}\,\boldsymbol{\theta}_p = \mathbf{curl}\,\widetilde{\boldsymbol{\theta}_p} \quad &\text{in } Y, \quad \text{from (A.11)} \\
\left\langle \widetilde{\boldsymbol{h}_c} \right\rangle_Y = \langle \boldsymbol{h}_c \rangle_Y \quad &\text{in } Y. \quad \text{from (A.14)}
\end{aligned}$$

Additionally, the steps taken to prove (A.11) can be used to prove

$$\mathbf{grad}\, \varphi_p = \mathbf{grad}\, \widetilde{\varphi_p} \quad \text{in } Y, \tag{A.15}$$

using the divergence equality from (2.85) and test functions ${\varphi_p}' \in H^{\#}(\mathbf{grad}; Y)$.

Finally, there is:

$$\begin{aligned}
\widetilde{\boldsymbol{h}_c} &= \mathbf{grad}\, \widetilde{\boldsymbol{\theta}}_p + \mathbf{curl}\, \widetilde{\varphi_p} + \left\langle\, \widetilde{\boldsymbol{h}_c}\, \right\rangle_Y && \text{from (A.9)} \\
&= \mathbf{grad}\, \boldsymbol{\theta}_p + \mathbf{curl}\, \varphi_p + \langle\, \boldsymbol{h}_c\, \rangle_Y && \text{from (A.11)-(A.15)-(A.14)} \\
&= \boldsymbol{h} - \langle\, \boldsymbol{h}\, \rangle_Y + \langle\, \boldsymbol{h}_c\, \rangle_Y && \text{from (A.8)} \\
&= \boldsymbol{h} - \boldsymbol{H} \\
\widetilde{\boldsymbol{h}_c} &= \boldsymbol{h}_c. && \square
\end{aligned}$$

Proof of Theorem 2.3
Let $\widetilde{\boldsymbol{m}_\varepsilon} \in \boldsymbol{H}_0(\mathbf{curl}; Y_\mathrm{C})$ such that

$$\mathbf{curl}\, \widetilde{\boldsymbol{m}_\varepsilon} = \mathbf{curl}\, \boldsymbol{h} \quad \text{in } Y_\mathrm{C}.$$

$\widetilde{\boldsymbol{m}_\varepsilon}$ is extended to the whole cell by setting $\widetilde{\boldsymbol{m}_\varepsilon} = \mathbf{0}$ in Y_N, the result is in $\boldsymbol{H}^{\#}(\mathbf{curl}; Y)$ because $\mathbf{0}\big|_{\partial Y}$ is periodic. Furthermore,

$$\mathbf{curl}\, \widetilde{\boldsymbol{m}_\varepsilon} = \mathbf{curl}\, \boldsymbol{h}$$

holds in Y because the null trace boundary condition of $\widetilde{\boldsymbol{m}_\varepsilon}$ on ∂Y_C, that is $\widetilde{\boldsymbol{m}_\varepsilon} \times \boldsymbol{n}\big|_{\partial Y_\mathrm{C}} = \mathbf{0}$, guarantees its tangential continuity with $\mathbf{0}\big|_{Y_\mathrm{N}}$ at the interface. So there are no surface currents in addition to $\boldsymbol{j}$ in $\mathbf{curl}\, \widetilde{\boldsymbol{m}_\varepsilon}$ on ∂Y_C.

Finally, the edge average of $\widetilde{\boldsymbol{m}_\varepsilon}$ is zero because $\widetilde{\boldsymbol{m}_\varepsilon}$ is null on γ_Y. So $\widetilde{\boldsymbol{m}_\varepsilon}$ fulfills all the hypothesis of Theorem 2.1, which means that

$$\langle\, \widetilde{\boldsymbol{m}_\varepsilon}\, \rangle_Y = \mathscr{M}_{\varepsilon\to\mathrm{H}}. \qquad \square$$

To note, such $\widetilde{\boldsymbol{m}_\varepsilon}$ may not exist if Y_C is not simply connected (if $\beta_1(Y_\mathrm{C}) \neq 0$). In this case, a simply connected domain enclosing Y_C should be used instead of Y_C, e.g. the inside of the convex hull of Y_C.

Analog of the theorems on the cell distribution of $\mathscr{M}_{\varepsilon\to\mathrm{H}}$ relating to that of $\mathscr{P}_{\varepsilon\to\mathrm{H}}$

The three following theorems are analog to the theorems 2.1, 2.2 and 2.3 used to compute the magnetization due to the cell bound current, but they relate to the computation of the polarization due to the cell bound charges. These theorems and their proof are nearly the same as the aforementioned one, but where the role of the curl and edge average is exchanged with the divergence and the boundary normal average.

These results could be useful to upscale the electric displacement $\boldsymbol{d}$ in electrostatic problems, where there are free charges ρ that can only move in Y_{C} but with a null total charge. In other word, when the cell electric displacement $\boldsymbol{d}$ is periodic, $\operatorname{div} \boldsymbol{d} = 0$ in Y_{N} and $\langle \operatorname{div} \boldsymbol{d} \rangle_Y = 0$.

Theorem A.1 *Let $\boldsymbol{d} \in \boldsymbol{H}^{\#}(div; Y)$. We define $\boldsymbol{D} := \langle \boldsymbol{d} \rangle_{\partial Y_\perp}$ the macroscopic value of $\boldsymbol{d}$ and $\mathscr{P}_{\varepsilon\to H} := \langle \boldsymbol{D} - \boldsymbol{d} \rangle_Y$ the polarization created by the displaced charges in Y_{C}.*
If $\widetilde{\boldsymbol{d}}_c \in \boldsymbol{H}^{\#}(div; Y)$ verifies

$$\begin{cases} div\, \widetilde{\boldsymbol{d}}_c = div\, \boldsymbol{d} \quad in\ Y, & \text{(A.16)} \\ \left\langle \widetilde{\boldsymbol{d}}_c \right\rangle_{\partial Y_\perp} = \boldsymbol{0}, & \text{(A.17)} \end{cases}$$

then $\left\langle \widetilde{\boldsymbol{d}}_c \right\rangle_Y = -\mathscr{P}_{\varepsilon\to H}$.

Theorem A.2 *Let $\boldsymbol{d} \in \boldsymbol{H}^{\#}(div; Y)$. Let $\boldsymbol{d}_c := \boldsymbol{d} - \langle \boldsymbol{d} \rangle_{\partial Y_\perp}$ be the periodic correction of $\boldsymbol{d}$.*
A periodic flux field $\widetilde{\boldsymbol{d}}_c \in \boldsymbol{H}^{\#}(div; Y)$ is equal to $\boldsymbol{d}_c$ if and only if

$$\begin{cases} \boldsymbol{curl}\, \widetilde{\boldsymbol{d}}_c = \boldsymbol{curl}\, \boldsymbol{d} \quad in\ Y, \\ div\, \widetilde{\boldsymbol{d}}_c = div\, \boldsymbol{d} \quad in\ Y, \\ \left\langle \widetilde{\boldsymbol{d}}_c \right\rangle_{\partial Y_\perp} = \boldsymbol{0}. \end{cases} \tag{A.18}$$

Theorem A.3 *Let $\boldsymbol{d}$ and $\mathscr{P}_{\varepsilon\to H}$ be defined as in Theorem A.1, and suppose that $div\, \boldsymbol{d} = 0$ in Y_N.*
If there exist $\widetilde{\boldsymbol{p}}_\varepsilon \in \boldsymbol{H}_0(div; Y_{\mathrm{C}})$ verifying

$$-\, div\, \widetilde{\boldsymbol{p}}_\varepsilon = div\, \boldsymbol{d} \quad in\ Y_{\mathrm{C}}, \tag{A.19}$$

then $\langle \widetilde{\boldsymbol{p}}_\varepsilon \rangle_Y = \mathscr{P}_{\varepsilon\to H}$ (where $\widetilde{\boldsymbol{p}}_\varepsilon$ is extended by $\boldsymbol{0}$ in Y_N).

Such $\widetilde{\boldsymbol{p}}_\varepsilon$ may not exist if Y_{C} is not connected (if its connected components have net charges). In this case, a connected domain enclosing Y_{C} should be used instead of Y_{C}, e.g. the inside the convex hull of Y_{C}.

List of Figures

List of Tables

Index

Résumé

Les matériaux et structures hétérogènes, tels que les bobines, tôles laminées et composites magnétiques doux (SMC), sont répandus en génie électrique. Ils ont la caractéristique d'être constitués de nombreux éléments plus petits que la taille de l'ensemble, rendant leur simulation numérique difficile.

Cette thèse étudie les méthodes multi-échelles de calcul des champs électromagnétiques permettant la résolution numérique de problèmes 3D non-linéaires transitoires avec forts couplages électromagnétiques, sur des structures ou matériaux hétérogènes de géométrie périodiques. La méthode numérique utilisée est la méthode multi-échelle hétérogène (HMM). Elle est basée sur une hypothèse de séparation d'échelle permettant une homogénéisation du matériau. La loi constitutive équivalente est calculée sur de petits volumes représentatifs aux comportements indépendants, résolus en parallèle aux points macroscopiques où cela est nécessaire.

L'apport principal de ce travail est d'introduire une nouvelle formule d'homogénéisation du champs H, avec plusieurs implémentations numériques. La méthode est robuste à la présence de fort courants localement confinés. Ces développements sont nécessaires à l'utilisation de la formulation B-conforme à haute fréquence. En effet, ces courants créent une aimantation additionnelle responsable d'hystérésis dynamique dans la loi de comportement magnétique macroscopique. Le modèle est validé sur des problèmes 3D linéaires et non-linéaires.

Abstract

Heterogeneous materials and structures, such as coils, laminations and soft magnetic composites (SMCs), are widespread in electrical engineering. They have the characteristic of being made up of many elements smaller than their own size, making their numerical simulation difficult.

This thesis investigates multiscale modeling techniques of electromagnetic field used for the numerical resolution of transient 3D nonlinear problems with strong electromagnetic couplings, on heterogeneous structures or materials with periodic geometries. The numerical method used is the Heterogeneous Multiscale Method (HMM). It is based on a scale separation hypothesis, enabling the homogenization of the material. The equivalent constitutive law is calculated on representative volumes elements with independent behaviors, solved in parallel at the macroscopic points where it is necessary.

The main contribution of this work is to introduce a new homogenization formula for the field H, with several numerical implementations. The method is robust to the presence of strong locally confined currents. These developments are necessary for the use of the B-conform formulation at high frequencies. Indeed, these currents create additional magnetization which is responsible for dynamic hysteresis in the macroscopic magnetic constitutive law. The model is validated on linear and non-linear 3D problems.